Advances in Planar Lipid Bilayers and Liposomes

Volume 6

VOLUME SIX

Advances in Planar Lipid Bilayers and Liposomes

EDITORIAL BOARD

VOLUME SIX

ADVANCES IN PLANAR LIPID BILAYERS AND LIPOSOMES

Editor

A. LEITMANNOVA LIU

Department of Physiology, Michigan State University, East Lansing, Michigan, USA

and

Centre for Interface Sciences, Microelectronics Department, Faculty of Electrical Engineering & Information Technology, Slovak Technical University, Bratislava, Slovak Republic

Founding Editor

H.T. TIEN

Department of Physiology, Michigan State University, East Lansing, Michigan, USA

ELSEVIER

Amsterdam • Boston • Heidelberg • London • New York • Oxford
Paris • San Diego • San Francisco • Singapore • Sydney • Tokyo
Academic Press is an Imprint of Elsevier

ACADEMIC PRESS

Academic Press is an imprint of Elsevier
84 Theobald's Road, London WC1X 8RR, UK
Radarweg 29, PO Box 211, 1000 AE Amsterdam, The Netherlands
Linacre House, Jordan Hill, Oxford OX2 8DP, UK
30 Corporate Drive, Suite 400, Burlington, MA 01803, USA
525 B Street, Suite 1900, San Diego, CA 92101-4495, USA

First edition 2008

ISBN-13: 978-0-12-373902-5
ISSN: 1554-4516

Printed and bound in USA

08 09 10 11 12 10 9 8 7 6 5 4 3 2 1

Contents

Preface *xi*

Contributors *xiii*

1. Stabilization of Hydrophilic Pores in Charged Lipid Bilayers by Anisotropic Membrane Inclusions **1**
Aleš Iglič, and Veronika Kralj-Iglič

1. Introduction 2
2. Geometrical Model of Hydrophilic Pore 3
3. Free Energy of the System 4
4. Electrostatic Energy of the Pore 6
5. Free Energy of the Inclusions 10
6. Theoretical Predictions 14
   6.1. Inclusion-Free Membrane 14
   6.2. Influence of Anisotropic Intrinsic Shape of Membrane Inclusions 15
   6.3. Influence of Salt Concentration (Ionic Stregth) 18
7. On the Role of Anisotropic Membrane Inclusions in Membrane Electroporation-Experimental Consideration 19
8. Discussion and Conclusions 21

References 23

2. Rapid Purification and Reconstruction of Recombinant Voltage-Gated Sodium Channels into Planar BLMs **27**
Yan Li Zhang, Julie E. Dalziel, James Dunlop, and Angelica Leitmannova Liu

1. Voltage-Gated Sodium Channels 28
2. Algal Toxins that Modulate Sodium Channel Activity 29
3. Ion Channels in Bilayer Lipid Membrane Biosensors 30
4. Ion Channel Purification 31
   4.1. Purification of Ion Channels for Reconstitution into pBLMs 31
   4.2. Purification of Ion Channels using Immobilised Metal Affinity Chromatography (IMAC) 31
   4.3. Purification of VGSC for Reconstitution into pBLMs 32
5. Methods 33
   5.1. Addition of His-Tag to *hSkM1* 33
   5.2. VGSC Expression in Insect Cells 34
   5.3. Purification of Recombinant VGSC using IMAC 35
6. Functional Reconstitution 39
   6.1. Reconstitution of Ion Channels into Liposomes 39
   6.2. Incorporation of Proteoliposomes into pBLMs 39
   6.3. Orientation of Reconstituted *hSkM1*-HT Channels in pBLMs 40
   6.4. Pharmacological Function of Reconstituted *hSkM1*-HT 40

7. Conclusion 43
Acknowledgements 44
References 44

3. Insights in the Organization and Dynamics of Erythrocyte Lipid Rafts 49
Ulrich Salzer, Ursula Hunger, and Rainer Prohaska

1. The Erythrocyte Membrane 51
2. Lipid Rafts 52
   2.1. Lipid Phases in Model Membranes and Cell Membranes 52
   2.2. Mutual Influence Between Lipid Phases and Proteins 53
   2.3. Detergent-Resistant Membranes 55
   2.4. Experimental Evidence for Lipid Rafts 55
   2.5. A Revised Version of the Lipid Raft Hypothesis 56
3. DRMs of the Erythrocyte Membrane 57
   3.1. Evidence for the Association of the Cytoskeleton with DRMs 58
   3.2. The Erythrocyte Cytoskeleton – DRM Complex: Possible Connections 65
4. Exovesiculation of Erythrocytes 66
   4.1. Cell Shape and Exovesiclulation 67
   4.2. DRMs of Exovesicles 68
5. Lipid Rafts of Erythrocytes: Hypothetical Considerations 70
   5.1. Rafts, Membrane Curvature and Vesiculation: Theoretical Considerations 72
   5.2. Rafts and Erythrocyte Vesiculation 72
   5.3. Rafts and Malarial Infection 74
6. Conclusions 75
References 75

4. Interactions of Erythroid and Nonerythroid Spectrins and other Membrane-Skeletal Proteins with Lipid Mono- and Bilayers 81
Aleksander F. Sikorski, Aleksander Czogalla, Anita Hryniewicz-Jankowska, Ewa Bok, Ewa Plażuk, Witold Diakowski, Anna Chorzalska, Adam Kolondra, Marek Langner, and Michał Grzybek

1. Introduction 82
2. Spectrin-Based Membrane Skeleton 83
3. Interactions of Erythroid and Nonerythroid Spectrins with Lipid Mono- and Bilayers and other Amphipathic Ligands 84
   3.1. Interaction of Erythroid Spectrin with Phospholipid Mono- and Bilayers, a Historical Perspective of Seventies and Early Eighties 84
   3.2. Binding Lipid Mono- and Bilayers by Spectrins 86
   3.3. Interactions of Erythroid and Nonerythroid Spectrins with Monolayers Prepared from Anionic Phospholipids 88
   3.4. Lipidic Spectrin-Binding Sites in Natural Membranes 88
   3.5. Dependence of Spectrin-Binding on the Fluidity of the Mono- and Bilayers 88
   3.6. Binding of Amphipatic Compounds by Spectrins 89
4. Spectrin–Lipid Interactions; a Molecular Approach 89
   4.1. Lipid-Binding Sites in Spectrins 89

4.2. Ankyrin-Dependent Lipid-Binding Site in β-Spectrins 91
4.3. Structure of Lipid-Binding Site of Ankyrin-Binding Domain 93
4.4. Possible Physiological Role of Spectrin–Phospholipid Interactions 94
5. Interactions of Other Skeletal Proteins with Membrane Mono- and Bilayers 95
5.1. Ankyrins 95
5.2. Protein 4.1 96
5.3. Protein p55 96
6. Concluding Remarks 97
Acknowledgement 97
References 97

5. Liposome-Based Biomembrane Mimetic Systems: Implications for Lipid–Peptide Interactions 103
Karl Lohner, Eva Sevcsik, and Georg Pabst

1. Introduction 104
1.1. Lipid Composition of Mammalian and Bacterial Cell Membranes 105
1.2. Effects of Antimicrobial Peptides on Lipid Bilayers 109
2. Understanding the Mechanism of Lipid–Peptide Interaction 110
2.1. Lipid Affinity of Antimicrobial Peptides Triggered by Electrostatic Interactions – Lipid–Peptide Domain Formation 110
2.2. Membrane Thinning as a Precursor of Pore Formation 113
2.3. Detergent-Like Effect – Micellar Lipid–Peptide Disk Formation 115
2.4. Promotion or Prevention of Non-Lamellar Phases 116
3. General Aspects of Model Membranes 117
3.1. Global and Local Membrane Properties 117
3.2. Domains-Rafts 120
4. X-ray Diffraction in Combination with a Global Data Analysis 121
5. Bacterial Model Membranes 125
6. The Antimicrobial Peptide LF11 – Influence of N-Acylation 127
7. Structural Information on Coexisting Membrane Domains 130
8. Outlook 132
References 132

6. Application of Spin-Labeling EPR and ATR-FTIR Spectroscopies to the Study of Membrane Heterogeneity 139
Janez Štrancar, and Zoran Arsov

1. Introduction 140
2. Experimental Methods to Approach Membrane Heterogeneity 142
2.1. Membrane Exploration by SL-EPR 144
2.2. Membrane Exploration by ATR–FTIR Spectroscopy 147
3. Membrane Hydration 149
3.1. Effect of the Level of Hydration on the Membrane Properties Studied by SL-EPR 149
3.2. Application of ATR–FTIR Spectroscopy to Distinguish Free and Lipid-Bound Water 150

4. Membrane Heterogeneity Characterization by SL-EPR 152
4.1. Comparison of Characterization by Different Spin Probes in Model Membranes 152
4.2. Effect of Spin Probe Partitioning on Membrane Heterogeneity Characterization 155
5. Membrane Heterogeneity Characterization by ATR–FTIR spectroscopy 157
6. Conclusions 160
Acknowledgements 160
References 161

7. Electroporation of Planar Lipid Bilayers and Membranes 165
Mojca Pavlin, Tadej Kotnik, Damijan Miklavčič, Peter Kramar, and Alenka Maček Lebar

1. Introduction 167
2. Experimental Investigation of Electroporation on Planar Lipid Bilayers 169
2.1. Breakdown Voltage 170
2.2. Capacitance 173
2.3. Conductance/Resistance 174
3. Attempts of Theoretical Explanation of Electroporation 175
3.1. The Hydrodynamic Model 177
3.2. The Elastic Model 178
3.3. The Hydroelastic Model 179
3.4. The Viscohydroelastic Model 181
3.5. The Phase Transition Model 183
3.6. The Domain-Interface Breakdown Model 186
3.7. The Aqueous Pore Formation Model 187
3.8. Extensions of the Aqueous Pore Formation Model 192
4. Electroporation of Cells-Experimental Observations and Analysis of Underlying Phenomena 194
4.1. Induced Transmembrane Voltage and Forces on the Cell Membrane 195
4.2. Maxwell Stress Tensor and Forces Acting on a Cell in an External Field 198
4.3. Transport of Molecules Across Permeabilized Membrane 199
4.4. Experimental Studies and Theoretical Analysis of Cell Electroporation *in vitro* 201
5. Comparison between Planar Lipid Bilayers and Cell Electroporation 211
Appendix A 213
A.1. The Instability in the Hydrodynamic Model 213
A.2. The Instability in the Elastic Model 213
A.3. The Instability in the Hydroelastic Model 214
A.4. The Instability in the Viscohydroelastic Model 215
A.5. The Energy of a Hydrophilic Pore 216
Appendix B 217
B.1. Calculation of the Fraction of Surface Area of Transient Pores 217
B.2. Quantification of Ion Diffusion and Long-Lived Pores 218
References 219

8. Cytoskeletal Proteins at the Lipid Membrane **227**
Wolfgang H. Goldmann, Burkhard Bechinger, and Tanmay Lele

1. Introduction *228*
2. Stopped-Flow Spectrophotometer *229*
   2.1. 'Slow' Temperature Jump Apparatus *230*
   2.2. Results *231*
   2.3. Binding Affinity of Myosin II (Associated/Inserted-Lipid) to Actin *232*
3. Differential Scanning Calorimetry (DSC) *233*
   3.1. Results *237*
4. Solid-State NMR Spectroscopy *238*
   4.1. Theory: The Anisotropy of Interactions Measured in Solid-State NMR Spectroscopy *240*
   4.2. Experimental Considerations *241*
   4.3. Results and Discussion *243*
5. Fluorescence Recovery after Photobleaching (FRAP) *244*
   5.1. Focal Adhesions and the Plasma Membrane *246*
   5.2. Quantifying Protein–Protein Binding Kinetics Inside Living Cells *246*
   5.3. Method and Setup of FRAP *246*
   5.4. Results *247*
   5.5. Quantitative Analysis of FRAP Experiments *249*

Acknowledgements *251*
References *251*

Subject Index **257**

Color Section at the End of the Book

This page intentionally left blank

Preface

Volume 6 is a continuation of the research chapters mostly on Bilayer Lipid Membranes (BLMs) based on a historic perspective of the lipid bilayer concept and its experimental realization. Many of the contributing authors collaborated in the past with the late Professor H. Ti Tien, the founding editor of this book series, whose 3rd anniversary of the untimely passing away we just commemorated in May 2007. Professor H. Ti Tien had a great vision of using supported BLMs for biosensors and molecular electronic devices development and dedicated to this research the last decades of his very fruitful scientific life.

In 1961, at the Symposium on the Plasma Membrane, when a group of researchers (Rudin, Mueller, Tien and Wescott) reported the reconstitution of a bimolecular lipid membrane *in vitro*, the report was met with skepticism. The research group began the report with a description of mundane soap bubbles, followed by 'black holes' in soap films, … ending with an invisible 'black' lipid membrane, made from lipid extracts of cow's brains. The reconstituted structure (6–9 nm thick) was created just like a cell membrane separating two aqueous solutions. As one of the members of the amused audience remarked, "… the report sounded like … cooking in the kitchen, rather than a scientific experiment!" That was in 1961, and the first report by the group was published a year later. In reaction to that report, Bangham, the major researcher on liposomes, wrote in a 1996 article entitled 'Surrogate cells or Trojan horses': "… a preprint of a paper was lent to me by Richard Keynes, then Head of the Department of Physiology (Cambridge), and my boss. This paper was a bombshell …. They (Rudin, Mueller, Tien and Wescott) described methods for preparing a membrane … not too dissimilar to that of a node of Ranvier …. The physiologists went mad over the model, referred to as a 'BLM', an acronym for Bilayer or by some for Black Lipid Membrane. They were as irresistible to play with as soap bubbles".

Today, after more than four decades of research and development, BLMs (also referred to nowadays as planar lipid bilayers), along with liposomes, have become established disciplines in certain areas of membrane biophysics and cell biology and in biotechnology. The lipid bilayer, existing in all cell membranes, is most unique, in that it serves not merely as a physical barrier among cells, but functions as a two-dimensional matrix for all sorts of reactions. Also, the lipid bilayer, after suitable modification, acts as a conduit for ion transport, as a framework for antigen–antibody binding, as a bipolar electrode for redox reactions, and as a reactor for energy conversion (e.g., light to electric to chemical). Furthermore, a modified lipid bilayer performs as a transducer for signal transduction (i.e., sensing), and numerous other functions as well. All these myriad activities require the ultrathin lipid bilayer of 5 nm thickness.

As of today, Black Lipid Membranes (BLMs or planar lipid bilayers) have been used in a number of applications ranging from fundamental membrane biophysics

including photosynthesis, practical AIDS research and 'microchips' study. In reactions involving light, BLMs have provided insights to the conversion of solar energy *via* water photolysis, and to photobiology comprising apoptosis and photodynamic therapy. Supported bilayer lipid membranes (s-BLMs) are being used in biosensor development. In addition, this volume reviews the studies of others in collaboration with our laboratory and also recent research of others on the use of BLMs as models of certain biomembranes.

With this background in mind, the present volume of *Advances* series on planar lipid membranes and liposomes continues to include invited chapters on a broad range of topics, ranging from theoretical research to specific studies and experimental methods, but also refers to practical applications in many areas. The author(s) of each chapter present the results of his/her laboratory. We continue in our endeavor to focus with this Series on newcomers in this interdisciplinary field, but we wish also to attract experienced scientists. All chapters in this volume have one feature in common: further exploring theoretically and experimentally the planar lipid bilayer systems and spherical liposomes. We are thankful to all contributor(s) for their expert knowledge in BLM research area, for the shared information about their work and also for their patience in preparation of this volume after unexpected death of the founding editor Professor H. Ti Tien. Their willingness to write these chapters in his memory is very much appreciated by the whole scientific community.

The previous three volumes 3, 4 and 5 of this book series were also dedicated to mark the BLM's 45th anniversary. Now, we intend to invite also some of our colleagues who already contributed to one of our previous volumes. Their work is just a living proof about the importance of this research and its practical applications worldwide.

We, the editor and the editorial board of this *Advances* series, would like to express our gratitude to all contributing authors for writing a chapter and for sharing their latest results. We also very much appreciate the continuous support and help of Dr. Kostas Marinakis, and all his coworkers, especially Deirdre Clark, in different stages of preparation of this book series. We will try our best to keep this *Advances* series alive and to pay in this way our tribute to the scientific work of Professor H. Ti Tien.

Angelica Leitmannova Liu
(Editor)

Contributors

Zoran Arsov
Jožef Stefan Institute, Department of Solid State Physics, Laboratory of Biophysics, Jamova 39, SI-1000 Ljubljana, Slovenia

Burkhard Bechinger
Université Louis Pasteur Strasbourg, CNRS, Institut de Chimie, UMR 7177-LC3, 4, rue Blaise Pascal, 67070 Strasbourg, France

Ewa Bok
Institute of Biochemistry and Molecular Biology, University of Wrocław, ul. Przybyszewskiego 63-77, PL-51-148 Wrocław, Poland

Anna Chorzalska
Institute of Biochemistry and Molecular Biology, University of Wrocław, ul. Przybyszewskiego 63-77, PL-51-148 Wrocław, Poland

Aleksander Czogalla
Institute of Biochemistry and Molecular Biology, University of Wrocław, ul. Przybyszewskiego 63-77, PL-51-148 Wrocław, Poland

Julie E. Dalziel
AgResearch, Grasslands Research Centre, Tennent Drive, Private Bag 11008, Palmerston North 4442, New Zealand

Witold Diakowski
Institute of Biochemistry and Molecular Biology, University of Wrocław, ul. Przybyszewskiego 63-77, PL-51-148 Wrocław, Poland

James Dunlop
AgResearch, Grasslands Research Centre, Tennent Drive, Private Bag 11008, Palmerston North 4442, New Zealand

Wolfgang H. Goldmann
Massachusetts General Hospital, Harvard Medical School, Charlestown, MA 02129, USA and Center for Medical Physics and Technology, Biophysics Group, Friedrich-Alexander-University of Erlangen-Nuremberg, Henkestrasse 91, 91052 Erlangen, Germany

Michał Grzybek

Institute of Biochemistry and Molecular Biology, University of Wrocław, ul. Przybyszewskiego 63-77, PL-51-148 Wrocław, Poland

Academic Centre for Biotechnology of Lipid Aggregates, Przybyszewskiego 63-77, 51148 Wrocław, Poland

Ursula Hunger
Department of Medical Biochemistry, Max F. Perutz Laboratories, Medical University of Vienna, Dr. Bohr-Gasse 9/3, Vienna A-1030, Austria

Anita Hryniewicz-Jankowska
Institute of Biochemistry and Molecular Biology, University of Wrocław, ul. Przybyszewskiego 63-77, PL-51-148 Wrocław, Poland

Aleš Iglič
Laboratory of Physics, Faculty of Electrical Engineering, University of Ljubljana, Tržaška 25, SI-1000 Ljubljana, Slovenia

Adam Kolondra
Institute of Biochemistry and Molecular Biology, University of Wrocław, ul. Przybyszewskiego 63-77, PL-51-148 Wrocław, Poland

Tadej Kotnik
University of Ljubljana, Faculty of Electrical Engineering, Tržaška 25, SI-1000 Ljubljana, Slovenia

Veronika Kralj-Iglič
Laboratory of Clinical Biophysics, Faculty of Medicine, University of Ljubljana, Lipičeva 2, SI-1000 Ljubljana, Slovenia

Peter Kramar
University of Ljubljana, Faculty of Electrical Engineering, Tržaška 25, SI-1000 Ljubljana, Slovenia

Marek Langner
Academic Centre for Biotechnology of Lipid Aggregates, Przybyszewskiego 63-77, 51148 Wrocław, Poland

Alenka Maček Lebar
University of Ljubljana, Faculty of Electric Engineering, Tržaška 25, SI-1000 Ljubljana, Slovenia

Tanmay Lele
Department of Chemical Engineering, University of Florida, Museum Road, Bldg. 723, Gainesville, FL 32611, USA

Angelica Leitmannova Liu
Physiology Department, Biomedical and Physical Sciences Building, Michigan State University, East Lansing, MI 48824, USA

Center for Interface Sciences, Microelectronics Department, Faculty of Electrical Engineering & Information Technology, Slovak Technical University (FEI STU), 812 19 Bratislava, Slovak Republic

Karl Lohner
Institute of Biophysics and Nanosystems Research, Austrian Academy of Sciences, Schmiedlstraße 6, A-8042 Graz, Austria

Damijan Miklavčič
University of Ljubljana, Faculty of Electrical Engineering, Tržaška 25, SI-1000 Ljubljana, Slovenia

Georg Pabst
Institute of Biophysics and Nanosystems Research, Austrian Academy of Sciences, Schmiedlstraße 6, A-8042 Graz, Austria

Mojca Pavlin
University of Ljubljana, Faculty of Electrical Engineering, Tržaška 25, SI-1000 Ljubljana, Slovenia

Ewa Plażuk
Institute of Biochemistry and Molecular Biology, University of Wrocław, ul. Przybyszewskiego 63-77, PL-51-148 Wrocław, Poland

Rainer Prohaska
Department of Medical Biochemistry, Max F. Perutz Laboratories, Medical University of Vienna, Dr. Bohr-Gasse 9/3, Vienna A-1030, Austria

Ulrich Salzer
Department of Medical Biochemistry, Max F. Perutz Laboratories, Medical University of Vienna, Dr. Bohr-Gasse 9/3, Vienna A-1030, Austria

Eva Sevcsik
Institute of Biophysics and Nanosystems Research, Austrian Academy of Sciences, Schmiedlstraße 6, A-8042 Graz, Austria

Aleksander F. Sikorski
Institute of Biochemistry and Molecular Biology, University of Wrocław, ul. Przybyszewskiego 63-77, PL-51-148 Wrocław, Poland

Academic Centre for Biotechnology of Lipid Aggregates, Przybyszewskiego 63-77, 51148 Wrocław, Poland

Janez Štrancar
Jožef Stefan Institute, Department of Solid State Physics, Laboratory of Biophysics, Jamova 39, SI-1000 Ljubljana, Slovenia

Yan Li Zhang
AgResearch, Grasslands Research Centre, Tennent Drive, Private Bag 11008, Palmerston North 4442, New Zealand

This page intentionally left blank

CHAPTER ONE

Stabilization of Hydrophilic Pores in Charged Lipid Bilayers by Anisotropic Membrane Inclusions

Aleš Iglič[1,*], *and* Veronika Kralj-Iglič[2]

Contents

1. Introduction 2
2. Geometrical Model of Hydrophilic Pore 3
3. Free Energy of the System 4
4. Electrostatic Energy of the Pore 6
5. Free Energy of the Inclusions 10
6. Theoretical Predictions 14
   6.1. Inclusion-Free Membrane 14
   6.2. Influence of Anisotropic Intrinsic Shape of Membrane Inclusions 15
   6.3. Influence of Salt Concentration (Ionic Stregth) 18
7. On the Role of Anisotropic Membrane Inclusions in Membrane Electroporation-Experimental Consideration 19
8. Discussion and Conclusions 21
References 23

Abstract

We present theoretical and experimental evidences on stable pores in in the presence of anisotropic membrane inclusions. The model is based on minimization of free energy which involves three contributions: the energy due to the line tension of the lipid bilayer at the rim of the pore, the electrostatic energy of the charged membrane with the pore, and the energy of anisotropic membrane inclusions. In order to calculate the electrostatic energy of the membrane with the pore, the electric potential in the vicinity of an infinite, uniformly charged plate with a circular pore was calculated analytically. It is shown that the optimal pore size in the charged bilayer membrane is determined by the ionic strength of the surrounding electrolyte solution and by the intrinsic shape of the anisotropic membrane inclusions. Saddle-like membrane inclusions favor small pores whereas more wedge-like inclusions give rise to larger pore sizes [1]. For ionic strength

* Corresponding author. Tel.: +386 1 4250 278; Fax: +386 1 4768 850;
E-mail address: ales.iglic@fe.uni-lj.si (A. Iglič).

[1] Laboratory of Physics, Faculty of Electrical Engineering, University of Ljubljana, Tržaška 25, SI-1000 Ljubljana, Slovenia
[2] Laboratory of Clinical Biophysics, Faculty of Medicine, University of Ljubljana, Lipičeva 2, SI-1000 Ljubljana, Slovenia

Advances in Planar Lipid Bilayers and Liposomes, Volume 6
ISSN 1554-4516, DOI 10.1016/S1554-4516(07)06001-2

bellow 0.05 mol/dm^3 the optimal size of the pore strongly increases with decreasing ionic strength. In accordance with theoretical predictions it was indicated experimentally that $C_{12}E_8$-induced anisotropic membrane inclusions may stabilize the hydrophilic pore in the membrane, presumably due to accumulation of $C_{12}E_8$ on toroidally shaped rim of the pore [2].

1. Introduction

The cell membrane is a semi-permeable barrier between the cell interior and its surroundings. One of the mechanisms for transmembrane transport involves the presence of pores in the lipid bilayer, through which a substantial flow of material can take place. For example, pores were observed in red blood cell ghosts [3–5], where the pore size depends on the ionic strength of the surrounding fluid [4].

The formation of pores in the membrane can be induced by application of high-intensity electric pulses of short duration [6]. This phenomenon is known as electroporation and has become widely used in medicine and biology [7–13]. A number of theoretical studies have been made to understand the physical basis of electroporation [14,15]. However, the mechanisms responsible for the energetics and stability of membrane pores still require further clarification.

The formation of hydrophilic pore in a lipid bilayer implies that lipid molecules near the edge of the pore rearrange themselves in a way that their polar head groups shield the hydrocarbon tails from the water [16,17]. In the model the excess energy due to modified packing of the phospholipid molecules at the edge of the pore is described by line tension, which makes the hydrophilic membrane pore energetically unfavorable. On the other hand, there are various examples where membrane pores live long enough to observe them experimentally [4,18,19]. The question arises what mechanisms could be responsible for stabilization of pores.

A possible mechanism has recently been suggested by Betterton and Brenner [20] for charged membranes, which is based on a competition between line tension and electrostatic repulsion between the opposed membrane rims within a pore. An analysis based on linearized Poisson–Boltzmann (PB) theory showed for certain combinations of model parameters the pore becomes energetically stabilized. However, the depth of the minimum is below kT (where k is Boltzmann's constant and T the absolute temperature) so that additional stabilizing effects are required to explain the existence of experimentally observed pores [20].

In this chapter we describe as a possible mechanism for the stabilization of pores in charged bilayer membranes, i.e., the non-homogeneous lateral distribution and orientational ordering of anisotropic membrane inclusions, i.e., their accumulation and orientation at the edge of the pore [1,2].

Anisotropic membrane inclusion may be a single molecule or a small complex of molecules (rigid or flexible) in biological or model membranes. If all in-plane orientations of anisotropic membrane component are not energetically equivalent, then the inclusion is referred to as anisotropic [21,22]. The inclusions may laterally distribute in such way as to minimize the membrane-free energy [21,23–28].

Besides the lateral distribution of membrane constituents in-plane orientational ordering of anisotropic inclusions has recently also been considered [22,29–31]. Non-homogeneous lateral and orientational distributions of anisotropic membrane constituents are internal degrees of freedom. A method has been developed [21,32] starting from the microscopic description of the membrane constituents and applying methods of statistical physics to obtain the membrane-free energy. To obtain the equilibrium configuration of the membrane, the membrane-free energy is minimized taking into account the relevant geometrical constraints. The intrinsic properties of membrane constituents and interactions between them are thereby revealed in the equilibrium shape of the membrane. Here we present this method while focusing on the effect of the intrinsic shape of anisotropic membrane inclusions on the equilibrium configuration of the membrane and the corresponding orientational ordering and lateral distribution of inclusions. The results presented may contribute to understanding the stability of pores in lipid bilayers.

Anisotropic membrane constituents are of special interest for the formation of membrane pores: the pore rim provides a geometry, which anisotropic inclusions favorably interact with [22,32–36]. Of particular interest in this respect are peptide [37–40] or detergent [2,41] stabilization of membrane pore. Detergents and certain antimicrobial peptides are amphipathic, often exhibiting their lytic activity [19,42,43], also through the formation of membrane pores. Antimicrobial peptides are typically elongated in shape, which renders their interaction with curved membranes highly anisotropic. Also the detergents or small complexes of the detergent with the surrounding membrane molecules may be anisotropic with the preference for high curvature of the pore rim due to their large hydrophilic part [2,43]. Examples for anisotropic membrane inclusions also include various lipids [44,45], glycolipids or lipoproteins [46], and gemini detergents [47].

We present the analysis of energetics of a single membrane pore in a binary lipid membrane, consisting of (charged) lipids and anisotropic inclusions [1,2]. The free energy of the inclusion-doped membrane contains the line tension contribution, the interaction energy between the anisotropic inclusions and the membrane, and the electrostatic energy of the charged lipids [1,2].

2. Geometrical Model of Hydrophilic Pore

We consider a planar lipid bilayer membrane that contains a single pore of aperture radius r, as schematically shown in Fig. 1. We locate a Cartesian coordinate system at the pore center with the axis of rotational symmetry (Z-axis) pointing normal to the bilayer midplane. Even though experimentally obtained evidence is currently not available, it seems a reasonable approximation to assume that the lipids within the rim assemble into a semi-toroidal configuration in order to shield the hydrocarbon chains from the contact with the aqueous environment. The bilayer thickness is $2b$.

A parameterization of the semi-toroidal pore is given by $x = b\cos\varphi\,((r/b) + 1 + \cos\theta)$, $y = b\sin\varphi\,((r/b) + 1 + \cos\theta)$, and $z = b\sin\theta$ with $0 \le \varphi \le 2\pi$ and

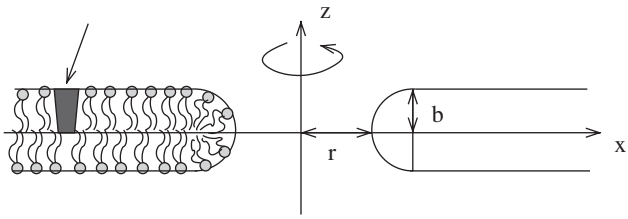

Figure 1 A planar lipid bilayer with a pore in the center [30]. The figure shows the cross-section in the x–z plane. Rotational symmetry around the z-axis is indicated. On the left side, the packing of the lipid molecules is shown schematically. The head groups of lipid molecules are represented by filled circles. The arrow denotes the membrane inclusion which is shown schematically.

$\pi/2 \leq \theta \leq 3\pi/2$. The principal curvatures (for definition see Fig. 2) of the membrane in the region of the pore rim

$$c_1 = \frac{1}{b}, c_2 = \frac{\cos\theta}{r + b(1 + \cos\theta)} \tag{1}$$

and the area element $\mathrm{d}A_P = b[r + b(1 + \cos\theta)]\mathrm{d}\varphi\mathrm{d}\theta$. The local geometry within the rim is saddle-like everywhere, and most pronounced at $\theta = \pi$, where $c_1/c_2 = -r/b$. Note again, the semi-toroidal shape of the pore rim is an assumption; alternative pore shape could be considered but is not expected to alter the conclusions of the present work.

3. Free Energy of the System

To obtain the equilibrium size of the pore, the overall free energy, F, of the pore is minimized. We assume that F is the sum of three contributions:

$$F = W_{\mathrm{edge}} + U_{\mathrm{el}} + F_{\mathrm{i}} \tag{2}$$

where W_{edge} is the energy due to the line tension of a lipid bilayer without the inclusions, U_{el} the electrostatic energy of the charged lipids, and F_{i} the energy due to the interactions between the membrane inclusions and the host membrane. We note that F is *excess* free energy, measured with respect to a planar, pore-free membrane [1].

For an inclusion-free membrane the energy W_{edge} is given by

$$W_{\mathrm{edge}} = 2\pi\Lambda r \tag{3}$$

where r is the radius of the circular membrane pore and Λ the line tension (i.e., excess energy per unit length of the pore edge in the lipid bilayer). One can obtain a rough estimate for Λ on the basis of the elastic energy required to bend a lipid monolayer into a semi-cylindrical pore rim [2,16]. Adopting the usual quadratic curvature expansion for the free energy according to Helfrich [48] one finds [16] $\Lambda = \pi k_c/2b$ where k_{c} is the lipid layers's bending rigidity. For $b = 2.5\,\mathrm{m}$ and

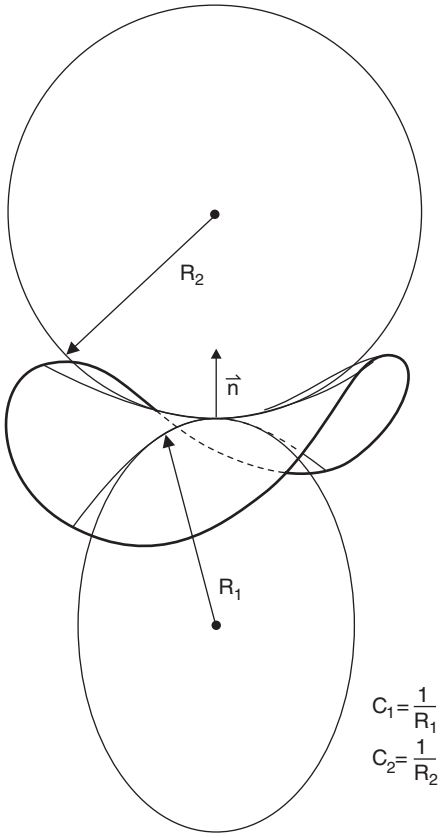

Figure 2 Definition of the two principal curvatures C_1 and C_2 (figure shows the saddle-like geometry).

$k_c = 10\,kT$ the values $\Lambda \approx 6\,kT/\text{nm} \approx 2 \times 10^{-11}\,\text{J/m}$ (at room temperature). This order of magnitude corresponds to experimental results for the line tension of lipid bilayers [18,49,50].

If rigid membrane inclusions are present within the membrane pore they replace some lipids. The replaced lipids do no longer contribute to the line tension W_{edge}. We shall account approximatively for this reduction in line tension by writing

$$W_{\text{edge}} = 2\Lambda(\pi r - N_{\text{P}} R_{\text{i}}) \tag{4}$$

where N_{P} denotes the number of inclusions within the pore rim and $2R_{\text{i}}$ the lateral extension of the cross-sectional shape of the inclusions. Steric interactions limit the number of inclusions within the membrane rim; $N_{\text{P}} \leq N_{\text{P}}^{\max} = \pi r/R_{\text{i}}$. Thus $W_{\text{edge}} \geq 0$, and the line tension always provides a tendency for the pore to shrink.

4. Electrostatic Energy of the Pore

The calculation of the electrostatic energy of the membrane pore follows Betterton and Brenner [20] who have derived an expression valid for a very thin membrane ($b \to 0$) and within linearized PB theory. To keep our model traceable we also adopt the result of linear PB theory where the equation [51]

$$\nabla^2 \phi = \kappa_d^2 \phi \tag{5}$$

determines the (dimensionless) electrostatic potential $\phi = e_0 \Psi / kT$ (electric potential Ψ is measured in mV) at given Debye length $l_D = \kappa_d^{-1}$:

$$\kappa_d = \sqrt{\frac{2 n_0 N_A e_0^2}{\varepsilon_w \varepsilon_0 kT}} \tag{6}$$

where ε_w is the dielectric constant of the aqueous solution, ε_0 the permittivity of free space, n_0 is the ionic strength of the surrounding electrolyte solution (i.e., bulk salt concentration; assuming a 1:1 salt such as NaCl), and N_A Avogadro's number and e_0 is the unit charge.

The solution of linearized PB (i.e., the electric potential Ψ_∞) for the case of infinite flat surface without a pore which satisfies the boundary conditions

$$\phi(z \to \infty) = 0 \tag{7}$$

$$\frac{\partial \phi}{\partial z}(z = 0) = -\frac{\sigma}{\varepsilon_w \varepsilon_0} \tag{8}$$

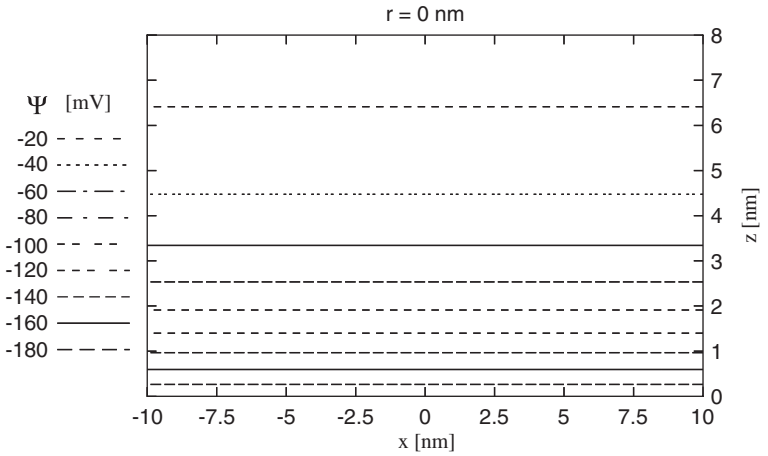

Figure 3 Equipotential surfaces in the vicinity of the charged plane in contact with the electrolyte solution. The values of the model parameters are: $\sigma = -0.05$ Å$/m^2$, $\varepsilon_w = 80$, $1/\kappa_d = 2.8$ *nm* **(adapted from [52]).**

can be written in the form [51] (Fig. 3):

$$\phi_\infty(z) = \frac{\sigma}{\varepsilon_w \varepsilon_0 \kappa_d} e^{-\kappa_d z} \tag{9}$$

where σ is the surface charge density. The solution of the linearized PB equation for planar lipid bilayer with the pore of radius r can be then written as the difference between the electrostatic potential of a flat infinite pore-free membrane (ϕ_∞) and the electrostatic potential of the circular flat membrane segment with the radius r (ϕ_p), both having constant surface charge density σ [52]:

$$\phi(x,z) = \phi_\infty(z) - \phi_p(x,z). \tag{10}$$

The electrical potential of circular flat membrane segment with the surface charge density σ and radius r is calculated using the cylindrical coordinates. For axisymmetric case the linearized PB equation in cylindrical coordinates reads:

$$\frac{1}{x}\frac{\partial}{\partial x}\left(x\frac{\partial \phi_p}{\partial x}\right) + \frac{\partial^2 \phi_p}{\partial z^2} = \kappa_d^2 \phi_p \tag{11}$$

where the origin of coordinate system is located at the pore center with the axis of rotational symmetry (z-axis) pointing normal to the bilayer midplane (Fig. 1). We seek for the solution of equation (11) by the ansatz

$$\phi_p(x,z) = R(x)Z(z) \tag{12}$$

where $R(x)$ is the function of x and $Z(z)$ the function of z. In this way equation (11) yields:

$$\frac{1}{R(x)}\frac{1}{x}\frac{\partial}{\partial x}\left(x\frac{\partial R(x)}{\partial x}\right) + \frac{1}{Z(z)}\frac{\partial^2 Z(z)}{\partial z^2} = \kappa_d^2. \tag{13}$$

Since the first term in equation (13) depends solely on the coordinate x, while the second term is the function of coordinate z only, the sum of both terms can be always equal to the constant κ_d^2 only if both terms are also constant. We take

$$\frac{1}{Z(z)}\frac{\partial^2 Z(z)}{\partial z^2} = \kappa_d^2 + k^2 \tag{14}$$

$$\frac{1}{R(x)}\frac{1}{x}\frac{\partial}{\partial x}\left(x\frac{\partial R(x)}{\partial x}\right) = -k^2. \tag{15}$$

The general solution of equation (14) has the form [53]:

$$Z(z) = Ce^{-\sqrt{\kappa_d^2+k^2}z} + C_1 e^{\sqrt{\kappa_d^2+k^2}z}. \tag{16}$$

By taking into account the boundary condition $\phi(z \to \infty) = 0$ we chose the value $C_1 = 0$ for the constant C_1 in equation (16), therefore:

$$Z = Ce^{-\sqrt{\kappa_d^2 + k^2}z}. \tag{17}$$

Equation (15) is rewritten in the form:

$$x^2 \frac{\partial^2 R}{\partial x^2} + x \frac{\partial R}{\partial x} + k^2 x^2 R = 0. \tag{18}$$

A regular solution of differential equation (18) is the Bessel function of the first kind [53]

$$R = CJ_0(kx). \tag{19}$$

The solution of equation (11) in the form of $\phi_p(x, z) = R(x)Z(z)$ (see equation (12)) is therefore:

$$\phi_p(x, z) = C(k)J_0(kx)e^{-\sqrt{\kappa_d^2 + k^2}z}. \tag{20}$$

The *general* solution of equation (11) is thus:

$$\phi_p(x, z) = \int_0^\infty dk C(k)J_0(kx)e^{-\sqrt{\kappa_d^2 + k^2}z}. \tag{21}$$

In the following equation (21) is first differentiated with respect to the coordinate z:

$$\frac{\partial \phi_p}{\partial z} = \int_0^\infty dk(-\sqrt{\kappa_d^2 + k^2})\, C(k)\, J_0(kx)\, e^{-\sqrt{\kappa_d^2 + k^2}z}. \tag{22}$$

At $z = 0$ it follows from above equation [52]:

$$\frac{\partial \phi_p}{\partial z}|_{z=0} = \int_0^\infty dk(-\sqrt{\kappa_d^2 + k^2})\, C(k)\, J_0(kx). \tag{23}$$

By using the Hankel transformation [53] the values of coefficients $C(k)$ can be calculated from equation (23) as follows:

$$C(k) = -\frac{k}{\sqrt{\kappa_d^2 + k^2}} \int_0^\infty dx\, xJ_0(kx) \frac{\partial \phi_p}{\partial z}|_{z=0}. \tag{24}$$

The integration in equation (24) is divided in to two parts [52]:

$$C(k) = -\frac{k}{\sqrt{\kappa_d^2 + k^2}} \left(\int_0^r dx\, xJ_0(kx) \frac{\partial \phi_p}{\partial z}|_{z=0} + \int_r^\infty dx\, xJ_0(kx) \frac{\partial \phi_p}{\partial z}|_{z=0} \right). \tag{25}$$

By taking into account the boundary conditions:

$$\frac{\partial \phi_{\mathrm{p}}}{\partial z}(z=0) = -\frac{\sigma}{\varepsilon_{\mathrm{w}}\varepsilon_0}, \quad x<r, \tag{26}$$

$$\frac{\partial \phi_{\mathrm{p}}}{\partial z}(z=0) = 0, \quad x \geq r, \tag{27}$$

it follows:

$$C(k) = \frac{\sigma}{k\varepsilon_{\mathrm{w}}\varepsilon_0\sqrt{\kappa_{\mathrm{d}}^2+k^2}}\int_0^r \mathrm{d}(kx)\, kxJ_0(kx). \tag{28}$$

Considering the relations [53],

$$krJ_1(kr) = \int_0^r \mathrm{d}(kx)k\, xJ_0(kx), \tag{29}$$

it follows from equation (28):

$$C(k) = \frac{\sigma r J_1(kr)}{\varepsilon_{\mathrm{w}}\varepsilon_0\sqrt{\kappa_{\mathrm{d}}^2+k^2}}. \tag{30}$$

If the calculated expression for $C(k)$ is inserted in equation (21), the electric potential $\phi_{\mathrm{p}}(x, z)$ can be written as [52]

$$\phi_{\mathrm{p}}(x,z) = \frac{\sigma r}{\varepsilon_{\mathrm{w}}\varepsilon_0}\int_0^\infty \mathrm{d}k \frac{J_0(kx)J_1(kr)}{\sqrt{\kappa_{\mathrm{d}}^2+k^2}}\mathrm{e}^{-\sqrt{\kappa_{\mathrm{d}}^2+k^2}z}, \tag{31}$$

where J_0 and J_1 are Bessel functions. By using equations (9), (10) and (31) we can determine the expression for electric potential of flat charged membrane with circular pore of radius r, being in contact with electrolyte solution [20] (Fig. 4, 5):

$$\phi(x,z) = \frac{\sigma}{\varepsilon_{\mathrm{w}}\varepsilon_0\kappa_{\mathrm{d}}}\mathrm{e}^{-\kappa_{\mathrm{d}}z} - \frac{\sigma r}{\varepsilon_{\mathrm{w}}\varepsilon_0}\int_0^\infty \mathrm{d}k \frac{J_0(kx)J_1(kr)}{\sqrt{\kappa_{\mathrm{d}}^2+k^2}}\mathrm{e}^{-\sqrt{\kappa_{\mathrm{d}}^2+k^2}z}. \tag{32}$$

The electrostatic-free energy [54] can be derived *via* a charging process [51,55]:

$$U_{\mathrm{el,\,tot}} = 2\pi\int_0^\infty \sigma(x)\phi(z=0)\, x\, \mathrm{d}x. \tag{33}$$

Equation (33) is processed analytically by using equation (32). By subtracting the electrostatic energy of the charged pore-free membrane, one obtains an explicit expression for *excess* electrostatic energy of the pore [1,20]:

$$U_{\mathrm{el}} = -\frac{\pi\sigma^2 r^2}{\varepsilon_{\mathrm{w}}\varepsilon_0\kappa_{\mathrm{d}}} + \frac{2\pi\sigma^2 r^3}{\varepsilon_{\mathrm{w}}\varepsilon_0}\int_0^\infty \frac{J_1(x)^2}{x\sqrt{x^2+\kappa_{\mathrm{d}}^2 r^2}}\,\mathrm{d}x. \tag{34}$$

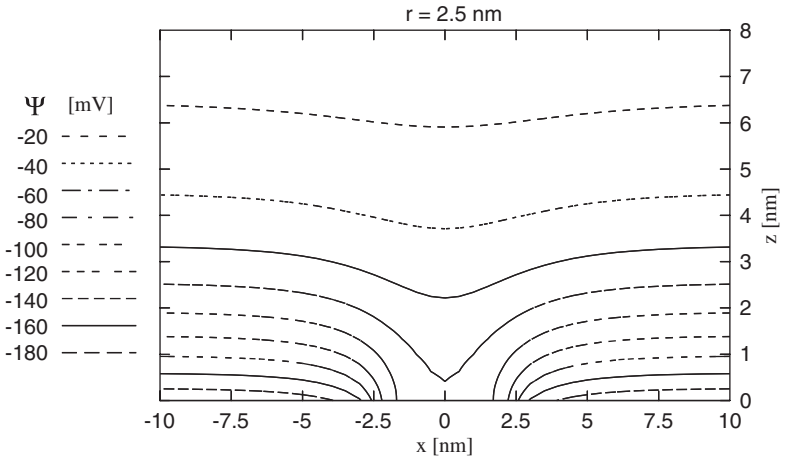

Figure 4 Equipotential surfaces in the vicinity of the charged plane with circular hole. The plane is in contact with the electrolyte solution. The radius of the circular pore (r) is 2.5 nm. The values of the model parameters are: $\sigma = -0.05$ Å$/\mathrm{m}^2$, $\varepsilon_w = 80$, $1/\kappa_\mathrm{d} = 2.8$ *nm* (adapted from [52]).

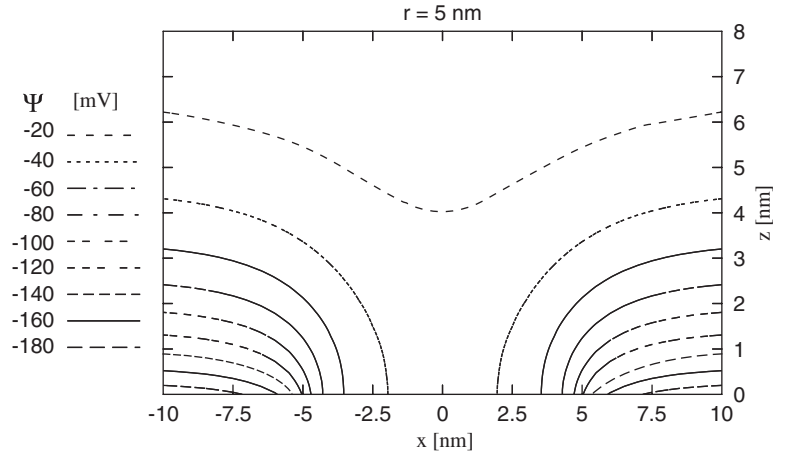

Figure 5 Equipotential surfaces in the vicinity of the charged plane. The plane is in contact with the electrolyte solution. The radius of the circular pore (r) is 5 *nm*. The values of the model parameters are: $\sigma = -0.05$ Å$/\mathrm{m}^2$, $\varepsilon_w = 80$, $1/\kappa_\mathrm{d} = 2.8$ *nm* (adapted from [52]).

5. Free Energy of the Inclusions

Any membrane constituent (single molecule or small complexes of molecules (Fig. 6)) may be treated as membrane inclusion in a two-dimensional continuum curvature field imposed by other membrane constituents. To describe the corresponding free energy, F_i, we use a phenomenological model [32,36,56] where the single-inclusion energy derives from the mismatch between the effective intrinsic

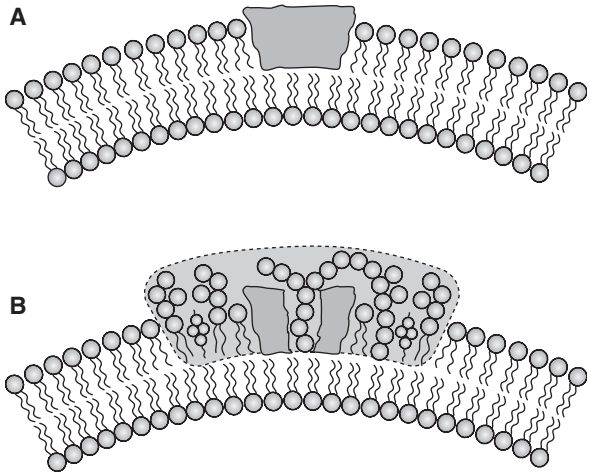

Figure 6 An inclusion can be a single molecule (A) [1] or small (flexible) complex of molecules (B) [60].

shape of the inclusions and the actual shape of the membrane at site of the inclusions. The actual shape of the membrane at the site of the inclusion can be described by the diagonalized curvature tensor $\mathbf{C}$,

$$\mathbf{C} = \begin{bmatrix} C_1 & 0 \\ 0 & C_2 \end{bmatrix}, \tag{35}$$

where C_1 and C_2 are the two principal curvatures (Fig. 2). The intrinsic shape of a given inclusion can be described by the diagonalized curvature tensor $\mathbf{C}_\mathrm{m}$ [32,36],

$$\mathbf{C}_\mathrm{m} = \begin{bmatrix} C_{1\mathrm{m}} & 0 \\ 0 & C_{2\mathrm{m}} \end{bmatrix}, \tag{36}$$

where $C_{1\mathrm{m}}$ and $C_{2\mathrm{m}}$ are two intrinsic principal curvatures of the inclusion (Fig. 7). The intrinsic principal curvatures are in general not identical. If they are identical ($C_{1\mathrm{m}} = C_{2\mathrm{m}}$), the intrinsic shape is isotropic (Fig. 7) and the in-plane orientation of the inclusion is immaterial. If $C_{1\mathrm{m}} \neq C_{2\mathrm{m}}$ the inclusion is called "anisotropic" (Fig. 7) [22,33,36,44,47].

The principal directions of the tensor $\mathbf{C}$ deviate in general from the principal directions of the tensor $\mathbf{C}_\mathrm{m}$; say, a certain angle ω quantifies this mutual rotation. The single-inclusion energy (E_i) can then be expressed in terms of the two invariants (trace and determinant) of the mismatch tensor $\mathbf{M} = \mathbf{R}\mathbf{C}_\mathrm{m}\,\mathbf{R}^{-1} - \mathbf{C}$ where $\mathbf{R}$ is the rotation matrix [56]

$$\mathbf{R} = \begin{bmatrix} \cos\omega & -\sin\omega \\ \sin\omega & \cos\omega \end{bmatrix}. \tag{37}$$

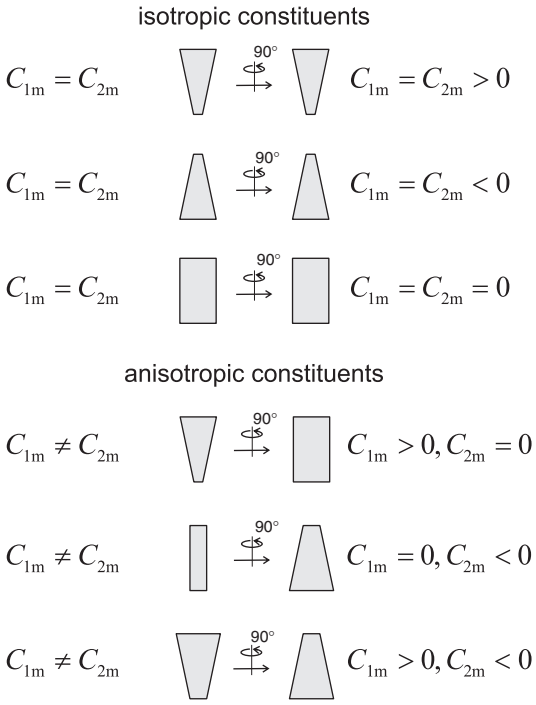

Figure 7 Schematic representation of different intrinsic shapes of some membrane constituents. Front and side views are shown. Upper: isotropic inclusion ($C_{1m} = C_{2m}$), lower: examples of anisotropic inclusions ($C_{1m} \neq C_{2m}$).

Terms up to second order in the elements of the tensor **M** are taken into account [32,56,57]:

$$E_i = \frac{K}{2}(\mathrm{Tr}\mathbf{M})^2 + \bar{K}\,\mathrm{Det}\,\mathbf{M}, \tag{38}$$

where K and $\bar{K}$ are the constants of interaction between the inclusion and the surrounding membrane. Using equations (35–38), the single-inclusion energy (E_i) can be written in the form [32,36]:

$$E_i = (2K + \bar{K})\,(H - H_m)^2 - \bar{K}\,(D^2 - 2DD_m\,\cos(2\,\omega) + D_m^2). \tag{39}$$

Quantities $H = (C_1 + C_2)/2$ and $H_m = (C_{1m} + C_{2m})/2$ are the respective mean curvatures, while $D = |C_1 - C_2|/2$ and $D_m = |C_{1m} - C_{2m}|/2$ are the curvature deviators. The curvature deviator D_m describes the intrinsic anisotropy of the single membrane inclusion (Fig. 7) [28,32,36,44]. The phenomenological expression for the inclusion energy, E_i contains interaction constants K and $\bar{K}$ and intrinsic curvatures H_m and D_m that have been recently estimated for the special case of rigid anisotropic inclusion (Fig. 6A) [31]. In the case of more flexible membrane inclusions (Fig. 6B) the constants K, $\bar{K}$, H_m, and D_m have the meaning of local elastic constants and the spontaneous curvatures [57].

The inclusions can rotate around the axis defined by the membrane normal at the site of the inclusion. The time scale for orientational changes of the anisotropic inclusions is usually small compared to shape changes of the lipid bilayer. Therefore the corresponding partition function, q, of a single inclusion is [22,36,44]

$$q = \frac{1}{\omega_0}\int_0^{2\pi} \exp\left(-\frac{E_i(\omega)}{kT}\right)\mathrm{d}\omega, \tag{40}$$

where ω_0 is an arbitrary angle quantum. Inclusions can also move laterally over the membrane bilayer, so that they can distribute laterally over the membrane in a way that is energetically the most favorable [33,36]. The lateral distribution of the inclusions in a bilayer membrane of overall area A is in general non-uniform. Treating inclusions as point-like, independent, and indistinguishable, the expression for the contribution of the inclusions to the membrane-free energy can be derived, based on equations (39) and (40) [36]:

$$\frac{F_i}{kT} = -N\ln\left[\frac{1}{A}\int_A q_c I_0\left(\frac{2\bar{K}}{kT}DD_m\right)\mathrm{d}A\right], \tag{41}$$

where N is the total number of inclusions in the membrane segment, while q_c is defined as

$$q_c = \exp\left(-\frac{2K+\bar{K}}{kT}(H^2 - 2HH_m) + \frac{\bar{K}}{kT}D^2\right), \tag{42}$$

and I_0 is the modified Bessel function. The integration in equation (41) is performed over the whole area of the membrane (A). For a large planar bilayer membrane that contains a single pore only those inclusions contribute to F_i that are located directly in the pore rim. In this case equation (41) can be rewritten in the form [1]:

$$\frac{F_i}{kT} = n\int_{A_p}\left[1 - q_c I_0\left(\frac{2\bar{K}}{kT}DD_m\right)\right]\mathrm{d}A_p, \tag{43}$$

where $n = N/A$ is the average area density of the inclusions in the membrane, and where the integration extends only over the area, A_p, of the membrane rim. The influence of the inclusion's anisotropy (Fig. 7) is contained in the Bessel function $I_0(2DD_m\bar{K}/kT)$. Because $I_0 \geq 1$ from equation (43) that anisotropy of inclusions always tends to lower F_i. Whether inclusions lower or increase F depends crucially on D_m and H_m, and on the interaction constants K and $\bar{K}$. The number of inclusions within the pore rim is [1]

$$N_P = n\int_{A_P} q_c I_0\left(\frac{2\bar{K}}{kT}DD_m\right)\mathrm{d}A_P. \tag{44}$$

If inclusions have no preference for partition into the pore rim ($q_c I_0 = 1$) then equation (44) predicts $N_P/A_P = n$. Combination of equations (43) and (44) yields [1]

$$\frac{F_i}{kT} = nA_P - N_P \tag{45}$$

Hence, inclusions that enter the membrane pore (in density that exceeds the bulk density) contribute $1kT$ per inclusions to the free energy. If the density of the inclusions within the pore region greatly exceeds the bulk density then $nA_P \ll N_P$ and thus $F_i \approx -N_p kT$ [1]. The inclusion size determines the maximal number of inclusions, N_P^{max} that can enter the pore rim. For rather large inclusions $R_i \approx b$ and small pores $r \approx b$ we expect that N_P^{max} is quite small, of the order of a very few inclusions [1]. This seems to indicate that F_i is hardly able to contribute to a substantial decrease in F. Below we show that nevertheless, for charged bilayer membranes, anisotropic inclusions can dramatically reduce F (much more than $-N_p kT$).

We note that equation (39) with $D_m = 0$ has the same structure as the Helfrich-bending energy for isotropic membranes. The corresponding interaction constants, K and $\bar{K}$ for a lipid membrane could thus be determined [44] by $K = k_c a_0$ where $k_c \approx 10kT$ is the bending constant of a nearly flat lipid monolayer (that is part of a bilayer membrane) and $a_0 = 0.6-0.8\,\mathrm{nm}^2$ is the cross-sectional area per lipid.

We assume that $k_c a_0 \approx 10kT\,\mathrm{nm}^2$ is at least an order of magnitude smaller than the interaction constant K in expression for a single-inclusion energy (equation (39)) [1]. Hence, sufficiently large and anisotropic membrane inclusions are expected to strongly partition into "appropriately curved" membrane regions.

We note that partitioning of membrane inclusions into the rim of a membrane pore replace some structurally perturbed lipids (besides causing an extra (*excess*) splay). These lipids no longer contribute to the energy of the pore. The corresponding energy gain is not contained in F_i because we have taken it into account already in W_{edge} (see equation (2)).

6. Theoretical Predictions

All the following results are presented for a thickness of the lipid layer $b = 2.5\,\mathrm{nm}$, for a line tension of $\Lambda = 10^{-11}\,\mathrm{J/m}$, and for a surface charge density $\sigma = -0.05\,\mathrm{Å/m}^2$ of the lipid layer [1]. Taking into account a cross-sectional area per lipid of $a_0 = 0.6-0.8\,\mathrm{nm}^2$ the value for σ would correspond roughly to a 1:4 mixture of (monovalent) charged and uncharged lipids. This is a common situation in biological and model bilayer membranes.

6.1. Inclusion-Free Membrane

In the case of inclusion-free membrane [20] the total membrane-free energy consists only of the line tension contribution (see equation 2) and the electrostatic-free energy (see equation (34)). The former favors shrinking, the latter widening (growing) of a membrane pore. For small values of Debye length l_D the pore closes, for large l_D the pore grows. Betterton and Brenner [20] have shown that for intermediate values of l_D there exists a very shallow local minimum of total membrane-free energy F as a function of the radius of the pore r. As an illustration, Fig. 8 shows the function $F(r)$ for three different values of l_D (dashed lines): 2.6 nm (a), 2.7 nm (b), and 2.8 nm (c). A local minimum of $F(r)$ is present only in curve

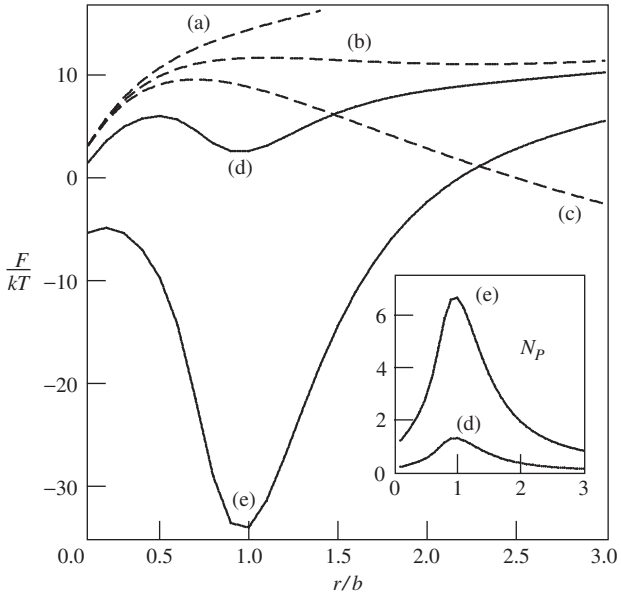

Figure 8 The pore-free energy, F, as a function of the pore size r [1]. The dashed lines correspond to a charged inclusion-free membrane of charge density of $\sigma = -0.05$ Å$/m^2$ with Debye length $l_D = 2.6$ nm **(a)**, $l_D = 2.8$ nm **(b)**, and $l_D = 3.0$ nm **(c)**. The solid lines describe the effect of adding anisotropic inclusions (characterized by $K = 50\ kT/nm^2$, $\bar{K} = 35kT/nm^2$, $c_{1m} = -c_{2m} = 1/b$) to the charged membrane with $\sigma = -0.1$ Å$/m^2$ and $l_D = 2.8$ nm. The average area density of inclusions n is : $1/70000\ nm^2$ **(d)** and $1/14000\ nm^2$ **(e)**. The inset shows the corresponding numbers of inclusions within the membrane rim (N_p) for curves (d) and (e) [1].

(b). Figure 8 (dashed lines) exemplifies a general finding for the inclusion-free isotropic and uniformly charged bilayer membrane: the local minimum of the membrane-free energy $F(r)$ is very shallow (below kT) and appears in a very narrow region of the values of the Debye length l_D. Based on these results it can be therefore concluded that the hydrophilic pore in isotropic and uniformly charged bilayer membrane cannot be stabilized solely by competition between the system electrostatic-free energy and the line tension energy of the pore rim [1,20].

6.2. Influence of Anisotropic Intrinsic Shape of Membrane Inclusions

In order to illustrate the effect of anisotropy of the membrane inclusions we chose an inclusion which favors saddle shape $c_{1m} = -c_{2m} = 1/b$ (Fig. 7). Figure 8 shows $F(r)$ for two values of average area density of inclusions (n): $1/70000\ nm^2$ (curve (d)) and $1/14000\ nm^2$ (curve (e)). The ability of anisotropic inclusions to lower the local minimum of the membrane-free energy $F(r)$ can be clearly seen. The anisotropic inclusions tend to accumulate within the rim of the hydrophilic pore [1]. The number of inclusions within the rim of the pore (N_P) is estimated by equation (44). This number is plotted in the inset of Fig. 8 for $n = 1/70000\ nm^2$ (d) and $n = 1/14000\ nm^2$ (e).

The depth of the minimum of $F(r)$ for $n = 1/14000\ \mathrm{nm}^2$ (curve (e) in Fig. 8) is approximately 30 kT. It arises predominantly from the accumulation of the anisotropic membrane inclusions in the region of the pore rim. On the other hand, equation (45) predicts that the inclusion energy $F_\mathrm{i} \approx N_\mathrm{P} kT$. The inset of Fig. 8 shows that $N_\mathrm{P} \leq 6$, therefore the deep minimum of $F(r)$ cannot arise solely from the inclusion contribution F_i [1]. To explain the deep minimum of $F(r)$ we recall that in the inclusion-free membrane the electrostatic energy and the line tension nearly balance each other for small enough values of r/b. If inclusions enter the pore region they reduce the line tension (see equation (4)). As a result U_el is no longer counterbalanced by positive W_edge and thus strongly lowers the total membrane-free energy F [1].

The minimum of $F(r)$ in Fig. 8 occurs at $r \approx b$ (see curves (d) and (e)). This reflects our choice of the saddle shape of the anisotropic inclusion: $c_{1\mathrm{m}} = 1/b, c_{2\mathrm{m}} = -1/b$ (see also Fig. 7). In fact, for $r = b$ the principal curvatures of the pore rim at $\theta = \pi$ (see equation (1)) are $c_1 = 1/b$ and $c_2 = -1/b$, coinciding with the inclusion's principal curvatures. This observation suggests the possibility to increase the optimal size of the pore by altering the shape of the membrane inclusions from a saddle-like ($c_{1\mathrm{m}} = 1/b$, $c_{2\mathrm{m}} = -1/b$) towards a more wedge-like ($c_{1\mathrm{m}} = 1/b$, $c_{2\mathrm{m}} \approx 0$, see also Fig. 7) [1]. The smaller the magnitude of $|c_{2\mathrm{m}}|$ the larger should the preferred pore size be (see also inset in Fig. 9). Regarding the

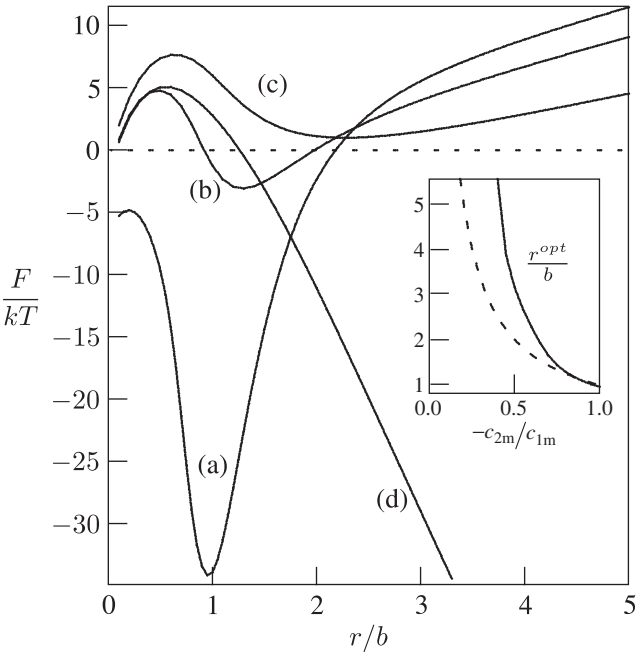

Figure 9 The pore-free energy, F, as a function of the pore size r for differently shaped, anisotropic inclusions: $c_{2\mathrm{m}}/c_{1\mathrm{m}} = -1$ **(a)**, $c_{2\mathrm{m}}/c_{1\mathrm{m}} = -0.8$ **(b)**, $c_{2\mathrm{m}}/c_{1\mathrm{m}} = -0.6$ **(c)**, and $c_{2\mathrm{m}}/c_{1\mathrm{m}} = 0$ **(d)** [1]. **In all cases the membrane is charged** ($\sigma = -0.05\ \mathrm{A/m}^2$, $l_\mathrm{D} = 2.8\ \mathrm{nm}$), $c_{1\mathrm{m}} = 1/b$ **and** $n = 1/14000\ \mathrm{nm}^2$. **The inset shows the position of the local minimum,** r^opt, **as a function of** $c_{2\mathrm{m}}/c_{1\mathrm{m}}$ **(solid line). The dashed line in the inset corresponds to** $-c_{2\mathrm{m}}/c_{1\mathrm{m}} = b/r^\mathrm{opt}$ [1].

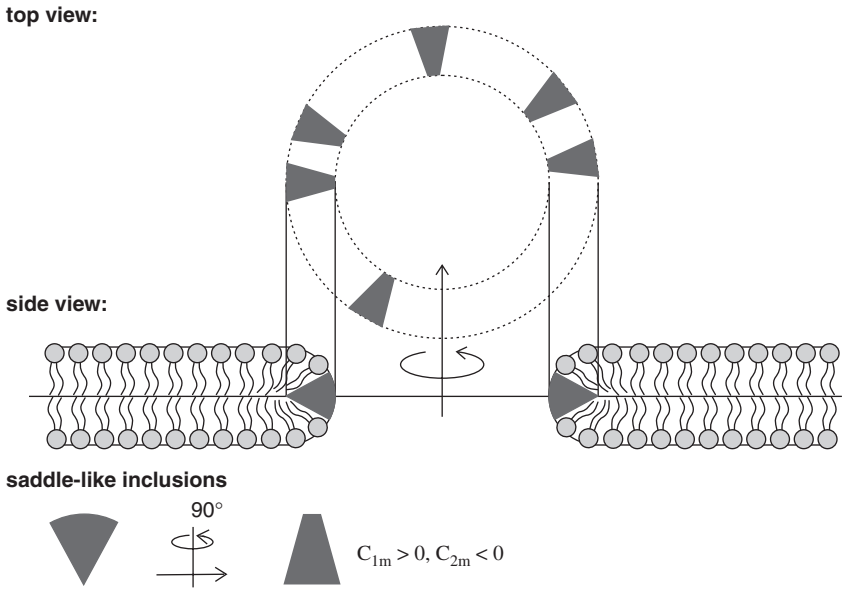

Figure 10 Schematic presentation of stabilization of hydrophilic pore in bilayer membrane by anisotropic saddle-like membrane inclusions.

principal curvatures at the waist of the rim, $c_1 = 1/b$ and $c_2 = -1/r$, one would expect that the optimal pore size (r^{opt}) is approximately determined by $c_{2m} = -1/r^{opt}$ and $c_{1m} = c_1 = 1/b$ leading to the approximative relation [1]

$$-\frac{c_{2m}}{c_{1m}} \approx \frac{b}{r^{opt}}. \tag{46}$$

In Fig. 9 [1] we consider anisotropic inclusions with intrinsic shape characterized by $c_{1m} = 1/b$ and c_{2m}/c_{1m}: -1 (a), -0.8 (b), -0.6 (c), and 0 (d). As it can be seen in Fig. 9 the local minimum of $F(r)$ shifts to larger pore sizes as the inclusions become more wedge-shaped (compare the position of the local minimum of curves (a)–(c)). The solid line in the inset of Fig. 9 shows how the optimal pore radius r^{opt} changes with c_{2m}/c_{1m}. The broken line in the inset displays the prediction according to approximative equation (46). Figure 9 also shows that below some critical values of the ratio $|c_{2m}/c_{1m}|$ the local minimum in $F(r)$ disappears (in Fig. 9 for $|c_{2m}/c_{1m}| < 0.4$), which means that the pore becomes unstable and starts to grow in the process which never stops. It should be also stressed that for isotropic inclusions where $c_{1m} = c_{2m}$ (see Fig. 7) we do not find energetically stabilized pores. The stabilization of the pore derives from the matching of the rim geometry with the inclusion's preference (Fig. 10). The pore rim provides a saddle-like geometry with different signs of c_1 and c_2 (see also Fig. 2). Consequently a saddle-like inclusion geometry (that is, different signs of c_{1m} and c_{2m}) is needed to stabilize the pore [1].

6.3. Influence of Salt Concentration (Ionic Stregth)

In all examples presented in Fig. 9 we have added anisotropic inclusions to charged membranes with specifically selected Debye length $l_D = 2.8$ nm [1] (Debye length l_D is inversely proportional to square root of ionic strength n_0, see also equation (6)). We recall from Fig. 8 that this was the choice for which already an inclusion-free membrane exhibits a very shallow minimum in $F(r)$ (see dashed curve (b) in Fig. 8). The question arises whether pores in the membrane with anisotropic inclusions can be stabilized also for other electrostatic conditions (i.e., other values of ionic strength). In this respect it is interesting to compare our theoretical predictions with experimental observation of stable pores in red blood cell ghosts for which data of the optimal pore radius r^{opt} as a function of the salt concentration n_0 exists [4]. Our theoretical approach [1] is able to reproduce these experimental data as presented in Fig. 11. Figure 11 shows the calculated and experimentally determined stable pore radius as a function of the salt concentration (ionic strength) in the suspension of red blood cell ghosts [1]. The inset of Fig. 11 shows the corresponding number of inclusions in the rim of the pore (N_P) (solid line) as well as the maximal possible number of inclusions in the rim of the pore $N_P^{\max} = \pi r^{\text{opt}}/R_i$ (broken line) at which the inclusions would sterically occupy the entire rim. The observation $N_P < N_P^{\max}$ indicates applicability of our approach for the selected average area density of the inclusions in the membrane $n = 1/2000\ \text{nm}^2$. Nevertheless, Fig. 11 should be

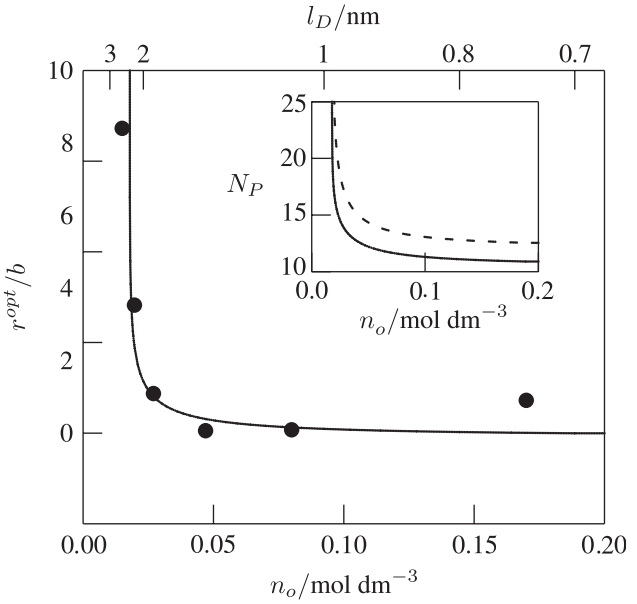

Figure 11 The optimal pore size r as a function of the ionic strength (salt concentration) of the surrounding electrolyte medium [1]. The charge density of the membrane is $\sigma = -0.05$ Å$/\text{m}^2$, the average area density of the inclusions is $n = 1/2000\ \text{nm}^2$, and the inclusion's preferred curvatures $c_{1\text{m}} = 1/b$ and $c_{2\text{m}}/c_{1\text{m}} = -0.4$. Experimental values [4] are also shown (•). The inset shows the actual number of inclusions (N_p) residing in the pore of optimal size, r^{opt} (solid line), and the maximal number, $N_P^{\max} = \pi r^{\text{opt}}/R_i$ (broken line) [1].

understood only as illustration of the principal ability of anisotropic membrane inclusions to stabilize membrane pores, under different electrostatic conditions.

7. On the Role of Anisotropic Membrane Inclusions in Membrane Electroporation-Experimental Consideration

Electroporation is a method for artificial formation of pores in biological membranes by applying an electric field across the membrane [8–10]. A problem in the electroporation of living tissue is that it often causes irreversible damage to the exposed cells and tissue [12]. Increasing the amplitude of the electric field in electroporation diminishes cell survival rates [13]. On the other hand, if the applied electric field is too low, stable pores are not formed. A way to improve the efficiency of electroporation is chemical modification of the membranes by surfactants. Little is known about the effect of surfactants on cell membrane fluidity and its relation to electroporation.

A recent electroporation experiment has shown that nonionic surfactant (detergent) polyoxyethylene glycol $C_{12}E_8$ does not affect the reversible electroporation, however, it significantly increases the irreversible electroporation (i.e., irreversible electroporation occurs at lower applied voltage in the presence of $C_{12}E_8$ (Fig. 12) [2]). The addition of $C_{12}E_8$ caused cell death at the same voltage at which the reversible electroporation takes place. This can be explained by pore stabilization effect of $C_{12}E_8$ [2] taking into account the results of above presented theoretical study of the influence of anisotropic membrane inclusions on the energetics and stability of hydrophilic membrane pores.

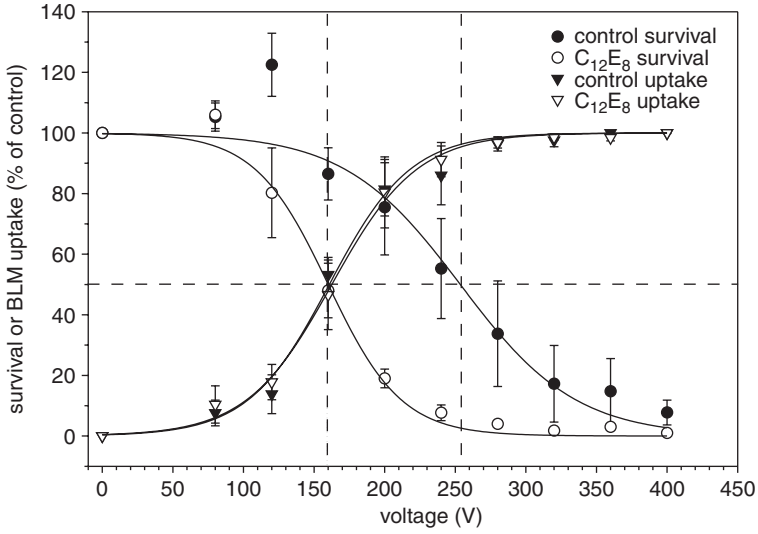

Figure 12 The effect of $C_{12}E_8$ on reversible electroporation (measured by bleomycin uptake) and irreversible electroporation measured by cell survival on cell line DC3F [2].

$C_{12}E_8$ incorporates in lipid bilayer with polar detergent head group at the level of polar phospate head groups and with detergent chain inserted in between acyl chains of fatty acids of the membrane phospholipids. Incorporation of $C_{12}E_8$ into the phospholipid bilayer leads to decreased average chain length and increased average area per chain and considerable perturbation of acyl chain ordering of neighboring phospholipid molecules. Consequently, the effective shape of phospholipids around $C_{12}E_8$ changes from cylinder to inverted truncated cone [58]. A cooperative interaction of one $C_{12}E_8$ molecule and some adjacent phospholipid molecules has been proposed [59]. Based on these experimental data an anisotropic effective shape of $C_{12}E_8$ phospholipids complex (inclusion) has been suggested recently [32,43,61].

In accordance with our theoretical predictions (Figs. 8 and 9) we therefore suggested that $C_{12}E_8$ induce anisotropic membrane inclusions [43] which stabilize the membrane hydrophilic pore by accumulating on toroidally shaped rim of the pore and attaining favorable orientation (Fig. 10) [2].

We presume that hydrophilic pores are formed at the voltages at which reversible electroporation takes place and that these pores are prerequisite for the bleomycin access to the cell interior that causes cell death. On the other hand, cell death that is a consequence of irreversible electroporation *is caused by electric field itself that provokes irreversible changes in the membrane*. In control cells, which were treated with $C_{12}E_8$ so that the pore stabilization did not occur, 50% of the cells survived the application of pulses of the amplitude of 250 V. In these cells, a resealing of the cell membrane took place while in the $C_{12}E_8$-treated cells no cells survived the application of pulses of the amplitude of 250 V, as resealing was prevented by $C_{12}E_8$ (Fig. 12). In control cells, we observed 50% of the permeabilization as determined by bleomycin uptake at 160 V [2]. At the same voltage, in the $C_{12}E_8$-treated cells we observed 50% of the permeabilization and also only 50% of cell survival after treatment with electric field (Fig. 12). This shows that the irreversible electroporation of the $C_{12}E_8$-treated cells is shifted to the same voltage at which reversible electroporation occur. In other words, electropermeabilization in the presence of $C_{12}E_8$ becomes irreversible as soon as it occurs. These results lead to the conclusion that stabilization of the hydrophilic membrane pores by $C_{12}E_8$ was induced by anisotropic membrane inclusions (Figs. 8–10).

To confirm this conclusion we performed additional experiments [2]. Namely, from above described experiments with $C_{12}E_8$ we could not distinguish between the pore stabilization effect of the $C_{12}E_8$-induced anisotropic membrane inclusions (Fig. 10) and the possibility that $C_{12}E_8$ could be toxic when it has access to the cell interior. Therefore in these additional experiments the molecules of $C_{12}E_8$ were added after the application of the train of 8 electric pulses. It was shown that $C_{12}E_8$ was not cytotoxic when it gained access to the cell interior (Fig. 13), as after electroporation the cell membrane remains permeable for relatively small molecules such as $C_{12}E_8$ [2]. From these results we concluded [2] that the cell death observed in the previous experiments (Fig. 12) is caused by bleomycin which is transported into the cell through pores which are stabilized by $C_{12}E_8$ (see Fig. 10). Also it was concluded that in order to show this effect $C_{12}E_8$ has to be incorporated in the cell membrane prior to application of the electric pulses.

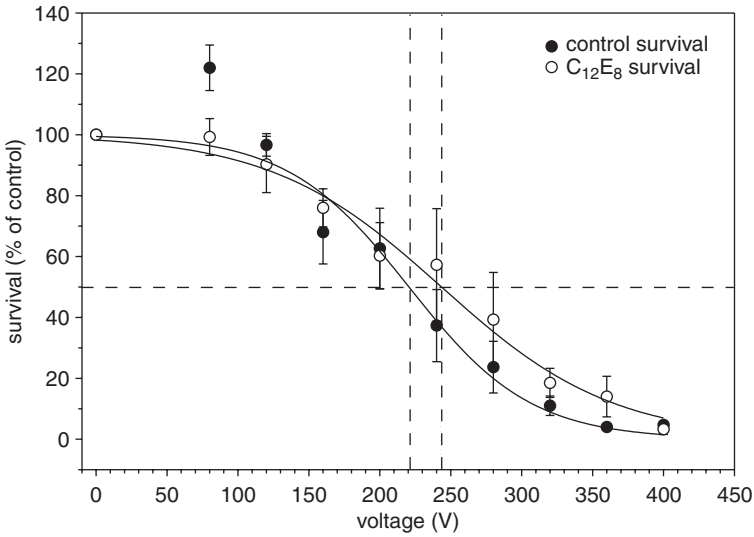

Figure 13 The effect of $C_{12}E_8$ added immediately after application of electric pulses on survival of DC3F cells [2].

8. Discussion and Conclusions

The influence that membrane inclusions have on the energetics of membrane pores is often interpreted in terms of altering the mezoscopic elastic properties of the membrane. For example, the effect of surfactants is often described by the surfactant dependent effective bending stiffness of a membrane bilayer and effective membrane spontaneous curvature [21,36]. In accordance it is assumed that the presence of cone-like or inverted cone-like membrane inclusions (see Fig. 7) can induce a shift in the spontaneous curvature [21,36]. This shift can be translated into a change of the line tension which may provide a simplified basis for analyzing the energetics of a membrane pore [18].

Our present theoretical approach contains isotropic inclusions only as a special case, namely the inclusions are isotropic for $D_m = 0$ (see also Fig. 7). Beyond the effect of cone-like and inverted cone-like inclusions, our present approach allows to analyze also other inclusion shapes, such as wedge-like or saddle-like (Fig. 7). Such inclusions can be characterized by an appropriate combination of H_m and D_m (or equivalently C_{1m} and C_{2m}).

In the case of *homogeneous lateral distribution* of membrane inclusions, the intrinsic spontaneous mean curvature of the inclusions (H_m) renormalize the membrane spontaneous curvature (see also [21,36]). However, if the lateral distribution of the inclusions is not homogeneous [21,29,36,60] the effect of the membrane inclusions (as for example surfactant-induced membrane inclusions, proteins, etc.) on membrane elasticity cannot be described simply by renormalization of membrane spontaneous curvature.

In the following we shortly discuss a few examples where we think that particularly the anisotropy of membrane-embedded inclusions could be relevant for the pore energetics.

Adding to the outer solution of the phospholipid membrane or the cell membrane a nonionic surfactant octaethyleneglycol dodecylether ($C_{12}E_8$) [2,41] causes a decrease of a threshold for irreversible electroporation (i.e., $C_{12}E_8$ decreases the voltage necessary for reversible electroporation) (Fig. 12). In other words, $C_{12}E_8$ molecules make transient pores in a membrane more stable [2]. In experiments the concentration of $C_{12}E_8$ was chosen so that it was not cytotoxic (Fig. 13) [2].

In order to explain the effect of $C_{12}E_8$ on reversible electroporation we suggested that $C_{12}E_8$-induced anisotropic membrane inclusions may stabilize the pore by accumulating on toroidal edge of the hydrophilic pore and by attaining a favorable orientation (Fig. 10). Our result could be thus considered as circumstantial evidence for the existence of hydrophilic pores that become stabilized by anisotropic membrane $C_{12}E_8$ inclusions that prevent membrane resealing.

Our theoretical approach could also help to better understand the pore energetics as recently investigated by Karatekin *et al.* [18]. For example, the authors have measured a dramatic increase of the transient pore lifetime induced by the detergent Tween 20 which has an anisotropic polar head group. The importance of the anisotropy of the polar heads of the detergents for the stability of anisotropic membrane structures has been indicated recently. It has been shown that a single-chained detergent with anisotropic dimeric polar head (dodecyl D-maltoside) may induce tubular nanovesicles [28,62] in a way similar as induced by strongly anisotropic dimeric detergents [47].

Our approach could add to better understanding of pore formation induced by some antimicrobial peptides [19,42]. These peptides have a pronounced elongated shape which arises from their alpha-helical backbone structure which renders them highly anisotropic. Some of these peptides are believed to cooperatively self-assemble into membrane pores. Thus, they can not only facilitate pore formation but they can *actively* induce it. Despite their importance there are currently only few theoretical investigations on the energetics of peptide-induced pore formation [37,38,40,63]. Our model provides a simple way to describe the underlying physics of peptide-induced pore formation in lipid membranes.

Our theoretical analysis of the stability and energetics of a single membrane pore is based on a simple and physically transparent model [1,2], which however involves a number of approximations.

As for example we have adopted a phenomenological expression for the membrane-inclusion interaction energy. This approach is (as in the Helfrich-bending energy [48]) valid if the local curvatures, C_1 and C_2, do not deviate too much from the preferred curvatures, C_{1m} and C_{2m}. On the other hand, the membrane rim provides local curvatures that differ greatly from those of the planar membrane. Hence, somewhere (either in the bulk membrane or within the rim) the deviations between the actual and the preferred curvatures are necessarily large. Yet, the Helfrich-bending energy describes well the line tension of an inclusion-free membrane (see for example [2]). On the same ground we are confident about the applicability of our expression for single-inclusion-free energy. There are also

approximations concerning the geometry of the membrane pore. Its shape is assumed to be circular, covered by a semi-toroidal rim [1,2]. However, there could be an inclusion-induced change in the cross-sectional shape of the membrane rim. Therefore we have performed additional calculations where we have allowed for a semi-ellipsoidal shape of the membrane rim. The free energy was then minimized with respect to the corresponding aspect ratio. With this additional degree of freedom we found qualitatively the same results as with the semi-toroidal rim [1] presented in this chapter.

The statistical mechanical approach to derive the inclusion-free energy F_i (equation (41)) assumes point-like inclusions, which interact only through a mean curvature field. Direct interactions between the inclusions [34] (which can be included in our theoretical approach [60,64,65]) may become important for the inclusions distributed in the pore rim where the distance between neighboring inclusions can be very small.

Nevertheless, none of the employed approximations can detract from our principal conclusion: anisotropic membrane inclusions can stabilize the pores in bilayer membrane [1,2].

Our theoretical approach takes into account the anisotropy of the membrane inclusions which enables us to describe various inclusion shapes: cone-like, inverted cone-like, wedge-like and saddle-like inclusions (see Fig. 7). In the model, the lateral density of the anisotropic inclusions is not kept constant so the inclusions may be predominantly localized in the energetically favorable regions [29,60], such as pore edges. Our model is simple, however it provides a lucid framework to analyze the energetics of pore formation in bilayer membranes [1] due to exogeneously bound molecules such as for example the detergent sodium cholate [18], detergent $C_{12}E_8$ [2], or the protein talin [66].

REFERENCES

[1] M. Fošnarič, V. Kralj-Iglič, K. Bohinc, A. Iglič, S. May, Stabilization of pores in lipid bilayers by anisotropic inclusions, J. Phys. Chem. 107 (2003) 12519–12526.
[2] M. Kandušer, M. Fosnarič, M. Šentjurc, V. Kralj-Iglič, H. Hägerstrand, A. Iglič, D. Miklavčič, Effect of surfactant polyoxyethylene glycol ($C_{12}E_8$) on electroporation of cell line DC3F, Coll. Surf. A 214 (2003) 205–217.
[3] M.R. Lieber, T.L. Steck, Dynamics of the holes in human-erythrocyte membrane ghosts, J. Biol. Chem. 257 (1982) 1660–1666.
[4] M.R. Lieber, T.L. Steck, A description of the holes in human-erythrocyte membrane ghosts, J. Biol. Chem. 257 (1982) 1651–1659.
[5] V.L. Lew, S. Muallem, C.A. Seymour, Properties of the Ca^{2+}-activated K^+ channel in one-step inside–out vesicles from human red-cellmembranes, Nature 296 (1982) 742–744.
[6] I.G. Abidor, V.B. Arakelyan, L.V. Chernomordik, Y.A. Chizmadzhev, V.F. Pastushenko, M.R. Tarasevich, Electric breakdown of bilayer lipid-membranes. 1. Main experimental facts and their qualitative discussion, Bioelectrochem. Bioener. 6 (1979) 37–52.
[7] E. Neumann, A.E. Sowers, C.A. Jordan (Ed.), Electroporation and Electrofusion in Cell Biology, Plenum Press, New York, 1989.
[8] P. Kramar, D. Miklavčič, A. Maček-Lebar, Determination of lipid bilayer breakdown voltage by means of linear rising signal, Bioelectrochem 70 (2007) 23–27.

[9] A. Maček-Lebar, G. Serša, S. Kranjc, A. Grošelj, D. Miklavčič, Optimisation of pulse parameters in vitro for in vivo electrochemotherapy, Anticancer Res. 22 (2002) 1731–1736.
[10] A. Maček-Lebar, G.C. Troiano, L. Tung, D. Miklavčič, Inter-pulse interval between rectangular voltage pulses affects electroporation threshold of artificial lipid bilayers, IEEE Trans. Nanobioscience 1 (2002) 116–120.
[11] M. Pavlin, M. Kandušer, M. Reberšek, G. Pucihar, F.X. Hart, R. Magjarevic, D. Miklavčič, Effect of cell electroporation on the conductivity of a cell suspension, Biophys. J. 88 (2005) 4378–4390.
[12] R.C. Lee, M.S. Kolodney, Electrical injury mechanisms-dynamics of the thermal response, Plast. Reconstr. Surg. 80 (1987) 663–671.
[13] H. Wolf, M.P. Rols, E. Boldt, E. Neumann, J. Teissie, Control by pulse parameters of electric field-mediated gene-transfer in mammalian-cells, Biophys. J. 66 (1994) 524–531.
[14] J.M. Crowley, Electrical breakdown of biomolecular lipid-membranes as an electromechanical instability, Biophys. J. 13 (1973) 711–724.
[15] H. Isambert, Understanding the electroporation of cells and artificial bilayer membranes, Phys. Rev. Lett. 80 (1998) 3404–3407.
[16] L.V. Chernomordik, M.M. Kozlov, G.B. Melikyan, I.G. Abidor, V.S. Markin, Y.A. Chizmadzhev, The shape of lipid molecules and monolayer membrane-fusion, Biochim. Biophys. Acta 812 (1985) 643–655.
[17] J.D. Litster, Stability of lipid bilayers and red blod cell membranes, Phys. Lett. 53 (1975) 193–194.
[18] E. Karatekin, O. Sandre, H. Guitouni, N. Borghi, P.H. Puech, F. Brochard-Wyart, Cascades of transient pores in giant vesicles: line tension and transport, Biophys. J. 84 (2003) 1734–1749.
[19] H.W. Huang, Action of antimicrobial peptides: two-state model, Biochemistry 39 (2000) 8347–8352.
[20] M.D. Betterton, M.P. Brenner, Electrostatic edge instability of lipid membranes, Phys. Rev. Lett. 82 (1999) 1598–1601.
[21] V. Kralj-Iglič, S. Svetina, B. Žekš, Shapes of bilayer vesicles with membrane embedded molecules, Eur. Biophys. J. 24 (1996) 311–321.
[22] J.B. Fournier, Nontopological saddle splay and curvature instabilities from anisotropic membrane constituents, Phys. Rev. Lett. 76 (1996) 4436–4439.
[23] V.S. Markin, Lateral organization of membranes and cell shapes, Biophys. J. 36 (1981) 1–19.
[24] E. Sackmann, Membrane bending energy concept of vesicle and cell shapes and shape transitions, FEBS Lett. 346 (1994) 3–16.
[25] P.B.S. Kumar, G. Gompper, R. Lipowsky, Budding dynamics of multicomponent membranes, Phys. Rev. Lett. 86 (2001) 3911–3914.
[26] R. Lipowsky, R. Dimova, Domains in membranes and vesicles, J. Phys. Condens. Matter 15 (2003) 531–545.
[27] M. Laradji, P.B.S. Kumar, Dynamics of domain growth in self-assembled fluid vesicles, Phys. Rev. Lett. 93 (2004) ; 1–4/198105.
[28] V. Kralj-Iglič, H. Hägerstrand, P. Veranič, K. Jezernik, B. Babnik, D.R. Gauger, A. Iglič, Amphiphile-induced tubular budding of the bilayer membrane, Eur. Biophys. J. 34 (2005) 1066–1070.
[29] A. Iglič, M. Fošnarič, H. Hägerstrand, V. Kralj-Iglič, Coupling between vesicle shape and the non-homogeneous lateral distribution of membrane constituents in Golgi bodies, FEBS Lett. 574/1–3 (2004) 9–12.
[30] V. Kralj-Iglič, B. Babnik, D.R. Gauger, S. May, A. Iglič, Quadrupolar ordering of phospholipid molecules in narrow necks of phospholipid vesicles, J. Stat. Phys. 125 (2006) 727–752.
[31] M. Fošnarič, K. Bohinc, D.R. Gauger, A. Iglič, V. Kralj-Iglič, S. May, The influence of anisotropic membrane inclusions on curvature elastic properties of lipid membranes, J. Chem. Inf. Model. 45 (2005) 1652–1661.
[32] A. Iglič, V. Kralj-Iglič, Effect of anisotropic properties of membrane constituents on stable shapes of membrane bilayer structure, in: H. Ti Tien, A. Ottova-Leitmannova (Eds.), Planar Lipid Bilayers (BLMs) and their Applications, Elsevier, Amsterdam, 2003, pp. 143–172.

[33] V. Kralj-Iglič, S. Svetina, B. Žekš, Shapes of bilayer vesicles with membrane embedded molecules, Eur. Biophys. J. 24 (1996) 311–321.
[34] S. Marčelja, Lipid-mediated protein interactions in membranes, Biophys. Biochim. Acta. 455 (1976) 1–7.
[35] S. Leibler, D. Andelman, Ordered and curved meso-structures in membranes and amphiphilic films, J. Phys. (Paris) 48 (1987) 2013–2018.
[36] V. Kralj-Iglič, V. Heinrich, S. Svetina, B. Žekš, Free energy of closed membrane with anisotropic inclusions, Eur. Phys. J. 10 (1999) 5–8.
[37] A. Zemel, D.R. Fattal, A. Ben-Shaul, Energetics and self-assembly of amphipathic peptide pores in lipid membranes, Biophys. J. 84 (2003) 2242–2255.
[38] M.J. Zuckermann, T. Heimburg, Insertion and pore formation driven by adsorption of proteins onto lipid bilayer membrane-water interfaces, Biophys. J. 81 (2001) 2458–2472.
[39] M.M. Sperotto, A theoretical model for the association of amphiphilic transmembrane peptides in lipid bilayers, Eur. Biophys. J. 26 (1997) 405–416.
[40] J.H. Lin, A. Baumgaertner, Stability of a melittin pore in a lipid bilayer: a molecular dynamics study, Biophys. J. 78 (2000) 1714–1724.
[41] G.C. Troiano, L. Tung, V. Sharma, K.J. Stebe, The reduction in electroporation voltages by the addition of a surfactant to planar lipid bilayers, Biophys. J. 75 (1998) 880–888.
[42] Y. Shai, Mechanism of the binding, insertion and destabilization of phospholipid bilayer membranes by alpha-helical antimicrobial and cellnon-selective membrane-lytic peptides, Biochim. Biophys. Acta 1462 (1999) 55–70.
[43] H. Hägerstrand, V. Kralj-Iglič, M. Fošnarič, M. Bobrovska-Hägerstrand, L. Mrowczynska, T. Söderström, A. Iglič, Endovesicle formation and membrane perturbation induced by polyoxyethyleneglycolalkylethers in human erythrocytes, Biochim. Biophys. Acta 1665 (2004) 191–200.
[44] V. Kralj-Iglič, A. Iglič, G. Gomišček, F. Sevšek, V. Arrigler, H. Hägerstrand, Microtubes and nanotubes of a phospholipid bilayer membrane, J. Phys. A Math. Gen. 35 (2002) 1533–1549.
[45] A. Chanturiya, J. Yang, P. Scaria, J. Stanek, J. Frei, H. Mett, M. Woodle, New cationic lipids form channel-like pores in phospholipid bilayers, Biophys. J. 84 (2003) 1750–1755.
[46] V.V. Malev, L.V. Schagina, P.A. Gurnev, J.Y. Takemoto, E.M. Nestorovich, S.M. Bezrukov, Syringomycin E channel: a lipidic pore stabilized by lipopeptide, Biophys. J. 82 (2002) 1985–1994.
[47] V. Kralj-Iglič, A. Iglič, H. Hägerstrand, P. Peterlin, Stable tubular microexovesicles of the erythrocyte membrane induced by dimeric amphiphiles, Phys. Rev. E 61 (2000) 4230–4234.
[48] W. Helfrich, Elastic properties of lipid bilayers: theory and possible experiments, Z. Naturforsch. 28 (1973) 693–703.
[49] C. Taupin, M. Dvolaitzky, C. Sauterey, Osmotic-pressure induced pores in phospholipid vesicles, Biochemistry 14 (1975) 4771–4775.
[50] J.D. Moroz, P. Nelson, Dynamically stabilized pores in bilayer membranes, Biophys. J. 72 (1997) 2211–2216.
[51] E.J. Verwey, J.Th.G. Overbeek, Theory of Stability of Lyophobic Colloids, Elsevier Publishing Company, New York, 1948.
[52] A. Iglič, K. Bohinc, M. Daniel, T. Slivnik, Effect of circular pore on electric potential of charged plate in contact with electrolyte solution, Electrotecn. Rev. (Slovenia) 71 (2004) ; 260.
[53] G.B. Arfken, H.J. Weber, Mathematical Methods for Physicists, Academic Press, San Diego, 1995.
[54] V. Kralj-Iglič, A. Iglič, A simple statistical mechanical approach to the free energy of the electric double layer including excluded volume effect, J. Phys. II (France) 6 (1996) 477–491.
[55] D. Andelman, Electrostatic properties of membranes: the Poisson–Boltzmann theory, in: R. Lipowsky, E. Sackmann (Eds.), Structure and Dynamics of Membranes, Elsevier, Amsterdam, 1995, pp. 603–642.
[56] V. Kralj-Iglič, M. Remškar, G. Vidmar, M. Fošnarič, A. Iglič, Deviatoric elasticity as a possible physical mechanism explaining collapse of inorganic micro and nanotubes, Phys. Lett. A 296 (2002) 151–155.

[57] A. Iglič, B. Babnik, U. Gimsa, V. Kralj-Iglič, On the role of membrane anisotropy in the beading transition of undulated tubular membrane structures, J. Phys. A: Math. Gen. 38 (2005) 8527–8536.
[58] R.L. Thormond, D. Otten, M.F. Brown, K. Beyer, Structure and packing of phosphatidylcholines in lamellar and hexagonal liquid-crystalline mixtures with a nonionic detergent: A wide-line deuterium and phosphorus-31 NMR Study, J. Phys. Chem. 98 (1994) 972–983.
[59] H. Heerklotz, H. Binder, H. Schmiedel, Excess enthalpies of mixing in phospholipid-additive membranes, J. Phys. Chem. B 102 (1998) 5363–5368.
[60] H. Hägerstrand, L. Mrowczynska, U. Salzer, R. Prohaska, K.A. Michelsen, V. Kralj-Iglič, A. Iglič, Curvature dependent lateral distribution of raft markers in the human erythrocyte membrane, Mol. Membr. Biol. 23 (2006) 277–288.
[61] M. Fošnarič, M. Nemec, V. Kralj-Iglič, H. Häägerstrand, M. Schara, A. Iglič, Possible role of anisotropic membrane inclusions in stability of torocyte red blood cell daughter vesicles, Coll. Surf. B 26 (2002) 243–253.
[62] H. Hägerstrand, V. Kralj-Iglič, M. Bobrowska-hagerstrand, A. Iglič, Membrane skeleton detachment in spherical and cylindrical microexovesicles, Bull. Math. Biol. 61 (1999) 1019–1030.
[63] P.C. Biggin, M.S.P. Sansom, Interactions of alpha-helices with lipid bilayers: a review of simulation studies, Biophys. Chem. 76 (1999) 161–183.
[64] A. Iglič, V. Kralj-Iglič, Budding of liposomes-role of intrinsic shape of membrane constituents, in: A. Leitmannova-Liu, H. Ti Tien (Eds.), Advances in Planar Lipid Bilayers and Liposomes, Vol. 4, Elsevier, Amsterdam, 2006, pp. 253–279.
[65] V. Kralj-Iglič, P. Veranič, Curvature-induced sorting of bilayer membrane constituents and formation of membrane rafts, in: A. Leitmannova-Liu, H. Ti Tien (Eds.), Advances in Planar Lipid Bilayers and Liposomes, Vol. 5, Elsevier, Amsterdam, 2006.
[66] A. Saitoh, K. Takiguchi, Y. Tanaka, H. Hotani, Opening-up of liposomal membranes by talin, Proc. Natl. Acad. Sci. USA 95 (1998) 1026–1031.

CHAPTER TWO

Rapid Purification and Reconstitution of Recombinant Voltage-Gated Sodium Channels into Planar BLMs

Yan Li Zhang[1], Julie E. Dalziel[1,*], James Dunlop[1], *and* Angelica Leitmannova Liu[2,3]

Contents

1. Voltage-Gated Sodium Channels 28
2. Algal Toxins that Modulate Sodium Channel Activity 29
3. Ion Channels in Bilayer Lipid Membrane Biosensors 30
4. Ion Channel Purification 31
   4.1. Purification of Ion Channels for Reconstitution into pBLMs 31
   4.2. Purification of Ion Channels using Immobilised Metal Affinity Chromatography (IMAC) 31
   4.3. Purification of VGSC for Reconstitution into pBLMs 32
5. Methods 33
   5.1. Addition of His-Tag to *hSkM1* 33
   5.2. VGSC Expression in Insect Cells 34
   5.3. Purification of Recombinant VGSC using IMAC 35
6. Functional Reconstitution 39
   6.1. Reconstitution of Ion Channels into Liposomes 39
   6.2. Incorporation of Proteoliposomes into pBLMs 39
   6.3. Orientation of Reconstituted *hSkM1*-HT Channels in pBLMs 40
   6.4. Pharmacological Function of Reconstituted *hSkM1*-HT 40
7. Conclusion 43
Acknowledgements 44
References 44

Abstract

Immobilised metal affinity chromatography (IMAC) is widely used for purification of proteins for use in biochemical studies. It is also suitable for purification of membrane

* Corresponding author. Tel: +64-6-3518098; Fax: +64-6-3518042;
E-mail address: julie.dalziel@agresearch.co.nz (J.E. Dalziel).

[1] AgResearch, Grasslands Research Centre, Tennent Drive, Private Bag 11008, Palmerston North 4442, New Zealand
[2] Physiology Department, Biomedical and Physical Sciences Building, Michigan State University, East Lansing, MI 48824, USA
[3] Center for Interface Sciences, Microelectronics Department, Faculty of Electrical Engineering & Information Technology, Slovak Technical University (FEI STU), 812 19 Bratislava, Slovak Republic

Advances in Planar Lipid Bilayers and Liposomes, Volume 6
ISSN 1554-4516, DOI 10.1016/S1554-4516(07)06002-4

proteins and their subsequent reconstitution into liposomes for use in planar lipid bilayer membrane (pBLM) studies to obtain an electrical measure of ionic current. However, there are few examples of recombinant eukaryotic ion channels being purified and reconstituted into pBLMs. This chapter contains protocols for the purification of histidine-tagged voltage-gated sodium ion channels from insect cell membranes and their reconstitution into pBLMs in a functionally active form. Technical problems encountered using IMAC to purify sodium channels for reconstitution are discussed. This method is relevant for applications where the ability of purified recombinant channels to open and close, and to be modulated by toxins or drugs is required. It would be useful for research using mutated ion channels where it is desirable to characterise their functional properties in pBLMs. It may also be useful in new technologies to screen for new drugs or pesticides, and in toxin detection.

1. Voltage-Gated Sodium Channels

Voltage-gated sodium channels (VGSC) have a fundamental role in excitation of cells in skeletal muscle, brain, and heart. They are activated by a change in membrane voltage which results in the flow of sodium ions into the cell, causing membrane depolarisation and subsequent propagation of action potentials [1,2]. VGSCs are major sites of action for therapeutic drugs including local anaesthetics, anti-arrythmics, anti-epileptics, and analgesics, and are therefore important targets for drug discovery [3,4]. They are also sites of action for harmful toxins including marine biotoxins, for example, brevetoxin-1 (PbTx-1) and saxitoxin (STX), and for insecticides [5].

In the 20 years since VGSCs were cloned [6], advances in molecular biology and electrophysiology (patch-clamp) techniques have provided powerful tools to understand the molecular structure and mechanisms of sodium channel function [7–9]. VGSCs belong to a superfamily of voltage-gated ion channels that are structurally homologous, including potassium and calcium channels. In the absence of a high-resolution crystal structure for VGSCs, much has been inferred from that determined for potassium ion channels [10–12]. VGSCs are composed of a complex of a 260 KDa α-subunit in association with one or more auxiliary β-subunits (for review see [1,2]). The α-subunit is required for function since it contains the ion-conducting aqueous pore. The primary amino acid sequence predicts that the α-subunit consists of four internally homologous domains labelled I–IV in Fig. 1 [13]. Each domain contains six transmembrane segments (S1–S6), where the N- and C-termini are intra-cellular. The voltage sensor is located in the S4 segment that contains positively charged amino acid residues. There is an inactivation gate between domains III and IV [14]. The pore loop and S6 regions of each of the four domains are thought to fold together to form a sodium ion-conducting pore. Some binding sites for toxins and drugs that modulate channel function have been located.

Neurotoxins that act via VGSCs have been important pharmacological tools for use in electrophysiological studies, for example tetrodotoxin (TTX) [2,5]. Because VGSCs inactivate in a matter of milliseconds, the whole-cell patch-clamp technique

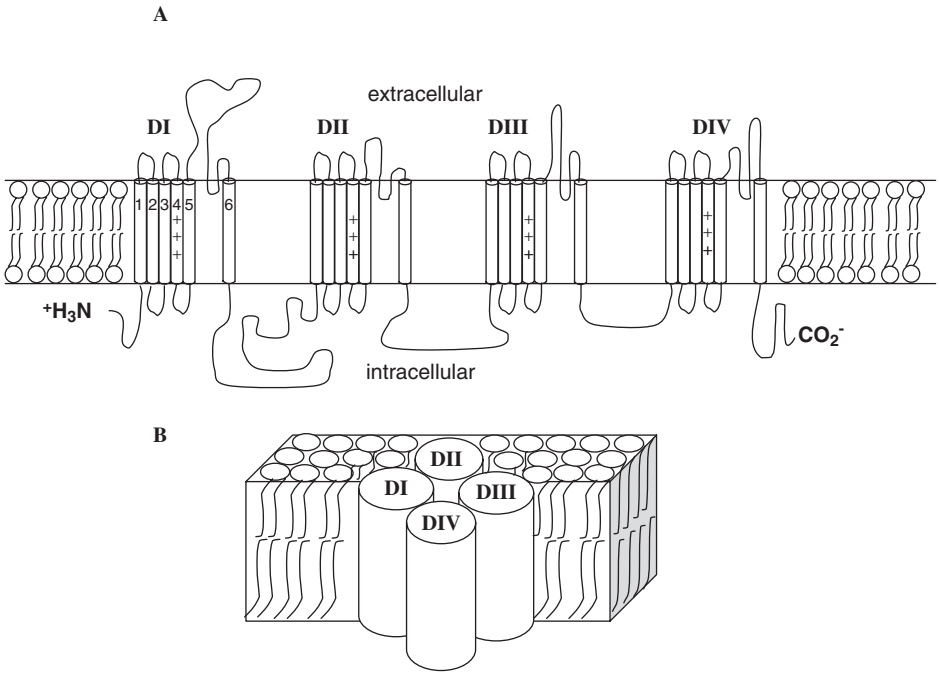

Figure 1 Voltage-gated sodium channel structure. Predicted secondary (A) and tertiary (B) structures [13].

has been used to study their rapidly decaying currents. A fast capacitive transient is induced by voltage-activation that can mask the initial current as channels activate. Many patch-clamp amplifiers can now largely compensate for this capacitive transient. The rapid inactivation of VGSCs when activated by voltage has made investigation of steady-state single channel properties difficult. Compounds that activate VGSCs such as batrachotoxin (BTX) [2,15–17] and veratridine (VTD) [2,18,19], have enabled continuous single channel activity to be recorded. BTX is from the Colombian frog genus *Phyllobates*, and VTD is a plant alkaloid from the *Liliaceae* family [2]. BTX is not commercially available. Substitution of key amino acids important for fast inactivation, isoleucine/phenylalanine/methionine each to glutamine (IFM to QQQ) in the DIII-DIV linker region (Fig. 1) has essentially removed fast inactivation and only the slowly inactivating current component remains [20].

2. Algal Toxins that Modulate Sodium Channel Activity

Other useful VGSC modulators that are also marine biotoxins are brevetoxins, such as PbTx-1 [21,22] which activates VGSCs, and STX [23] which inhibits them. These toxins are produced by algae and become problematic when they reach high

levels during toxic algal blooms when they accumulate in shellfish and may pose a risk to human health. PbTx-1 is produced by the dinoflagellate, *Karenia brevis*, prevalent in red tide algal blooms [24]. The toxic effects of brevetoxins are incoordination, paralysis, and convulsions [24]. STX is produced by marine dinoflagellates and also by freshwater cyanobacteria. Saxitoxins can enter the food chain and cause more serious neurological effects including, numbness, tingling of the skin, ataxia, fever, and in severe cases: muscle incoordination, respiratory distress, and sometimes death [2,24]. Currently the only internationally validated biological-based method to measure the toxicity of these compounds is the mouse bioassay, which has problems with inconsistencies, lack of specificity, ethical justification, and because assay time is lengthy sample turn around time is slow [25]. There are many cell-based assays that rely upon responses to activation and inhibition of sodium channels, and subsequent cell death or survival, respectively [26–30]. Whilst these are predictive of toxicity, assay times are also lenghty and none of the assays have been internationally validated [25]. Development of a sensitive, more rapid and reliable VGSC-based biosensor to detect the presence of modulatory toxins would be a valuable adjunct to the mouse bioassay. It would not only detect the presence of sodium channel modulators but would be indicative of toxicity.

3. Ion Channels in Bilayer Lipid Membrane Biosensors

Planar bilayer lipid membranes (pBLMs) provide an artificial membrane system in which to study the electrical function of ion channels [31]. Since Miller and Racker developed the technique to fuse liposomes with BLMs in the 1970s [32], this method has been widely used to study the properties and pharmacological function of ion channels, including VGSCs. pBLMs allow researchers to study ion channels under controlled conditions, in which the composition of solution on either side of the membrane is easily accessible, and background or leak currents produced by untargeted proteins are avoided by using isolated purified proteins. pBLMs are often used to study the function of ion channels that originate from intracellular membranes as these are not easily amenable to patch-clamping.

pBLMs provide the fundamental basis for the utilisation of ion channels as biosensors because they provide a simple model of an artificial membrane where ion channels generally function in a similar manner to that in their native biological membranes. Significant technical issues have had to be overcome in the development of ion channel biosensors, including the fragility of the bilayer lipid membranes in which the ion channels are embedded. The use of supporting structures has improved membrane stability, but is limited by the requirement for solution to be present on both sides of the membrane for channels to operate. To overcome this, a bilayer may be tethered to a support [33], suspended over a support [34], or an array format used containing multiple planar bilayers in parallel [35] (for reviews see [36,37]). Ion channel activity has been recorded in horizontally oriented bilayers

formed across a hole in a silicon microchip [38], and indeed a horizontal bilayer format is now used by many ion channel researchers [39].

The production of purified recombinant ion channels with normal pharmacological function is not only useful for research studies using ion channels, but also in using channels as functional-sensing elements in future technologies for biosensors or in drug discovery. Thus a source of large quantities of pure VGSC protein would be valuable for the development of a VGSC-based toxin biosensor not only in detection of toxins but also in high-throughput-screening technologies. As bilayer stability is improved, the use of reconstituted ion channels in high-throughput drug screening and for use in biosensors will become a reality. Such assays will require a source of functional recombinant protein.

4. Ion Channel Purification

4.1. Purification of Ion Channels for Reconstitution into pBLMs

Isolating and purifying ion channels in a functionally active form can be challenging because typically they are large hydrophobic proteins that are integral to cell membranes. Their association with a hydrophobic environment helps to maintain their structural and functional integrity. This is maintained either by keeping the protein in the membrane and isolating the membrane fraction, or by using detergents. The use of detergents to solubilise the protein produces micelles which provide the necessary hydrophobic environment and enable subsequent chromatography purification procedures to be performed.

There are many well established techniques to obtain eukaryotic ion channels from native tissues for reconstitution into bilayer membranes [40]. Some methods isolate the protein without solubilisation, often relying solely on ultra-centrifugation. Others purify the channel and therefore require solubilisation followed by chromatography where the protein is selected for on the basis of its specific properties such as charge, hydrophobicity, or antigenicity.

In the past, channels were mostly purified from native tissue, but since many ion channel genes have been cloned, the use of heterologous expression systems has enabled the use of recombinant tags. However, there are few examples of recombinant ion channel proteins being purified and reconstituted into pBLMs. Many affinity purification tags are now available and are suitable for purification. For example, both flag-tagged and tandem affinity purification (TAP) -tagged affinity purification methods have been used successfully to reconstitute human membrane-associated polycystin-2 channels into pBLMs [41,42].

4.2. Purification of Ion Channels using Immobilised Metal Affinity Chromatography (IMAC)

IMAC was first described over 30 years ago [43]. It is a method to purify recombinant fusion proteins containing an affinity tag consisting of approximately six

histidine amino acids (for review see Ref. [44]). Divalent metal ions (Fe^{2+}, Co^{2+}, Ni^{2+}, Cu^{2+}, Zn^{2+}) are immobilised on a matrix and interact with the imidazole ring of the histidine amino acid. The protein can be eluted by adding free imidazole or by adjusting the pH. While IMAC is a commonly used purification method in many biochemical studies, it is less commonly used for purification of integral membrane proteins. However, IMAC has been used successfully to purify the mammalian ion channels, the cystic fibrosis transmembrane conductance regulator [45,46], and aquaporin [42], from eukaryotic cells, where the purpose of their reconstitution into liposomes is to obtain channel activity in planar lipid bilayers.

4.3. Purification of VGSC for Reconstitution into pBLMs

Methods for functional reconstitution of VGSCs into pBLMs were developed over 20 years ago. In some studies, non-solubilised voltage-gated sodium channels

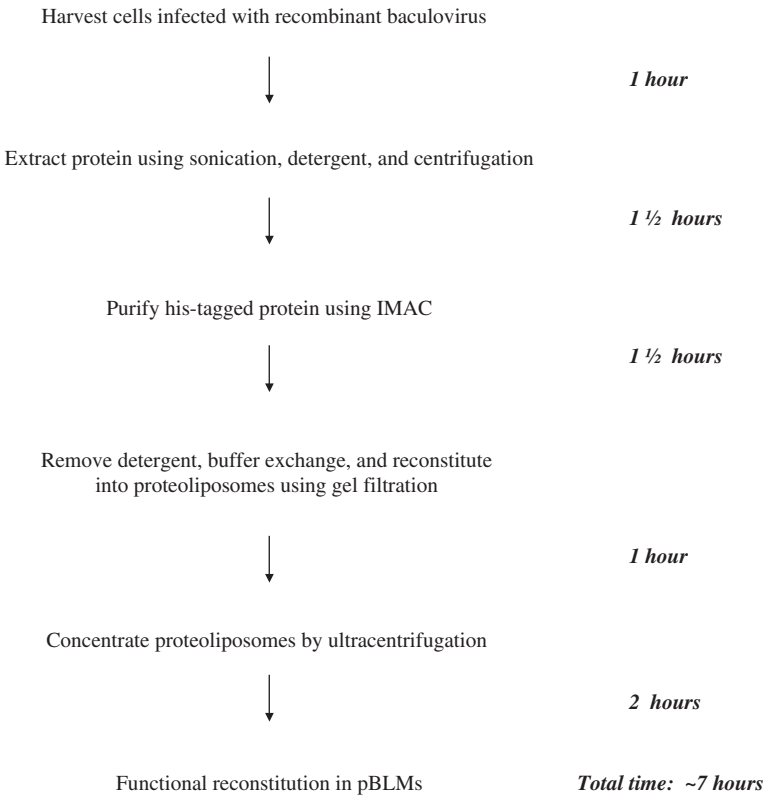

Figure 2 Flow chart of protein purification procedures.

originating in brain or skeletal muscle have been isolated from membrane fragments using sucrose density gradient centrifugation [40,47–52]. Detergent solubilisation using NP40 has been used to isolate muscle VGSCs from rabbit T-tubular membranes, with subsequent purification by ion exchange and affinity chromatography [53]. Comparison of the characteristics of unpurified (non-solubilised) in the related VGSC from eel electroplax, with that solubilised using 3-[(3-cholamidopropyl)dimethylammonio]-1-propanesulfonate (CHAPS) and purified using covalent chromatography, revealed no differences in function, but membrane stability was greater and recordings less noisy for purified material [54].

More recently, addition of a histidine tag (His-tag) to the C-terminus of the human skeletal muscle sodium channel (*hSkM1* or SCN4A) has been shown not to alter channel function when expressed in human embryonic kidney 293 cells [55,56]. Research in our laboratory has further shown that His-tagged VGSCs purified using IMAC retain their channel activity when reconstituted into pBLMs [56]. The following methods will provide details for expression of human skeletal muscle VGSCs in insect cells, their purification using IMAC, and assessment of channel function following reconstitution into pBLMs. The steps involved in purification of His-tagged VGSCs are summarised in Fig. 2.

5. Methods

5.1. Addition of His-Tag to *hSkM1*

An advantage of the His-tag is its relatively short length compared to other available tags, which means that it is unlikely to affect function, thus removal of the tag is generally not necessary. The effect of additional amino acids on function is of particular concern for ion channels because small changes in structure often alter a channel's functional properties. Many vectors are commercially available that contain His-tags at the C- or N-terminus, into which ion channel cDNA may be subcloned. It is important that the codons remain in-frame and that incorporation of additional amino acids is minimised to prevent structural changes that might affect function. PCR was therefore used to add nucleotides coding for six histidine residues to the C-terminus of the *hSkM1* gene (*hSkM1-HT*) followed by a stop codon, and a new restriction endonuclease site. This approach avoided inclusion of extra residues that might affect channel function, while also enabling subcloning of *hSkM1-HT* into the pFastBac™ baculovirus expression vector (Invitrogen, Carlsbad, California). Recombinant baculovirus in the form of a bacmid was produced in *Escherichia. coli* by site-specific transposition using the Bac-to-Bac™ baculovirus expression system (Invitrogen, Carlsbad, California). This method enables production of recombinant baculovirus without the need for plaque isolation. A new rapid method of baculovirus production is also now available in which the gene of interest is incorporated by site-specific recombination into a linear baculovirus DNA construct that contains an N- or C-terminal His-tag

(BaculoDirect™, Invitrogen). An anti-viral is then used to select against non-recombinant baculovirus.

Using the Bac-to-Bac™ baculovirus expression system, pFastBac/*hSkM1*-HT was transformed into DH10-Bac *E. coli* and colonies were selected on the basis of their resistance to the antibiotics: kanamycin, gentamycin, tetracycline, and by blue/white colony screening using IPTG and X-gal. Recombinant bacmid is large >135 kb, therefore care must be taken to purify it intact. We recommend using DNA mini-preparation purification columns that empty by gravity flow rather than by centrifugation. Bacmid colonies were screened by PCR analysis to identify those containing *hSkM1*-HT. At this point it is also advantageous to confirm the presence of intact bacmid DNA by gel electrophoresis. The recombinant bacmid generated can then be transformed into the DH10-B *E. coli* strain which lacks a helper plasmid as it is no longer required.

5.2. VGSC Expression in Insect Cells

The baculovirus expression system is well suited for heterologous expression of eukaryotic proteins [57,58]. A major advantage of this system is the high-infection efficiency of cells by the recombinant baculovirus, resulting in many cells expressing the gene of interest. In addition, high levels of protein can be produced and this is amenable to being scaled up for commercial production [59,60]. Different subunits may be co-expressed producing hetero-oligomeric channels. This may be achieved by co-infection of more than one recombinant baculovirus, or by the use of dual- or multi-promotor baculovirus transfer vectors, for example wild type and mutated GABA A receptor subunits have been coexpressed in this way [61–63]. Insect cells support post-translational modifications which is particularly relevant for VGSCs because they are heavily glycoslyated, comprising 30% carbohydrate [64]. While glycolsyation is not essential for VGSC function it does modulate channel-opening properties [65,66].

Insect cells grow at close to room temperature (25 °C) and do not require special aeration conditions for volumes of up to 1 l. Baculoviruses are also safer to work with than most mammalian viruses since they are non-infectious to vertebrates. Of the several types of insect cell lines available, *Sf*9 cells were chosen as these are suitable for expression of non-secreted proteins. Cells were grown in Grace's Insect medium (Sigma) supplemented with 10% foetal bovine serum, 2% yeastolate, 3.3 mg/ml lactalbumin, pH 6.2. Cells were routinely seeded at a density of 5×10^5 cells/ml and grown to $2–3 \times 10^6$ cells/ml in 40 ml volume of media in a 50 ml capacity spinner flask at 25 °C.

To obtain stocks of *hSkM1*-HT recombinant baculovirus, *Sf*9 insect cells were infected with purified recombinant bacmid DNA according to the manufacturer's instructions. One exception was that the resultant P1 viral supernatant was harvested after five days rather than only three to give a sufficiently high titre ($\geq 1 \times 10^7$ PFU/ml). The virus was propagated twice more by infecting cells growing at 5×10^5 cells/ml at a multiplicity of infection (MOI) of 0.1 for five days to obtain a 500 ml volume of recombinant baculovirus as a working stock. Virus titre was determined by plaque assay.

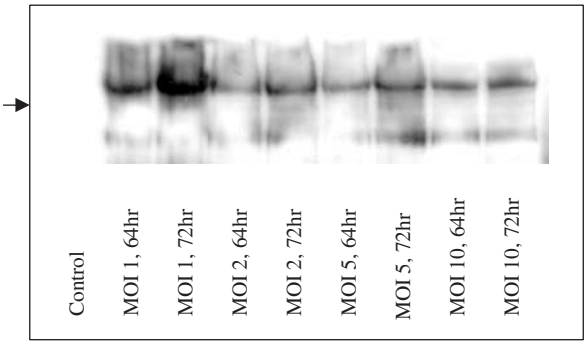

Figure 3 Expression of His-tagged voltage-gated sodium channels in insect cells. Western blot of *Sf*9 insect cells infected with *hSkM1*-HT recombinant baculovirus at a multiplicity of infection of 1, 2, 5, or 10, and harvested at 64 or 72 h post-infection. Protein expression was detected using an anti-Pan Na_V antibody. The control was uninfected *Sf*9 cells (adapted from Zhang *et al.* [56]).

For protein production, cells were grown to a density of 2×10^6 cells/ml, then infected with baculovirus ($1–2 \times 10^7$ PFU/ml). Protein production in *Sf*9 cells infected with *hSkM1*-HT recombinant baculovirus was verified by electrophoresis and Western blot analysis using an anti-Pan Na_v channel antibody (Alomone Labs, Jerusalem) (1:400), a secondary peroxidase conjugated goat anti-rabbit antibody (Amersham, England) (1:2000), and visualised using chemiluminesence (ECL™, Amersham, England). Expression of *hSkM1*-HT in *Sf*9 insect cells was confirmed by gel electrophoresis and immunodetection (Fig. 3). Protein expression was maximised by establishing the MOI and post-infection time for harvest of infected *Sf*9 insect cells that produced the most protein. MOIs of 1, 2, 5, and 10 were tested in cells harvested at 64 or 72 h. An MOI of 1 after 72 h of infection gave the highest level of protein expression and was routinely used (Fig. 3). To ascertain whether the addition of the His-tag has affected channel function, patch-clamping cells infected with recombinant baculovirus is an ideal functional test to use prior to purification. We have used this method previously to confirm function of *hSkM1*-HT [56].

To generate protein for purification, the culture volume was scaled up to 400 ml and grown in a 1000 ml spinner flask to provide adequate aeration. As before cells were seeded at 5×10^5 cells/ml and cells were grown to a density of 2×10^6 cells/ml, then infected with baculovirus ($1–5 \times 10^7$ PFU/ml). After addition of baculovirus the total culture volume was approximately 500 ml.

5.3. Purification of Recombinant VGSC using IMAC

Purification of intact and functional VGSC protein is challenging due to its large size (260 kDal) and its tendency to degrade rapidly during isolation. This has been

attributed to calcium-dependent proteases, therefore calcium chelators or protease inhibitors are important ingredients throughout the purification procedure. Ethylenediaminetetraacetic acid (EDTA) is often used as a calcium chelator but since it inhibits metal ion binding, IMAC compatible protease inhibitors were used. For successful reconstitution it is important that the protein be solubilised but not denatured. To purify the protein in a form that would remain functional it was solubilised under non-denaturing conditions using the non-ionic detergent, nonidet P-40, which can be easily removed using gel filtration. Triton X-100 is another commonly used detergent in membrane protein biochemistry, but it was not used since it can be difficult to remove, has been shown to form channels in BLMs [67] and can interfere with VGSC function [67,68].

In optimising the metal affinity chromatography method for the sodium channel we identified key factors that were important for improving protein yield. Protease inhibitors reduced but did not eliminate protein degradation, therefore we shortened the length of the procedure in an attempt to reduce this further. The initial 16-h overnight extraction was reduced to just 30 min, as the cells were sufficiently lysed after this time and were less prone to protein degradation during subsequent steps (Fig. 4). Thus the total time from harvest of infected cells until the formation of proteoliposomes was less than 8 h. Another key factor in the optimisation was the addition of phospholipids during the purification steps. Lipid was added to binding, wash, and elution buffers to help maintain the conformational integrity of the protein [69].

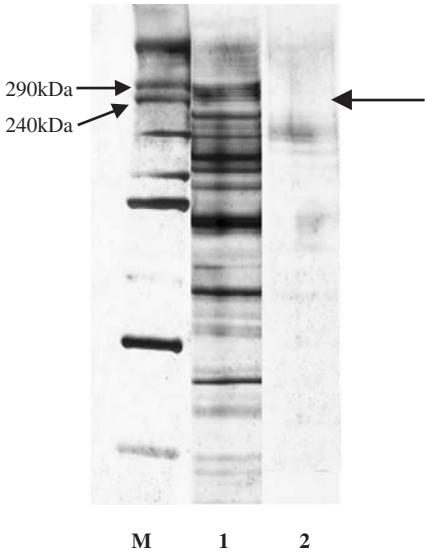

Figure 4 Detection of IMAC-purified VGSCs. Silver-stained polyacrlyamide gel electrophoresis (PAGE) of purified *hSkM1*-HT protein fractions from a Ni^{2+} affinity column, following extraction for 30 min (1), or 16 h (2).

Virus-infected cells (500 ml) were harvested 72 h post-infection by centrifugation at 2000 × g, washed three times in ice cold phosphate-buffered saline, transferred to microfuge tubes and pelleted at 13,000 rpm in a bench-top centrifuge. In some cases cell pellets were stored at –80 °C until use. Cells were resuspended in (20 ml) sonication buffer containing: 100 mM NaCl, 50 mM Tris-HCl, 10% glycerol, and protease inhibitor cocktail tablets (complete mini EDTA-free, Roche, Germany), pH 7.9. These protease inhibitors are compatible with IMAC, being EDTA-free, and they inhibit serine and cysteine proteases, but not metalloproteases. Cells were sonicated at medium intensity (Vibracell, Sonics and Materials Inc., Danbury, USA) in three, 40 s bursts, at 1 min intervals and kept on ice. The addition of 2% NP-40 completed the lysis buffer and the cells were gently agitated on a rocker for 30 min at 4 °C, then centrifuged at 100,000 × g for 40 min at 4 °C.

The supernatant was passed through an agarose matrix preloaded with Ni–NTA (nitrilotriacetic acid) resin (Invitrogen, Carlsbad, USA). Solution flow through the column was by gravity flow. Following equilibration, the column was loaded with the solubilised protein extract in lysis buffer. Ten volumes of binding buffer containing: 500 mM NaCl, 20 mM Tris-HCl, 5 mM imidazole, 10% glycerol, pH 7.9 were added, followed by 10 volumes of wash buffer (binding buffer containing 15 mM imidazole). Washing conditions were optimised by altering the imidazole concentration. It was found that 15 mM imidazole was the highest concentration at which the target protein was retained in the matrix column and much of the non-specific protein was removed. The protein was eluted with five volumes of elution buffer (binding buffer containing 250 mM imidazole, plus protease inhibitor, pH 7.9). Because subsequent steps to remove detergent utilised a binding matrix, all eluate fractions were collected. Samples of the eluate were analysed by sodium dodecyl (lauryl) sulfate-polyacrylamide gel electrophoresis (SDS-PAGE) and the different extraction times compared (Fig. 4). This showed that more protein was present when the extraction time was 30 min compared to 16 h.

SDS/tris-glycine gel electrophoresis indicated a molecular mass of 260 kDa, as determined by Western blot analysis using anti-Pan Na_v antibody (Alomone Labs, Jerusalem, Israel) (Fig. 5A). The protein degraded in the elution buffer after only 12 h at 4 °C, even in the presence of protease inhibitor. However, if freshly purified *hSkM1*-HT protein was reconstituted immediately into liposomes, it did not degrade (Fig. 5A and 5B). Since the protein was more stable when in liposomes, *hSkM1*-HT protein was reconstituted immediately following purification. Under these conditions, channel activity was still present after storage at –80 °C for 4 months. The presence of contaminating bands in the silver-stained gel (Fig. 5B) indicated that the preparation would benefit from further purification, such as size exclusion chromatography. However, since uninfected cells undergoing the same procedure gave no channel activity when reconstituted, the level of purity was considered sufficient for this application.

Detergent removal is an important issue for pBLM research, since its presence will disturb the formation of liposomes and the stability of lipid bilayers. The

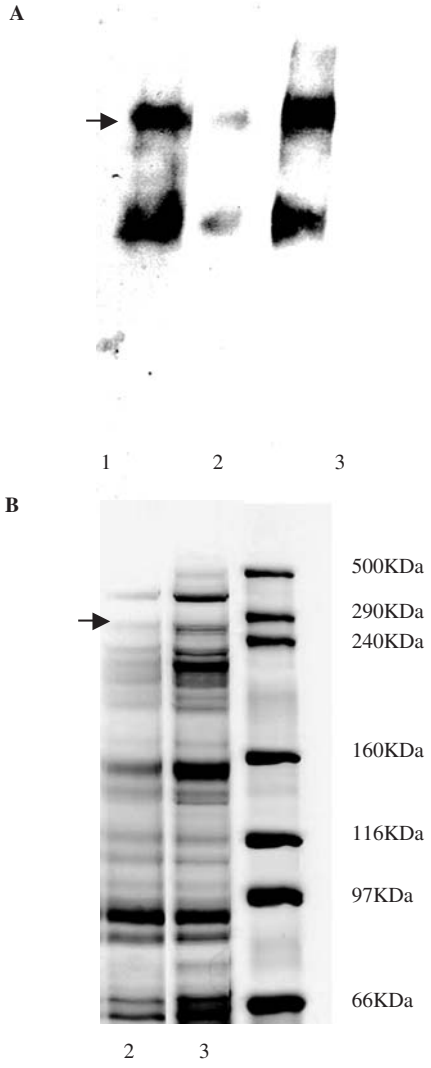

Figure 5 VGSC reconstituted into liposomes. PAGE of purified *hSkM1*-HT protein in eluate or in proteoliposomes detected by Western blot (A) and silver staining (B). Lane 1 – freshly purified protein eluate. Lane 2 – purified protein eluate stored at 4 °C overnight, Lane 3 – purified protein reconstituted into liposomes and stored at 4 °C overnight (adapted from Zhang *et al.* [56]).

dialysis technique is widely used to remove detergent and to buffer exchange, but is time-consuming, usually taking more than 10 h. Affinity purification provides an alternative efficient means of detergent removal. The detergent was, therefore, removed using an Extracti-Gel® D column (Pierce, Rockford, USA). By adding lipids to the detergent-removing gel elution buffer, the detergent could be removed and the protein reconstituted into liposomes in a single procedure.

6. Functional Reconstitution

6.1. Reconstitution of Ion Channels into Liposomes

To reconstitute VGSC protein into liposomes, the composition of phospholipids is important for subsequent fusion of proteoliposomes with pBLMs. Mixed lipids containing acidic lipids, such as phosphatidylserine (PS) can facilitate fusion [70,71]. We used a 10% lipid stock mixture containing a 5:3:1:1 ratio of phosphoethanolamine (PE), phosphatidylserine (PS), phosphatidylcholine (PC) (extracted from egg yolk [72]) and cholesterol (CH) (Avanti Polar Lipids), dispersed by sonication in 10 mM potassium phosphate, pH 7.2. For reconstitution of *hSkM1*-HT channels into liposomes, the lipid stock mix was diluted 1:20 in 10 ml of eluate from the Ni–NTA column, giving a final lipid concentration of 0.5%. The gel filtration column was pre-equilibrated with 0.5% lipid mixture in the phosphate buffer. The protein was also eluted in 10 ml of the phosphate buffer. This resulted in formation of proteoliposomes in the eluate. To concentrate the liposomes the eluate mixture was centrifuged at 100,000 × g for one hour. The supernatant was discarded and liposomes were resuspended in a reconstitution buffer containing: 300 mM NaCl, 15 mM HEPES (*N*-[2-Hydroxyethyl]-piperazine-*N*′-[2-ethanesulfonic acid]), 200 mM sucrose, adjusted to pH 7.4 with KOH, and were either used immediately for pBLM experiments, or stored at −80 °C for later use.

6.2. Incorporation of Proteoliposomes into pBLMs

Theories and methods on fusion of proteoliposomes with lipid bilayers have been illustrated in many books and research articles [40,73,74]. Fusion is reported to occur in two stages. First, contact occurs between the liposome and the bilayer, and this is followed by fusion. The probability of fusion may be increased by swelling the vesicles (proteoliposomes). Miller and Racker [32] found that successful fusion required the presence of acidic lipids, a small amount of Ca^{2+} in the vesicle-containing (*cis*) side, and loading the vesicles with membrane impermeable solute such as sucrose. Establishing an osmotic gradient across the pBLM has been reported to further increase the probability of fusion [75,76]. An osmotic gradient can be achieved by setting up asymmetric *cis* and *trans* solutions. The swelling would be induced via water flow across the vesicle membrane. In theory, once incorporation occurs, fusion can be stopped by addition of an osmicant to the opposite chamber or replacement of the solution in the *cis* chamber with the same solution as that in the *trans* chamber. We found that establishment of such conditions was not necessary because fusion occurred within 15–20 min.

pBLMs were formed from a mixture of 5% PC and 2% CH in *n*-octane across a 200 μm diameter hole in a polystyrene cup separating two chambers. Each chamber contained 1 ml of filter-sterile buffer containing: 300 mM NaCl, 10 mM HEPES, pH 7.4. Single channel recordings from planar bilayer membrane experiments were filtered at 3 kHz, sampled at 150 μs intervals and analysed using TAC 4.2.0 (Bruxton, Seattle) single channel analysis software.

STX dihydrochloride was obtained from the National Research Council of Canada. PbTx-1 was from Calbiochem (San Diego, United States). VTD was purchased from Sigma. TTX was purchased from Alomone Labs (Jerusalem, Israel).

6.3. Orientation of Reconstituted *hSkM1*-HT Channels in pBLMs

To determine the orientation of the reconstituted channels in the pBLM we used membrane impermeant VGSC inhibitors that inhibit by binding to the extracellular face of the channel. TTX and STX inhibit VGSCs by binding to a common site near the extracellular mouth of the pore. The chamber to which *hSkM1*-HT proteoliposomses were added was defined as *cis*. Single or multiple channel events observed in the presence of 100 μM VTD could be blocked completely by TTX or STX, from which we inferred the directionality of the extracellular side of the channel. Our results showed that the *hSkM1*-HT reconstituted channels faced either orientation in pBLMS, but that the STX/TTX-binding site tended to face the side to which liposomes were added (*cis*). This suggests that when in the liposomes, the channels tend to be oriented in the same direction as they are in the cell plasma membrane, with the extracellular STX/TTX-binding site facing the outside. Reconstituted VGSC have been reported to face either the same side, the opposite side, or both sides, from which vesicles are added [49,54,77]. Orientation differences of protein in liposomes are likely to be related to how disruptive the isolation/purification method is; that is how much of the original cell membrane remains intact *versus* how fragmented it becomes prior to reconstitution into liposomes.

6.4. Pharmacological Function of Reconstituted *hSkM1*-HT

Since channel insertion could occur in either orientation, proteoliposomes- (20–40 μl) containing *hSkM1*-HT were added to both *cis* and *trans* chambers to increase the probability of incorporation. We recently investigated the pharmacological integrity of the channel by examining the ability of known activators and inhibitors that bind to different sites on the channel, to modulate its activity [56]. VTD and PbTx-1 promote sodium channel opening by binding to receptor sites 2 and 5, respectively, whereas the VGSC-specific inhibitors, TTX and STX, bind to receptor site 1 at the external mouth of the pore [2]. As sodium channel currents rapidly inactivate, we used the channel activator veratridine which slows their inactivation and allows the channels to be observed under steady-state conditions where the membrane potential is held constant.

Control experiments using liposomes prepared from uninfected cells that underwent the same purification procedure as for infected cells showed no channel activity. This showed that the untargeted protein present (Fig. 5B) did not produce ion channel activity. Protein purified from cells infected with *hSkM1*-HT recombinant baculovirus showed channel activity in the presence of 100 μM VTD (Fig. 6A). The potent and selective sodium channel blocker, TTX, at a concentration of 100 nM, inhibited channel activity (Fig. 6B and 6C). This confirmed the

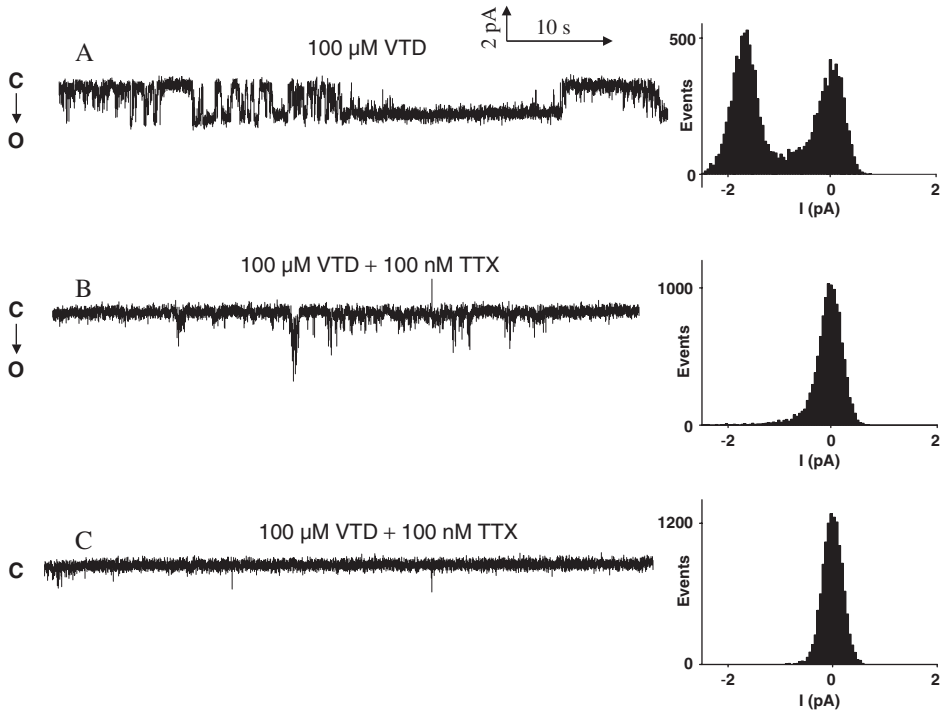

Figure 6 Reconstituted *hSkM1*-HT channels activated by veratridine and inhibited by TTX. Representative channel activity and relative histograms recorded over 1 min are shown for protein reconstituted into liposomes and incorporated into pBLMs. Protein was purified from cells infected with *hSkM1*-HT recombinant baculovirus, recorded at –80 mV in the presence of 100 μM veratridine. (A) control, (B) 8 min after addition of 100 nM TTX, and (C) 10 min after TTX was added. The records shown were filtered at 300 Hz. The arrow indicates the direction of channel opening; C is closed and O is open.

identity of the activity as that of sodium channels. VTD-activated channels were also inhibited by 100 nM STX (Fig. 7). In the example shown in Fig. 7, there were at least two active channels that were partially inhibited after 7 min of exposure to STX and were completely inhibited after a further 20 min of exposure; *hSkM1*-HT channels activated by the algal toxin, PbTx-1, were inhibited by STX (Fig. 8). We also noted that channels activated by VTD or PbTx-1 differed in their maximal conductance level (Fig. 9). VTD-activated channel openings had a slope conductance of 21 pS (Fig. 5H), whereas PbTx-1-activated channels had a slope conductance of 16 pS. *hSkM1* channels activated by voltage alone have a reported slope conductance of 25 pS [78]. Lower conductance levels for VGSCs activated by VTD or PbTx-1 have been reported previously [79–81]. It has been suggested that VTD stabilises the open conformation by blocking the open channel to reduce its unitary conductance [82]. Subconductance levels were prevalent in the single channel recordings in the presence of either VTD or PbTx-1, as reported for native VGSCs (Fig. 8A) [79,80]. The results showed that the reconstituted VGSCs retained their expected pharmacological profile.

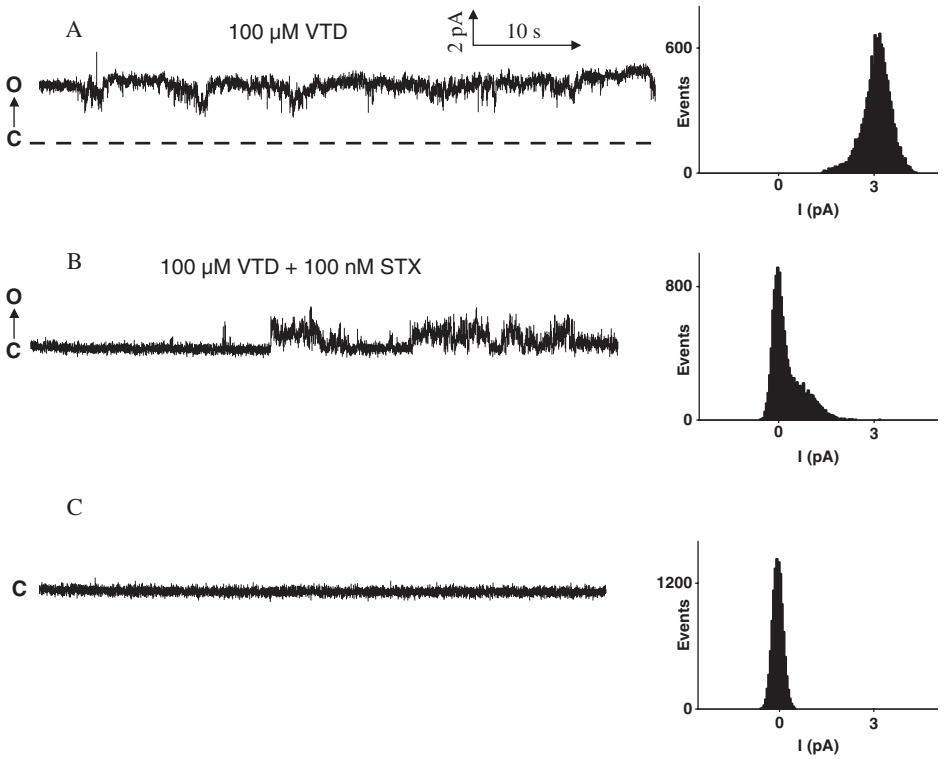

Figure 7 Reconstituted *hSkM1*-HT channels activated by veratridine and inhibited by STX. Channel activity for *hSkM1*-HT at +80 mV in the presence of 100 μM veratridine. (A) control, (B) 7 min, and (C) 27 min after 100 nM STX was presented. The baseline (0 pA) is indicated by the broken line in A. The records shown were filtered at 300 Hz. The arrow indicates the direction of channel opening; C is closed and O is open (data are from a representative experiment).

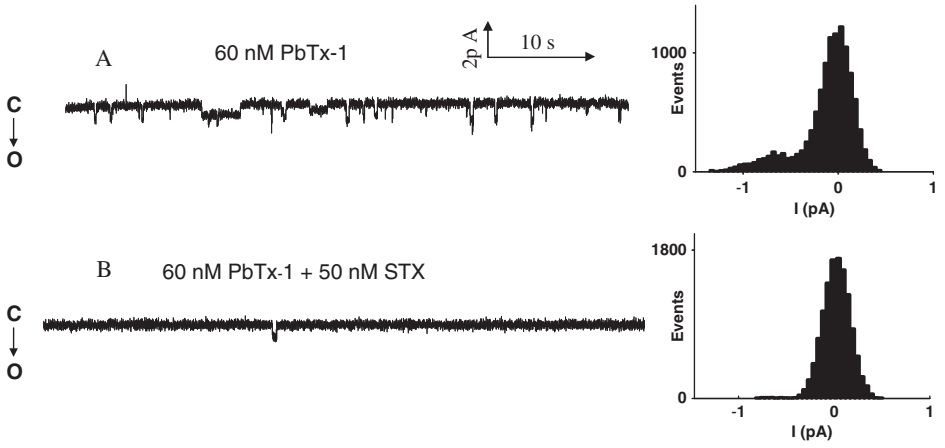

Figure 8 Reconstituted *hSkM1*-HT channels activated by brevetoxin. Channel activity and relative histograms for a representative experiment obtained at −80 mV in the presence of 50 nM PbTx-1. (A) control and (B) 6 min after 60 nM STX was added. The records shown were filtered at 300 Hz.

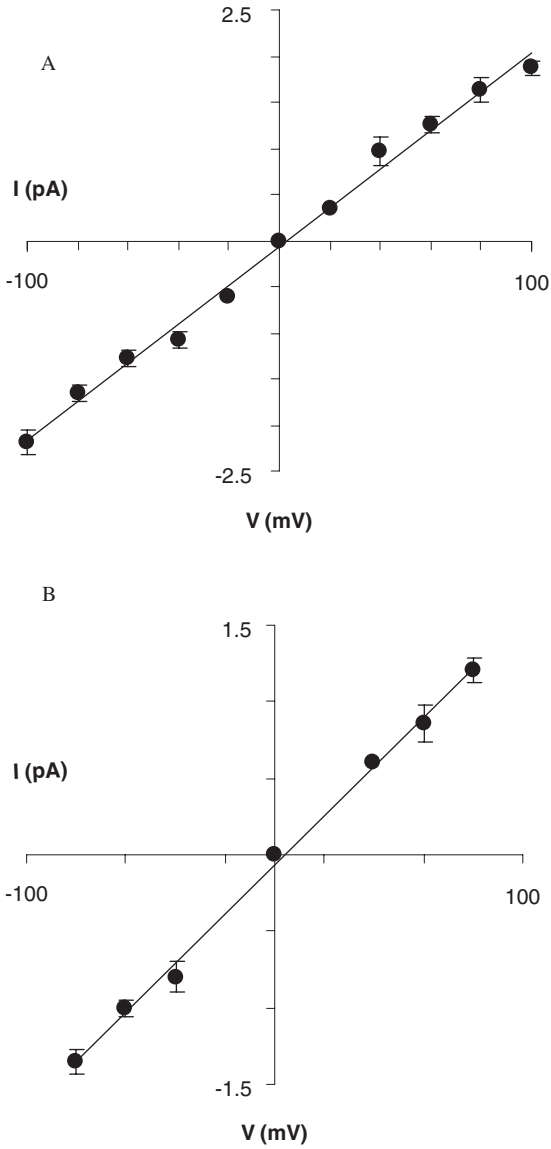

Figure 9 Current–voltage relationship for single *hSkM1*-HT channels activated by (A) veratridine and (B) PbTx-1 in symmetrical 300 mM NaCl solutions (data are from three or more experiments and Fig. 9A is from *Zhang et al.* [56]).

7. Conclusion

This chapter describes a rapid and simplified technique for the purification and reconstitution of VGSCs. This method could be applied to a broad range of

membrane proteins to allow characterisation of their activity in planar BLMs and in supported BLM systems. The development of ion channel sensors for toxin detection, drug and insecticide discovery awaits the merging of robust biomimetic membrane systems with a readily available supply of functional ion channel protein.

ACKNOWLEDGEMENTS

This chapter is dedicated to the memory of Professor H. T. Tien who passed away on 30 May 2004, and who was very helpful in establishing the Biomembrane Laboratory at AgResearch. This work was supported by an AgResearch Postdoctoral Fellowship and funding from the Foundation for Research, Science and Technology, New Zealand.

REFERENCES

[1] W.A. Catterall, From ionic currents to molecular mechanisms: the structure and function of voltage-gated sodium channels, Neuron 26 (2000) 13–25.
[2] H. Denac, M. Mevissen, G. Scholtysik, Structure, function and pharmacology of voltage-gated sodium channels, Naunyn–Schmiedeberg's Arch. Pharmacol. 362 (2000) 453–479.
[3] J.J. Clare, S.N. Tate, M. Nobbs, M.A. Romanos, Voltage-gated sodium channels as therapeutic targets, Drug Discov. Today 5 (2000) 506–520.
[4] A.C. Errington, T. Stohr, G. Lees, Voltage gated ion channels: targets for anticonvulsant drugs, Curr. Top. Med. Chem. 5 (2005) 15–30.
[5] K.M. Blumenthal, A.L. Seibert, Voltage-gated sodium channel toxins: poisons, probes, and future promise, Cell Biochem. Biophys. 38 (2003) 215–238.
[6] M. Noda, S. Shimizu, T. Tanabe, T. Takai, T. Kayano, T. Ikeda, H. Takahashi, H. Nakayama, Y. Kanaoka, N. Minamino, Primary structure of Electrophorus electricus sodium channel deduced from cDNA sequence, Nature 312 (1984) 121–127.
[7] M. Stephan, W.S. Agnew, Voltage-sensitive Na^+ channels: motifs, modes and modulation, Curr. Opin. Cell Biol. 3 (1991) 676–684.
[8] H.L. Tan, C.R. Bezzina, J.P. Smits, A.O. Verkerk, A.A. Wilde, Genetic control of sodium channel function, Cardiovasc. Res. 57 (2003) 961–973.
[9] E. Marban, T. Yamagishi, G.F. Tomaselli, Structure and function of voltage-gated sodium channels, J. Physiol. 508 (Pt 3) (1998) 647–657.
[10] D.A. Doyle, J. Morais Cabral, R.A. Pfuetzner, A. Kuo, J.M. Gulbis, S.L. Cohen, B.T. Chait, R. MacKinnon, The structure of the potassium channel: molecular basis of K+ conduction and selectivity, Science 280 (1998) 69–77.
[11] G.M. Lipkind, H.A. Fozzard, KcsA crystal structure as framework for a molecular model of the Na(+) channel pore, Biochemistry 39 (2000) 8161–8170.
[12] S.B. Long, E.B. Campbell, R. Mackinnon, Crystal structure of a mammalian voltage-dependent Shaker family K+ channel, Science 309 (2005) 897–903.
[13] G.G. Matthews, Cellular Physiology of Nerve and Muscle, 2nd edition, Blackwell, Boston, 1991.
[14] W. Stuhmer, F. Conti, H. Suzuki, X.D. Wang, M. Noda, N. Yahagi, H. Kubo, S. Numa, Structural parts involved in activation and inactivation of the sodium channel, Nature 339 (1989) 597–603.
[15] W.N. Green, L.B. Weiss, O.S. Andersen, Batrachotoxin-modified sodium channels in planar lipid bilayers. Characterization of saxitoxin- and tetrodotoxin-induced channel closures, J. Gen. Physiol. 89 (1987) 873–903.
[16] E. Moczydlowski, S.S. Garber, C. Miller, Batrachotoxin-activated Na^+ channels in planar lipid bilayers. Competition of tetrodotoxin block by Na^+, J. Gen. Physiol. 84 (1984) 665–686.
[17] A. Uehara, E. Moczydlowski, Blocking mechanisms of batrachotoxin-activated Na channels in artificial bilayers, Membr. Biochem. 6 (1986) 111–147.

[18] M.D. Leibowitz, J.B. Sutro, B. Hille, Voltage-dependent gating of veratridine-modified Na channels, J. Gen. Physiol. 87 (1986) 25–46.
[19] J.B. Sutro, Kinetics of veratridine action on Na channels of skeletal muscle, J. Gen. Physiol. 87 (1986) 1–24.
[20] J.W. West, D.E. Patton, T. Scheuer, Y. Wang, A.L. Goldin, W.A. Catterall, A cluster of hydrophobic amino acid residues required for fast Na(+)-channel inactivation, Proc. Natl. Acad. Sci. USA 89 (1992) 10910–10914.
[21] M.Y. Dechraoui, J. Naar, S. Pauillac, A.M. Legrand, Ciguatoxins and brevetoxins, neurotoxic polyether compounds active on sodium channels, Toxicon 37 (1999) 125–143.
[22] C. Mattei, M.Y. Dechraoui, J. Molgo, F.A. Meunier, A.M. Legrand, E. Benoit, Neurotoxins targetting receptor site 5 of voltage-dependent sodium channels increase the nodal volume of myelinated axons, J. Neurosci. Res. 55 (1999) 666–673.
[23] B. Hille, Ionic Channels of Excitable Membranes, 2nd edition, Sinauer Associates Inc., Sunderland, 1992.
[24] I. Garthwaite, Keeping shellfish safe to eat: a brief review of shellfish toxins, and methods for their detection, Trends Food Sci. Technol. 11 (2000) 235–244.
[25] G.P. Rossini, Functional assays in marine biotoxin detection, Toxicology 207 (2005) 451–462.
[26] J. Blay, A.S. Poon, Use of cultured permanent lines of intestinal epithelial cells for the assay of okadaic acid in mussel homogenates, Toxicon 33 (1995) 739–746.
[27] R.L. Manger, L.S. Leja, S.Y. Lee, J.M. Hungerford, M.A. Kirkpatrick, T. Yasumoto, M.M. Wekell, Detection of paralytic shellfish poison by rapid cell bioassay: antagonism of voltage-gated sodium channel active toxins *in vitro*, J. AOAC Int. 86 (2003) 540–543.
[28] M. Okumura, H. Tsuzuki, B. Tomita, A rapid detection method for paralytic shellfish poisoning toxins by cell bioassay, Toxicon 46 (2005) 93–98.
[29] M.A. Quilliam, Phycotoxins, J. AOAC Int. 82 (1999) 773–781.
[30] P. Velez, J. Sierralta, C. Alcayaga, M. Fonseca, H. Loyola, D.C. Johns, G.F. Tomaselli, E. Marban, B.A. Suarez-Isla, A functional assay for paralytic shellfish toxins that uses recombinant sodium channels, Toxicon 39 (2001) 929–935.
[31] H.T. Tien, A.L. Ottova, The lipid bilayer concept and its experimental realization: from soap bubbles, kitchen sink, to bilayer lipid membranes, J. Membr. Sci. 189 (2001) 83–117.
[32] C. Miller, E. Racker, Fusion of phospholipid vesicles reconstituted with cytochrome c oxidase and mitochondrial hydrophobic protein, J. Membr. Biol. 26 (1976) 319–333.
[33] B.A. Cornell, V.L. Braach-Maksvytis, L.G. King, P.D. Osman, B. Raguse, L. Wieczorek, R.J. Pace, A biosensor that uses ion-channel switches, Nature 387 (1997) 580–583.
[34] Y. Cheng, R.J. Bushby, S.D. Evans, P.F. Knowles, R.E. Miles, S.D. Ogier, Single ion channel sensitivity in suspended bilayers on micromachined supports, Langmuir 17 (2001) 1240.
[35] M. Mayer, J.K. Kriebel, M.T. Tosteson, G.M. Whitesides, Microfabricated teflon membranes for low-noise recordings of ion channels in planar lipid bilayers, Biophys. J. 85 (2003) 2684–2695.
[36] A. Janshoff, C. Steinem, Transport across artificial membranes – an analytical perspective, Anal. Bioanal. Chem. 385 (2006) 433–451.
[37] M. Tanaka, E. Sackmann, Polymer-supported membranes as models of the cell surface, Nature 437 (2005) 656–663.
[38] R. Pantoja, D. Sigg, R. Blunck, F. Bezanilla, J.R. Heath, Bilayer reconstitution of voltage-dependent ion channels using a microfabricated silicon chip, Biophys. J. 81 (2001) 2389–2394.
[39] R.J. French, G.W. Zamponi, Voltage-gated sodium and calcium channels in nerve, muscle and heart, IEEE Trans. Nanobioscience 4 (2005) 58–69.
[40] C. Miller, Ion Channel Reconstitution, Plenum Press, New York, 1986.
[41] S. Gonzalez-Perrett, K. Kim, C. Ibarra, A.E. Damiano, E. Zotta, M. Batelli, P.C. Harris, I.L. Reisin, M.A. Arnaout, H.F. Cantiello, Polycystin-2, the protein mutated in autosomal dominant polycystic kidney disease (ADPKD), is a $Ca2^{+}$-permeable nonselective cation channel, Proc. Natl. Acad. Sci. USA 98 (2001) 1182–1187.
[42] Q. Li, X.Q. Dai, P.Y. Shen, H.F. Cantiello, E. Karpinski, X.Z. Chen, A modified mammalian tandem affinity purification procedure to prepare functional polycystin-2 channel, FEBS Lett. 576 (2004) 231.

[43] J. Porath, J. Carlsson, I. Olsson, G. Belfrage, Metal chelate affinity chromatography, a new approach to protein fractionation, Nature 258 (1975) 598–599.
[44] J.A. Bornhorst, J.J. Falke, Purification of proteins using polyhistidine affinity tags, in: J. Thorner, S.D. Emr, J.N. Abelson (Eds.), Methods in Enzymology, Academic Press, New York, 2000, pp. 245–254.
[45] P. Huang, Q. Liu, G.A. Scarborough, Lysophosphatidylglycerol: a novel effective detergent for solubilizing and purifying the cystic fibrosis transmembrane conductance regulator, Anal. Biochem. 259 (1998) 89–97.
[46] M. Ramjeesingh, C. Li, I. Kogan, Y. Wang, L.J. Huan, C.E. Bear, A monomer is the minimum functional unit required for channel and ATPase activity of the cystic fibrosis transmembrane conductance regulator, Biochemistry 40 (2001) 10700–10706.
[47] X.T. Guo, A. Uehara, A. Ravindran, S.H. Bryant, S. Hall, E. Moczydlowski, Kinetic basis for insensitivity to tetrodotoxin and saxitoxin in sodium channels of canine heart and denervated rat skeletal muscle, Biochemistry 26 (1987) 7546–7556.
[48] B.K. Krueger, R.W. Ratzlaff, G.R. Strichartz, M.P. Blaustein, Saxitoxin binding to synaptosomes, membranes, and solubilized binding sites from rat brain, J. Membr. Biol. 50 (1979) 287–310.
[49] B.K. Krueger, J.F. Worley 3rd, R.J. French, Single sodium channels from rat brain incorporated into planar lipid bilayer membranes, Nature 303 (1983) 172–175.
[50] E. Moczydlowski, R. Latorre, Gating kinetics of $Ca2^{+}$-activated K^{+} channels from rat muscle incorporated into planar lipid bilayers. Evidence for two voltage-dependent Ca2+ binding reactions, J. Gen. Physiol. 82 (1983) 511–542.
[51] E.G. Moczydlowski, R. Latorre, Saxitoxin and ouabain binding activity of isolated skeletal muscle membrane as indicators of surface origin and purity, Biochim. Biophys. Acta 732 (1983) 412–420.
[52] H.C. Wartenberg, B.W. Urban, Single sodium channels from human skeletal muscle in planar lipid bilayers: characterization and response to pentobarbital, J. Anesth. 18 (2004) 100–106.
[53] S.D. Kraner, J.C. Tanaka, R.L. Barchi, Purification and functional reconstitution of the voltage-sensitive sodium channel from rabbit T-tubular membranes, J. Biol. Chem. 260 (1985) 6341–6347.
[54] E. Recio-Pinto, D.S. Duch, S.R. Levinson, B.W. Urban, Purified and unpurified sodium channels from eel electroplax in planar lipid bilayers, J. Gen. Physiol. 90 (1987) 375–395.
[55] Z. Chen, C. Alcayaga, B.A. Suarez-Isla, B. O'Rourke, G. Tomaselli, E. Marban, A "minimal" sodium channel construct consisting of ligated S5-P-S6 segments forms a toxin-activatable ionophore, J. Biol. Chem. 277 (2002) 24653–24658.
[56] Y.L. Zhang, J. Dunlop, J.E. Dalziel, Recombinant human voltage-gated skeletal muscle sodium channels are pharmacologically functional in planar lipid bilayers, Biosens. Bioelectron. 22 (2007) 1006–1012.
[57] D.H.L. Bishop, Baculovirus-based expression systems, in: G.W. Gould, (Ed.), Membrane Protein Expression Systems – A Users Guide, Portland Press, London, 1994, pp. 83–124.
[58] A. Kamb, J.I. Korenbrot, J. Kitajewski, Expression of ion channels in cultured cells using baculovirus, in: B. Rudy, L.E. Iverson (Eds.), Methods in Enzymology, Academic Press Inc., Pasadena, 1992, pp. 423–431.
[59] L. Ikonomou, Y.J. Schneider, S.N. Agathos, Insect cell culture for industrial production of recombinant proteins, Appl. Microbiol. Biotechnol. 62 (2003) 1–20.
[60] L.P. Sutugina, S.N. Belzhelarskaya, O.M. Filenko, V.M. Trush, L.P. Buchatskii, K.G. Skryabin, Large-scale technique for recombinant baculovirus production in suspension-cultured insect Sf9 cells, Mol. Biol. 30 (1996) 245–247.
[61] B. Birnir, M.L. Tierney, N.P. Pillai, G.B. Cox, P.W. Gage, Rapid desensitization of alpha 1 beta 1 GABA A receptors expressed in Sf9 cells under optimized conditions, J. Membr. Biol. 148 (1995) 193–202.
[62] C.E. Lindquist, J.E. Dalziel, B.A. Cromer, B. Birnir, Penicillin blocks human alpha 1 beta 1 and alpha 1 beta 1 gamma 2S GABAA channels that open spontaneously, Eur. J. Pharmacol. 496 (2004) 23–32.

[63] J.E. Dalziel, G.B. Cox, P.W. Gage, B. Birnir, Mutating the highly conserved second membrane-spanning region 9′ leucine residue in the alpha(1) or beta(1) subunit produces subunit-specific changes in the function of human alpha(1)beta(1) gamma-aminobutyric Acid(A) receptors, Mol. Pharmacol. 57 (2000) 875–882.
[64] R.H. Roberts, R.L. Barchi, The voltage-sensitive sodium channel from rabbit skeletal muscle. Chemical characterization of subunits, J. Biol. Chem. 262 (1987) 2298–2303.
[65] E. Bennett, M.S. Urcan, S.S. Tinkle, A.G. Koszowski, S.R. Levinson, Contribution of sialic acid to the voltage dependence of sodium channel gating. A possible electrostatic mechanism, J. Gen. Physiol. 109 (1997) 327–343.
[66] N.B. Cronin, A. O'Reilly, H. Duclohier, B.A. Wallace, Effects of deglycosylation of sodium channels on their structure and function, Biochemistry 44 (2005) 441–449.
[67] T.K. Rostovtseva, C.L. Bashford, A.A. Lev, C.A. Pasternak, Triton channels are sensitive to divalent cations and protons, J. Membr. Biol. 141 (1994) 83–90.
[68] J.A. Lundbaek, P. Birn, A.J. Hansen, R. Sogaard, C. Nielsen, J. Girshman, M.J. Bruno, S.E. Tape, J. Egebjerg, D.V. Greathouse, G.L. Mattice, R.E. Koeppe 2nd, O.S. Andersen, Regulation of sodium channel function by bilayer elasticity: the importance of hydrophobic coupling. Effects of Micelle-forming amphiphiles and cholesterol, J. Gen. Physiol. 123 (2004) 599–621.
[69] W.S. Agnew, R.L. Rosenberg, S.A. Tomiko, Reconstitution of the sodium channel from electrophorus electricus, in: C. Miller, (Ed.), Ion Channel Reconstitution, Plenum press, New York, 1986, p. 307.
[70] A.M. Correa, W.S. Agnew, Fusion of native or reconstituted membranes to liposomes, optimized for single channel recording, Biophys. J. 54 (1988) 569–575.
[71] P. Labarca, R. Latorre, Insertion of ion channels into planar lipid bilayers by vesicle fusion, in: B. Rudy, L.E. Iverson (Eds.), Methods in Enzymology, Academic Press, Inc., New York, 1992, p. 447.
[72] W.S. Singleton, M.S. Gray, M.L. Brown, J.L. White, Chromatographically Homogeneous Lecithin From Egg Phospholipids, J. Am. Oil Chem. Soc. 42 (1965) 53–56.
[73] F.S. Cohen, W.D. Niles, Reconstituting channels into planar membranes: a conceptual framework and methods for fusing vesicles to planar bilayer phospholipid membranes, in: N. Duzgunes, (Ed.), Methods Enzymol, Academic Press, San Diego, 1993, p. 50.
[74] A.J. Williams, The measurement of the function of ion channels reconstituted into artificial membranes, in: R.H. Ashley, (Ed.), Ion Channels, a Practical Approach, Oxford University Press, Oxford, 1995, p. 43.
[75] F.S. Cohen, J. Zimmerberg, A. Finkelstein, Fusion of phospholipid vesicles with planar phospholipid bilayer membranes. II. Incorporation of a vesicular membrane marker into the planar membrane, J. Gen. Physiol. 75 (1980) 251–270.
[76] J. Zimmerberg, F.S. Cohen, A. Finkelstein, Fusion of phospholipid vesicles with planar phospholipid bilayer membranes. I. Discharge of vesicular contents across the planar membrane, J. Gen. Physiol. 75 (1980) 241–250.
[77] R.E. Furman, J.C. Tanaka, P. Mueller, R.L. Barchi, Voltage-dependent activation in purified reconstituted sodium channels from rabbit T-tubular membranes, Proc. Natl. Acad. Sci. USA 83 (1986) 488–492.
[78] M. Chahine, P.B. Bennett, A.L. George Jr., R. Horn, Functional expression and properties of the human skeletal muscle sodium channel, Pflugers Arch. 427 (1994) 136–142.
[79] S. Barnes, B. Hille, Veratridine modifies open sodium channels, J. Gen. Physiol. 91 (1988) 421–443.
[80] E. Sigel, Properties of single sodium channels translated by Xenopus oocytes after injection with messenger ribonucleic acid, J. Physiol. 386 (1987) 73–90.
[81] A.M. Corbett, M.A. Vander Klok, Sodium channel subtypes in the rat display functional differences in the presence of veratridine, Biochem. Biophys. Res. Commun. 199 (1994) 1305–1312.
[82] G.K. Wang, S.Y. Wang, Veratridine block of rat skeletal muscle Nav1.4 sodium channels in the inner vestibule, J. Physiol. 548 (2003) 667–675.

This page intentionally left blank

CHAPTER THREE

Insights in the Organization and Dynamics of Erythrocyte Lipid Rafts

Ulrich Salzer*, Ursula Hunger, *and* Rainer Prohaska

Contents

1. The Erythrocyte Membrane 51
2. Lipid Rafts 52
   2.1. Lipid Phases in Model Membranes and Cell Membranes 52
   2.2. Mutual Influence Between Lipid Phases and Proteins 53
   2.3. Detergent-Resistant Membranes 55
   2.4. Experimental Evidence for Lipid Rafts 55
   2.5. A Revised Version of the Lipid Raft Hypothesis 56
3. DRMs of the Erythrocyte Membrane 57
   3.1. Evidence for the Association of the Cytoskeleton with DRMs 58
   3.2. The Erythrocyte Cytoskeleton – DRM Complex: Possible Connections 65
4. Exovesiculation of Erythrocytes 66
   4.1. Cell Shape and Exovesiclulation 67
   4.2. DRMs of Exovesicles 68
5. Lipid Rafts of Erythrocytes: Hypothetical Considerations 70
   5.1. Rafts, Membrane Curvature and Vesiculation: Theoretical Considerations 72
   5.2. Rafts and Erythrocyte Vesiculation 72
   5.3. Rafts and Malarial Infection 74
6. Conclusions 75
References 75

Abstract

Lipid rafts are domains of a liquid-ordered lipid phase enriched in cholesterol and sphingolipids that are thought to reversibly form within the mainly liquid-disordered lipid phase of biological membranes. Specific types of membrane proteins preferentially partition into lipid rafts and thereby might influence the stability and the size of these lipid domains. Studies on model membranes mimicking the lipid composition of the erythrocyte membrane and analyses of erythrocyte detergent-resistant membranes indicate that lipid domains are present in these cells. The glycosylphosphatidylinositol-anchored

* Corresponding author. Tel: +43-1-4277-61661; Fax: +43-1-4277-9616
E-mail address: ulrich.salzer@meduniwien.ac.at (U. Salzer).

Department of Medical Biochemistry, Max F. Perutz Laboratories, Medical University of Vienna, Dr. Bohr-Gasse 9/3, Vienna A-1030, Austria

Advances in Planar Lipid Bilayers and Liposomes, Volume 6
ISSN 1554-4516, DOI 10.1016/S1554-4516(07)06003-6

proteins acetylcholinesterase, CD55 and CD59 and the oligomeric proteins stomatin, flotillin-1 and flotillin-2 are the major integral proteins of erythrocyte detergent-resistant membranes. We show that cytoskeletal components like spectrin and actin are tightly linked to detergent-resistant membranes thereby suggesting a role for the cytoskeleton in the regulation of membrane raft domains presumably by influencing their mobility and size. Rafts seem to be involved in the erythrocyte exovesiculation process since detergent-resistant membranes can be isolated from vesicles and specific raft proteins are found to be concentrated at the tips of echinocytic membrane protrusions. The differential enrichment or depletion of raft proteins in vesicles indicates that various types of rafts co-exist at the erythrocyte membrane and segregate during exovesiculation probably due to differences in their specific intrinsic curvatures or in the degree of association with the cytoskeleton. We propose a model of a raft-driven vesiculation mechanism by assuming that raft domains may specifically aggregate in membrane regions that are uncoupled from the underlying cytoskeleton and that this local phase separation leads to the spontaneous formation of a spherical bud to minimize the line tension at the border between the lipid phases. Erythrocytes seem to exploit this behaviour of co-existing lipid phases to prevent complement-mediated cell lysis by releasing vesicles that contain assembled membrane attack complexes. It is also conceivable that the malaria parasite *Plasmodium falciparum* uses a similar mechanism for transforming the erythrocyte host membrane into the parasitophorous vacuolar membrane during erythrocyte infection.

Abbreviations

AChE	acetylcholinesterase
AFM	atomic force microscopy
CTB	cholera toxin subunit B
DAF	decay accelerating factor
DRMs	detergent-resistant membranes
FcεRI	IgE receptor
FRAP	fluorescence recovery after photobleaching
FRET	fluorescence resonance energy transfer
GPI	glycosylphosphatidylinositol
GUVs	giant unilamellar vesicles
HD	high density
HS	hereditary spherocytosis
ID	intermediate density
IgG	immunoglobulin G
LD	low density
l_d	liquid-disordered
l_o	liquid-ordered
MβCD	methyl-β-cyclodextrin
MAC	membrane attack complex
NEGC	non-equilibrium gradient centrifugation
PC	phosphatidylcholine
PIP_2	phosphatidylinositol-4,5–bisphosphate
PLAP	placental alkaline phosphatase

PVM	parasitophorous vacuolar membrane
SLP-2	stomatin-like protein 2
SM	sphingomyelin
s_o	solid-ordered
TBS	tris-buffered saline
TX-100	Triton X-100

1. The Erythrocyte Membrane

Erythrocytes are highly specialized cells that transport oxygen to the peripheral tissues and contribute to the delivery of carbon dioxide to the lungs. The plasma membrane of human erythrocytes is the only lipid confinement, as these cells lack the nucleus and other intracellular organelles. An outstanding property of erythrocytes is their deformability which is necessary to enable the passage through the narrow pores of the capillary vasculature. The unique cell shape, a biconcave disc of 8 μm in diameter, confers these properties to the cells by allowing reversible shape changes without increasing the surface area of the membrane. The cytoskeleton which coats the cytoplasmic side of the membrane as a polygonal lattice, is the main determinant of the cell shape and the mechanical properties of an elastic semi-solid. This property allows the storage of energy during brief periods of deformation and restores the original shape when the deformation stops [1]. The legs of the polygons are formed by spectrin and the junction points are formed by short actin filaments. Spectrin is a flexible rod-shaped molecule of 200 nm in length. Laterally associated dimers of spectrin α and β isoforms interact at one end with the respective end of a second spectrin dimer and on the other end with the actin filaments. A group of accessory proteins, like protein 4.1, dematin, adducin, tropomyosin and tropomodulin are present at the spectrin–actin junctions [2]. There are two major linkage points to the membrane: the first is represented by ankyrin which binds to spectrin in the proximity to the interaction site of the two spectrin dimers and to the N-terminal domain of the major erythrocyte membrane protein, the anion exchanger 1 (AE1, also termed band 3 protein). The second membrane attachment point is formed by a ternary complex of the transmembrane protein glycophorin C, the palmitoylated p55 protein and the 4.1 protein that is located at the spectrin–actin junction [3].

Apart from the direct interaction of the cytoskeleton with integral membrane proteins, the cytoskeleton has a major structuring impact on membrane components as highlighted by a study of the lateral diffusion of the band 3 protein [4]. Mobile band 3 protein – about 60% are not bound to the cytoskeleton – exhibits a so-called hop-diffusion by being temporarily corralled in a mesh of about 100 nm in diameter. This indicates that the underlying cytoskeleton acts as a fence that strongly limits the mobility of integral membrane proteins. Moreover, several types of cytoskeleton–lipid association have been reported. Spectrin binds to anionic phosphatidylserine [5] and protein 4.1 has recently been shown to be a

phosphatidylinositol-4,5-bisphosphate (PIP_2) binding protein [6]. Moreover, a strong connection between the cytoskeleton and the membrane cholesterol has been indicated [7]. These data show that the protein and lipid membrane components in erythrocytes are intimately coupled to and organized by the spectrin–actin membrane skeleton.

2. Lipid Rafts

The concept of "lipid rafts" originally proposed by Simons and Ikonen [8] suggests the existence of assemblies of sphingolipids and cholesterol that segregate from the bulk of membrane lipids due to the formation of a liquid-ordered (l_o) phase and thereby represent platforms within the membrane where specific membrane proteins are selectively included. This concept gained outstanding attention since lipid rafts have been implicated to play roles in various signal transduction pathways, in intracellular trafficking processes and in cell entry and exit mechanisms of viruses. Yet, in contrast to the simplicity and the theoretical utility of the raft hypothesis, it has been proven difficult to obtain unequivocal, experimental evidence regarding the size, lipid composition, stability and even existence of lipid rafts in cellular membranes. The main difficulty is that rafts are too small to be directly observed by fluorescence microscopy. Recently, several advanced imaging approaches have been applied to investigate the membrane microdomain structure and provided data which will have to be integrated in an adapted and refined version of the lipid raft concept.

2.1. Lipid Phases in Model Membranes and Cell Membranes

The biophysical membrane research assumes that the behaviour of the plasma membrane can be anticipated by studying simple hydrated phospholipid bilayers, which are the basic structures of cellular membranes. From these studies, it is known that for a particular lipid composition there is a specific temperature at which a transition from a solid-ordered (s_o) to a liquid-disordered (l_d) phase occurs. This transition is characterized by an increase in the lateral mobility of the lipids and disorder of the acyl side chains. When cholesterol is included in the lipid mixture, a third phase can be observed which displays the lateral mobility of a liquid phase but the tight acyl side chain packaging of the s_o state and is therefore named l_o. The condensing effect of cholesterol might be due to an "umbrella" function of the phospholipids for cholesterol. The phospholipid head groups are suggested to shield the hydrophobic cholesterol from the contact with water at the membrane water interface [9]. Within the membrane, the rigid sterol ring structure exerts an ordering influence on the phospholipid side chains. Compared to side chains that contain one or more double bonds, saturated acyl chains can be packed more tightly. Cholesterol has been shown to preferentially interact with lipids that have fully saturated lipid side chains [10]. Interestingly, cholesterol induces the formation of nanoscopic domains of immiscible phases in mixtures of dipalmitoyl-phosphatidylcholine (PC) and

dilauroyl-PC [11]. Moreover, compared to phospholipids, there is a clear preference of cholesterol to interact with sphingolipids. Sphingolipids, like sphingomyelin (SM) or gangliosides, are derivatives of the ceramide structure which consists of sphingosine with a long, generally, fully saturated fatty acid attached to an amide bond. Recently, a ternary phase diagram of palmitoyl-SM, 1-palmitoyl-2-oleoyl-PC and cholesterol has been published [12]. These three lipid species roughly reflect the lipid composition of the exoplasmic leaflet of plasma membranes. These data may be cautiously extrapolated to the cellular context and thereby may provide valuable information on the phase status of cell membranes. The phase diagram has been experimentally determined at 23°C and a hypothetical diagram for the physiological 37°C temperature point is also presented. Interestingly, at lipid concentrations that are normally observed in cell membranes, there is a co-existence of l_d and l_o phases thereby giving biophysical support for the hypothesis that lipid rafts are present in cellular membranes. Various studies have been assigned to investigate the phase status of lipid mixtures in supported monolayers, planar lipid bilayers and giant unilamellar vesicles [13,14]. Phase separation can be studied by light microscopy when fluorescent probes are used that partition preferentially in one of the phases. Cholesterol-extracting agents like methyl-β-cyclodextrin (MβCD) abolish the phase separation thereby showing the critical dependence of phase domain formation on the cholesterol concentration. In contrast to studies in model membranes, it is very difficult to determine the phase status of intact cellular membranes and to approach the question whether domains of immiscible lipid phases also occur in the cellular context. Recently, Meder *et al*. provided evidence for the coexistence of at least two different lipid bilayer phases in the apical plasma membrane of epithelial cells [15]. In fluorescence recovery after photobleaching (FRAP) experiments, they observed differences in the diffusion rate and the fraction of recovery dependent on the type of membrane protein studied. Proteins that preferentially partition in l_o phases (so-called raft proteins) showed a faster diffusion and full recovery, whereas proteins that are known to be excluded from l_o phases were slower and displayed only partial recovery. As this phenomenon was only observed when the cells were studied at 25°C, the authors concluded that at this temperature the plasma membrane of these cells exhibit a continuous raft phase (l_o) with interspersed islands of non-raft liquid phases (probably l_d) so that the raft proteins can diffuse freely whereas non-raft proteins are rather confined to the l_d domains and are restricted in their diffusion.

2.2. Mutual Influence Between Lipid Phases and Proteins

One of the essential predictions of the lipid raft hypothesis is that raft domains can selectively enrich and exclude different types of membrane proteins and that this lateral protein segregation is crucial for various cellular functions. Typical raft proteins are the glycosylphosphatidylinositol (GPI)-anchored proteins at the exoplasmic membrane leaflet and doubly acylated proteins such as heteromeric G proteins or tyrosine kinases of the Src family that reside at the cytoplasmic leaflet of the membrane bilayer. Using brush border membrane lipids in a supported monolayer membrane model system, it was shown that the GPI-linked Thy-1 protein preferentially partitions into l_o domains. In synthetic lipid mixtures, the l_o-specific

distribution of Thy-1 was reduced to 40%, indicating that the molecular packing in the l_o phase of synthetic mixtures is tighter than in cell membranes [16]. In giant unilamellar vesicles (GUVs) composed of a similar synthetic lipid mixture, 30% of the GPI-anchored placental alkaline phosphatase (PLAP) associates with the l_o phase, whereas a non-raft protein was virtually excluded therefrom [17]. Moreover, Wang *et al.* [18] investigated the partition behaviour of differentially lipidated peptides and found that peptides with two saturated fatty acids (the membrane anchor of a typical cytoplasmic raft protein) were also specifically located at l_o domains. It is understandable that for proteins which are associated with the membrane solely by lipid anchors, these lipid modifications determine the differential affinity of the proteins for co-existing lipid phases. But also specific transmembrane proteins have been shown to be raft associated; as l_o domains are known to be thicker than l_d domains, the length of the hydrophobic transmembrane helix seems to be an important factor influencing the partition coefficient of the respective protein. Interestingly, the glutamate receptor which is a G-protein coupled seven-helix transmembrane protein alters its conformation and ligand binding affinity in dependence of the surrounding lipid phase [19]. Therefore, it is conceivable that in the cellular context different mechanisms exist to modulate the affinity of signalling proteins for lipid phases and that this is another level of regulating raft-based signalling processes.

As outlined above, it is well-established that lipid phases influence the spatial distribution of proteins within the plane of the membrane. Conversely, there is also evidence that protein-based processes can influence phase separation in lipid bilayers. Hammond *et al.* [20] used mixtures of PC, SM and cholesterol in compositions to give either a uniform l_d or l_o phase. These mixtures also contained a small but constant mole fraction of the ganglioside GM1. Addition of cholera toxin subunit B (CTB), a bacterial protein known to bind to several molecules of GM1, resulted in a large-scale reorganization of the model membrane by causing the phase-separation of large, co-existing l_d and l_o domains. Moreover, after GM1 cross-linking by CTB a transmembrane raft peptide marker that was reconstituted in this model membrane was specifically localized to the l_o domains. This result demonstrates how cross-linking of one membrane component can alter the localization of other proteins and lipids and thereby could be a model for membrane domain formation e.g., in immune-recognition receptor signalling in B and T cells [21]). The formation of caveolae, which are cholesterol-rich, flask-shaped membrane invaginations on the plasma membrane of specific cells is another prototypic example for such a process. The major protein constituent, caveolin which associates with rafts due to its three palmitic-acid modifications and its cholesterol-binding property, is thought to drive this process by the formation of large homo-oligomeric complexes [22]. Cross-linking and oligomerization of raft components should not only be considered as events to locally increase the size of lipid rafts but may also act as protein-driven mechanisms that have a global impact on the phase status of the membrane. Moreover, it has been suggested that specific membrane proteins might have an impact on the stability of small l_o domains by localizing to the l_o–l_d phase boundary and thereby decreasing the line tension between the phases [23]. Specifically, transmembrane proteins might act as "surfactants" at the phase boundaries but also peripherally associated proteins have been shown to reside at the borders of

membrane domains. The signalling proteins phospholipase Cγ1 and phosphatidylinositol 3-kinase are located at the border of specific raft domains possibly due to their conflicting localization signals of their membrane anchors, a saturated fatty acid modification and a C-terminal unsaturated prenyl anchor [24,25]. H-ras is involved in the formation of non-raft membrane microdomains thereby determining the final composition of the H-ras signalling complex [26]. In summary, there seem to be various possibilities how membrane proteins influence the organization of lipids and hence membrane domains in the bilayer.

2.3. Detergent-Resistant Membranes

Detergent-resistant membranes (DRMs) are the most controversial aspect in the context of the lipid raft hypothesis. It was originally observed by Brown and Rose that GPI-linked proteins become resistant to extraction by Triton X-100 (TX-100) during their passage through the Golgi complex [27]. These DRM complexes could be separated from the bulk TX-100 soluble protein by density-gradient ultracentrifugation: due to their high lipid content, DRMs floated to the low-density (LD) region of the gradient. As the DRMs were specifically enriched in cholesterol, SM and glycolipids, it was suggested that the DRMs might be correlated with the previously postulated lipid rafts at the cell membrane [28]. However, it is obvious that DRMs cannot be assumed as being identical with cellular raft domains in their lipid and protein composition. First, various types of rafts that are assumed to co-exist at the membrane will always be irreversibly mixed and fused in DRMs. Second, the low temperature required for DRM preparations (0–4°C) might influence the phase state of the membrane for thermodynamic reasons. And third, it has been shown that TX-100 affects the formation of l_o domains in synthetic lipid mixtures [29,30]. In analysing DRMs, one has always to keep in mind that over- or under-representation of raft proteins or lipids in DRMs is likely to be the case. Experimental evidence for an over-representation of a raft protein in DRMs was shown in a model membrane system. GPI-linked PLAP reconstituted in GUVs was nearly completely insoluble in TX-100 although only 30% is localized to l_o domains in the unperturbed vesicles [17]. DRM preparation protocols should be carefully established for each cell system to minimize additional artefacts. For example, a sufficiently high detergent/lipid ratio is essential to avoid incomplete solubilization of non-raft components [31]. However, in spite of these caveats, the DRM methodology has been proven useful, because most of the proteins that are typically present in DRMs have been shown to be raft associated when tested by different methods (Section 2.4) [32]. Recently, a quantitative proteomic approach was applied to classify DRM proteins with respect to the cholesterol sensitivity of their DRM association; thereby, this study revealed a set of about 250 authentic lipid raft proteins [33].

2.4. Experimental Evidence for Lipid Rafts

Cross-linking of raft components can induce the formation of large raft aggregates at the plasma membrane; however, in the resting state, lipid rafts have been proven to be too small to be studied by normal microscopic techniques. Several different

advanced techniques have been used in order to determine the existence and size of raft domains in the plasma membrane. Fluorescence resonance energy transfer (FRET) studies showed a partial clustering of GPI-linked proteins in nanoscale domains that were sensitive to cholesterol depletion [34,35]. Pralle *et al.* [36] applied photonic force microscopy and found that the viscous drag of three different raft proteins mediated by bead-coupled specific antibodies was significantly higher than that of non-raft proteins. This difference was abolished when rafts were destroyed by incubating the cells with MβCD. In this experiment, the size of the rafts was estimated to be about 50 nm. A similar size (44 nm) was obtained in an immuno-electron microscopy study that analyzed the distribution of a raft marker on the cytoplasmic leaflet of the plasma membrane by spatial point pattern analysis [37]. MβCD treatment resulted in a random distribution of the marker. Interestingly, cross-linking of a GPI-linked outer-leaflet raft protein influenced the distribution of the inner-leaflet raft marker and indicates that there is a loose association between inner and outer-leaflet rafts. Moreover, also non-raft microdomains specified by their resistance to MβCD treatment have been identified. Wilson *et al.* [38] studied the distribution of 4 different raft markers, i.e. the ganglioside GM1, the GPI-linked Thy-1, the palmitoylated LAT protein and cross-linked IgE receptors FcεRI, at the plasma membrane of a mast cell line by immunoelectron microscopy. In resting cells, Thy-1 and FcεRI are found in small clusters (20–50 nm), whereas GM-1 is rarely clustered at all, thereby indicating that various types of rafts regarding their composition and size might co-exist at the membrane. Upon cross-linking, these three markers form independent larger clusters and LAT was found to co-cluster with Thy-1 complexes. The large GM1 and Thy-1 clusters accumulate components of the endocytic machinery indicating that aggregation of these specific rafts leads to a local endocytic event. In summary, these data actually support the view of the raft hypothesis that small cholesterol-rich microdomains are present at the plasma membrane where raft proteins are specifically enriched.

2.5. A Revised Version of the Lipid Raft Hypothesis

Hancock recently proposed a revised version of the lipid raft hypothesis suggesting a dominant role for plasma membrane proteins in the formation and maintenance of lipid domains [23]. Small, transiently forming l_o domains might be captured by a raft protein, thereby conferring stability to the lipid raft. Protein interaction and oligomerisation might eventually increase both the size and the lifetime of these lipid domains which might be involved in specific cellular processes. On the other hand, it would be expected that small protein-stabilized l_o domains coalesce in ever larger domains to minimize the line of tension at the l_o–l_d phase boundary. As such, large complexes are usually not observed in the plasma membrane, an active mechanism seems to prevent large-scale phase separation. It is suggested that endocytosis might be the cellular process that limits the raft-domain size [39]. Large rafts might be removed from the plasma membrane by endocytosis and smaller, disassembled raft units might recycle back to the plasma membrane by recycling endosomes or other vesicular transport pathways. In fact, endocytosis is a raft-based process and is known to be increased upon cross-linking rafts into larger domains

[40]. The revised raft hypothesis stresses that proteins play an active role in the organization of the plasma membrane by exploiting the intrinsic properties of lipid mixtures to form co-existing liquid phases. This dynamic, complex and interactive model replaces the "old" view of rafts as stable units within the membrane that govern the lateral distribution of membrane proteins.

3. DRMs of the Erythrocyte Membrane

It was actually a solubilization study of erythrocyte membranes 33 years ago that led to the first description of DRMs, although the term "DRM" was not used then. Yu *et al.* [41] showed that upon extraction with the non-ionic detergent TX-100 glycerolipids were solubilized, whereas sphingolipids remained associated with the "detergent-insoluble ghost residue". When studied by electron microscopy, these membrane residues appeared to be a "filamentous reticulum with adherent lipoid sheets and vesicles". However, the main focus of that work was to characterize the differential solubilization behaviour of non-glycosylated polypeptides (mostly cytoskeletal components) and externally oriented glycoproteins (integral membrane proteins). Nearly 30 years later, detergent resistance of erythrocyte membrane components has regained vital interest as this feature is a prerequisite for proteins and lipids to be classified as lipid raft components. The characterization of DRMs is the main approach in the raft research of erythrocytes, because other methods are difficult or even impossible to apply to these cells. Using washed erythrocyte membranes (ghosts), Civenni *et al.* [42] showed that the GPI-linked proteins AChE and CD59 were mainly associated with the detergent-insoluble fraction upon TX-100 treatment. Unlike the endogenous proteins, *in vitro* incorporated GPI-linked proteins were not resistant to membrane extraction thereby indicating that exogenously added GPI proteins do not co-distribute with the endogenous proteins in lipid rafts. Lauer *et al.* [43] showed that the Duffy antigen, a heptahelical transmembrane protein, and the signalling protein Gαs also resist membrane extraction and are partially found in the LD region of a sucrose gradient in flotation experiments. Our flotation experiments revealed that stomatin, flotillin-1 and flotillin-2 are the most abundant integral membrane proteins in erythrocytes [44]. Whereas stomatin was a well-described erythrocyte membrane protein (also termed band 7 protein, or protein 7.2b) [45,46] that has been shown to be absent in erythrocytes of overhydrated hereditary stomatocytosis (OHSt) patients [47,48], the flotillins have not been described as erythrocyte membrane proteins before. The association with lipid rafts is a prominent feature of the flotillin proteins; in A498 kidney cells they have been described to be present in caveolae where they form hetero-oligomeric complexes with caveolin [49] and in neurons they were shown to co-cluster in membrane microdomains with activated GPI-linked cell adhesion proteins [50,51]. Stomatin and the flotillins are distantly related proteins that share a common structural domain, the SPFH domain named after the most prominent representatives: **S**tomatin, **P**rohibitins, **F**lotillins and the bacterial **H**flK and C proteins [52]. For stomatin, it has been shown that it is an untypical integral

membrane protein with both the N- and the C-terminus facing the cytoplasm and with a long hydrophobic stretch probably being inserted into the membrane like a hairpin loop [53]. Caveolins are the only other membrane protein class that show such a peculiar monotopic membrane association [22]. Protease sensitivity experiments in baby hamster kidney [54] cells and intact red blood cells (data not shown) suggest that the flotillin proteins are not transmembrane proteins but are also monotopically associated with the cytoplasmic face of the plasma membrane. As the flotillin proteins and stomatin form large oligomeric complexes in the erythrocyte membrane [44], it is tempting to assume that these proteins function as scaffolding proteins at the cytoplasmic leaflet of erthrocyte lipid rafts [55].

In contrast to reports by Samuel *et al.* [56] and Murphy *et al.* [57], we found that a fraction of the major erythrocyte cytoskeletal components, spectrin, actin, protein 4.2 and protein 4.1, is co-distributing with the integral raft proteins stomatin and the flotillins in the LD region of the sucrose gradient [44]. In the following section, we will present biochemical data that further suggest an association between DRMs and the erythrocyte membrane skeleton and we will discuss possible candidate molecules that might mediate this association. Moreover, we will try to explain the seeming discrepancy between the data of our and Kasturi Haldar's group.

3.1. Evidence for the Association of the Cytoskeleton with DRMs

When we routinely isolated red blood cell DRMs by our published method [44], we often noticed donor-dependent variations regarding the degree of DRM buoyancy and cytoskeleton association. To clarify which parameters might be responsible for these variations, we undertook a series of experiments with different methodological variations of the established protocols for DRM preparation and developed three different DRM preparation protocols. In protocol I, erythrocytes are diluted in four volumes of tris-buffered saline (TBS, 150 mM NaCl, 10 mM Tris pH = 7.5) and this suspension is lysed by mixing with an equal volume of ice-cold 2% TX-100 in TBS for 20 min. This lysate is centrifuged for 10 min at 13,000 rpm to concentrate the insoluble material consisting of the cytoskeleton and DRMs; this pellet is resuspended in 1% TX-100 in TBS and then mixed with the appropriate sucrose solution to give the bottom layer of the sucrose step gradient. This protocol is preferably applied when whole erythrocytes are used as starting material, because the high haemoglobin content in the original total lysate can be reduced this way. In protocol II, the pelleting step is omitted and the TX-100 lysate is directly mixed with the high-density sucrose solution for subsequent flotation experiments. This protocol can be used when ghosts are used as starting material or in experiments with whole erythrocyte lysates when the analysis of the high-density bottom fraction can be neglected (due to its high haemoglobin content which would interfere with Western blot analysis). This protocol was specifically designed to address the question whether the association between the DRMs and the cytoskeleton is already present in the lysate or only occurs after the centrifugation step due to the dense packing of DRMs and the cytoskeleton in the pellet. Protocol III is a variation of protocol I where the cytoskeleton-DRM pellet is resuspended in 0.2 M sodium carbonate instead of TBS to dissolve the cytoskeletal network and to impair

its interaction with DRMs. To generally obtain a separation of the DRMs with higher density from the TX-100 soluble material, we increased the sucrose density in the bottom layer and expanded the intermediate density region of the gradient compared to the method published in [44].

The flotation experiments according to protocols I and III are compared in Fig. 1. Using the protocol I with erythrocytes as starting material, the typical distribution of protein and lipid markers in the density gradient of a flotation experiment is shown in Fig. 1A. Only small amounts of the DRM marker proteins stomatin, flotillin-2 and AChE are present in the LD fraction 1, whereas the major pool of these markers co-distributes at intermediate densities (ID) in fractions 3–6. Cholesterol partially co-distributes with AChE, flotillin-2 and stomatin in the LD and the ID region. Moreover, we found that SM was nearly exclusively present in the LD and ID region (data not shown), which is in line with results from Koumanov *et al.* [58]. The silver-stained gel in Fig. 1A reveals that the overall protein concentration is highest in the bottom layer (HD) of the gradient. For appropriate silver staining, the bottom fractions were diluted because of the high amount of protein (see figure legends), whereas equal volumes of the fractions were used for the immunoblot, AChE, cholesterol and SM analyses. The silver stain in Fig. 1A shows that LD fraction 1 contains only a small amount of the proteins stomatin and the flotillins, whereas a large amount of these DRM markers is found in the ID fractions 3–6. A considerable amount of the cytoskeletal components spectrin and actin co-distribute with the DRM markers in the ID region of the gradient.

These data reveal two pools of DRMs at different densities in the gradient: a small pool at LD containing the typical DRM markers, and a large pool of DRMs at IDs that is associated with considerable amounts of cytoskeletal proteins. The cytoskeleton–DRM association is not a procedural artefact due to the tight packing of DRMs and the cytoskeleton during the pelleting step of protocol I, because the cytoskeleton–DRM complexes are also obtained by protocol II, which lacks this pelleting step (data not shown). Moreover, we excluded the possibility that the presence of high amounts of haemoglobin during lysis influences the result of a DRM flotation experiment; several experiments that directly compared the DRMs from erythrocytes and ghosts did not reveal major differences (data not shown). In order to assess the relative amounts of the cytoskeleton-free and the cytoskeleton-loaded DRM pools and to estimate the magnitude of the donor-specific variations, we performed a statistical analysis of the results of six independent flotation experiments (protocol I) with erythrocytes from different donors. We estimated the relative amounts of each DRM and cytoskeletal marker in the fractions by densitometry of silver-stained gels and/or quantitative immunoblotting and assessed their relative distribution in the LD, ID and HD regions. Fig. 2 reveals that only 5% to maximally 20% of the DRM markers stomatin, flotillin, AChE, SM and cholesterol are present in the cytoskeleton-free DRM pool in the LD region, whereas 60–80% of these markers are found in the cytoskeleton-associated DRM pool at ID. Moreover, about 40% of the cytoskeletal components actin and spectrin are associated with this DRM pool in the ID region. We want to stress here that these values of the DRM markers give the percentage of the TX-100 insoluble fraction and that 100% does not refer to the total amount of the respective marker in the cell because

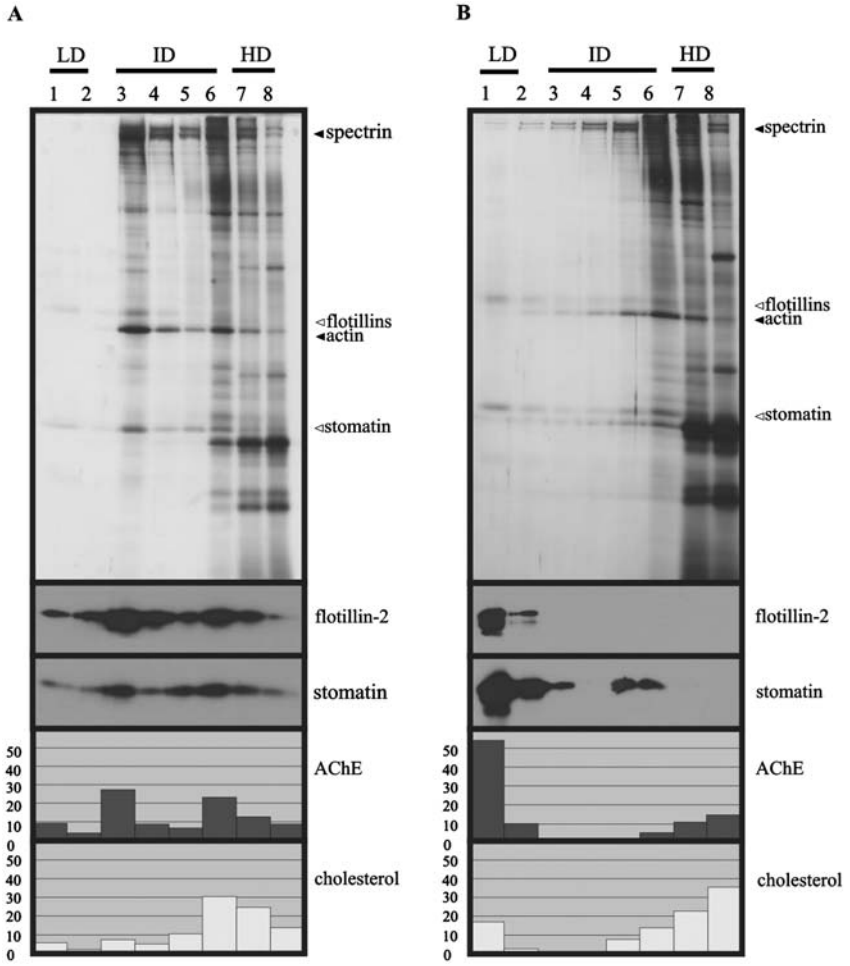

Figure 1 Comparison of cytoskeleton-loaded and cytoskeleton-free DRMs. DRMs were prepared from erythrocytes according to protocol I (A) or protocol III (B). 150 µl packed erythrocytes were resuspended in 550 µl TBS, cooled, lysed with 700 µl of ice-cold 2% Triton X-100, 10 mM EDTA, and proteinase inhibitors in TBS, incubated for 20 min on ice, and centrifuged at 15000 × *g* for 10 min, 4°C. The pellet was resuspended in cold 1% Triton X-100 containing 5 mM EDTA and proteinase inhibitors in TBS to give 300 µl. Protocol III is identical to protocol I except that the pellet is resuspended in 0.2 M sodium carbonate to disrupt the cytoskeleton. These suspensions are then mixed with 500 µl 80% sucrose in TBS, placed in a centrifuge tube (Beckman 13 × 51 mm), overlaid with 1 ml 40%, 2 ml 35%, 0.5 ml 20%, and 0.5 ml 5% sucrose in TBS, and centrifuged in a pre-cooled SW55 rotor (Beckman) for 18 h at 235,000 × *g*, 4°C. Eight fractions of 600 µl were collected from the top and equal aliquots of these fractions were analysed for AChE (acetylcholinesterase) activity, and cholesterol content, and by 11% SDS-PAGE/Western blotting as indicated. For silver staining (top panels), the following relative volumes of the fractions were applied to the gels: 1.00 (fractions 1 and 2), 0.40 (fractions 3–5) and 0.25 (fractions 6–8). LD, ID and HD indicate low-, intermediate- and high-density regions, respectively. The distribution of AChE and cholesterol is given in relative percentages. Open triangles indicate the positions of lipid raft marker proteins, filled triangles indicate the positions of cytoskeletal proteins. DRM markers are preferentially found in the ID region (A), but shift to the LD region upon disruption of the cytoskeleton (B).

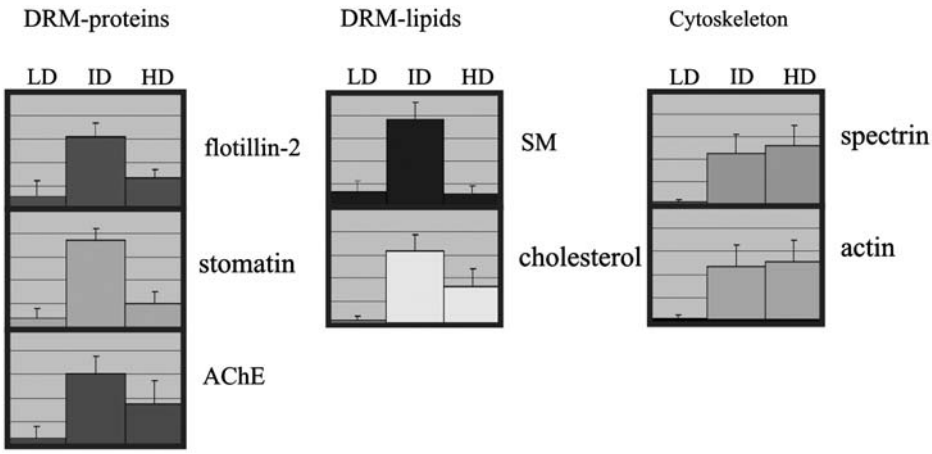

Figure 2 Distribution of protein and lipid markers within the density gradient. A statistical analysis of 20 independent flotation experiments using erythrocytes from six different donors according to protocol I is shown. The amount of the indicated protein and lipid markers in the eight fractions was assessed by densitometry of silver-stained gels, quantitative immunoblotting, and quantitative analysis, respectively, and the relative distribution of the markers in the LD (fractions 1and 2), ID (fractions 3–6), and HD region (fraction 7 and 8) of the gradient is shown (relative percent). LD, ID, and HD indicate low-, intermediate-, and high-density regions, respectively. Error bars indicate the standard deviation. AChE (acetylcholinesterase), SM (sphingomyelin).

the TX-soluble fraction is removed in the pelleting step in protocol I. The TX-100 insoluble fraction comprises 50, 80, 90, 95 and 95% of the total cell cholesterol, stomatin, AChE, SM and flotillin, respectively (data not shown), and 100% of the cytoskeletal components actin and spectrin.

We have previously described that cytoskeleton-free DRMs can be prepared by alkaline extraction of the TX-100 lysates or pellets [44] indicating that the cytoskeletal interactions are disrupted under alkaline conditions, whereas the integrity of DRMs is not affected. Using protocol III, which is a modified version of the original stripping method [44], we analysed the changes in the DRM distribution after disruption of the cytoskeleton (Fig. 1B). The major amounts of the flotillins, stomatin and AChE, and about 20% of cholesterol are present in the LD fractions of the gradient. The abundance of the cytoskeletal proteins spectrin and actin in the ID region is strongly reduced and they are mainly found in the dense fractions (compare silver stains of Fig. 1A and 1B). The disruption of cytoskeletal interactions strongly diminishes the ID DRM pool and leads to a large increase of DRMs at LD. This indicates that the heavy protein load of cytoskeletal components associated with DRMs normally prevents the migration of these DRMs to LDs.

As already mentioned above, Murphy *et al.* [57] did not find cytoskeletal proteins associated with DRMs and suggested that differences in the detergent-to-lipid ratio might account for this discrepancy with our previously published data [37]. In order to test whether the DRM–cytoskeleton association was due to incomplete

lysis, we performed flotation experiments according to protocol I with increasing detergent-to-lipid ratios during lysis (Fig. 3). The silver stains in Fig. 3 show no major differences in the distribution of the cytoskeletal and DRM marker proteins within the density gradients of the three experiments, irrespective of whether erythrocytes or ghosts are used as starting material. Therefore, this result does not support the explanation of incomplete lysis for the cytoskeleton–DRM association.

To study the cytoskeleton–DRM interaction in more detail, we developed another new method to efficiently and quickly separate cytoskeleton–DRM complexes by non-equilibrium gradient centrifugation (NEGC). TX-100 lysates of ghosts or erythrocytes are placed on top of a sucrose step gradient and subjected to ultracentrifugation for 1 h at 38,000 × *g*. Using this method, the TX-100-soluble and cytosolic proteins can be recovered in the first two fractions of the gradient comprising the loading zone and part of the 20% sucrose layer, whereas the cytoskeleton is present at the interphase between the 35% and the 60% sucrose layer. Compared to the flotation method that needs at least 16 h of centrifugation, this NEGC is a quick procedure with the respective advantages. Fig. 4A shows a typical NEGC experiment of a ghost lysate. Most of the band 3 membrane protein and band 6 are found in the first two fractions, and the major amounts of spectrin, protein 4.1 and actin are present in fractions 9 and 10. A high percentage of the DRM markers stomatin, flotillins, AChE, SM and about 50% of the membrane cholesterol co-distribute together with the cytoskeleton in fractions 9 and 10 supporting our view of an association of DRMs with the cytoskeleton. An aliquot of fraction 9 was diluted, incubated with an alkaline buffer (pH 11) on ice to disrupt the cytoskeleton and then subjected to a short ultracentrifugation step. The resulting pellet and supernatant were analysed for the distribution of the cytoskeletal and DRM markers. As expected, the cytoskeletal components were found in the supernatant, whereas all the lipid and protein DRM markers were recovered in the pellet (data not shown) indicating the presence of intact DRMs in this fraction. As already shown in Fig. 1B, alkaline treatment disrupts the cytoskeletal interactions, whereas DRM integrity is unaffected.

To dissolve DRMs, we performed an identical experiment as described in Fig. 1A except that the lysis temperature was 37°C. As expected, the DRM markers are exclusively found in the TX-100-soluble fraction at the top of the gradient, whereas the cytoskeleton is present in the bottom fraction demonstrating that the

Figure 3 DRM preparations are independent of the investigated lipid-to-detergent ratios. 50 µl erythrocytes (A, B, and C) or ghosts (D, E, and F) are diluted with 100 µl (A, D), 250 µl (B, E) or 550 µl (C, F) and lysed with 150 µl (A, D), 300 µl (B, E), or 600 µl (C, F) of ice-cold 2% Triton X-100, 10 mM EDTA, and proteinase inhibitors in TBS, incubated for 10 min on ice, and centrifuged at 15,000*xg* for 20 min, 4°C. The pellets were resuspended in cold 1% Triton X-100 containing 5 mM EDTA and proteinase inhibitors in TBS to give 300 µl. The sucrose gradients, ultracentrifugation, and gradient fractionation were performed as described in Fig. 1. The following relative volumes of the fractions were analysed by 11% SDS-PAGE and silver staining: 1.00 (fractions 1 and 2), 0.40 (fractions 3–5) and 0.25 (fractions 6–8). LD, ID and HD indicate low-, intermediate-, and high-density regions, respectively. Open triangles indicate the positions of lipid raft marker proteins, filled triangles indicate the positions of cytoskeletal proteins.

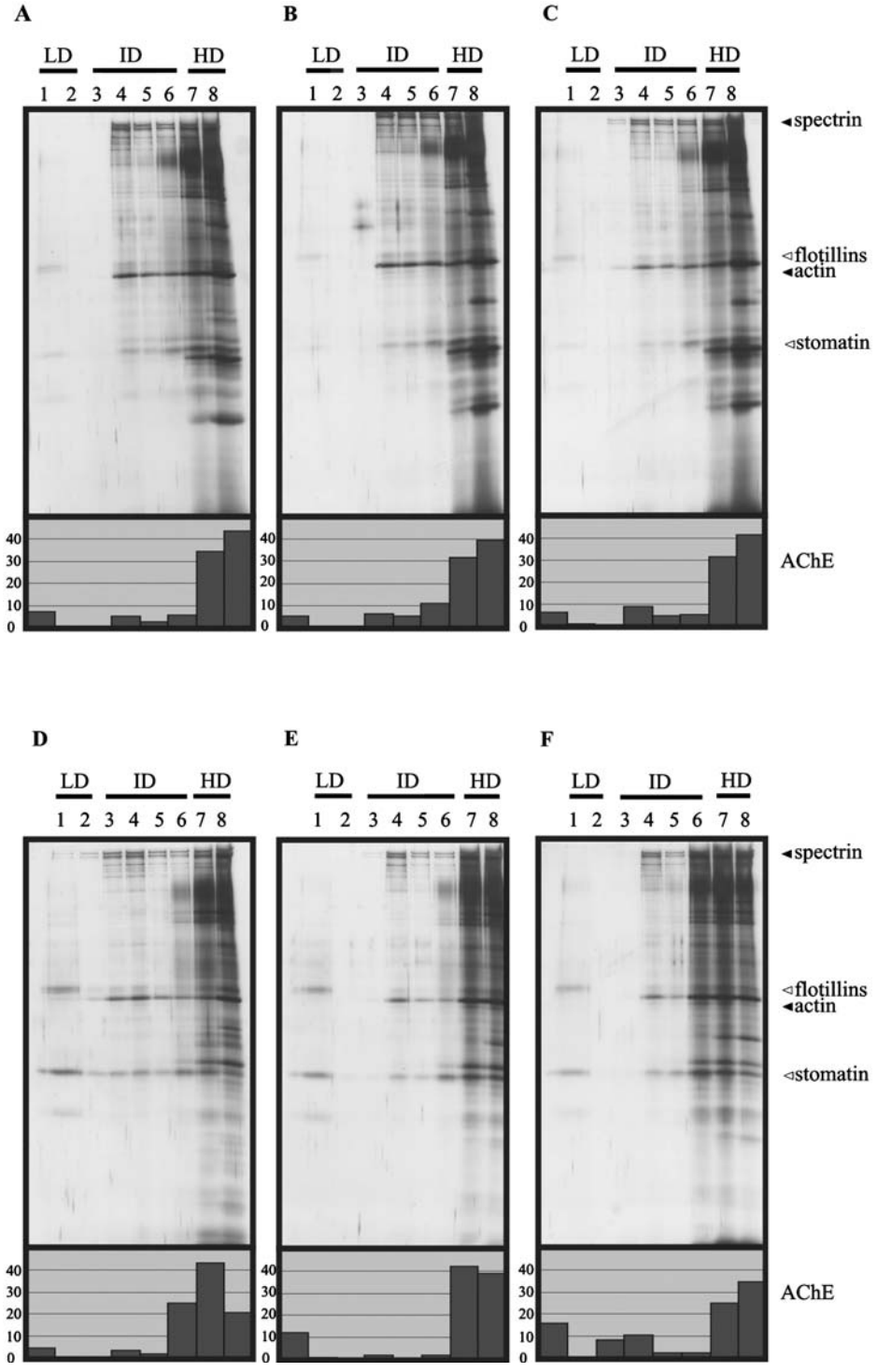
A
B
C
LD
ID
HD
1 2 3 4 5 6 7 8
spectrin
flotillins
actin
stomatin
AChE
40
30
20
10
0
D
E
F

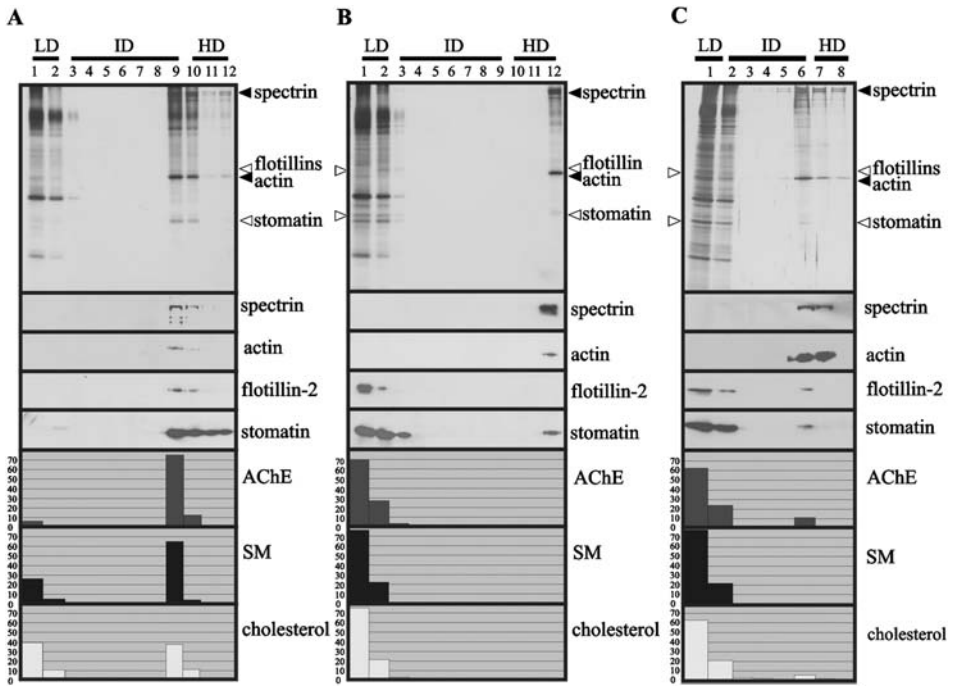

Figure 4 Analysis of the DRM-cytoskeleton association by NEGC. 50 µl ghosts were diluted with 200 µl TBS and lysed with 250 µl 2% TX-100, 10 mM EDTA, and proteinase inhibitors in TBS (A, B) or in 3 M sodium chloride, 10 mM Tris (pH = 7.5) (C) at 4°C (A, C) or at 37°C (B). The lysates were placed on top of sucrose gradients consisting of 0.7 ml 80%, 0.7 ml 60%, 1 ml 40%, 1.6 ml 35%, and 0.5 ml 20% sucrose in TBS (A, B) or in 3 M sodium chloride, 10 mM Tris (pH = 7.5) (C) and centrifuged in a SW55 rotor (Beckman) for 1 hour at 20,000 rpm, 4°C. Twelve (A, B) or eight (C) fractions were collected from the top. Equal aliquots of these fractions were analysed by 11% SDS-PAGE/silver staining (top panels) and Western blotting as indicated, and for AChE (acetylcholinesterase) activity and SM (sphingomyelin) and cholesterol content. LD, ID, and HD indicate low-, intermediate- and high-density regions, respectively. The distribution of AChE, SM, and cholesterol is given in relative percentages. Open triangles indicate the positions of lipid raft marker proteins, filled triangles indicate the positions of cytoskeletal proteins. DRMs and the cytoskeleton co-migrate (A) unless DRMs are dissolved at 37°C (B) or their association is impaired due to high ionic strength (C).

disruption of DRMs completely separates the cytoskeleton from the DRM markers (Fig. 4B). Moreover, the shift of the cytoskeleton from the intermediate density fractions 9 and 10 in Fig. 1A to fraction 12 in Fig. 1B shows that the cytoskeleton–DRM complex has a lower density than the DRM-free cytoskeleton.

To investigate whether polar interactions are involved in the complex formation between the cytoskeleton and DRMs, we performed an alternative NEGC experiment using high salt conditions. Ghosts were lysed and centrifuged in the presence of high salt. We find a prominent shift in the distribution of the DRM markers: the major parts of stomatin, the flotillins and other lipid raft markers are present in the first two fractions of the gradient, whereas the cytoskeletal proteins

are found in the dense fractions at the bottom indicating that the actin–spectrin network remained intact (Fig. 4C). Conversely, when DRMs are prepared from ghosts in the presence of high salt and subjected to a flotation experiment, a large pool of cytoskeleton-free DRMs can be recovered from the LD region of the gradient (data not shown). Therefore, we conclude that the high salt concentration disrupts the polar interactions between the cytoskeleton and DRMs, whereas the integrity of both the DRMs and the actin–spectrin network are not affected.

3.2. The Erythrocyte Cytoskeleton – DRM Complex: Possible Connections

Our previously published [44] data and the results shown here show an interaction between DRMs and the membrane cytoskeleton in erythrocytes. Similar results were recently obtained by Ciana *et al.* [59]. However, in contrast, Murphy *et al.* [57] did not find cytoskeletal proteins associated with their DRM preparations. In light of the data presented here, we offer the following explanation for this seeming discrepancy: the DRMs analyzed by Murphy *et al.* correspond to the small DRM pool at LDs described in the present study. We also find that this DRM pool is often completely free of cytoskeletal components. However, this DRM pool in the LD region comprises only a minor fraction of the DRM markers whereas the major DRM pool is retained in the ID region of the gradient due to the heavy protein load of associated cytoskeleton. The observed variations in the distribution of the cytoskeleton-associated DRMs within the density gradient are donor-dependent and we assume that they may be accounted for by small inter-individual differences in the red cell membrane lipid composition.

Interactions between DRMs and the membrane skeleton have been described already in other cell types like neutrophils, platelets and mast cells. Nebl *et al.* [60] show that a subset of plasma membrane skeleton proteins from bovine neutrophils co-isolates with cholesterol-rich DRMs. In similarity to our data, these skeleton-enriched DRMs exhibit a relatively high buoyant density in sucrose. Bodin *et al.* [61] describe that a large fraction of platelet lipid rafts specifically associates with the actin cytoskeleton upon activation. This integrin-dependent cytoskeleton–raft interaction seems to be functionally involved in clot retraction. In RBL-2H3 mast cells, the interactions between Lyn and cross-linked IgE-FcεRI are regulated by stimulated F-actin polymerization suggesting that the actin cytoskeleton is involved in the segregation of anchored raft components (IgE-FcεRI) from more mobile ones (Lyn) [62]. Moreover, CD44 has been reported to be present in rafts at the apical side of polarized mammary epithelial cells and to be immobilized there by interaction with the actin cytoskeleton [63].

The molecular linkers that enable the interaction between DRMs and the cytoskeleton in erythrocytes are yet unknown, however, several possibilities can be envisaged.

- A small subpopulation of the band 3 protein (the anion exchanger 1) is reproducibly found in DRMs [57,64]. This protein may provide a "classical" bridge to the cytoskeleton via the spectrin-binding ankyrin protein.

- A direct interaction of the spectrin network with DRMs can also be assumed because Mariani *et al.* [65] showed that a small spectrin subpopulation can be ^{3}H-palmitoylated and is tightly membrane associated. Palmitoylated proteins are frequently found to be DRM-associated.
- DRM-cytoskeleton interactions via the major integral DRM proteins, stomatin, flotillin-1 and flotillin-2, must also be taken into account. These proteins form large oligomeric complexes at the cytoplasmic face of DRMs and might thereby function as platforms for the interaction with the cytoskeleton. Flotillin-1 has been implicated in the organization of the actin cytoskeleton in PC12 cells and adipocytes [66,67]. Stomatin might provide a linkage to the cytoskeleton via stomatin-like protein 2 (SLP-2). SLP-2 is a recently identified, low abundant erythrocyte membrane protein that lacks the membrane-anchor region typical for proteins of the stomatin family. It might form hetero-oligomeric complexes with stomatin and is thought to interact with the erythrocyte cytoskeleton [68].
- PIP_2 is present in erythrocyte DRMs (data not shown) and might provide a lipid-mediated link between DRMs and the cytoskeleton. PIP_2 is known to be involved in the regulation of the cytoskeleton–membrane association [69] and is present at least partly in caveolae and/or DRMs of different cell types [70,71]. Moreover, it has been implicated to mediate the interaction of the cytoskeleton to lipid rafts in activated platelets [61]. However, the presence of PIP_2 in rafts has recently been challenged by FRET analyses suggesting a uniform distribution of PIP_2 in the plasma membrane of HEK293 cells and showing that low, sublytic amounts of TX-100 induce non-pre-existing PIP_2 clusters [72]. In contrast to HEK293 cells, a compartmentation of PIP_2 rather than a uniform distribution of this lipid at the erythrocyte membrane has been suggested by kinetic analyses of polyphosphoinositide labelling [73–75]. These studies revealed the existence of a metabolically inactive pool of PIP_2 indicating that PIP_2 forms relatively stable associations with protein components at the inner surface of the erythrocyte membrane, thus limiting the turnover of their monoester phosphate groups. In fact, interaction of PIP_2 with the band 4.1 proteins has been reported [6,76]. Recently, it has been shown that a minor pool of the erythrocyte β-spectrin is represented by the isoform βIΣ2, which contains a PH domain in its extended C-terminus thereby providing a potential interaction site between the cytoskeleton and PIP_2 [77]. It is therefore tempting to assume that the association between the cytoskeleton and DRMs is at least partly maintained by PIP_2.

4. Exovesiculation of Erythrocytes

Exovesiculation is thought to continuously take place throughout the lifespan of erythrocytes. During the approximately 120 days of circulation through the vascular system, erythrocytes become denser and shrink due to the loss of about 20% of their cell surface in the process of microvesiculation [78]. The vesicles are rapidly removed from the circulation by Kupffer cells in the liver [79]. The vesicles contain high concentrations of a glycated and carbamoylated haemoglobin fraction

similar to that found in the oldest erythrocytes [80]. Moreover, the vesicular membrane is thought to contain the senescence antigen; these breakdown products of the major band 3 proteins are also enriched in the oldest erythrocyte fraction and cause the binding of immunoglobulin G (IgG) molecules to these cells [70]. This indicates that the vesiculation process is a sort of a "waste disposal system" for erythrocytes and is essential for their survival and proper functioning. The spleen plays an important, but yet not fully understood role in this process. Moreover, as highlighted by a recent study on erythrocytes of patients suffering from hereditary spherocytosis (HS), cytoskeleton–membrane interactions seem to have an important impact on the microvesiculation process [81]. Upon splenectomy of different types of HS patients, band 3-deficient erythrocytes were shown to be heavily bound by IgG whereas spectrin-/ankyrin-deficient erythrocytes contained normal levels of associated IgG. It is assumed that in band 3-deficient erythrocytes the vesiculation and thereby the removal of senescent antigen is impaired due to a strong association of the remaining band 3 to the intact cytoskeleton. Whereas in both types of deficiencies the membrane–cytoskeleton association is partially impaired, the vesiculation-dependent removal of senescent antigen seems to be intact in the spectrin-/ankyrin-deficient erythrocytes.

Erythrocytes are known to shed vesicles *in vitro* under several conditions. When erythrocytes are depleted of their ATP content by incubation at 37°C for several hours in the absence of glucose, they begin to release vesicles with a diameter of about 180 nm [82]. Allan *et al*. found that erythrocytes shed vesicles of a similar size when the intracellular calcium level is increased upon treatment with the ionophore A23187 in the presence of calcium [83]. In a subsequent study, Allan *et al*. [84] could show that a small amount of another vesicle type was also present in the supernatant that was smaller in size and therefore named "nanovesicles" to be distinguished from the larger "microvesicles". Using atomic force microscopy (AFM), we determined the mean diameter of microvesicles and nanovesicles to be 180 and 80 nm, respectively [85]. A third way to obtain vesicles *in vitro* is the treatment of erythrocytes with amphiphiles [86].

4.1. Cell Shape and Exovesiclulation

The amphiphile-induced vesiculation indicates that cell shape is an important factor for the vesicle release from erythrocytes. Amphiphiles are amphipathic drugs that – in line with the bilayer couple hypothesis [87] – preferentially insert into one of the two membrane leaflets thereby causing an expansion of one half-layer relative to the other and a corresponding change in cell shape [88]. Anionic amphiphiles were shown to preferentially intercalate into the exoplasmic leaflet and cause an echinocytic shape change of the erythrocytes with the characteristic spicules that emanate from a rounded cell body. Cationic amphiphiles that show a preference for the cytoplasmic membrane leaflet due to the high content of negatively charged phosphatidylserine induce a stomatocytic shape transformation characterized by a mouth-like invagination of the erythrocyte. Several theoretical studies showed that these peculiar shapes that an erythrocyte can adopt are in accordance with the bilayer couple hypothesis when the shear elastic energy of the cytoskeleton is

considered [89–91]. Moreover, it was shown that the amphiphile-induced increase of the area difference between the outer and the inner membrane leaflets could also account for the formation of spherical microexovesicles [92]. Echinocytic shape transformation seems to be an important factor for exovesicle-formation with the vesicles being released from the tips of the membrane spikes.

The mechanism behind the calcium-induced vesicle release is not fully understood yet, however, cell shape transformation seems to play a role in this type of vesiculation, too. The rise of cytosolic calcium in erythrocytes that finally leads to the release of vesicles induces also several other changes within the cell: a partial degradation of cytoskeletal components [93], a breakdown of polyphosphoinositides [94], shrinkage of the cell due to the loss of potassium by the Gardos channel and cell water by the aquaporins [95] and a prominent echinocytic shape transformation [96]. The calcium-induced shape change is caused by intrinsic membrane processes probably mainly due to a calcium-dependent scramblase activity that redistributes the membrane phospholipids between the inner and the outer leaflets [97]. It is assumed that the translocation rate for SM, which is preferentially located at the outer leaflet, is much smaller than that for the glycerophospholipids thereby causing an area difference between the leaflets and an echinocytic shape change [98]. Kamp *et al.* [99] showed that this scramblase-dependent shape transformation and cell shrinkage are the major factors that determine the calcium-induced vesiculation process.

4.2. DRMs of Exovesicles

Since it is very probable that vesicle budding occurs at the tip of the membrane protrusions, membrane protein and lipid analyses of the vesicles will show the approximate membrane composition at the tips of the protrusions. The correlation between the vesicular enrichment of membrane proteins and their localization to membrane protrusions has been recently shown [96]. GPI-linked proteins like AChE or decay accelerating factor (DAF) have previously been found to be enriched in calcium-induced [42] and amphiphile-induced [86] vesicles and in vesicles obtained upon ATP depletion [82]. In contrast, cytoskeletal components are essentially absent from the vesicles obtained by the different *in vitro* vesiculation methods [82,85,96] thereby indicating that echinocytic membrane protrusions are free of cytoskeleton. It can be assumed that local detachments from the underlying cytoskeleton might be a prerequisite for the formation of membrane protrusions. We could show that apart from the cytoskeletal components all major membrane proteins are depleted from the calcium-induced microvesicles to various degrees [64,85]. On the other hand, besides the GPI-linked proteins, stomatin is the only major erythrocyte membrane protein that is enriched in these vesicles relative to ghosts. The segregation between stomatin and the cytoskeletal component actin in calcium-/A23187-treated erythrocytes is highlighted in Fig. 5. Stomatin is specifically enriched at the tips of the echinocytic membrane protrusions and the actin-specific labelling is continuous at the membrane but absent from these protrusions. Two cytosolic and calcium-binding proteins, synexin (also named annexin 7) and sorcin were found to be enriched in calcium-induced microvesicles and turned out

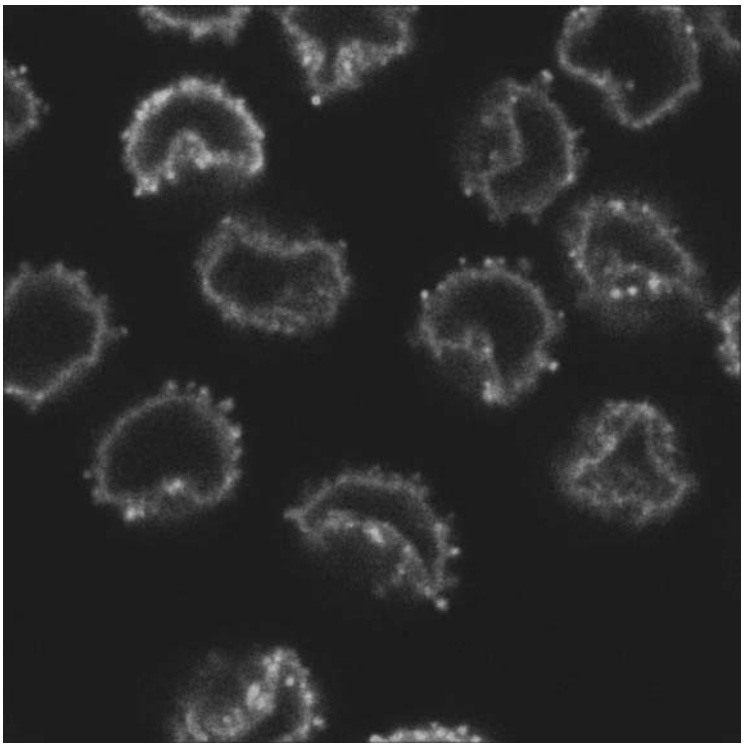

Figure 5 Calcium induces the segregation of stomatin and the cytoskeleton. Erythrocytes were incubated with 1 mM calcium chloride and 5 μM A23187 in TBS at 37°C for 5 minutes, bound to poly-L-lysine coated coverslips, fixed with 4% paraformaldehyde, quenched in 50 mM ammonium chloride and shortly lysed in 0.1% TX-100 at 4°C. The cells were blocked in 5% foetal calf serum, incubated with anti-stomatin monoclonal mouse antibody (GARP50 [46]) for 1 hour, washed and then incubated with rhodamine-labelled phalloidine (red) and fluorescein-labelled anti-mouse antibody (green). A Leica TCS SP microscope was used for confocal laser microscopy. Stomatin is preferentially found at the tips of membrane protrusions, whereas actin is absent therefrom (please see plate no. 1 in the color section).

to be the most abundant proteins in nanovesicles apart from haemoglobin [85]. Upon rise of cytosolic calcium, these proteins are known to form a calcium-mediated complex with acidic phospolipids at the membrane. The enrichment of DRM marker proteins like AChE or stomatin in microvesicles indicates that rafts might be involved in the segregation of membrane proteins at the tips of the membrane protrusions. In fact, as shown in Fig. 6, DRMs can be prepared from microvesicles with stomatin being the major microvesicular DRM component. Both, synexin and sorcin are also associated with DRMs when calcium is included in the sucrose gradient (Fig. 6A) but are absent therefrom in the presence of EDTA (Fig. 6B). Fig. 7 shows that DRMs can also be prepared from nanovesicles. AChE is partially present in these DRMs, and synexin and sorcin are the most abundant, yet calcium-dependent DRM proteins. Compared to these proteins, stomatin is strongly depleted from nanovesicles [85] and, interestingly, residual nanovesiclular

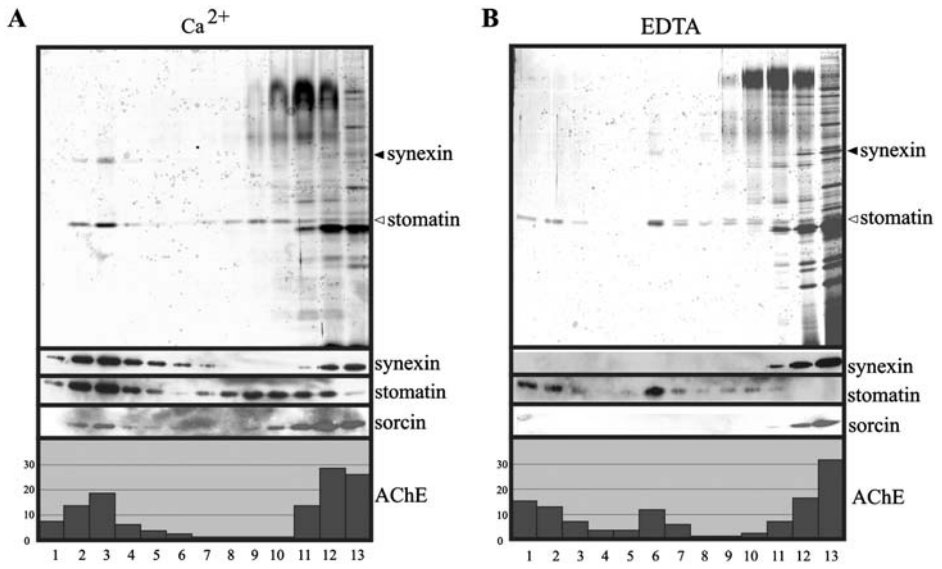

Figure 6 Characterization of DRMs from microvesicles. Calcium-induced microvesicles were obtained as described [84], resuspended in 50 µl TBS nd lysed with 50 µl 1% TX-100 in TBS containing 2 mM calcium chloride (A) or 10 mM EDTA (B), incubated for 20 min on ice, and mixed with 100 µl 80% sucrose, 0.5% TX-100 in TBS containing 1 mM calcium chloride (A) or 5 mM EDTA (B). The resulting suspensions were placed in centrifuge tubes, overlaid with 1250 µl and 333 µl of 30% and 10% sucrose, respectively, in TBS containing 1 mM calcium chloride (A) or 5 mM EDTA (B), and centrifuged in a SW50.1 rotor (Beckman) at 50,000 rpm, 4°C for 17 h. Thirteen fractions were collected from the top and equal aliquots of these fractions were analyzed by 12% SDS-PAGE/silver staining (top panels) and Western blotting as indicated, and for AChE (acetylcholinesterase). The distribution of AChE is given in relative percentage. Open triangles indicate the positions of the calcium-independent DRM marker protein stomatin, filled triangles indicate the positions of the calcium-dependent DRM marker protein synexin.

stomatin is not associated with DRMs (Fig. 7). Other erythrocyte DRM markers like flotillin-1, flotillin-2 and aquaporin-1 are depleted from both microvesicles and nanovesicles [64,85]. These findings indicate that different types of rafts might co-exist at the erythrocyte membrane and that they segregate during the vesiculation process.

5. Lipid Rafts of Erythrocytes: Hypothetical Considerations

As already outlined above (Section 2), there is hardly any direct experimental evidence that lipids laterally separate into co-existing lipid phases within biological membranes. However, an ever-increasing amount of indirect data from different biological research areas strongly indicates that this is the case. Specifically, an

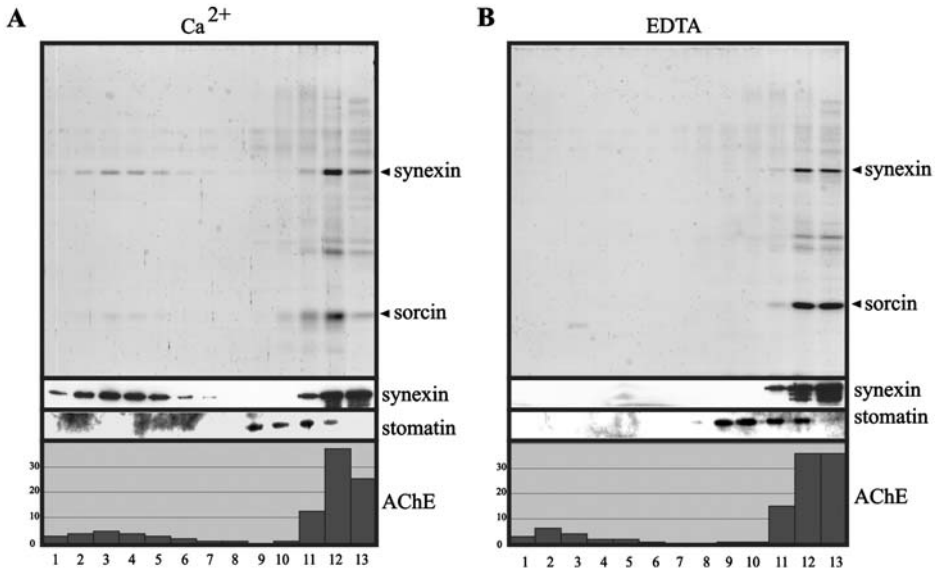

Figure 7 Characterization of DRMs from nanovesicles. Calcium-induced nanovesicles were obtained as described [84], resuspended in 50 µl TBS, and lysed with 50 µl 1% TX-100 in TBS containing 2 mM calcium chloride (A) or 10 mM EDTA (B), incubated for 20 min on ice, and mixed with 100 µl 80% sucrose, 0.5% TX-100 in TBS containing 1 mM calcium chloride (A) or 5 mM EDTA (B). The resulting suspensions were placed in centrifuge tubes, overlaid with 1250 µl and 333 µl of 30% and 10% sucrose, respectively, in TBS containing 1 mM calcium chloride (A) or 5 mM EDTA (B), and centrifuged in a SW50.1 rotor (Beckman) at 50,000 rpm, 4°C for 17 h. Thirteen fractions were collected from the top and equal aliquots of these fractions were analysed by 12% SDS-PAGE/silver staining (top panels) and Western blotting as indicated, and for AChE (acetylcholinesterase). The distribution of AChE is given in relative percentage. Filled triangles indicate the positions of the calcium-dependent DRM marker protein synexin. Stomatin is essentially absent from DRMs in nanovesicles.

epifluorescence microscopy study on model membranes recently indicated that l_d and l_o phases might actually co-exist at the erythrocyte membrane. Keller *et al.* [100] showed that lipid monolayers of reconstituted lipids simulating the compositions of the exoplasmic and cytoplasmic leaflet of human erythrocytes form immiscible liquid phases. This study suggests that the erythrocyte bilayer is near a miscibility critical point which should significantly affect the biophysical membrane properties.

The co-existence of lipid phases in the erythrocyte membrane might have a structuring effect by laterally segregating membrane proteins according to their relative partitioning behaviour in the respective lipid phases. On the other hand, and in line with the revised lipid-raft hypothesis, lipid domain formation and maintenance might be a process that is at least influenced, maybe even regulated by membrane proteins. A mutual influence between lipid phases and membrane proteins can be envisioned; lipids and proteins might constitute a system of high organizational complexity. We want to give same examples how erythrocyte membrane proteins might influence lipid domains at the membrane. (i) The erythrocytes

have a variety of lipid-specific enzymes like lipases, scramblases and phospholipid translocases that either directly modify membrane lipids or regulate the membrane-lipid gradient between the inner and the outer leaflets. These enzymes might directly influence the formation and stability of raft domains at both membrane leaflets. (ii) The abundant monotopic erythrocyte raft proteins, stomatin, flotillin-1 and flotillin-2, form oligomeric complexes at the membrane and might nucleate and stabilize l_o domains at the cytoplasmic membrane leaflet. (iii) Assuming that the observed association between the cytoskeleton and DRMs reflects some sort of interaction between cytoskeletal components and l_o domains *in vivo*, it is conceivable that the cytoskeleton might be the main regulator of lipid phases in the erythrocyte membrane by immobilizing raft domains and thereby preventing a large-scale phase separation.

5.1. Rafts, Membrane Curvature and Vesiculation: Theoretical Considerations

In a series of papers Lipowsky and co-workers provided a theoretical model for membrane budding and vesicle formation due to the existence of membrane domains that have a different phase state than the surrounding membrane [101–104]. As the definition of domains by Lipowsky correlates with the cell-biological definition of rafts (l_o domains), his model might be well-applicable for rafts within cellular membranes. The driving force for the formation of a bud is the minimization of the edge energy or line tension/energy at the border between the domain (l_o or raft) and the surrounding matrix (l_d domain). The edge energy is minimal when the domain is extruded from the plane of the membrane in the form of a spherical bud that is connected with the matrix only by an infinitesimal neck. The edge energy, which increases with the size of the flat domain, is only counteracted by the bending energy of the membrane and budding will therefore occur when the edge energy of the flat domain is of the same order of magnitude as the bending energy. If the "mother vesicle" is not a sphere but an elongated axisymmetric structure with two caps, the domain budding will preferentially occur at the caps since this configuration is most symmetric and energetically favoured [103] and is reminiscent of the presumed bud formation and vesicle fission at the tips of echinocytic membrane protrusions in erythrocytes [105]. The validity of this theoretical model was recently highlighted by studies on model membranes. Baumgart *et al.* [106] showed that l_o and l_d domains segregate in liposomes, adopt bud-like shapes and preferentially separate into smaller vesicles of uniform domain composition. In thin tubular structures, it was shown that phase separation and domain formation is essential for membrane fission, which preferentially occurs at the phase boundaries [107].

5.2. Rafts and Erythrocyte Vesiculation

Combining these theoretical considerations with our data of erythrocyte DRMs and vesicles, we will now outline a hypothetical model of a raft-based vesiculation mechanism in erythrocytes. Local detachment of the membrane skeleton [108] and

possibly also echinocytic shape transformation seem to be requirements for erythrocyte exovesiculation to occur. We assume that the uncoupling of the membrane from the cytoskeleton and thus the absence of the presumed immobilizing and regulative effect of the cytoskeleton on rafts allows the coalescence of small rafts and the formation of large l_o domains within the echinocytic membrane protrusions. The aggregating raft domain will be located at the tip of the protrusion and will constantly grow by fusion with small raft domains. Specific protein–protein interactions of raft-based proteins like the formation of oligomeric complexes by stomatin or synexin might stabilize the raft domain and possibly enhance the process of lipid phase separation. When the size of the raft domain exceeds a certain limit, the line tension between the l_o and the l_d phases will be strong enough to drive bud formation and vesicle fission at the boundary between the lipid phases. Strong evidence for this raft-driven vesicle formation are provided by the findings that raft-based GPI-linked proteins are specifically enriched in all types of exovesicles [42,82,86] and that DRMs can be prepared from microvesicles (Fig. 6) and nanovesicles (Fig. 7) [77]. Civenni *et al.* [42] found that exogenously added GPI proteins were not present in DRMs and did not enrich in exovesicles. While it is unclear why there is no co-distribution of exogenous and endogenous GPI proteins, this finding clearly indicates that raft-association of these proteins is essential for their enrichment in exovesicles.

But how can we account for the fact that different raft markers are enriched within the vesicles whereas others are depleted? Various types of rafts containing a specific set of raft proteins/lipids are likely to co-exist at the erythrocyte membrane. As they might exhibit various kinds and strengths of associations with the cytoskeleton, their free diffusion into echinocytic membrane protrusions might be differentially inhibited. It has previously been shown that in mechanically deformed erythrocytes the enrichment of membrane proteins within the induced cytoskeleton-free membrane protrusion was inversely related to the degree of association with the cytoskeleton [109]. Additionally, as suggested recently [96], raft domains might have various intrinsic curvatures and thereby they might preferentially partition into membrane regions where the membrane curvature matches their specific intrinsic curvature. This curvature-driven segregation might specifically account for the calcium-dependent raft protein synexin which has a convex membrane binding side [110] and might thereby preferentially partition into the highly curved membrane region at the tips of the protrusions in calcium-/A23187-treated erythrocytes [96] and in the shed nanovesicles [77]. It is also conceivable that narrow constraints of the specific intrinsic curvature of stomatin rafts might be the reason why they are depleted from the strongly curved nanovesicles (Fig. 7), whereas they are enriched in the larger and less curved microvesicles (Fig. 6) [77].

There is increasing evidence that exovesiculation is the major line of defence in erythrocytes against complement-mediated cell lysis. Upon complement attack, human erythrocytes eliminate the terminal complement components C5b-9, membrane attack complex (MAC), from the membrane in the form of microvesicles and thereby escape destruction [111]. Calcium-induced vesiculation *in vitro* seems to be a good model since it was shown that this process was dependent on the presence of calcium and sheep erythrocytes, which do not show a calcium-induced

vesiculation, are not protected. Protection was not only due to the prevention of MAC assembly by CD59 but also due to the selective elimination of MAC that was 10-fold enriched in the released vesicles. Based on our raft-dependent vesiculation model, we will now suggest a possible mechanism for the specific MAC elimination process. Extracellular calcium flowing through the membrane pore of a MAC complex will cause a protease-mediated local destruction of the cytoskeleton [93] and a scramblase-induced local area difference between the outer and the inner membrane leaflets resulting in the formation of an echinocytic membrane protrusion [98,99]. Thereby, the conditions for the segregation of lipid phases and line tension-driven vesiculation would be given. The specific enrichment of MAC in the budding vesicle might be due to (i) its possible raft localization, (ii) binding to raft-based GPI-linked CD59 molecules and/or (iii) its specific intrinsic curvature. This model suggests that erythrocytes might exploit the properties of lipid phases for protein sorting and the energy at the border between the phases for vesicle fission.

5.3. Rafts and Malarial Infection

Erythrocyte membrane rafts have recently been shown to be involved in the process of invasion of the cell by the malaria parasite *Plasmodium falciparum* [43]. Attachment of the apical end of the parasite to the erythrocyte membrane is shown to be the first phase of the invasion process. Close to the apical attachment point, a junction is formed which is seen as an electron-dense area in a region where the membranes of the erythrocyte and the parasite are closely apposed. During the parasite-driven erythrocyte membrane invagination and formation of the parasitophorous vacuolar membrane (PVM), this junction moves along the axis of the parasite as a circumferential band [112]. The PVM has been shown to contain only host proteins that were also present in DRMs whereas non-raft membrane proteins and cytoskeletal components are absent [14,43,57,113]. The only exception from this rule is the raft marker protein stomatin, which is absent from the vacuolar membrane; however, interestingly, a parasite-encoded homologous protein of stomatin has been found to be present at the PVM [114]. These data indicate that raft domains are specifically involved in the formation of the vacuole. Similar to our exovesiculation model, we suggest here that the parasite induces the separation of lipid phases at the erythrocyte membrane and uses the line energy at the border of the lipid phases to drive membrane invagination and PVM formation. In line with this hypothesis is the finding that destruction of erythrocyte rafts by MβCD treatment inhibits malarial infection [56]. Cholesterol-depletion of infected erythrocytes was also shown to release the parasite from the cells without cell lysis [43] thereby indicating that rafts are not only necessary for the formation but also for the maintenance of the PVM. Moreover, absence of GPI-linked proteins in erythrocytes of paroxysmal nocturnal haemoglobinuria patients does not affect the efficiency of *P. falciparum* infection and thus indicates that infection is rather dependent on lipid phases than on specific raft proteins [56]. We assume that local destruction of the erythrocyte cytoskeleton at the membrane attachment point of the parasite is crucial and may be sufficient for the raft aggregation and phase separation to occur. One might speculate that the

parasite-derived junction is located at the l_o/l_d phase boundary and is involved in the local destruction of the host-membrane skeleton. The selective enrichment of host proteins at the PVM might only reflect the partitioning behaviour of the respective membrane proteins between l_o and l_d phases rather than their specific importance for the PVM.

6. Conclusions

Studies on erythrocyte DRMs and on model membranes with erythrocyte-specific lipid composition suggest the existence of lipid rafts/l_o domains at the erythrocyte membrane. We find a strong association between the cytoskeleton and DRMs and conclude that the cytoskeleton which is the main structuring factor of the erythrocyte membrane is also involved in the regulation of rafts presumably by influencing the mobility, stability and size of raft domains. Rafts are indicated to be involved in the process of exovesiculation and we suggest a model of a raft-driven vesiculation mechanism. Rafts may specifically aggregate in membrane regions that are uncoupled from the cytoskeleton and sufficiently large raft domains are thought to spontaneously form spherical buds to minimize the line tension at the border between the lipid phases. We suggest that the erythrocytes exploit this property of co-existing lipid phases in their defence strategy against complement-mediated cell lysis by shedding assembled MAC complexes in exovesicles. As suggested, a similar mechanism might be used by the malarial parasite for erythrocyte infection and PVM formation.

REFERENCES

[1] E.A. Evans, R.M. Hochmuth, A solid–liquid composite model of the red cell membrane, J. Membr. Biol. 30 (1977) 351–362.
[2] V. Bennett, D.M. Gilligan, The spectrin-based membrane skeleton and micron-scale organization of the plasma membrane, Annu. Rev. Cell Biol. 9 (1993) 27–66.
[3] W. Nunomura, Y. Takakuwa, M. Parra, J. Conboy, N. Mohandas, Regulation of protein 4.1R, p55, and glycophorin C ternary complex in human erythrocyte membrane, J. Biol. Chem. 275 (2000) 24540–24546.
[4] M. Tomishige, Y. Sako, A. Kusumi, Regulation mechanism of the lateral diffusion of band 3 in erythrocyte membranes by the membrane skeleton, J. Cell Biol. 142 (1998) 989–1000.
[5] X. An, X. Guo, H. Sum, J. Morrow, W. Gratzer, N. Mohandas, Phosphatidylserine binding sites in erythroid spectrin: location and implications for membrane stability, Biochemistry 43 (2004) 310–315.
[6] X. An, X. Zhang, G. Debnath, A.J. Baines, N. Mohandas, Phosphatidylinositol-4,5-biphosphate (PIP2) differentially regulates the interaction of human erythrocyte protein 4.1 (4.1R) with membrane proteins, Biochemistry 45 (2006) 5725–5732.
[7] M.R. Clark, S. Mel, F. Lupu, D.S. Friend, Influence of the membrane undercoat on filipin perturbation of the red blood cell membrane, Exp. Cell Res. 171 (1987) 321–330.
[8] K. Simons, E. Ikonen, Functional rafts in cell membranes, Nature 387 (1997) 569–572.
[9] J. Huang, G.W. Feigenson, A microscopic interaction model of maximum solubility of cholesterol in lipid bilayers, Biophys. J. 76 (1999) 2142–2157.

[10] J.R. Silvius, Role of cholesterol in lipid raft formation: lessons from lipid model systems, Biochim. Biophys. Acta 1610 (2003) 174–183.
[11] G.W. Feigenson, J.T. Buboltz, Ternary phase diagram of dipalmitoyl-PC/dilauroyl-PC/cholesterol: nanoscopic domain formation driven by cholesterol, Biophys. J. 80 (2001) 2775–2788.
[12] R.F. de Almeida, A. Fedorov, M. Prieto, Sphingomyelin/phosphatidylcholine/cholesterol phase diagram: boundaries and composition of lipid rafts, Biophys. J. 85 (2003) 2406–2416.
[13] C. Dietrich, L.A. Bagatolli, Z.N. Volovyk, N.L. Thompson, M. Levi, K. Jacobson, E. Gratton, Lipid rafts reconstituted in model membranes, Biophys. J. 80 (2001) 1417–1428.
[14] A.V. Samsonov, I. Mihalyov, F.S. Cohen, Characterization of cholesterol–sphingomyelin domains and their dynamics in bilayer membranes, Biophys. J. 81 (2001) 1486–1500.
[15] D. Meder, M.J. Moreno, P. Verkade, W.L. Vaz, K. Simons, Phase coexistence and connectivity in the apical membrane of polarized epithelial cells, Proc. Natl. Acad. Sci. USA 103 (2006) 329–334.
[16] C. Dietrich, Z.N. Volovyk, M. Levi, N.L. Thompson, K. Jacobson, Partitioning of Thy-1, GM1, and cross-linked phospholipid analogs into lipid rafts reconstituted in supported model membrane monolayers, Proc. Natl. Acad. Sci. USA 98 (2001) 10642–10647.
[17] N. Kahya, D.A. Brown, P. Schwille, Raft partitioning and dynamic behavior of human placental alkaline phosphatase in giant unilamellar vesicles, Biochemistry 44 (2005) 7479–7489.
[18] T.Y. Wang, R. Leventis, J.R. Silvius, Partitioning of lipidated peptide sequences into liquid-ordered lipid domains in model and biological membranes, Biochemistry 40 (2001) 13031–13040.
[19] C. Eroglu, B. Brugger, F. Wieland, I. Sinning, Glutamate-binding affinity of Drosophila metabotropic glutamate receptor is modulated by association with lipid rafts, Proc. Natl. Acad. Sci. USA 100 (2003) 10219–10224.
[20] A.T. Hammond, F.A. Heberle, T. Baumgart, D. Holowka, B. Baird, G.W. Feigenson, Cross-linking a lipid raft component triggers liquid ordered-liquid disordered phase separation in model plasma membranes, Proc. Natl. Acad. Sci. USA 102 (2005) 6320–6325; Epub 2005 Apr 6325.
[21] M. Dykstra, A. Cherukuri, H.W. Sohn, S.J. Tzeng, S.K. Pierce, Location is everything: lipid rafts and immune cell signaling, Annu. Rev. Immunol. 21 (2003) 457–481.
[22] R.G. Parton, M. Hanzal-Bayer, J.F. Hancock, Biogenesis of caveolae: a structural model for caveolin-induced domain formation, J. Cell. Sci. 119 (2006) 787–796.
[23] J.F. Hancock, Lipid rafts: contentious only from simplistic standpoints, Nat. Rev. Mol. Cell Biol. 7 (2006) 456–462.
[24] B.S. Wilson, J.R. Pfeiffer, Z. Surviladze, E.A. Gaudet, J.M. Oliver, High resolution mapping of mast cell membranes reveals primary and secondary domains of Fc(epsilon)RI and LAT, J. Cell Biol. 154 (2001) 645–658.
[25] S. Moffett, D.A. Brown, M.E. Linder, Lipid-dependent targeting of G proteins into rafts, J. Biol. Chem. 275 (2000) 2191–2198.
[26] J.F. Hancock, R.G. Parton, Ras plasma membrane signalling platforms, Biochem. J. 389 (2005) 1–11.
[27] D.A. Brown, J.K. Rose, Sorting of GPI-anchored proteins to glycolipid-enriched membrane subdomains during transport to the apical cell surface, Cell 68 (1992) 533–544.
[28] K. Simons, G. van Meer, Lipid sorting in epithelial cells, Biochemistry 27 (1988) 6197–6202.
[29] H. Heerklotz, Triton promotes domain formation in lipid raft mixtures, Biophys. J. 83 (2002) 2693–2701.
[30] H. Heerklotz, H. Szadkowska, T. Anderson, J. Seelig, The sensitivity of lipid domains to small perturbations demonstrated by the effect of Triton, J. Mol. Biol. 329 (2003) 793–799.
[31] H. Shogomori, D.A. Brown, Use of detergents to study membrane rafts: the good, the bad, and the ugly, Biol. Chem. 384 (2003) 1259–1263.
[32] K. Simons, W.L. Vaz, Model systems, lipid rafts, and cell membranes, Annu. Rev. Biophys. Biomol. Struct. 33 (2004) 269–295.

[33] L.J. Foster, C.L. De Hoog, M. Mann, Unbiased quantitative proteomics of lipid rafts reveals high specificity for signaling factors, Proc. Natl. Acad. Sci. USA 100 (2003) 5813–5818; Epub 2003 Apr 5830.
[34] P. Sharma, R. Varma, R.C. Sarasij, Ira K. Gousset, G. Krishnamoorthy, M. Rao, S. Mayor, Nanoscale organization of multiple GPI-anchored proteins in living cell membranes, Cell 116 (2004) 577–589.
[35] R. Varma, S. Mayor, GPI-anchored proteins are organized in submicron domains at the cell surface, Nature 394 (1998) 798–801.
[36] A. Pralle, P. Keller, E.L. Florin, K. Simons, J.K. Horber, Sphingolipid-cholesterol rafts diffuse as small entities in the plasma membrane of mammalian cells, J. Cell Biol. 148 (2000) 997–1008.
[37] I.A. Prior, C. Muncke, R.G. Parton, J.F. Hancock, Direct visualization of Ras proteins in spatially distinct cell surface microdomains, J. Cell Biol. 160 (2003) 165–170; Epub 2003 Jan 2013.
[38] B.S. Wilson, S.L. Steinberg, K. Liederman, J.R. Pfeiffer, Z. Surviladze, J. Zhang, L.E. Samelson, L.H. Yang, P.G. Kotula, J.M. Oliver, Markers for detergent-resistant lipid rafts occupy distinct and dynamic domains in native membranes, Mol. Biol. Cell 15 (2004) 2580–2592.
[39] M.S. Turner, P. Sens, N.D. Socci, Nonequilibrium raftlike membrane domains under continuous recycling, Phys. Rev. Lett. 95 (2005) 168301.
[40] M. Kirkham, A. Fujita, R. Chadda, S.J. Nixon, T.V. Kurzchalia, D.K. Sharma, R.E. Pagano, J.F. Hancock, S. Mayor, R.G. Parton, Ultrastructural identification of uncoated caveolin-independent early endocytic vehicles, J. Cell Biol. 168 (2005) 465–476.
[41] J. Yu, D.A. Fischman, T.L. Steck, Selective solubilization of proteins and phospholipids from red blood cell membranes by nonionic detergents, J. Supramol. Struct. 1 (1973) 233–248.
[42] G. Civenni, S.T. Test, U. Brodbeck, P. Butikofer, In vitro incorporation of GPI-anchored proteins into human erythrocytes and their fate in the membrane, Blood 91 (1998) 1784–1792.
[43] S. Lauer, J. VanWye, T. Harrison, H. McManus, B.U. Samuel, N.L. Hiller, N. Mohandas, K. Haldar, Vacuolar uptake of host components, and a role for cholesterol and sphingomyelin in malarial infection, Embo J. 19 (2000) 3556–3564.
[44] U. Salzer, R. Prohaska, Stomatin, flotillin-1, and flotillin-2 are major integral proteins of erythrocyte lipid rafts, Blood 97 (2001) 1141–1143.
[45] C.M. Hiebl-Dirschmied, B. Entler, C. Glotzmann, I. Maurer-Fogy, C. Stratowa, R. Prohaska, Cloning and nucleotide sequence of cDNA encoding human erythrocyte band 7 integral membrane protein, Biochim. Biophys. Acta 1090 (1991) 123–124.
[46] C.M. Hiebl-Dirschmied, G.R. Adolf, R. Prohaska, Isolation and partial characterization of the human erythrocyte band 7 integral membrane protein, Biochim. Biophys. Acta 1065 (1991) 195–202.
[47] D. Wang, W.C. Mentzer, T. Cameron, R.M. Johnson, Purification of band 7.2b, a 31-kDa integral phosphoprotein absent in hereditary stomatocytosis, J. Biol. Chem. 266 (1991) 17826–17831.
[48] G.W. Stewart, B.E. Hepworth-Jones, J.N. Keen, B.C. Dash, A.C. Argent, C.M. Casimir, Isolation of cDNA coding for an ubiquitous membrane protein deficient in high Na+, low K+ stomatocytic erythrocytes, Blood 79 (1992) 1593–1601.
[49] D. Volonte, F. Galbiati, S. Li, K. Nishiyama, T. Okamoto, M.P. Lisanti, Flotillins/cavatellins are differentially expressed in cells and tissues and form a hetero-oligomeric complex with caveolins *in vivo*. Characterization and epitope-mapping of a novel flotillin-1 monoclonal antibody probe, J. Biol. Chem. 274 (1999) 12702–12709.
[50] T. Schulte, K.A. Paschke, U. Laessing, F. Lottspeich, C.A. Stuermer, Reggie-1 and reggie-2, two cell surface proteins expressed by retinal ganglion cells during axon regeneration, Development 124 (1997) 577–587.
[51] D.M. Lang, S. Lommel, M. Jung, R. Ankerhold, B. Petrausch, U. Laessing, M.F. Wiechers, H. Plattner, C.A. Stuermer, Identification of reggie-1 and reggie-2 as plasmamembrane-associated proteins which cocluster with activated GPI-anchored cell adhesion molecules in non-caveolar micropatches in neurons, J. Neurobiol. 37 (1998) 502–523.

[52] N. Tavernarakis, M. Driscoll, N.C. Kyrpides, The SPFH domain: implicated in regulating targeted protein turnover in stomatins and other membrane-associated proteins, Trends Biochem. Sci. 24 (1999) 425–427.
[53] U. Salzer, H. Ahorn, R. Prohaska, Identification of the phosphorylation site on human erythrocyte band 7 integral membrane protein: implications for a monotopic protein structure, Biochim. Biophys. Acta 1151 (1993) 149–152.
[54] I.C. Morrow, S. Rea, S. Martin, I.A. Prior, R. Prohaska, J.F. Hancock, D.E. James, R.G. Parton, Flotillin-1/reggie-2 traffics to surface raft domains via a novel golgi-independent pathway. Identification of a novel membrane targeting domain and a role for palmitoylation, J. Biol. Chem. 277 (2002) 48834–48841.
[55] M.F. Langhorst, A. Reuter, C.A. Stuermer, Scaffolding microdomains and beyond: the function of reggie/flotillin proteins, Cell. Mol. Life Sci. 62 (2005) 2228–2240.
[56] B.U. Samuel, N. Mohandas, T. Harrison, H. McManus, W. Rosse, M. Reid, K. Haldar, The role of cholesterol and glycosylphosphatidylinositol-anchored proteins of erythrocyte rafts in regulating raft protein content and malarial infection, J. Biol. Chem. 276 (2001) 29319–29329; Epub 22001 May 29314.
[57] S.C. Murphy, B.U. Samuel, T. Harrison, K.D. Speicher, D.W. Speicher, M.E. Reid, R. Prohaska, P.S. Low, M.J. Tanner, N. Mohandas, K. Haldar, Erythrocyte detergent-resistant membrane proteins: their characterization and selective uptake during malarial infection, Blood 103 (2004) 1920–1928; Epub 2003 Oct 1930.
[58] K.S. Koumanov, C. Tessier, A.B. Momchilova, D. Rainteau, C. Wolf, P.J. Quinn, Comparative lipid analysis and structure of detergent-resistant membrane raft fractions isolated from human and ruminant erythrocytes, Arch. Biochem. Biophys. 434 (2005) 150–158.
[59] A. Ciana, C. Balduini, G. Minetti, Detergent-resistant membranes in human erythrocytes and their connection to the membrane-skeleton, J. Biosci. 30 (2005) 317–328.
[60] T. Nebl, K.N. Pestonjamasp, J.D. Leszyk, J.L. Crowley, S.W. Oh, E.J. Luna, Proteomic analysis of a detergent-resistant membrane skeleton from neutrophil plasma membranes, J. Biol. Chem. 277 (2002) 43399–43409; Epub 42002 Aug 43328.
[61] S. Bodin, C. Soulet, H. Tronchere, P. Sie, C. Gachet, M. Plantavid, B. Payrastre, Integrin-dependent interaction of lipid rafts with the actin cytoskeleton in activated human platelets, J. Cell. Sci. 118 (2005) 759–769; Epub 2005 Jan 2025.
[62] D. Holowka, E.D. Sheets, B. Baird, Interactions between Fc(epsilon)RI and lipid raft components are regulated by the actin cytoskeleton, J. Cell. Sci. 113 (2000) 1009–1019.
[63] S. Oliferenko, K. Paiha, T. Harder, V. Gerke, C. Schwarzler, H. Schwarz, H. Beug, U. Gunthert, L.A. Huber, Analysis of CD44-containing lipid rafts: Recruitment of annexin II and stabilization by the actin cytoskeleton, J. Cell Biol. 146 (1999) 843–854.
[64] U. Salzer, R. Prohaska, Segregation of lipid raft proteins during calcium-induced vesiculation of erythrocytes (letter), Blood 101 (2003) 3751–3753.
[65] M. Mariani, D. Maretzki, H.U. Lutz, A tightly membrane-associated subpopulation of spectrin is 3H-palmitoylated, J. Biol. Chem. 268 (1993) 12996–13001.
[66] K. Haglund, I. Ivankovic-Dikic, N. Shimokawa, G.D. Kruh, I. Dikic, Recruitment of Pyk2 and Cbl to lipid rafts mediates signals important for actin reorganization in growing neurites, J. Cell. Sci. 117 (2004) 2557–2568; Epub 2004 May 2505.
[67] J. Liu, S.M. Deyoung, M. Zhang, L.H. Dold, A.R. Saltiel, The stomatin/prohibitin/flotillin/HflK/C domain of flotillin-1 contains distinct sequences that direct plasma membrane localization and protein interactions in 3T3-L1 adipocytes, J. Biol. Chem. 280 (2005) 16125–16134; Epub 12005 Feb 16114.
[68] Y. Wang, J.S. Morrow, Identification and characterization of human SLP-2, a novel homologue of stomatin (band 7.2b) present in erythrocytes and other tissues, J. Biol. Chem. 275 (2000) 8062–8071.
[69] D. Raucher, T. Stauffer, W. Chen, K. Shen, S. Guo, J.D. York, M.P. Sheetz, T. Meyer, Phosphatidylinositol 4,5-bisphosphate functions as a second messenger that regulates cytoskeleton-plasma membrane adhesion, Cell 100 (2000) 221–228.

[70] H.R. Hope, L.J. Pike, Phosphoinositides and phosphoinositide-utilizing enzymes in detergent-insoluble lipid domains, Mol. Biol. Cell 7 (1996) 843–851.
[71] T. Laux, K. Fukami, M. Thelen, T. Golub, D. Frey, P. Caroni, GAP43, MARCKS, and CAP23 modulate PI(4,5)P(2) at plasmalemmal rafts, and regulate cell cortex actin dynamics through a common mechanism, J. Cell Biol. 149 (2000) 1455–1472.
[72] J. van Rheenen, E. Mulugeta Achame, H. Janssen, J. Calafat, K. Jalink, PIP(2) signaling in lipid domains: a critical re-evaluation, Embo J. 21 (2005) 21.
[73] E. Muller, H. Hegewald, K. Jaroszewicz, G.A. Cumme, H. Hoppe, H. Frunder, Turnover of phosphomonoester groups and compartmentation of polyphosphoinositides in human erythrocytes, Biochem. J. 235 (1986) 775–783.
[74] C.E. King, L.R. Stephens, P.T. Hawkins, G.R. Guy, R.H. Michell, Multiple metabolic pools of phosphoinositides and phosphatidate in human erythrocytes incubated in a medium that permits rapid transmembrane exchange of phosphate, Biochem. J. 244 (1987) 209–217.
[75] P. Gascard, E. Journet, J.C. Sulpice, F. Giraud, Functional heterogeneity of polyphosphoinositides in human erythrocytes, Biochem. J. 264 (1989) 547–553.
[76] P. Gascard, T. Pawelczyk, J.M. Lowenstein, C.M. Cohen, The role of inositol phospholipids in the association of band 4.1 with the human erythrocyte membrane, Eur. J. Biochem. 211 (1993) 671–681.
[77] D. Pradhan, K. Tseng, C.D. Cianci, J.S. Morrow, Antibodies to betaISigma2 spectrin identify inhomogeneities in the erythrocyte membrane skeleton, Blood Cells Mol. Dis. 32 (2004) 408–410.
[78] G.J. Bosman, F.L. Willekens, J.M. Werre, Erythrocyte aging: a more than superficial resemblance to apoptosis? Cell. Physiol. Biochem. 16 (2005) 1–8.
[79] F.L. Willekens, J.M. Werre, J.K. Kruijt, B. Roerdinkholder-Stoelwinder, Y.A. Groenen-Dopp, A.G. van den Bos, G.J. Bosman, T.J. van Berkel, Liver Kupffer cells rapidly remove red blood cell-derived vesicles from the circulation by scavenger receptors, Blood 105 (2005) 2141–2145.
[80] F.L. Willekens, B. Roerdinkholder-Stoelwinder, Y.A. Groenen-Dopp, H.J. Bos, G.J. Bosman, A.G. van den Bos, A.J. Verkleij, J.M. Werre, Hemoglobin loss from erythrocytes *in vivo* results from spleen-facilitated vesiculation, Blood 101 (2003) 747–751.
[81] R. Reliene, M. Mariani, A. Zanella, W.H. Reinhart, M.L. Ribeiro, E.M. del Giudice, S. Perrotta, A. Iolascon, S. Eber, H.U. Lutz, Splenectomy prolongs *in vivo* survival of erythrocytes differently in spectrin/ankyrin- and band 3-deficient hereditary spherocytosis, Blood 100 (2002) 2208–2215.
[82] H.U. Lutz, S.C. Liu, J. Palek, Release of spectrin-free vesicles from human erythrocytes during ATP depletion. I. Characterization of spectrin-free vesicles, J. Cell Biol. 73 (1977) 548–560.
[83] D. Allan, M.M. Billah, J.B. Finean, R.H. Michell, Release of diacylglycerol-enriched vesicles from erythrocytes with increased intracellular (Ca2+), Nature 261 (1976) 58–60.
[84] D. Allan, P. Thomas, A.R. Limbrick, The isolation and characterization of 60 nm vesicles ('nanovesicles') produced during ionophore A23187-induced budding of human erythrocytes, Biochem. J. 188 (1980) 881–887.
[85] U. Salzer, P. Hinterdorfer, U. Hunger, C. Borken, R. Prohaska, Ca(++)-dependent vesicle release from erythrocytes involves stomatin-specific lipid rafts, synexin (annexin VII), and sorcin, Blood 99 (2002) 2569–2577.
[86] H. Hagerstrand, B. Isomaa, Vesiculation induced by amphiphiles in erythrocytes, Biochim. Biophys. Acta 982 (1989) 179–186.
[87] M.P. Sheetz, S.J. Singer, Biological membranes as bilayer couples. A molecular mechanism of drug-erythrocyte interactions, Proc. Natl. Acad. Sci. USA 71 (1974) 4457–4461.
[88] M.P. Sheetz, S.J. Singer, Equilibrium and kinetic effects of drugs on the shapes of human erythrocytes, J. Cell Biol. 70 (1976) 247–251.
[89] A. Iglic, A possible mechanism determining the stability of spiculated red blood cells, J. Biomech. 30 (1997) 35–40.
[90] H.W.G. Lim, M. Wortis, R. Mukhopadhyay, Stomatocyte-discocyte-echinocyte sequence of the human red blood cell: evidence for the bilayer- couple hypothesis from membrane mechanics, Proc. Natl. Acad. Sci. USA 99 (2002) 16766–16769.
[91] R. Mukhopadhyay, H.W.G. Lim, M. Wortis, Echinocyte shapes: bending, stretching, and shear determine spicule shape and spacing, Biophys. J. 82 (2002) 1756–1772.

[92] A. Iglic, H. Hagerstrand, Amphiphile-induced spherical microexovesicle corresponds to an extreme local area difference between two monolayers of the membrane bilayer, Med. Biol. Eng. Comput. 37 (1999) 125–129.
[93] D.R. Anderson, J.L. Davis, K.L. Carraway, Calcium-promoted changes of the human erythrocyte membrane. Involvement of spectrin, transglutaminase, and a membrane-bound protease, J. Biol. Chem. 252 (1977) 6617–6623.
[94] D. Allan, R. Watts, R.H. Michell, Production of 1,2-diacylglycerol and phosphatidate in human erythrocytes treated with calcium ions and ionophore A23187, Biochem. J. 156 (1976) 225–232.
[95] D. Allan, P. Thomas, Ca2+-induced biochemical changes in human erythrocytes and their relation to microvesiculation, Biochem. J. 198 (1981) 433–440.
[96] H. Hagerstrand, L. Mrowczynska, U. Salzer, R. Prohaska, K.A. Michelsen, V. Kralj-Iglic, A. Iglic, Curvature-dependent lateral distribution of raft markers in the human erythrocyte membrane, Mol. Membr. Biol. 23 (2006) 277–288.
[97] S. Lin, E. Yang, W.H. Huestis, Relationship of phospholipid distribution to shape change in Ca(2+)-crenated and recovered human erythrocytes, Biochemistry 33 (1994) 7337–7344.
[98] E.F. Smeets, P. Comfurius, E.M. Bevers, R.F. Zwaal, Calcium-induced transbilayer scrambling of fluorescent phospholipid analogs in platelets and erythrocytes, Biochim. Biophys. Acta 1195 (1994) 281–286.
[99] D. Kamp, T. Sieberg, C.W. Haest, Inhibition and stimulation of phospholipid scrambling activity. Consequences for lipid asymmetry, echinocytosis, and microvesiculation of erythrocytes, Biochemistry 40 (2001) 9438–9446.
[100] S.L. Keller, W.H. Pitcher, W.H. Huestis, H.M. McConnell, Red Blood Cell Lipids Form Immiscible Liquids, Phys. Rev. Lett. 81 (1998) 5019–5022.
[101] R. Lipowsky, Budding of membranes induced by intramembrane domains, J. Phys. II 2 (1992) 1825–1840.
[102] F. Julicher, R. Lipowsky, Domain-induced budding of vesicles, Phys. Rev. Lett. 70 (1993) 2964–2967.
[103] F. Julicher, R. Lipowsky, Shape transformations of vesicles with intramembrane domains, Phys. Rev. E Stat. Phys., Plasmas, Fluids, Relat. Interdiscip. Topics 53 (1996) 2670–2683.
[104] P.B. Sunil Kumar, G. Gompper, R. Lipowsky, Budding dynamics of multicomponent membranes, Phys. Rev. Lett. 86 (2001) 3911–3914.
[105] H. Hagerstrand, B. Isomaa, Morphological characterization of exovesicles and endovesicles released from human erythrocytes following treatment with amphiphiles, Biochim. Biophys. Acta 1109 (1992) 117–126.
[106] T. Baumgart, S.T. Hess, W.W. Webb, Imaging coexisting fluid domains in biomembrane models coupling curvature and line tension, Nature 425 (2003) 821–824.
[107] A. Roux, D. Cuvelier, P. Nassoy, J. Prost, P. Bassereau, B. Goud, Role of curvature and phase transition in lipid sorting and fission of membrane tubules, Embo J. 24 (2005) 1537–1545.
[108] H. Hagerstrand, V. Kralj-Iglic, M. Bobrowska-Hagerstrand, A. Iglic, Membrane skeleton detachment in spherical and cylindrical microexovesicles, Bull. Math. Biol. 61 (1999) 1019–1030.
[109] D.W. Knowles, L. Tilley, N. Mohandas, J.A. Chasis, Erythrocyte membrane vesiculation: model for the molecular mechanism of protein sorting, Proc. Natl. Acad. Sci. USA 94 (1997) 12969–12974.
[110] S. Liemann, I. Bringemeier, J. Benz, P. Gottig, A. Hofmann, R. Huber, A.A. Noegel, U. Jacob, Crystal structure of the C-terminal tetrad repeat from synexin (annexin VII) of Dictyostelium discoideum, J. Mol. Biol. 270 (1997) 79–88.
[111] K. Iida, M.B. Whitlow, V. Nussenzweig, Membrane vesiculation protects erythrocytes from destruction by complement, J. Immunol. 147 (1991) 2638–2642.
[112] T.J. Hadley, Invasion of erythrocytes by malaria parasites: a cellular and molecular overview, Annu. Rev. Microbiol. 40 (1986) 451–477.
[113] S.C. Murphy, N.L. Hiller, T. Harrison, J.W. Lomasney, N. Mohandas, K. Haldar, Lipid rafts and malaria parasite infection of erythrocytes, Mol. Membr. Biol. 23 (2006) 81–88.
[114] N.L. Hiller, T. Akompong, J.S. Morrow, A.A. Holder, K. Haldar, Identification of a stomatin orthologue in vacuoles induced in human erythrocytes by malaria parasites. A role for microbial raft proteins in apicomplexan vacuole biogenesis, J. Biol. Chem. 278 (2003) 48413–48421.

CHAPTER FOUR

Interactions of Erythroid and Nonerythroid Spectrins and Other Membrane-Skeletal Proteins with Lipid Mono- and Bilayers

Aleksander F. Sikorski[1,2,*], Aleksander Czogalla[1], Anita Hryniewicz-Jankowska[1], Ewa Bok[1], Ewa Plażuk[1], Witold Diakowski[1], Anna Chorzalska[1], Adam Kolondra[1], Marek Langner[2], *and* Michał Grzybek[1,2]

Contents

1. Introduction 82
2. Spectrin-Based Membrane Skeleton 83
3. Interactions of Erythroid and Nonerythroid Spectrins with Lipid Mono- and Bilayers and other Amphipathic Ligands 84
   3.1. Interaction of Erythroid Spectrin with Phospholipid Mono- and Bilayers, a Historical Perspective of Seventies and Early Eighties 84
   3.2. Binding Lipid Mono- and Bilayers by Spectrins 86
   3.3. Interactions of Erythroid and Nonerythroid Spectrins with Monolayers Prepared from Anionic Phospholipids 88
   3.4. Lipidic Spectrin-Binding Sites in Natural Membranes 88
   3.5. Dependence of Spectrin-Binding on the Fluidity of the Mono- and Bilayers 88
   3.6. Binding of Amphipatic Compounds by Spectrins 89
4. Spectrin–Lipid Interactions; a Molecular Approach 89
   4.1. Lipid-Binding Sites in Spectrins 89
   4.2. Ankyrin-Dependent Lipid-Binding Site in β-Spectrins 91
   4.3. Structure of Lipid-Binding Site of Ankyrin-Binding Domain 93
   4.4. Possible Physiological Role of Spectrin–Phospholipid Interactions 94
5. Interactions of Other Skeletal Proteins with Membrane Mono- and Bilayers 95
   5.1. Ankyrins 95
   5.2. Protein 4.1 96
   5.3. Protein p55 96

* Corresponding author. Tel.: +4871-3756-233; Fax: +4871-3756-208;
E-mail address: afsbc@ibmb.uni.wroc.pl (A.F. Sikorski).

[1] Institute of Biochemistry and Molecular Biology, University of Wrocław, ul. Przybyszewskiego 63-77, PL-51-148 Wrocław, Poland
[2] Academic Centre for Biotechnology of Lipid Aggregates, Przybyszewskiego 63-77, 51148 Wrocław, Poland

Advances in Planar Lipid Bilayers and Liposomes, Volume 6
ISSN 1554-4516, DOI 10.1016/S1554-4516(07)06004-8

6. Concluding Remarks 97
Acknowledgement 97
References 97

Abstract

The object of the chapter is to review the studies on the interactions of erythroid and nonerythroid spectrins and other membrane-skeletal proteins with lipids in model membranes. An important progress on the identification of lipid-binding sites has recently been made although many questions remain still unanswered. In particular, our understanding of the physiological role of such interactions is still limited. Important issue is the mechanism(s) involved in these interactions.

Abbreviations:

DMPC	1,2-dimyristoyl-sn-glycero-3-phosphocholine
DMPG	1,2-dimyristoyl-sn-glycero-3-phosphoglycerol
FERM	four point one-ezrin-radixin-moesin
FRET	fluorescence resonance energy transfer
GUK	Guanylate Kinase like
SABD	spectrin–actin-binding domain
CTD	C-terminal domain
PDZ	PSD-95/Disc large/ZO-1
SH3	Sarc Homology 3
SPR	surface plasmon resonance

1. Introduction

Membrane-skeletal proteins apart from interacting with membrane integral proteins bind directly to the lipids of the bilayer. In this sense skeletal proteins behave as the soluble ones i.e., they associate with membranes through well-defined structural domains, such as FERM, FYVE, PH, PX (phox) [1] and C2, (http://www.smart.embl-heidelberg.de), or amphipathic helices and/or unstructured motifs. The latter interact through nonspecific ionic and/or hydrophobic interactions. Important role in some protein–lipid interactions play tryptophanyl residues which are often exposed into interacting surface (for review see Ref. [2,3]) or posttranslational modification with lipid-molecule, such as fatty acyl chain (miristoyl or palmitoyl) and/or prenyl (farnesyl or geranylgeranyl) group [4]. Some of the above-mentioned mechanisms have been identified to be responsible for membrane bilayer skeletal proteins interactions, majority however still awaits elucidation. The objective of this chapter is to review interactions of spectrins and other membrane-skeletal proteins with lipids of the membrane bilayer. Most of the studies quoted here were performed by using either monolayer or bilayer (lipid vesicles) as the major experimental model systems.

2. Spectrin-Based Membrane Skeleton

Spectrin, a high molecular weight flexible rod-like protein formed by head-to-head association of two heterodimers composed of α- (280 kD) and β- (247 kD) subunits [5,6] is a major component of a dense, well-organised protein network called the membrane skeleton. The remarkable mechanical properties of the red cell membrane stem from the presence of this structure on the erythrocyte membrane cytoplasmic surface. Spectrin heterodimers are formed by antiparallel double helical association of α- and β-subunits, each of which form predominantly a segmental triple-helical molecule. The detailed structure of the triple-helical segment, which is 106 amino acid residues long, was first solved by X-ray crystallography and also by NMR studies on an expressed fragment of *Drosophila* spectrin [7]. Further structural studies gave many details at the atomic resolution level providing background for studying mechanical properties of this protein (and the membrane skeleton) also in the pathological membranes [7–11]. Five to six spectrin tetramers interact with a short (37 nm) actin protofilament to form a structure known as the junctional complex [12]. Amino terminus of the β-spectrin contains actin-binding domain which is nonhomologous to the spectrin repeat and is conserved in many proteins that belong to spectrin superfamily of proteins [8,13,14]. The structure of this domain which is composed of two tandem CH domains has been solved at the atomic level [8]. Several other proteins: protein 4.1; adducin; dematin; p55; tropomyosin; and tropomodulin are also involved in forming the junction. Both protein 4.1 and adducin are known to promote high affinity binding of spectrin to actin filaments which otherwise would bind very weakly. Thus the formation of spectrin tetramers (i.e., dimer–dimer interaction) and the junctional complex are responsible for the planar integrity of the membrane skeleton. These skeletons can be isolated from either intact cells or from membranes by extraction with non-ionic detergent solution [15]. The membrane skeleton of the red blood cell is attached to the lipid bilayer with embedded integral membrane proteins through two main pathways of interaction, i.e., spectrin-ankyrin-AE1(band 3) protein (e.g., [16–19] and protein 4.1-glycophorin C and D [20] and the ternary interaction protein 4.1-p55-glycophorin C [21], or a recently discovered connection involving Rh, RhAG, CD47, protein 4.2 and/or ankyrin [22,23]. Schematic representation of the protein interactions forming the erythrocyte membrane skeleton is shown in Fig. 1.

Nonerythroid spectrins bear a high-sequence homology to erythroid spectrins and have α- and β-subunits of 283 and 275 kD, respectively [24–26]. The structure of the membrane skeleton, the reciprocal interactions of its components and its interactions with membrane proteins in nonerythroid cells are known to a much lesser extent, largely because of their much higher stuctural complexity. However, since many animal cell membranes contain spectrin and spectrin-binding proteins (analogues of erythrocyte membrane proteins and other spectrin-binding proteins) the existence of a similar protein network, which is tightly associated with membrane proteins, is anticipated [27]. As well as being a component of the membrane skeleton, nonerythroid spectrin (in particular αIIΣ1/βIIΣ1 isoform) is thought to be involved in the regulation of exocytosis, in particular in the regulation of

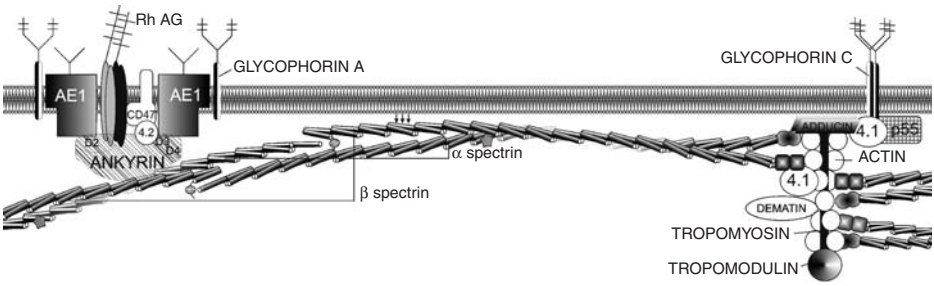

Figure 1 Erythrocyte membrane skeleton, a schematic representation. Arrows depict lipid-binding activity of the spectrin molecule. Other details in the text.

neurotransmitter release, in which its interaction with small synaptic vesicles *via* synapsin was shown to play a crucial role [28,29]. Numerous interactions of spectrin with other proteins have been inferred from using the yeast two hybrid system (for a review see Ref. [30]).

The above-mentioned high-affinity protein–protein interactions responsible for membrane skeleton attachment to the membrane have been the subject of many excellent reviews (e.g., [27]) but the direct interactions of this and other membrane-skeletal proteins with the lipid bilayer has attracted much less attention from the researchers.

3. Interactions of Erythroid and Nonerythroid Spectrins with Lipid Mono- and Bilayers and other Amphipathic Ligands

3.1. Interaction of Erythroid Spectrin with Phospholipid Mono- and Bilayers, a Historical Perspective of Seventies and Early Eighties

Spectrin was discovered and named by Marchesi and Steers [31] and its interaction with membrane lipids or phospholipids has been studied since early seventies. The first indication of the possibility of binding spectrin to lipids was observed in model system in which crude low ionic strength solution extract of the erythrocyte membranes (ghosts) which contained mostly spectrin but also actin and other skeletal proteins were used [32].

In 1970 the interaction of spectrin with model membrane systems was studied using liposomes, in conditions eliminating electrostatic interactions as the basis for its binding to the bilayer in the natural membrane. Spectrin bound to negatively charged liposomes constructed from PC, dicetyl phosphate and cholesterol, independently of ionic strength and also to positively charged liposomes prepared by substitution of stearyl amine for dicetyl phosphate [32].

In 1971 Juliano *et al.* [33] observed that the surface pressure of PS and PC monolayers is increased by the addition of spectrin into interphase and that spectrin interacts with sonicated PS vesicles. Spectrin bound to monolayers and liposomes at pH values below or near its isoelectric point. At pH 7.4 spectrin failed to interact

significantly with negatively charged vesicles. Ca^{2+} neither increased the effect of spectrin on PC vesicles nor altered the penetration of spectrin into PS monolayers. The possibility of both electrostatic attractions between spectrin and phospholipids and conformational changes in the protein-mediated penetration of spectrin into the phospholipid bilayer, was postulated. No effect of spectrin on positively charged stearyl amine/PC vesicles at pH 7.4 was observed [33]. Further studies showed changes in the enthalpy of phase transition of phospholipids in the presence of spectrin which lead to conclusion for a hydrophobic binding of spectrin to negatively charged phospholipids [34]. An interaction between sonicated, well-defined vesicles constructed from DMPC, DMPG and mixtures of these two lipids and a spectrin–actin complex isolated from human erythrocyte membranes was demonstrated. Spectrin was also shown to spontaneously interact with the synthetic bilayers and these lipid–protein interactions stabilised the planar bilayer orientation of the lipid molecules. It also protected the bilayer against the Ca^{2+} and Mg^{2+} and prevented fusion of lipid vesicles which easily occurred when divalent ions were added to pure lipid vesicles. The same laboratory performed experiments on the interaction of PS and PS/PC vesicles with spectrin–actin from human erythrocyte ghosts [35]. DMPS vesicles showed a decrease in enthalpy change of the lipid phase transition upon addition of spectrin–actin. These vesicles collapsed and fused into multilamellar structures in the presence of spectrin–actin. The data obtained from both calorimetric and NMR techniques showed the difference between PS and PC and showed that the negatively charged lipid polar headgroups are important for the hydrophobic interaction of spectrin with phospholipids. The observed changes in thermotropic properties of lipid mixtures showed that both electrostatic and as well as hydrophobic interactions are involved in binding of spectrin to lipids. The presence of Ca^{2+} and less strongly of Mg^{2+} affected the spectrin–PS interaction [5]. More detailed studies on the effect of spectrin on Ca^{2+}–PS vesicles interaction indicated that addition of this cation caused aggregation of PS vesicles and at temperature above 25°C induced the formation of an "anhydrous" complex of closely apposed membranes with highly ordered crystalline acyl chains. Addition of Mg^{2+} produced much more hydrated complex with PS, without crystallisation of the acyl chains. Both Ca^{2+} and Mg^{2+} evoked synergistic effect between the two cations, which resulted in an enhancement of the ability of Ca^{2+} to form its specific complex with PS at lower concentrations. The presence of the spectrin inhibited this synergism and interfered with the formation of the specific PS/Ca^{2+} complex. It also inhibits the fusion of PS vesicles [36].

The interactions of synthetic and natural phospholipids with spectrin purified from human erythrocyte membranes were more precisely examined by using a monolayer technique, at constant surface pressure [37]. High penetration of negatively charged phospholipid monolayers by spectrin was observed, maximal for PG and PS and this penetration was strongly affected by the subphase pH, surface pressure and salt concentration. Also the lipid fatty acid composition in natural phospholipids proved to be an important parameter. Zwitterionic or neutral lipids, such as PC, showed only poor affinity for spectrin. Both lipids condensed upon the addition of Ca^{2+}, but only in the case of PS this was accompanied by the extrusion of spectrin from the monolayer what led the authors to propose the model of this

phenomenon. Interaction of spectrin with phospholipid vesicles was stronger in the case of mixtures of PS with another phospholipid than in the case of PS alone. Also replacement of PC by PE improved binding [35].

The sites of lipid binding contain probably tryptophan residues, as binding of amphipatic ligands and phospholipids were shown to quench protein-intrinsic (tryptophan) fluorescence [38–40]. It should be noted that binding of spectrin to membrane phospholipids was also determined on intact cells, for example it was labelled with hydrophobic agents phenyl isothiocyanate or naphtyl isothiocyanate [41,42]. Studies on treatment of human erythrocytes with SH–oxidizing agents, such as tetrathionate and diamide showed that spectrin interacted with phospholipids of the inner leaflet of membrane bilayer and this interaction was thought essential for the maintenance of the phospholipid asymmetry in the erythrocyte membrane [43]. Spectrin role in the maintenance of phospholipid asymmetry was also suggested in studies on sickled, hereditary spherocytosis human cells [44].

Also anilinonaphtyl-labelled spectrin, that exhibited a fluorescence emission spectrum characteristic of a highly hydrophobic environment, seemed to penetrate the lipid bilayer. The changes in the fluorescence emission spectrum obtained in the presence of PS vesicles showed the specificity of interaction towards PS, with one spectrin-binding site per about 750 exposed phospholipids [45].

To study the interaction of spectrin with PS vesicles, ultrastructural methods such as an electron microscopy of rotary-shadowed platinum replicas of spectrin dimer–PS complexes were used. PS vesicles were crosslinked by spectrin dimers with stoichiometry that suggested the existence of multiple binding sites to PS throughout the spectrin dimer molecule and identifying some of these in the proximity of the tail end of spectrin. The association between spectrin dimers and PS was demonstrated by nondenaturing gel electrophoresis. The obtained bands corresponded with spectrin dimers connected to the ^{14}C-PS. The data provided ultrastructural and biochemical evidence that spectrin binds to PS at multiple sites as in higher concentrations the cross-linking of PS vesicles was observed [46]. Similar results were obtained with tetrameric spectrin; the binding sites were localised mainly at the ends of the tetramer molecule. Interesting fact is that the authors carried out similar experiments on other phospholipids and found similar results on vesicles prepared from PE and PS/PE vesicles but their results on PS vesicle binding are mostly cited in the literature. Further specificity studies on the interaction of anionic phospholipid monolayers with separated α- or β-spectrin subunits indicated a preferential binding by the β-subunit [47].

3.2. Binding Lipid Mono- and Bilayers by Spectrins

3.2.1. Red blood cell spectrin

As was mentioned above, there are many indications coming from various studies on cells, isolated membranes, and model systems that direct protein–lipid interactions contribute to the attachment of the membrane skeleton to the membrane hydrophobic domain.

In the eighties, interaction of red blood cell spectrin with membrane phospholipids became well documented, but the main lipid partner in the inner layer of membrane for spectrin is still a matter of debate. Some studies, such as mentioned above, indicated PS, but there also appeared reports observing the lack of specificity in the binding of spectrin to PS compared with PC and pointed to PE as a main binding phospholipid [37,40,46,48]. On the other hand, ^{2}H and ^{31}P NMR studies of bilayers constructed from DMPC and DMPS/DMPC (1:1) bound to spectrin argued against any strong interaction of spectrin with PS. Neither the phase transition of the DMPS/DMPC mixtures nor the spin-lattice relaxation time (T1) of the deuterated DMPS head group was affected by spectrin [48].

Phospholipid suspensions prepared of PE, PS and their mixtures quenched the intrinsic protein fluorescence of spectrin [14]. In the case of PE suspension up to 75% of protein fluorescence could be quenched. The pH and ionic strength values had an effect on the interaction of phospholipid vesicles with spectrin. Phospholipids, particularly PE, seemed to have a "stabilizing" effect against the changes of protein fluorescence induced by increase of ionic strength and by thermal denaturation [14]. The phospholipid suspensions influenced the proteolysis of spectrin. In the presence of the suspension prepared from PE/PS (3:2) mixture and of PC were observed qualitative changes in the proteolytic patterns of spectrin that resulted probably from changes in the accessibility of some peptide bonds upon the interaction of spectrin with phospholipids [49].

Spectrin was found to interact strongly with hydrophobic agaroses such as Phenyl- or Octyl-Sepharose, in the presence of EDTA. The binding capacity of spectrin depended not on the ionic strength but on its pH value. The fragments obtained by proteolysis of spectrin also bound strongly to phenyl-agarose and were eluted with ethylene glycol as two closely related polypeptides of 65 and 60 kDa [50].

Ray and Chakrabarti [51] studying an interaction of DMPE containing DMPC vesicles with red blood cell spectrin dimer found that K_D increased with an increase of DMPE, content (from 57 nM for pure DMPC vesicles up to 720 nM for 80% DMPE in these vesicles). However, when vesicles were prepared from pure DMPE, the K_D values dropped to 0.7 nM in the fluid phase and 2.6 nM in the gel phase. These and other results led authors to the suggestion that binding site for pure DMPE is located only at one end of the spectrin dimer.

3.2.2. Nonerythroid spectrin

Our studies revealed that nonerythroid (brain, mostly αIIβII) spectrin also binds to membrane phospholipids [52]. Saturable binding isotherms were observed for FAT-liposomes with K_D values in the nanomolar range (i.e. from 16 nM at pH 7.5 for liposomes prepared from total lipid mixture extracted from synaptic plasma membrane to ~500 nM for PC liposomes at pH 6.0). Purified brain spectrin induced an increase in surface pressure in lipid monolayers composed of PE/PC, PS/PC (3:2) and PC. The maximal effect ($\Delta\pi$) was observed when monolayers contained PE in the mixture, in particular, when PE was 50–60% of the monolayer-forming lipid. This interaction occurred optimally at pH 7.5, both in the pelleting assays and in monolayer experiments. There was also an ionic strength optimum, corresponding

to 0.15 M NaCl. Monolayer experiments revealed similarly, as in the case of red blood cell spectrin, that the major lipid-binding site is located in the β-subunit of the brain protein [53].

3.3. Interactions of Erythroid and Nonerythroid Spectrins with Monolayers Prepared from Anionic Phospholipids

As mentioned above many early studies indicated specificity towards anionic phospholipids, in particular PS-containing mono- and bilayers. Our monolayer experiments on anionic phospholipids including PI and PIP2 binding to purified brain spectrin showed that a monolayer formed of PI or PI/PC bound brain spectrin efficiently while red blood cell spectrin exerted much smaller effect on these monolayers. We assumed that this event was connected to the presence of the PH domain and had a regulatory role [54]. However, monolayers of PIP2 or PIP2/PC were penetrated by purified brain spectrin to much lower extent than PI monolayers [55], suggesting a larger than erythroid spectrin affinity of brain spectrin for anionic phospholipids.

3.4. Lipidic Spectrin-Binding Sites in Natural Membranes

Our studies proved also that natural membranes contain spectrin-binding sites which are independent of proteins. Natural, erythrocyte or neuronal membranes were treated in such a way as to remove protein receptors, i.e., NaOH extraction and/or treated with proteases. The affinities of these stripped membrane preparations for spectrin were similar to those found in other model systems. Moreover, this binding is competitively inhibited by lipid vesicles [56].

3.5. Dependence of Spectrin-Binding on the Fluidity of the Mono- and Bilayers

Interaction of spectrins with monolayers prepared from membrane phospholipids of various fluidity seem to be dependent on the ways this parameter is regulated. Our data [57] indicates that the presence of up to 10–20% cholesterol in the PE/PC monolayer facilitates the penetration of the monolayer by both types of spectrin. For monolayers constructed from mixtures of PI/PC and cholesterol, the effect of spectrins was characterised by the presence of two maxima (at 5 and 30% cholesterol) of surface pressure for erythroid spectrin, and a single maximum (at 20% cholesterol) for brain spectrin. The binding assay results indicated a small but easily detectable decrease in the affinity of erythrocyte spectrin for FAT-liposomes prepared from a PE/PC mixture containing cholesterol, and a two- to five-fold increase in maximal binding capacity (B_{max}) depending on the cholesterol content. On the other hand, the results from experiments with a monolayer constructed from homogenous fatty acid synthetic phospholipids indicated an increase in $\Delta\pi$ change with the decrease in the fluidity of the phospholipids used to prepare the monolayer. This result was further confirmed by a pelleting experiment. Adding spectrins into the subphase of raft-like monolayers constructed from DOPC,

SM and cholesterol (1:1:1) induced an increase in surface pressure. The $\Delta\pi$ change values were, however, much smaller than those observed in the case of a natural PE/PC (3:2) monolayer. An increased binding capacity of liposomes prepared from a "raft-like" mixture of lipids for spectrins could also be concluded from the pelleting assay [57].

3.6. Binding of Amphipatic Compounds by Spectrins

As was mentioned above, purified spectrin had the ability to bind hydrophobic and amphipatic ligands such as 2-bromostearic acid and 9,10- and 17,18-dibromostearic acids [38,39], fatty acids and detergents like SDS, CTAB and LDAO [40]. The hydrophobic fluorescent probe Prodan binds to the self-associating domain of spectrin with 1:1 stoichiometry with a K_D of 0.4 μM. Analysis of the docking results suggests that the binding of Prodan to the self-associating domain of spectrin involves hydrophobic and hydrophilic groups of Prodan [58,59]. The same group found several other ligands to be bound by erythroid spectrin, i.e., aureolic acid group of antitumor antibiotics, chromomycin A3 and mithramycin, which are well established as transcription inhibitors. The interaction leads to a change in the tertiary structure of the protein. Also dibucaine, the quinoline-based tertiary amine (but not benzene-based e.g., procaine, tetracaine or lidocaine) local anaesthetic was found to bind the hydrophobic sites in red blood cell spectrin but with lower affinity (K_D~35 μM).

Our studies on binding antracycline cytostatic mitoxantrone to erythroid or nonerythroid spectrin indicated strong interactions (K_D 4.6 and 1.4 μM for erythroid and nonerythroid spectrin) and stoichiometry of 4 per erythroid spectrin dimer and 7 molecules per nonerythroid spectrin tetramer. The K_D values were similar to those obtained for PE/PC (3:2) liposomes. Analysing the effect of the presence of mitoxantrone on the interaction of both erythroid and nonerythroid spectrins with the monolayer prepared from PE/PC (3:2) an interesting phenomenon was observed: the effect of spectrin on the surface pressure change increased several-fold (see Fig. 2). The complex was also found to evoke larger change in the fluidity of the PE/PC membrane as measured by using EPR technique with 5′-doxyl-stearate spin label. It was also observed that mitoxantrone possibly induces a small change in the secondary structure of spectrins [60].

4. Spectrin–Lipid Interactions; a Molecular Approach

4.1. Lipid-Binding Sites in Spectrins

Spectrins are multidomain proteins which show specific structural features: one of them is formation of an elongated segmental structure built of a series of repeating units, each of about 106 amino acid residues folded in a triple-helical motif. The other feature is the fact that outside typical segments and within them there are domains responsible for the multiple functions of spectrin. The most important functional domains outside typical spectrin repeats are actin-binding domain (two

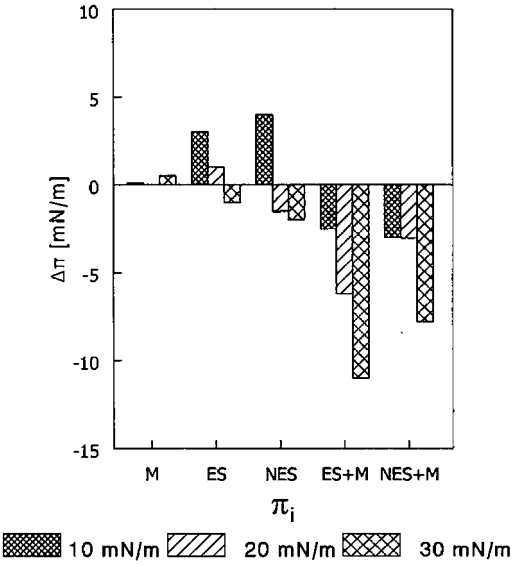

Figure 2 The effect of 72 nM mitoxantrone on the effect of spectrins on the surface pressure change of PE/PC monolayer. ES, erythroid spectrin; NES, nonerythroid spectrin; M, mitoxantrone. Bars represent the $\Delta\pi$ value observed at 72 nM mitoxantrone, at 8 nM erythroid or nonerythroid spectrin or at 8 nM spectrins and 72 nM mitoxantrone. Data obtained at three values of initial surface pressure (10, 20 and 30 mN/m) of PE/PC (3:2) monolayer are shown. (data taken from [60] with permission of Publisher, Taylor and Francis[R], http://www.informaworld.com).

CH motifs located at amino terminal region of β-subunit of spectrin) [13] and SH3 domain present in atypical, 10th segment of α-spectrin. Examples of other domains are ankyrin-binding domain located in part in 14th repeat and in 15th unit of β-spectrin [61,62] and Ca^{2+}-binding EF-hand motifs located in carboxyl terminal region of α-subunit [63].

The consequence of this multifunctionality is the existence of several lipid-binding activities connected with the occurrence of different binding sites: (1) a "general" phospholipid-binding activity characteristic for the spectrin repeat motif [64–66], (2) specific for aminophospholipids (PE and/or PS-binding sites located in the β-subunits, (e.g., [67–70]) and (3) specific for phosphatidylinositol 4,5-bis-phosphate, characteristic only for longer β-spectrin isoforms which poses Pleckstrin Homology (PH) domain [54,71,72].

The first kind of the lipid-binding activity that could be attributed to the spectrin repeat motif was actually studied by using a series of constructs containing the second repeat of the human dystrophin rod domain [73]. DeWolf *et al.* [65] observed that properly folded fragment corresponding to the second repeat unit of the rod domain is able to modify the properties of lipid membranes (inducing a large increase in surface shear viscosity of the monolayer) containing anionic phosphatidylserine. Moreover, this property is dependent on the native structure as the unfolded expressed fragment had no effect. Further studies of Le Rumeur *et al.* [66] showed

the engagement of tryptophan residues in this binding, as in the presence of small, unilammellar vesicles containing PS the fluorescence characteristics changed dramatically, indicating the tryptophan residues changed their environment into more hydrophobic. The accessibility of these residues from the hydrophilic solvent for quenchers was also limited. These authors conclude that dystrophin rod lies along the membrane surface [66]. Similar experimental approach should be undertaken to determine whether or not the same conclusion could be drawn with respect to spectrin–phospholipids interactions.

The second class of lipid-binding sites seems to be confined to certain regions of spectrin molecule which show some aminophospholipid and anionic phospholipids specificity. One of the approaches to identify this class of sites was to clone and express systematically all the fragments of both subunits of erythrocyte spectrin and test their binding to liposomes prepared from PS and its mixture with PC. Studies of An *et al.* [68,69], indicate that binding sites for PS-containing vesicles are located in repeats 8–10 of the α-subunit, in repeats 2–4, 12–14 and in the nonhomologous amino terminal region of the β-subunit. Their further studies [67] concerning nonerythroid spectrin indicated that PS-binding site is located in repeats 9–11 and in the amino terminus of α-subunit and in amino terminal region and repeat units 2 and 3 of the β-subunit. To this class of binding sites belongs, as we believe, the ankyrin-dependent lipid-binding site which is discussed in more details below.

Pleckstrin homology domain is an example of the third kind of lipid-binding sites specific for phosphoinositides. This kind of PIP2-binding site which is present in nonerythroid spectrins, βIΣ2 and βIIΣ2 and also in many regulatory and cytoskeletal proteins [54,74] is approximately 100 amino acid residues long. Binding of PIP2 is inhibited competitively by IP3 indicating the specificity for inositol ring [71].

4.2. Ankyrin-Dependent Lipid-Binding Site in β-Spectrins

Our early attempt to identify the main amphipathic compound-binding site of spectrin revealed its close proximity to the ankyrin-binding domain [50] what suggested a functional relationship between ankyrin and lipid binding by erythroid spectrin. Indeed, when the effect of purified ankyrin on spectrin binding to phospholipid vesicles was tested, an inhibition of this interaction was observed [75]. The effect was greater for the vesicles containing PE (PE/PC 3:2) for which 60% inhibition was found compared to 10–20% inhibition for PS/PC vesicles. Almost identical results were obtained using a monolayer technique. Dixon-type [76] analysis indicated a competitive mechanism of inhibition of PE/PC vesicles or monolayer binding to spectrin by ankyrin. Tetrameric spectrin bound similarly to PE/PC monolayer but inhibition with ankyrin suggests that only one of the two possible binding sites is engaged in this interaction [77]. Moreover, when interactions of nonerythroid (brain) spectrin with PE/PC monolayers in the presence of ankyrin were analysed, a similar level of inhibition of these interactions by ankyrin was observed [53]. Also, when isolated erythroid spectrin β-subunit was introduced into the subphase of PE/PC monolayers in the presence of ankyrin, the inhibition was even stronger, i.e., a three-fold lower concentration of ankyrin was needed to

induce the same effect. If the α-subunit was used instead of β its effect on the monolayer surface pressure was small and entirely insensitive to incubation with ankyrin [53,77]. It should be noted also that binding of brain spectrin to anionic phospholipid monolayers was also competitively inhibited by purified erythrocyte ankyrin [55].

As this event could have a regulatory role and could be engaged in the possible mechanism of function of the membrane skeleton we decided to test whether an ankyrin-binding domain which was identified by Kennedy *et al.* [61] would show the same lipid-binding properties as spectrin molecule and to identify an ankyrin-sensitive, lipid-binding site in erythroid and nonerythroid spectrins [70,70a]. The results of the experiments document further the ability of cloned, expressed and purified erythroid β-spectrin's ankyrin-binding domain to bind PE-rich mono- and bilayers. We found that full-length ankyrin-binding domain binds PE/PC mono- and bilayers with affinity similar to that of native spectrin dimer and this binding is inhibited by erythrocyte ankyrin. Binding studies were performed by (i) pelleting assay using PE/PC liposomes and fluorescently labelled expressed polypeptides, (ii) inhibition assay in which unlabelled, expressed polypeptides were used to inhibit binding of purified, labelled red blood cell spectrin to PE/PC liposomes and (iii) surface plasmon resonance technique experiments where binding of purified, expressed polypeptides to PE/PC monolayer deposited on hydrophobic sensor surface was observed. Results of these experiments indicate that ankyrin-binding domain truncated mutants, that retain amino terminal part bind the PE/PC mono- and bilayers with affinity and capacity comparable to full-length ankyrin-binding domain. They also effectively compete for lipids with purified, labelled spectrin. On the other hand, truncated mutants which lack 8 or 38 amino acid residues from N-terminal region show, at least an order of magnitude lower affinity and much higher maximal binding capacity. They also compete weakly with spectrin for phospholipid vesicles. The expressed full-length domain induced small decrease in order parameter of PE/PC membranes when probed with 5′-doxylstearate similar to the effect of purified spectrin, while mutant-lacking 38 residues from amino terminus induced small increase in order parameter which was similar to the effect of bovine serum albumin.

As the amino terminal part of ankyrin-binding domain of known β-spectrins shows high degree of conservation in evolution (see Fig. 3 and also [62]), we expected similar results in the case of nonerythroid βII spectrin. Indeed, cloned and expressed fragments of nonerythroid (human brain) β-spectrin encompassing a sequence corresponding to an ankyrin-binding domain was found to bind phospholipid mono- and bilayers in a similar way to intact molecule of brain spectrin or erythroid spectrin. Again, truncated mutant of this domain which retained amino terminal region bound lipid mono- and bilayers with the affinity similar to the full-length domain. Mutants in which this region was deleted bound phospholipids with lower affinities and higher capacities and this binding was insensitive to inhibition with purified ankyrin.

Transient expression of HeLa cells with GFP-conjugated constructs encoding full-length ankyrin-binding domain of either erythroid or nonerythroid β-spectrins induced changes in cell morphology and aggregation of membrane skeleton. These

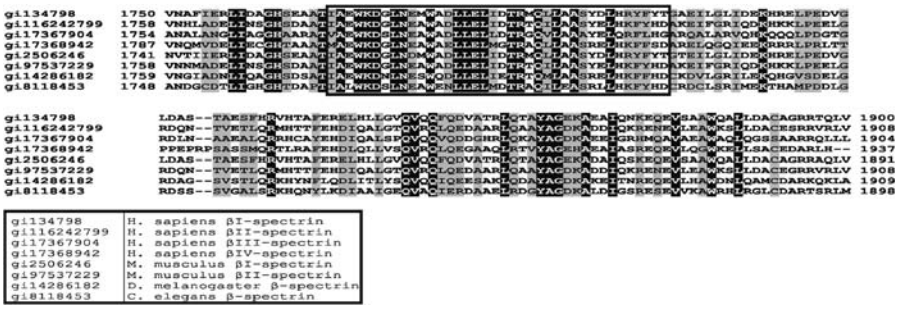

Figure 3 Alignment of known β-spectrin sequences corresponding to ankyrin-binding domain.

changes were observed neither in cells transfected with a construct encoding GFP-conjugated ankyrin-binding domain truncated at amino terminus by 38 amino acid residues nor in cells transfected with a vector encoding only GFP (Bok *et al.*, submitted). Also the results obtained by using site-directed mutagenesis on the entire ankyrin-binding domain of the βI spectrin confirm that replacing hydrophobic with hydrophilic (serine) residues in the middle of this domain (residues 1782, 1785 and 1786) remained without effect while replacing hydrophobic residues in the region of first 8 of them (residues 1771, 1775 and 1778) gave substantial increase in K_D for the interaction with PE/PC monolayers and vesicles (Bok *et al.*, to be published).

The above-mentioned experimental results indicate that at least in erythroid spectrin the binding site located within or close to ankyrin-binding domain were identified by our and Mohandas groups. It seems that there is a good chance that these sites (segment 12–14 and amino terminal part of the ankyrin-binding domain) are overlapping. The difference concerns nonerythroid β-spectrin; our results indicate essentially the same features for both β-spectrins, while Mohandas group could not identify this site in their constructs. In our hands binding of PS/PC (3:2) monolayer to bacterially expressed ankyrin-binding domain and its deletion mutants retaining N-terminal region of nonerythroid β-spectrin occurred with K_D's in nanomolar range what was measured by SPR and FRET techniques [70a].

4.3. Structure of Lipid-Binding Site of Ankyrin-Binding Domain

Ankyrin-sensitive lipid-binding site of ankyrin-binding domain is located in typical triple-helical spectrin repeat rod region of the β-spectrin (helix C of the segment 14).

We studied its structure by constructing a series of single and double spin-labelled β-spectrin-derived peptides and analysing their spin–spin distances *via* electron paramagnetic resonance spectroscopy and the Fourier deconvolution method. The results indicate that the whole ankyrin-sensitive lipid-binding site of β-spectrin exhibits a helical conformation revealing a distinct 3_{10}-helix contribution at its N-terminus (especially the stretch 1768 IAEWKD 1773). The start of the helix was located five residues upstream along the sequence compared to the

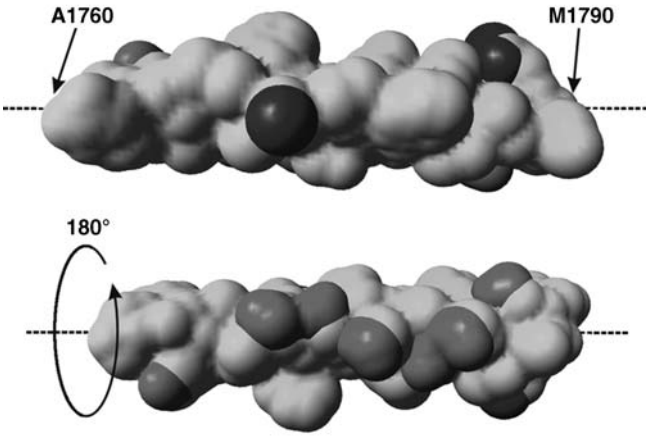

Figure 4 Structural model [78] of the lipid-binding site surface of the ankyrin-binding domain of the β-spectrin (with the permission from the Publisher, Taylor and Francis®, http://www.informaworld.com). Blue are positively and red are negatively charged residues. Hydrophobic residues are marked yellow (please see plate no. 2 in the color section).

theoretical predictions based on known structures of spectrin repeats. We built a model based on the obtained distances which provides direct evidence that the examined lipid-binding site is a highly amphipathic helix. The latter is correlated with the specific conformation of its N-terminal fragment (a structural model is presented in Fig. 3) [78].

In general, inter-helical interactions are fundamental for spectrin repeat stability, and the majority of them are van der Waals contacts (highly conserved tryptophan residues playing a dominant role) with a small amount of electrostatic and hydrogen bond interactions [79,80]. Some spectrin repeats are stabilised mainly by the latter types of interaction [81], which raises the possibility that some of the negatively (and/or positively) charged groups of the structure presented here might be engaged in inter-helical interactions, thus leaving free the hydrophobic residues (at least some of them) for interaction with lipids. However, the exact mechanisms of such interactions still awaits discovery (Fig. 4).

4.4. Possible Physiological Role of Spectrin–Phospholipid Interactions

It was suggested previously that the sites of interactions of spectrin with lipids function as additional support points of the membrane bilayer increasing its mechanical stability. This would be the function of the "general" sites, best characterised in the case of dystrophin repeat segment (see above). It should be noted that almost every fragment of spectrin studied in our laboratory to date, display lipid-binding activity, characterised with a $\underline{K}_D$ in the range of 10^{-5}–10^{-6} M. Some of the lipid-binding activities are confined to the specific regions or domains such as PH

domain with high specificity towards PIP2 characteristic only for certain isoforms. These particular interactions are thought to play signalling/regulatory role.

Lipid-binding sites of limited specificity and moderate-to-high affinity (K_D $\sim 10^{-7}$–10^{-8} M) are confined essentially to two regions of spectrin molecule: one located to the centre of the tetramer and another located near its end and they coincide with, or are close to, the attachment sites for the proteins that mediate linkage with membrane bilayer. An *et al*. [68] suggested that the interactions with PS modulate interactions of spectrin with linking proteins such as ankyrin or protein 4.1. They also suggest that spectrin regulates the state of the bilayer, possibly generating or stabilising PS patches [69]. As was mentioned above, we found that binding of aminophospholipid mono- or bilayers at one of these sites was inhibited by ankyrin [75,77]. The same was observed for nonerythroid spectrin [53] and moreover, for cloned and bacterially expressed ankyrin-binding domain [70] and its truncated mutants (for details see above). We have proposed that PE-rich domains (and also to lesser extent PS or anionic phospholipid-rich domains) would serve as membrane attachment site for spectrin in situations in which ankyrin is either deficient or its affinity for spectrin is reduced [75,82]. Some examples of evidence of such situations are (i) erythrocytes of mutant mice, whose erythroblasts fail to synthesise ankyrin, still accumulate about 50% of normal amount of spectrin [83], (ii) erythrocytes of ankyrin-deficient mice which contain normal skeletons but lack AE1 tetramers [84] and (iii) also the phosphorylation of ankyrin decreases its ability to bind spectrin [85]. In all these situations, aminophospholipid-rich (primarily PE) domains would serve as anchors substituting ankyrin and ensuring preservation of the mechanical properties in the membrane-skeletal lattice. This would explain why mice with a disrupted gene coding for AE1 protein are characterised by severe spherocytosis despite the presence of normal membrane skeletons [86] in contrast to the above-mentioned cases of ankyrin deficiency. Possibly in this case ankyrin inhibits binding of spectrin to the inner layer of membrane lipids.

Recent data obtained by transgene rescue strategy in *Drosophila* test the contribution of ankyrin-binding site of β-spectrin to its assembly and function [87]. Removal of the putative ankyrin-binding site was found to have mild phenotype with no effect on spectrin targetting to the plasma membrane, indicating that spectrin functions upstream of ankyrin in the membrane skeleton biogenesis. Interesting fact is that the authors did not include highly homologous "lipid binding" region of the full-length ankyrin-binding domain. As ankyrin is not the primary "anchor" for spectrin in contrast to PH domain, perhaps lipid-binding homologous region would be one of them.

5. Interactions of Other Skeletal Proteins with Membrane Mono- and Bilayers

5.1. Ankyrins

Ankyrins are a group of erythroid and nonerythroid membrane-skeletal proteins which are present as many isoforms (encoded in humans by three genes)

functioning as adaptor proteins attaching membrane skeleton to the membrane integral proteins such as ion channels and cell adhesion molecules (for a review see Refs. [27,88,89,89a]). To date, an interaction of this protein with membrane lipids was not studied in details. The only published data for the erythrocyte protein come from Gratzer's laboratory and show the ability of ankyrin to bind hydrophobic and amphipatic compounds as its intrinsic fluorescence could be quenched by brominated fatty acids [39]. In our experiments it appeared that purified ankyrin penetrated phospholipid monolayers but with much lower affinity than spectrins (Białkowska K. Ph.D. Thesis, University of Wrocław, 1995).

5.2. Protein 4.1

Human erythrocyte membrane protein 4.1 (4.1 R) consists of 864 amino acid residues (molecular weight: 97017 Da) and is a product of human gene epb41 (UniProtKB-/Swiss-Prot: P11171). It should be noted that there are more residues in isoforms containing exons 17A and 17B and fewer in isoforms translated from ATG2 or ATG 3. Protein 4.1R consists of four structural and functional domains: FERM, 16 kDa, SABD and CTD (for a review, see Ref. [90,91]).

Apart from binding of membrane proteins, protein 4.1 was shown to interact directly with membrane phospholipids, mainly phosphatidylserine (PS), through the N-terminal FERM (30 kDa) domain of protein 4.1, as characterised by Sato and Onishi [92]. Other investigators essentially confirmed the above finding and also found that protein 4.1 penetrates PS monolayers and estimated equilibrium dissociation constant for 3.3×10^{-7} M [93,94]. The PS-binding site was found in the sequences encoded by exons 10 and/or 11[95]. The positively charged YKRS motif (residues 442–445) proved important for the initiation of interaction between protein 4.1 and the negatively charged surface of PS. Furthermore, a tight hydrophobic interaction of fatty acyl chains with the cluster of hydrophobic residues near the YRKS motif was suggested [95]. Association with PS prevents the interaction of 4.1 with any of the membrane proteins. The localisation of a PS-binding site in the FERM domain, which is present in most of the protein 4.1 superfamily members, could be a clue for the biological significance of the domain.

The recently published data showed that 4.1R bound to PIP2-containing liposomes through its FERM domain and this binding induced a conformational change in this domain. Binding of PIP2 to 4.1R selectively modulated the ability of 4.1R of interaction with its different partners, e.g., PIP2 significantly enhanced binding of 4.1R to glycophorin C *in situ* in the membrane [96]. This is in contrast to the FERM domain of focal adhesion kinase (FAK), which does not bind PIP2 [97].

5.3. Protein p55

Protein p55 primary structure of which includes a PDZ, SH3 and GUK domain is an example of fatty (palmitoyl) acyl-modified membrane protein. In erythrocyte membrane it is the major palmitoylated protein incorporating more than 75% of exogenous palmitate in intact erythrocytes *in vitro*. It has a characteristic of

peripheral protein but could be extracted from the membrane only with isotonic solution (150 mM KCl) of 0.5% Triton X-100 [98]. Data from the same laboratory suggest that this protein functions as an adaptor protein linking protein 4.1 and glycophorin C. Binding of glycophorin C occurs *via* PDZ domain [99,100]. The presence of p55 increases the affinity of protein 4.1 for glycophorin C by a factor of 100 [21].

6. Concluding Remarks

Plasma membrane of most animal cells conforms to the membrane skeleton and cytoskeleton. The role of the membrane–skeleton interactions in the regulation of cell shape and various events taking place at membrane–skeleton interface such as endo- and exocytosis, formation of blebs and lamellipodia, as well as formation of the diffusion barrier for the membrane lipids like this in tight junctions is studied to great details. Spectrin was suggested to form, *via* its interactions with membrane lipids, a considerable barrier to lipid lateral diffusion even though the inhibition of the integral membrane proteins lateral diffusion is significantly greater (for a review see Ref. [101]). The role of other membrane-skeletal proteins, in particular, protein 4.1 and p55 interacting with the membrane lipids should be also considered in the future studies. The particular mechanisms of interactions with the bilayer membrane lipids used by the skeletal proteins are known to various extent, some of which involve interaction of specialised domains such as PH domain (present in some spectrin isoforms) binding PIP2 are known at the atomic resolution [71], for a review see Ref. [2], while others such as other spectrin lipid- (mainly aminophospholipid) binding domain(s) await elucidation.

ACKNOWLEDGEMENT

This work was supported by the grant from KBN 2P04A 02127 and COST/13/2005.

REFERENCES

[1] C.A. Worby, J.E. Dixon, Sorting out the cellular functions of sorting nexins, Nat. Rev. Mol. Cell Biol. 3 (2002) 919–931.
[2] J.H. Hurley, S. Misra, Signaling and subcellular targeting by membrane-binding domains, Annu. Rev. Biophys. Biomol. Struct. 29 (2000) 49–79.
[3] S.H. White, W.C. Wimley, Hydrophobic interactions of peptides with membrane interfaces, Biochim. Biophys. Acta 1376 (1998) 339–352.
[4] M.D. Resh, Fatty acylation of proteins: new insights into membrane targeting of myristoylated and palmitoylated proteins, Biochim. Biophys. Acta 1451 (1999) 1–16.
[5] K. Sahr, P. Laurila, L. Kotula, A. Scarpa, E. Coupal, T. Leto, A. Linnenbach, J. Winkelmann, D. Speicher, V. Marchesi, P. Curtis, B. Forget, The complete cDNA sequences of human erythroid a-spectrin, J. Biol. Chem. 265 (1990) 4434–4443.
[6] J. Winkelmann, J.-G. Chang, W. Tse, A. Scarpa, V. Marchesi, B. Forget, Full-length sequence of the cDNA for human erythroid beta-spectrin, J. Biol. Chem. 264 (1990) 11827–11832.

[7] Y.E. Yan, A. Winograd, T. Viel, S. Cronin, S. Harrison, D. Branton, Crystal structure of the repetitive segments of spectrin, Science 262 (1993) 2027–2030.
[8] K. Djinovic-Carugo, P. Young, M. Gautel, M. Saraste, Structure of the alpha-actinin rod: molecular basis for cross-linking of actin filaments, Cell 98 (4) (1999) 537–546.
[9] V.L. Grum, D.N. Li, R.I. MacDonald, A. Mondragon, Structures of two repeats of spectrin suggest models of flexibility, Cell 98 (1999) 523–535.
[10] Z.S. Zhang, S.A. Weed, P.G. Gallagher, J.S. Morrow, Dynamic molecular modeling pathogenic mutations spectrin self-association domain, Blood 98 (2001) 1645–1653.
[11] D.E. Discher, P.E. Carl, New insights into red cell network structure, elasticity, and spectrin unfolding – a current review, Cell. Mol. Biol. Lett. 6 (2001) 593–606.
[12] T. Byers, D. Branton, Visualization of the protein associations in the erythrocyte membrane skeleton, Proc. Natl. Acad. Sci. U.S.A 82 (1985) 6153–6157.
[13] A.M. Karinch, W.E. Zimmer, S.R. Goodman, The identification and sequence of the actin binding domain of human red blood cell beta-spectrin, J. Biol. Chem. 265 (1990) 11833–11840.
[14] J.H. Hartwig, Actin binding proteins. 1. Spectrin superfamily, Protein Profile 2 (1995) 703–800.
[15] J. Yu, D.A. Fishman, T.L. Steck, Selective solubilization of proteins and phospholipids from red blood cell membrane by non-ionic detergents, J. Supramol. Struct. 1 (1973) 233–248.
[16] V. Bennett, D. Branton, Selective associations of spectrin with the cytoplasmic surface of human erythrocyte membranes. Quantitative determination with purified (^{32}P) spectrin, J. Biol. Chem. 252 (1977) 2753–2763.
[17] V. Bennett, P. Stenbuck, Association between ankyrin and the cytoplasmic domains of band 3 isolated from human erythrocyte membrane, J. Biol. Chem. 255 (1980) 6424–6432.
[18] J. Yu, S.R. Goodman, Syndeins: spectrin-binding protein(s) from the human erythrocyte membrane, Proc. Natl. Acad. Sci. U.S.A. 76 (1979) 2340–2344.
[19] V. Bennett, P. Stenbuck, The membrane attachment protein for spectrin is associated with band 3 in human erythrocyte membrane, Nature 280 (1979) 468–473.
[20] J.C. Pinder, A. Chung, M.E. Reid, W.B. Gratzer, Membrane attachment sites for the membrane cytoskeletal protein 4.1 of the red blood cell, Blood Cells Mol. Dis. 82 (1993) 3482–3488.
[21] N.J. Hemming, D.J. Anstee, M.A. Staricoff, M.J. Tanner, N. Mohandas, Identification of the membrane attachment sites for protein 4.1 in the human erythrocyte, J. Biol. Chem. 270 (1995) 5360–5366.
[22] I. Mauro-Chanteloup, J. Delaunay, P. Gane, V. Nicolas, M. Johansen, E.J. Brown, L.L. Peters, C.L. Van Kim, J.P. Cartron, Y. Colin, Evidence that the red cell skeleton protein 4.2 interacts with the Rh membrane complex member CD47, Blood Cells Mol. Dis. 101 (2003) 338–344.
[23] V. Nicolas, C. Le Van Kim, P. Gane, C. Birkenmeier, J.P. Cartron, Y. Colin, I. Mauro-Chanteloup, Rh-RhAG/ankyrin-R, a new interaction site between the membrane bilayer and the red skeleton, is impaired by Rh(null)-associated mutation, J. Biol. Chem. 278 (2003) 25526–25533.
[24] S.R. Goodman, I.S. Zagon, R.R. Kulikowski, Identification of spectrin-like proteins in nonerythroid cells, Proc. Natl. Acad. Sci. U.S.A. 78 (1981) 7570–7574.
[25] Y. Ma, W.E. Zimmer, B.M. Riederer, M.L. Bloom, J.E. Barker, S.M. Goodman, S.R. Goorman, The complete amino acid sequence for brain beta spectrin (beta fodrin): relationship to globin sequences, Brain Res. Mol. Brain Res. 18 (1993) 87–99.
[26] R.T. Moon, A.P. McMahon, Generation of the diversity in nonerythroid spectrins, J. Biol. Chem. 265 (1990) 4427–4433.
[27] V. Bennett, A.J. Baines, Spectrin and ankyrin-based pathways: metazoan inventions for integrating cells into tissues, Physiol. Rev. 81 (2001) 1353–1392.
[28] A.F. Sikorski, G. Terlecki, I.S. Zagon, S.R. Goodman, Synapsin I mediated interaction of brain spectrin with small synaptic vesicles, J. Cell Biol. 114 (1991) 313–318.
[29] A.F. Sikorski, J. Sangerman, S.R. Goodman, S.D. Critz, Spectrin (bSpIIS1) is an essential component of synaptic transmission, Brain Res. 852 (2000) 161–166.

[30] M.A. De Matteis, J.S. Morrow, Spectrin tethers and mesh in the biosynthetic pathway, J. Cell Sci. 113 (2000) 2331–2343.
[31] V.T. Marchesi, E. Steers Jr., Selective solubilization of a protein component of the red cell membrane, Science 159 (1968) 203–204.
[32] C. Sweet, J.E. Zull, Interaction of erythrocyte-membrane protein, spectrin with model membrane systems, Biochem. Biophys. Res. Commun. 41 (1970) 135–141.
[33] R.L. Juliano, H.K. Kimelberg, D. Paphadjopoulos, Synergistic effect of membrane protein, spectrin and Ca^{2+} on Na^{+} permeability of phospholipid vesicles, Biochim. Biophys. Acta 241 (1971) 894–905.
[34] C. Mombers, P.W. van Dijck, L.L. van Deenen, J. de Gier, A.J. Verkleij, The interaction of spectrin-actin and synthetic phospholipids, Biochim. Biophys. Acta 470 (1977) 152–160.
[35] C. Mombers, A.J. Verkleij, J. de Gier, L.L. van Deenen, The interaction of spectrin-actin and synthetic phospholipids. II. The interaction with phosphatidylserine, Biochim. Biophys. Acta 551 (1979) 271–281.
[36] A. Portis, C. Newton, W. Pangborn, D. Papahadjopoulos, Studies on the mechanism of membrane fusion: evidence for an intermembrane Ca^{2+}-phospholipid complex, synergism with Mg^{2+}, and inhibition by spectrin, Biochemistry 18 (1979) 780–790.
[37] C. Mombers, J. DeGier, R. Demel, L.L.M. van Deenen, Spectrin-phospholipid interaction. A monolayer study, Biochim. Biophys. Acta 603 (1980) 52–62.
[38] G. Isenberg, J.G. Kenna, N.M. Green, W.B. Gratzer, Binding of hydrophibic ligands to spectrin, FEBS Lett. 129 (1981) 109–112.
[39] E. Kahana, J.C. Pinder, K. Smith, W.B. Gratzer, Fluorescence quenching of spectrin and other red cell membrane cytoskeletal proteins. Relation to hydrophobic binding sites, Biochem. J. 282 (1992) 75–80.
[40] A.F. Sikorski, K. Michalak, M. Bobrowska, A. Kozubek, Interaction of erythrocyte spectrin with amphipathic coumpounds, Stud. Biophys. 121 (1987) 20–26.
[41] A.F. Sikorski, M. Kuczek, Labelling of erythrocyte spectrin 'in situ' with phenylisothiocyanate, Biochim. Biophys. Acta 820 (1985) 147–153.
[42] A.F. Sikorski, M. Kuczek, Z. Nyczka, Z.J. Kubiak, Hydrophobic labelling of erythrocyte spectrin in erythrocytes using arylisothiocyanates, Biomed. Biochim. Acta 46 (1987) 76–82.
[43] C.W. Haest, G. Plasa, D. Kamp, B. Deuticke, Spectrin as a stabilizer of the phospholipid asymmetry in the human erythrocyte membrane, Biochim. Biophys. Acta 509 (1978) 21–32.
[44] W.H. Sawyer, J.S. Hill, G.J. Howlett, J.S. Wiley, Hereditary spherocytosis of man. Defective cytoskeletal interactions in the erythrocyte membrane, Biochem. J. 211 (1983) 349–356.
[45] D. Bonnet, E. Begard, Interaction of anilinonaphtyl labeled spectrin with fatty acids and phospholipids: a fluorescence study, Biochem. Biophys. Res. Commun. 120 (1984) 344–350.
[46] A.M. Cohen, S.C. Liu, L.H. Derick, J. Palek, Ultrastructural studies of the interaction of spectrin with phosphatidylserine liposomes, Blood 68 (1986) 920–926.
[47] D. Schubert, F. Herbst, H. Marie, V. Rudloff, Interactions of the isolated spectrin peptides (bands 1 and 2) with phosholipid monolayers, in: H. Peeters, (Ed.), Protides of Biological Fluids Proceedings of 29th Colloquium, Pergamon Press, Oxford, 1981.
[48] M. Bitbol, C. Dempsey, A. Watts, P.F. Devaux, Weak interaction of spectrin with phosphatidylcholine-phosphatidylserine multilayers: a 2H and 31P NMR study, FEBS Lett. 244 (1989) 217–222.
[49] A.F. Sikorski, A. Kozubek, J. Szopa, Proteolysis of Spectrin in the Presence of Phospholipid Suspensions with Trypsin and Pronase, Acta Biochim. Polon. 35 (1988) 71–82.
[50] A.F. Sikorski, Interaction of spectrin with hydrophobic agaroses, Acta Biochim. Polon. 35 (1988) 19–27.
[51] S. Ray, A. Chakrabarti, Membrane interaction of erythroid spectrin: surface density-dependent high-affinity binding to phosphatidylethanolamine, Mol. Membr. Biol. 21 (2004) 93–100.
[52] W. Diakowski, A.F. Sikorski, Interaction of brain spectrin (fodrin) with phospholipids, Biochemistry 34 (1995) 13252–13258.

[53] W. Diakowski, A. Prychidny, M. Swistak, M. Nietubyć, K. Bialkowska, J. Szopa, A.F. Sikorski, Brain spectrin (fodrin) interacts with phospholipids as revealed by intrinsic fluorescence quenching and monolayer experiments, Biochem. J. 338 (1999) 83–90.
[54] D.-S. Wang, R. Miller, R. Shaw, G. Shaw, The pleckstrin homology domain is targeted to plasma membrane in vivo, Biochem. Biophys. Res. Commun. 225 (1996) 420–426.
[55] W. Diakowski, A.F. Sikorski, Brain spectrin exerts much stronger effect on anionic phospholipid monolayers than erythroid spectrin, Biochim. Biophys. Acta 1564 (2002) 403–411.
[56] W. Diakowski, J. Szopa, A.F. Sikorski, Occurrence of lipid receptors inferred from brain and erythrocyte spectrns binding NaOH-extracted and protease-treated neuronal and erythrocyte membranes, Biochim. Biophys. Acta 1611 (2003) 115–122.
[57] W. Diakowski, Ł. Ozimek, E. Bielska, S. Bem, M. Langner, A.F. Sikorski, Cholesterol affects spectrin-phospholipid interactions in a manner different from changes resulting from alterations in membrane fluidity due to fatty acyl chain composition, Biochim. Biophys. Acta 1758 (2006) 4–12.
[58] M. Bhattacharyya, S. Ray, S. Bhattacharya, A. Chakrabarti, Chaperone activity and prodan binding at the self-associating domain of erythroid spectrin, J. Biol. Chem. 279 (2004) 55080–55088.
[59] M. Bhattacharyya, C. Mukhopadhyay, A. Chakrabarti, Specificity of prodan for the self-associating domain of spectrin: a molecular docking study, J. Biomol. Struct. Dyn. 24 (2006) 269–276.
[60] P.M. Dubielecka, A. Trusz, W. Diakowski, M. Grzybek, A. Chorzalska, B. Jaźwiec, M. Lisowski, A. Jezierski, A.F. Sikorski, Mitoxantrone changes spectrin-aminophospholipid interactions, Mol. Membr. Biol. 23 (2006) 235–243.
[61] S.P. Kennedy, S.L. Warren, B.G. Forget, J.S. Morrow, Ankyrin binds to the 15th repetirive unit of erythroid and nonerythroid beta-spectrin, J. Cell Biol. 115 (1991) 267–277.
[62] A.J. Baines, Comprehensive analysis of all triple helical repeats in b-spectrins reveals patterns of selective evolutionary conservation, Cell. Mol. Biol. Lett. 8 (2003) 195–214.
[63] A. Buevich, S. Lundberg, I. Sethson, U. Edlund, L. Backman, NMR studies of calcium-binding to mutant a-spectrin EF-hands, Cell. Mol. Biol. Lett. 9 (2004) 167–186.
[64] C. DeWolf, P. McCauley, J.C. Pinder, Regulation of the mechanical properties of the red cell membrane by protein-protein and protein-lipid interactions, Cell. Mol. Biol. Lett. 1 (1996) 89–96.
[65] C. DeWolf, P. McCauley, A.F. Sikorski, C.P. Winlove, A.I. Bailey, E. Kahana, J.C. Pinder, W.B. Gratzer, Interaction of dystrophin fragments with model membranes, Biophys. J. 72 (1997) 2599–2604.
[66] E. Le Rumeur, Y. Fichou, S. Pottier, F. Gaboriau, C. Rondeau-Mouro, M. Vincent, J. Gallay, A. Bondon, Interaction of dystrophin rod domain with membrane phospholipids. Evidence of a close proximity between tryptophan residues and lipids, J. Biol. Chem. 278 (2003) 5993–6001.
[67] X. An, X. Guo, W. Gratzer, N. Mohandas, Phospholipid binding by proteins of the spectrin family, Biochem. Biophys. Res. Commun. 327 (2005) 794–800.
[68] X. An, X. Guo, Y. Wu, N. Mohandas, Phosphatidylserine binding sites in red cell spectrin, Blood Cells Mol. Dis. 32 (2004) 430–432.
[69] X. An, X. Guo, H. Sum, J. Morrow, W. Gratzer, N. Mohandas, Phosphatidylserine binding sites in erythroid spectrin: location and implications for membrane stability, Biochemistry 43 (2004) 310–315.
[70] A. Hryniewicz-Jankowska, E. Bok, P. Dubielecka, A. Chorzalska, W. Diakowski, A. Jezierski, M. Lisowski, A.F. Sikorski, Mapping of an ankyrin-sensitive, phosphatidylethanolamine/phosphatidylcholine mono- and bilayer binding site in erythroid b-spectrin, Biochem. J. 382 (2004) 677–685.
[70a] E. Bok, E. Plażuk, A. Hryniewicz-Jankowska, A. Chorzalska, A. Szmaj, P.M., Dubielecka, K.Stebelska, W. Diakowski, M. Lisowski, M. Langner, A.F. Sikorski, The lipid-binding role of the betaII-spectrin ankyrin-binding domain. Cell Biology International, accepted (available online July 16, 2007).

[71] M. Saraste, M. Hyvonen, PH domain. A fact file, Curr. Opin. Struct. Biol. 5 (1995) 403–408.
[72] M. Grzybek, M. Chorzalska, E. Bok, A. Hryniewicz-Jankowska, A. Czogalla, W. Diakowski, A.F. Sikorski, Spectrin-phospholipid interactions. Existence of multiple kinds of bindong sites? Chem. Phys. Lipids 141 (2006) 133–141.
[73] E. Kahana, W.B. Gratzer, Minimum folding unit of dystrophin rod domain, Biochemistry 34 (1995) 8110–8114.
[74] V. Niggli, Structural properties of lipid-binding sites in cytoskeletal proteins, TIBS 26 (2001) 604–611.
[75] K. Białkowska, A. Zembroń, A.F. Sikorski, Ankyrin inhibits binding of erythrocyte spectrin to phospholipid vesicles, Biochim. Biophys. Acta 1191 (1994) 21–26.
[76] M. Dixon, The determination of enzyme-inhibitor constants, Biochem. J. 55 (1953) 170–171.
[77] K. Białkowska, J. Leśniewski, M. Nietubyć, A.F. Sikorski, Interaction of spectrin with phospholipids is inhibited by isolated erythrocyte ankyrin, Cell. Mol. Biol. Lett. 4 (1999) 203–218.
[78] A. Czogalla, A.R. Jaszewski, W. Diakowski, E. Bok, A. Jezierski, A.F. Sikorski, Structural insight into an ankyrin-sensitive lipid-binding site of erythroid β-spectrin, Mol. Membr. Biol. 24 (2007) 215–224.
[79] H. Kusunoki, G. Minasov, R.I. MacDonald, A. Mondragon, Independent movement, dimerization and stability of tandem repeats of chicken brain α-spectrin, J. Mol. Biol. 344 (2004) 495–511.
[80] X. An, X. Guo, X. Zhang, A.J. Baines, G. Debnath, D. Moyo, M. Salomao, N. Bhasini, C. Johnson, D. Discher, W.B. Gratzer, N. Mohandas, Conformational stabilities of the structural repeats of erythroid spectrin and their functional implications, J. Biol. Chem. 281 (2006) 10527–10532.
[81] H. Kusunoki, R.I. MacDonald, A. Mondragon, Structural insights into the stability and flexibility of unusual erythroid spectrin repeats, Structure 12 (2004) 645–656.
[82] A.F. Sikorski, K. Białkowska, Interactions of spectrins with membrane intrinsic domain, Cell. Mol. Biol. Lett. 1 (1996) 97–104.
[83] D.M. Bodine 4th, C.S. Birkenmeier, J.E. Barker, Spectrin deficient inherited anemias in the mouse: characterization by spectrin synthesis and mRNA activity in reticulocytes, Cell 37 (1984) 721–729.
[84] S. Yi, S.-C. Liu, L.H. Derick, J. Murray, J.E. Barker, M.R. Cho, J. Palek, D.E. Golan, Red cell membranes of ankyrin-deficient nb/nb mice lack band 3 tetramers but contain normal skeletons, Biochemistry 36 (1997) 9596–9604.
[85] P. Liu, C.-J. Soong, M. Tao, Phosphorylation of ankyrin decreases its affinity for spectrin tetramer, J. Biol. Chem. 260 (1985) 14958–14964.
[86] C.D. Southgate, A.H. Chishti, B. Mitchel, S.J. Yi, J. Palek, Targeted disruption of the murine band 3 gene results in spherocytosis and severe hemolytic anemia despite normal membrane skeleton, Nat. Genet. 14 (1996) 227–230.
[87] A. Das, C. Base, S. Dhulipala, R.R. Dubreuil, Spectrin functions upstream of ankyrin in a spectrin cytoskeleton assembly pathway, J. Cell Biol. 175 (2006) 325–335.
[88] P.J. Mohler, V. Bennett, Ankyrin-based cardiac arrhytmias: a new class of channelopathies due to loss of cellular targeting, Curr. Opion. Cardiol 20 (2005) 189–193.
[89] A.C.A. Hryniewicz-Jankowska, E. Bok, A.F. Sikorski, Ankyrins, multifunctional proteins involved in many cellular pathways, Folia Histochem. Cytobiol. 40 (2002) 239–249.
[89a] K. Białkowska, Dependence of spectrin-lipid interaction on ankyrin. Ph.D. Thesis. University of Wrocław, 1995.
[90] W. Diakowski, M. Grzybek, A.F. Sikorski, Protein 4.1, a component of the erythrocyte membrane skeleton, and its related homologue proteins forming the protein 4.1/FERM superfamily, Folia Histochem. Cytobiol. 44 (2006) 231–248.
[91] J.G. Conboy, Structure, function, and molecular genetics of erythroid membrane skeletal protein 4.1 in normal and abnormal red blood cells, Semin. Hematol. 30 (1993) 58–73.
[92] S.B. Sato, S. Onishi, Interaction of a peripheral protein of the erythrocyte membrane, band 4.1 with phosphatidylserine-containing liposomes and erythrocyte inside-out vesicles, Eur. J. Biochem. 130 (1983) 19–25.

[93] K.A. Shiffer, J. Goerke, N. Duzgunes, J. Fedor, S.B. Shohet, Interaction of erythrocyte protein 4.1 with phospholipids. A monolayer and liposome study, Biochim. Biophys. Acta 937 (1988) 269–280.
[94] A.M. Cohen, S.-C. Liu, J. Lawler, L. Derick, J. Palek, Identification of the protein 4.1 binding site to phosphatidylserine vesicles, Biochemistry 27 (1988) 614–619.
[95] X.-L. An, Y. Takakuwa, S. Manno, B.-G. Han, P. Gascard, N. Mohandas, Structural and functional characterization of protein 4.1R-phosphatidylserine interaction: potential role in 4.1R sorting within cells, J. Biol. Chem. 276 (2001) 35778–35785.
[96] X. An, X. Zhang, G. Debnath, A.J. Baines, N. Mohandas, Phosphatidylinositol-4,5-biphosphate (PIP2) differentially regulates the interaction of human erythrocyte protein 4.1 (4.1R) with membrane proteins, Biochemistry 45 (2006) 5725–5732.
[97] D.F. Ceccarelli, H.K. Song, F. Poy, M.D. Schaller, M.J. Eck, Crystal structure of the FERM domain of focal adhesion kinase, J. Biol. Chem. 281 (2006) 252–259.
[98] P. Ruff, D.W. Speicher, A.H. Chishti, Molecular identification of a major palmitoylated erythrocyte membrane protein containing the src homology 3 motif, Proc. Natl. Acad. Sci. U.S.A. 88 (1991) 6595–6599.
[99] S.M. Marfatia, J.H. Morais-Cabral, A.C. Kim, O. Byron, A.H. Chishti, The PDZ domain of human erythrocyte p55 mediates its binding to the cytoplasmic carboxyl terminus of glycophorin C. Analysis of the binding interface by *in vitro* mutagenesis, J. Biol. Chem. 272 (1997) 24191–24197.
[100] N. Alloisio, N. Dalla Venezia, A. Rana, K. Andrabi, P. Texier, F. Gilsanz, J.P. Cartron, J. Delaunay, A.H. Chishti, Evidence that red blood cell protein p55 may participate in the skeleton-membrane linkage that involves protein 4.1 and glycophorin C, Blood 82 (1993) 1323–1327.
[101] M.P. Sheetz, J.E. Sable, H.-G. Dobereiner, Continuous membrane-cytoskeleton adhesion requires continous accommodation to lipid and cytoskeleton dynamics, Annu. Rev. Biophys. Biomol. Struct. 35 (2006) 417–434.

CHAPTER FIVE

Liposome-Based Biomembrane Mimetic Systems: Implications for Lipid–Peptide Interactions

Karl Lohner*, Eva Sevcsik, *and* Georg Pabst

Contents

1. Introduction 104
   1.1. Lipid Composition of Mammalian and Bacterial Cell Membranes 105
   1.2. Effects of Antimicrobial Peptides on Lipid Bilayers 109
2. Understanding the Mechanism of Lipid–Peptide Interaction 110
   2.1. Lipid Affinity of Antimicrobial Peptides Triggered by Electrostatic Interactions – Lipid–Peptide Domain Formation 110
   2.2. Membrane Thinning as a Precursor of Pore Formation 113
   2.3. Detergent-Like Effect – Micellar Lipid–Peptide Disk Formation 115
   2.4. Promotion or Prevention of Non-Lamellar Phases 116
3. General Aspects of Model Membranes 117
   3.1. Global and Local Membrane Properties 117
   3.2. Domains-Rafts 120
4. X-ray Diffraction in Combination with a Global Data Analysis 121
5. Bacterial Model Membranes 125
6. The Antimicrobial Peptide LF11 – Influence of N-Acylation 127
7. Structural Information on Coexisting Membrane Domains 130
8. Outlook 132
References 132

Abstract

The fundamental structural unit of biological membranes is mostly a highly dynamic, liquid-crystalline phospholipid bilayer that acts as a permeability barrier. The concept of a characteristic lipid composition for a given cell membrane is well-accepted and is of considerable interest, when studying the molecular mechanism(s) of membrane damage by membrane-active agents such as toxins or antimicrobial peptides. Despite the wealth of information and experimental data we still do not fully understand at a molecular level how these peptides disrupt the barrier function of cell membranes. Therefore, lipid

* Corresponding author. Tel: +43-316-4120-323, Fax: +43-316-4120-390
E-mail address: Karl.lohner@oeaw.ac.at (K. Lohner).

Institute of Biophysics and Nanosystems Research, Austrian Academy of Sciences, Schmiedlstraße 6, A-8042 Graz, Austria

Advances in Planar Lipid Bilayers and Liposomes, Volume 6
ISSN 1554-4516, DOI 10.1016/S1554-4516(07)06005-X

model membranes mimicking the more complex biological membranes have attracted scientists from various fields. Structural and thermodynamic characterization of these biomembrane mimetic systems such as liposomes is a prerequisite for the understanding of lipid–peptide interactions. The focus of this contribution will be on how X-ray scattering techniques contribute to the characterization of liposomes and in turn to the elucidation of the mechanisms of peptide–membrane interaction. First, we summarize the current models for the mode of action of antimicrobial peptides as well as general aspects of model membranes followed by a detailed description of X-ray scattering in combination with a global data analysis. The applicability of this new approach is exemplary shown on selected model membrane and lipid–peptide systems demonstrating a tight coupling between the peptide properties and those of the lipid bilayer.

1. Introduction

An enormous variety of lipid classes is found in nature, which exhibit a great diversity in their molecular and supramolecular structure with a number of biological functions. For example, phospholipids act as signaling molecules in cellular processes and as a storage form of metabolic energy, but most importantly contribute to the structural definition of cell membranes. The fundamental structural unit of biological membranes is mostly a highly dynamic, liquid-crystalline phospholipid bilayer that functions as a permeability barrier defining in- and outside compartments. Membrane composition can be very diverse. Both the phospholipid content and the composition in different types of biological membranes vary considerably [1–3].

Membrane phospholipid, fatty acid and sterol composition can be modified in many different ways, which may alter membrane fluidity and affect a number of cellular functions [4]. Hence, it may not be surprising that membranes from different tissues or organelles of one species have different lipid contents and compositions due to their different functionality. On the other hand, the same types of membranes from different species are often characterized by similar lipid composition and content. Although the maintenance of stable lamellar structures is essential to normal membrane function, it is well-known that cell membranes contain substantial quantities of so-called non-lamellar phase forming lipids. These lipids may play a regulatory role in response to variations in environmental conditions, as suggested for thylakoid membranes in plants [5] or mitochondrial membranes in amoeba [6]. Furthermore, it was shown that many biological membranes have a lipid composition in a narrow window close to a lamellar to non-lamellar phase boundary. For example, several microorganisms such as *Acholeplasma laidlawii* or *Escherichia coli* precisely regulate the amounts of lamellar and non-lamellar lipids [7].

Thus, given the large variation of lipids found in natural membranes it appears obvious that lipid bilayers may also play an active role in regulating membrane proteins. Hence, knowledge on the specific lipid composition is of fundamental importance for questions related to membrane–protein interactions. In the following, we elaborate briefly on the most significant differences between bacterial

and mammalian cell membranes, which are of importance to understand selective membrane disruption by membrane-active peptides, the topic of this contribution. These peptides should rupture only bacterial cell membranes, but leave mammalian cell membranes intact (see also Section 1.2).

1.1. Lipid Composition of Mammalian and Bacterial Cell Membranes

1.1.1. Mammalian membranes

The membrane of red blood cells, which serves as an archetype of mammalian cytoplasmic cell membranes, consists to a large extent of lipids (about 60% of phospholipids and 25% of cholesterol [1] and is characterized by an asymmetric distribution of phospholipids between the outer and the inner lipid leaflets of the bilayer [8–10]. The amino phospholipids, phosphatidylserine (PS) and phosphatidylethanolamine (PE), are found almost exclusively on the cytoplasmic side of the membrane, while the choline phospholipids, phosphatidylcholine (PC) and sphingomyelin (SM), occur predominantly in the external leaflet of the bilayer. Thus, a model membrane consisting of PC, SM and cholesterol will suit well for studies related to the interaction of membrane-active compounds with the outer leaflet of mammalian cell membranes. In many biological systems, these two choline phospholipids appear to occupy similar cellular compartments and their content is tightly regulated. Interestingly, in red blood cells the ratio of the choline phospholipids can vary strongly depending on the organism (Table 1), which in turn may affect the interaction with peptides, as higher contents of SM may result in a more rigid membrane [11].

The asymmetric distribution of the choline and amino phospholipids is maintained by an ATP-dependent amino phospholipid translocase [12]. The current knowledge of various mechanisms of transbilayer movement of phospholipids in biogenic membranes was reviewed recently [13], whereby a model was suggested in which phospholipid translocation is also mediated *via* membrane-spanning

Table 1 Phospholipid composition of red blood cells (percentage of total phospholipid) from various organisms listed according to increasing sphingomyelin content. Choline phospholipids are predominantly found in the outer leaflet of the membrane, while amino phospholipids are almost exclusively located in the inner leaflet of the bilayer.

Organism	PC	SM	Total choline phospholipids	PE	PS	Total amino phospholipids	Others
Rat	47.5	12.8	60.3	21.5	10.8	32.3	7.4[a]
Rabbit	33.9	19.0	52.9	31.9	12.2	44.1	3.0[b]
Human	34.7	20.1	54.8	28.0	14.3	42.3	2.9[c]
Pig	23.3	26.5	49.8	29.7	17.8	47.5	2.7[a]
Sheep	–	51.0	51.0	26.2	14.1	40.3	8.7[a]

[a]Mainly phosphatidylinositol.
[b]Phosphatidylinositol and phosphatidic acid.
[c]Mainly phosphatidic acid.
Source: Data taken from ref. [189].

segments of a subset of proteins, characterized by a small number of transmembrane helices. Nevertheless, stimulation of the nonspecific lipid scramblase or inactivation of the amino phospholipid inward transport can abolish the preferential location of these phospholipids. In particular, the exposure of PS to the surface of mammalian cells has important physiological implications triggering a coagulation-cascade and cell-scavenging processes, but is also used as a recognition mechanism for macrophages to eat the apoptotic cells [14,15]. Moreover, PS was also found on the surface of cancerous and other pathological cells [16].

1.1.2. Bacterial membranes

Considering lipid architecture one has to differentiate between Gram-positive and Gram-negative bacteria. The cell envelope of Gram-negative bacteria is a complex structure consisting of two bilayers, a unique outer membrane and an inner, cytoplasmic membrane (Fig. 1). The periplasmic space in between these two membranes is filled with an intervening layer of peptidoglycan [17]. The outer membrane has a distinctive composition, which is highly asymmetric. Lipopolysaccharides are located exclusively in the outer leaflet, while phospholipids, to a large extent PE (Table 2), are confined to the inner layer of the outer membrane [18]. In addition, Gram-negative bacteria can stabilize their outer membrane by an increased degree of acylation of the lipid A moiety [19].

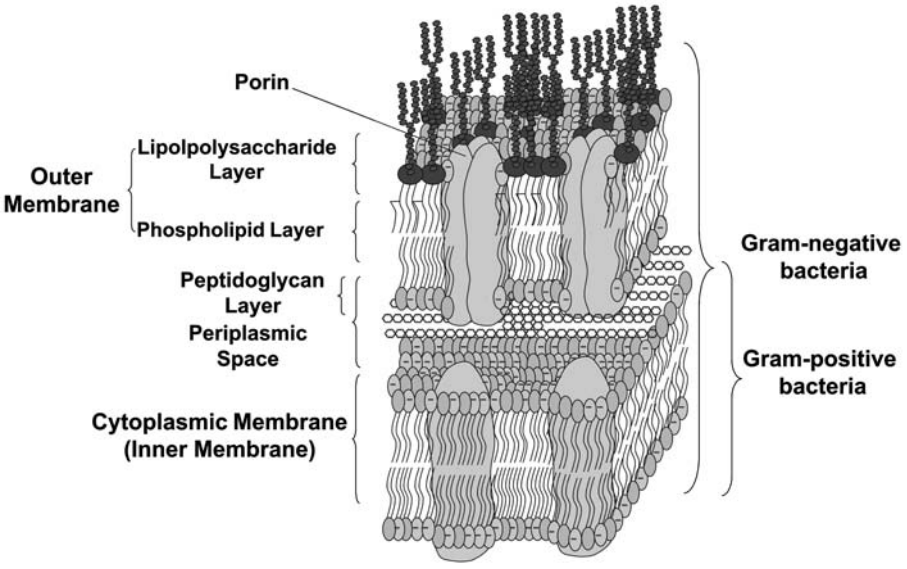

Figure 1 Schematic presentation of the molecular organization of bacterial cell membranes. Gram-negative bacteria consist of an outer membrane with an asymmetric distribution of LPS and phospholipids, predominantly PE and a cytoplasmic or inner membrane, while Gram-positive bacteria only have a cytoplasmic membrane protected by a peptidoglycan layer, which is also found in the periplasmic space of Gram-negative bacteria. PG is the most abundant negatively charged phospholipid species found in both bacteria.

Table 2 Phospholipid composition of some selected species of Gram-negative and Gram-positive bacteria (percentage of total phospholipid).

Bacteria Species		PG	DPG	L-lysyl PG	PE	Others
Gram-negative						
Erwinia carotovora	OIM[a]	14	8	0	78	0
Eschericha coli	OM[b]	3	6	0	91	0
	CM[c]	6	12	0	82	0
Salmonella typhimurium	OM	17	2	0	81	0
	CM	33	7	0	60	0
Pseudomonas cepacia	OM	13	0	0	87	0
	CM	18	0	0	82	0
Gram-positive						
Bacillus megaterium	CM	40	5	15	40	0
Bacillus subtilis	CM	29	47	7	10	6[d]
Micrococcus luteus	CM	26	67	0	0	7[e]
Staphylococcus aureus	CM	57	5	38	0	Trace

[a]Phospholipid composition not differentiated between outer and inner membrane.
[b]OM, outer membrane.
[c]CM, cytoplasmic membrane.
[d]Including phosphatidic acid and glycolipids.
[e]Almost exclusively phosphatidylinositol.
Source: Data taken from refs. [18,23].

The inner, cytoplasmic membrane of Gram-negative bacteria is essentially a lipid bilayer consisting again to a large extent of PE. In addition, there is also a considerable amount of negatively charged phosphatidylglycerol (PG) and diphosphatidylglycerol (DPG or cardiolipin) incorporated into the membrane (Table 2). Phosphatidic acid (PA) is only found in traces, most likely due to the rapid turnover of this lipid, as it serves as a precursor for all other phospholipids [20,21]. Although PC is a widely distributed and quantitatively important phospholipid in animals and higher plants, it is generally not found in bacteria. Only some species in particular of the genera *Brucella* and *Rhodopseudomonas* show a marked amount of this zwitterionic phospholipid [22].

In contrast, Gram-positive bacteria only contain a cytoplasmic membrane, which supposedly reflects an early evolutionary stage, in which the genetic imperative for lipids is primarily the formation of a cell membrane [23]. A peptidoglycan–teichoic acid network forms the cell wall, which like LPS can convey some protection against membrane-active peptides. Thereby, mutants characterized by an increased net negative surface charge were more sensitive than the wild type to a number of antimicrobial peptides [24]. The phospholipids constitute up to 80% of the total cellular lipids and consist to a large extent of PG. Moreover, aminoacyl derivatives of PG, such as e.g., lysyl-PG in *S. aureus* and several species of *Bacillus* or ornithine-PG in *B. cereus* [22], are found besides DPG (Table 2). However, it seems that the phospholipid composition varies from one species to another to a larger extent in Gram-positive than in Gram-negative bacteria. For example, *Micrococcus*

luteus possesses an extremely high amount of DPG, while *B. megaterium* exhibits a rather high content of PE (Table 2). Furthermore, many Gram-positive species are characterized by a high content of branched fatty acids, which are less often found in Gram-negative bacteria.

Less insight exists regarding the distribution of phospholipids between the outer and inner leaflets of the cytoplasmic bacterial membranes [20], although early studies on *Erwinia carotovora* indicated an asymmetric distribution of PE not only for the outer but also for the inner membrane, as also observed for the cytoplasmic membranes of *M. lysodeikticus*, *B. subtilis* and *megaterium* [25–28].

As can be deduced from the brief description above, natural membranes can hardly be precisely rebuilt and one is constantly confronted with a compromise between simplicity and accuracy. Nevertheless, important insight into the nature of biological membranes can be gained by studying bilayers consisting of a single type of phospholipid or mixtures of phospholipids. Thus, a wealth of data on the interaction of peptides and membrane lipid exists from model systems, whereby the structural and thermodynamic characterization of the membrane mimetic system is a prerequisite for the understanding of lipid–peptide interaction as is the proper choice of lipids to mimic the biological membrane of interest. Although supported oriented bilayers have become increasingly interesting as revealed by a number of contributions within this series, we shall limit our discussion to liposomes, depicted in Fig. 2. As this article will focus on the action of membranolytic peptides, especially antimicrobial peptides, we shall devote a large extent to the discussion of liposomes composed of PG and PE mimicking bacterial cell membranes. Furthermore, we shall elaborate on recent progress in X-ray techniques, which will allow gaining additional structural information on the bilayer level. This will be helpful to

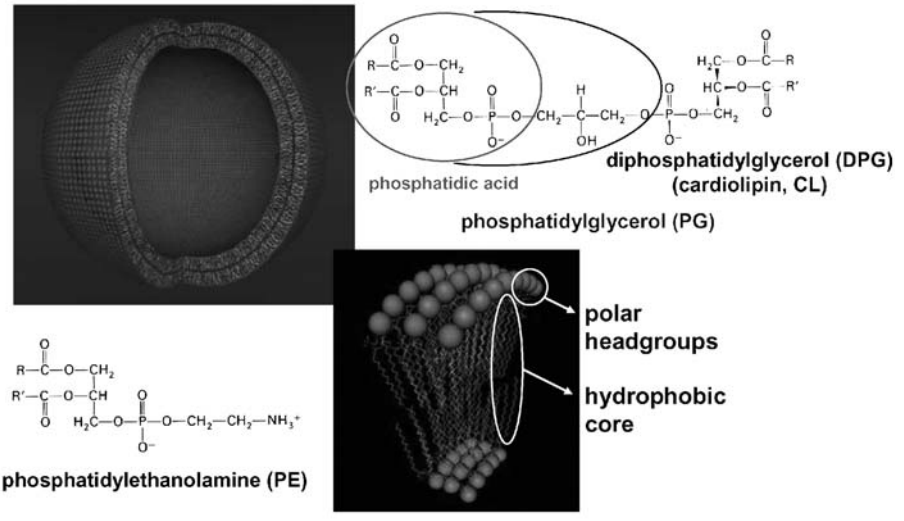

Figure 2 Scheme of a unilamellar liposome mimicking the more complex cell membrane as a model system. The bilayer is enlarged showing the polar headgroups and hydrophobic core. Further, the most abundant phospholipids of bacterial membranes are given.

obtain a more complete picture on both the molecular mechanism(s) of action of membrane-active peptides and the role of the lipids in determining the mode of interaction. Although biophysical studies using model systems have already revealed quite some insight into the molecular mechanisms of action of membrane-active peptides, the specificity towards particular lipid components is not yet totally understood, and the occurrence of binding preferences to certain lipid types cannot be quantitatively related to the peptide specificity toward given cell membranes [29]. Therefore, care has to be taken, when these results are related to the biological activity of these peptides.

1.2. Effects of Antimicrobial Peptides on Lipid Bilayers

Given the rapid emergence of antibiotic-resistant bacterial strains, the development of alternatives to conventional antibiotics has become an imperative [30]. Antimicrobial peptides (or host-defense peptides), effector molecules of the innate immune system, which confer a first-line defense against bacteria, viruses, fungi and even cancer cells promise to be a solution to this problem [30–35]. The main advantage of this class of substances, when considering bacterial resistance, is their mode of action. Whereas conventional antibiotics act rather slowly up to hours *via* interference with protein synthesis, cell-wall formation or DNA replication of bacteria, antimicrobial peptides unfold their effect within minutes, faster than the growth-rate of bacteria, which makes the development of resistance less likely. The mechanisms, by which antimicrobial peptides can kill bacterial cells are diverse and range from direct disruption of the cell membrane *via* pore formation, micellization or other modes of membrane damage to binding to specific lipids or cytoplasmic targets [36,37]. However, independent from the killing mechanism, the peptides have to interact with the cell membrane by either disrupting or transversing this barrier. Antimicrobial peptides distinguish between foreign, e.g., bacterial and host cells based on differences in the composition of the cell membrane. Therefore, it is essential to consider membrane architecture and lipid compositions in order to understand the molecular mechanism and target-cell specificity of these peptides. As outlined before, the outer layer of eukaryotic cell membranes predominantly contains zwitterionic PC, SM and cholesterol, whereas bacterial cell membranes are composed of negatively charged PG and neutral PE. Due to their cationic nature, most antimicrobial peptides preferentially interact with negatively charged membranes; however, lipid molecular shape and global membrane properties play a role, as well. Thus, understanding the parameters of peptide–membrane interaction is crucial for the elucidation of the molecular mechanisms of action. This knowledge, in turn, will allow the design of novel peptide antibiotics killing their target cells by destruction of their phospholipid membrane integrity.

Naturally, the mode of interaction of antimicrobial peptides (AMPs) with membranes is, on the one hand, dependent on the nature of the peptide and, on the other hand, on the membrane lipid composition, a factor that, in the past, has often been overlooked [36]. Two classical models regarding membrane permeation and disruption have originally been proposed: the "carpet" mechanism and formation of transmembrane pores [38,39]. Numerous studies have been aimed at elucidating

the structure of these pores and two different lipid–peptide arrangements were identified: the barrel-stave type, where peptide aggregates form a pore, and the toroidal or wormhole pore, in which the lipid headgroups and antimicrobial peptides together line the inside of the pore. Such a pore structure was first proposed by Matsuzaki [40] based on the observation that magainin 2 induces rapid lipid flip-flop coupled with pore formation and structurally verified by Huang [41] by neutron in-plane scattering. A barrel-stave mechanism of membrane disruption has so far only been suggested for alamethicin [42,43]. Other peptides suggested to act *via* the toroidal pore mechanism are protegrin-1 [44] and melittin [45].

The "carpet" mechanism proposes initial covering of the membrane surface by the peptides in a carpet-like manner without deeply inserting into the hydrophobic core of the bilayer (for a review see [46]). Thereby, the presence of negatively charged lipids supports the formation of a dense peptide alignment, as they reduce the repulsive electrostatic forces between the positively charged peptides. Once a threshold concentration is reached, different mechanisms of membrane damage occur such as membrane permeabilization by defects due to lipid–peptide aggregate formation or a "detergent-like" disruption of membrane integrity. This mechanism does not require any specific structure or sequence of a peptide, but rather seems to depend on an appropriate balance between hydrophobicity and a net positive charge of the peptide. Both carpet mechanism and toroidal pore formation rely on a threshold concentration, where membrane penetration of peptides occur, whereas in the "barrel-stave" model only a few peptide molecules are sufficient to form a pore and thus to be able to punch a hole in the membrane.

Other, less copiously investigated mechanisms that may lead to membrane dysfunction involve the formation of lipid–peptide domains [47,48] or induction of non-lamellar phases [49,50]. In these cases, AMPs induce a lipid reorganization within the plane of the bilayer or a supramolecular rearrangement of the bilayer structure. These structural changes can be detected by a number of biophysical techniques. Thus, in the following section we shall give an overview on the current knowledge on how antimicrobial peptides affect membrane structure. Spectroscopic and thermodynamic methods are helpful to gain respective information, but scattering techniques play a dominant role, when considering structural information on the molecular level of the bilayer. Therefore, the focus will be on how X-ray structure research can contribute to the elucidation of the mechanisms of lipid–peptide interaction.

2. Understanding the Mechanism of Lipid–Peptide Interaction

2.1. Lipid Affinity of Antimicrobial Peptides Triggered by Electrostatic Interactions – Lipid–Peptide Domain Formation

Since the majority of antimicrobial peptides are positively charged, the most straightforward explanation for the selectivity of AMPs for the negatively charged bacterial cell membranes is electrostatic attraction. This aspect has been mostly

investigated using liposomes and monolayers composed of negatively charged PG mimicking bacterial membranes and of zwitterionic PC as mimic for mammalian membranes, respectively [30,51]. For example, synchrotron grazing incidence and X-ray diffraction (GIXD) were used to characterize the thermodynamic and structural properties of mixed DSPC (distearoyl-PC)/PGLa (Peptidyl-glycylleucine-carboxamide) and DSPG (distearoyl-PG)/PGLa monolayers at the air–water interface and to assess the ordering of lipid molecules on an atomic scale [52] suggesting that the peptide was aligned parallel to the interface. Interestingly, X-ray data of DSPC/PGLa were found to be composed of the individual components indicating that the frog skin peptide PGLa does not mix at a molecular level with zwitterionic phospholipids, but rather forms separate islands. On the other hand, the peptide penetrated readily into DSPG monolayers and strongly perturbed the acyl-chain order (Fig. 3). In a subsequent publication, an increase of the bending rigidity of DSPG monolayers was observed in the presence of PGLa, whereas the opposite effect was found for DSPC monolayers [53]. Similarly, GIXD data showed

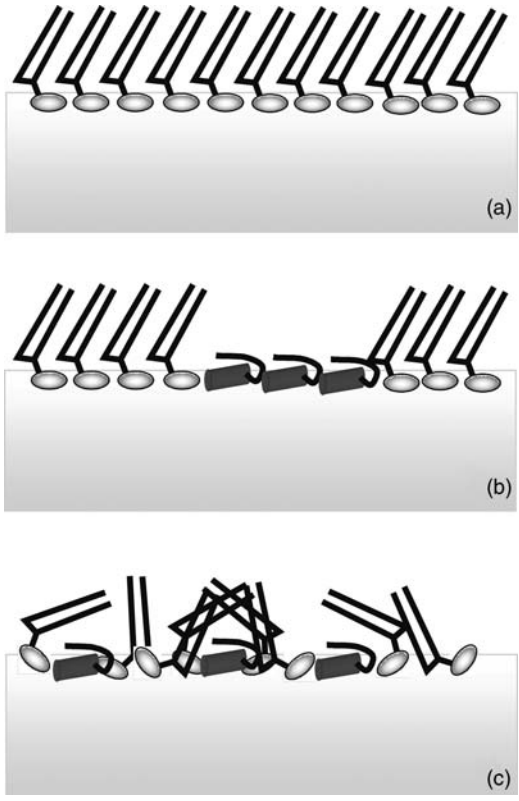

Figure 3 Model of the lipid organization derived from X-ray reflectivity and grazing incidence diffraction for DSPC and DSPG monolayers with and without the antimicrobial peptide, PGLa; pure lipid monolayer (a), DPSC and PGLa showing islands of lipid and peptide molecules (b), respectively and DSPG and PGLa indicating the lipid disorder induced by the molecular interaction between the two components (c).

a disordering of the lipid packing upon protegrin-1 insertion into dipalmitoyl-PG (DPPG) monolayers, less in DPPC and even less in dipalmitoyl-PE (DPPE) [54].

In support of these premises, X-ray diffraction and differential scanning calorimetry studies on liposomal systems indicated that a number of antimicrobial peptides discriminate between negatively charged and zwitterionic model membranes [51]. At a given concentration these peptides strongly affected the phase behavior of PG lipsomes, while PC liposomes remained unaffected. Several of these peptides such as the frog skin peptide, PGLa [47], the human neutrophil peptide, HNP-2 [48] and the cyclic peptide rhesus theta defensin, RTD-1 [55] induced lipid segregation in liposomes composed of negatively charged PG, most likely resulting in peptide-depleted and peptide-rich lipid domains. The latter were characterized by an increase of the chain-melting transition temperature, which suggests that the peptide-enriched lipid domains are characterized by a stabilization of the rigid hydrocarbon chain packing. Indeed, wide-angle X-ray diffraction data revealed a gel-phase packing for these domains at temperatures, where the peptide-depleted lipid domains are already in a melted state [47,55]. Domain formation was also observed in the presence of protegrin-1 from porcine leukocytes, which in contrast to the peptides above leads to a transition to the fluid state below the chain-melting transition of pure PG [56]. Recent work in our laboratory revealed further details of this peptide-stabilized PG domains, which will be briefly addressed in Section 7.

Phase separation is not restricted to PG liposomes, but was also detected in binary mixtures of zwitterionic PE and negatively charged PG, which mimic more closely the cytoplasmic membranes of Gram-positive as well as Gram-negative bacteria. For example, HNP-2 or PGLa were shown to induce lipid segregation in model membranes composed of the binary mixture of DPPE/DPPG, involving a depletion of PG molecules from the lipid mixture and, consequently, the formation of peptide-enriched PG domains (Fig. 4), most likely in consequence of preferential interaction of the peptides with PGs due to electrostatic interactions [47,48,51]. A synthetic antimicrobial peptide consisting of alternating alpha- and beta-amino acid residues, termed alpha-/beta-peptide II, was also shown to have the ability to induce phase segregation of anionic and zwitterionic lipids in PE/PG mixtures

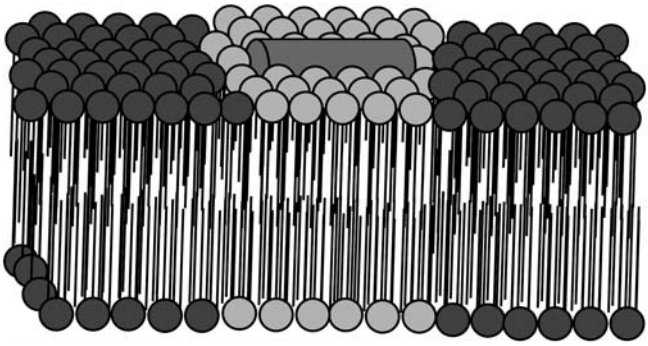

Figure 4 Schematics of peptide-induced phase separation due to preferential interaction between cationic peptides and negatively charged phospholipids resulting in distinct domains.

[57]. Furthermore, a preferential interaction of nisin with PG was also observed in PG/PC mixtures [58]. Such membrane domain formations may have various effects on the membrane integrity. Amongst others, domain formation can result in a different lipid environment of membrane proteins affecting their function, in-line defects leading to increased membrane permeability and in the formation of PE-rich membrane domains, which may destabilize the bilayer owing to its intrinsic property to form highly curved, non-bilayer structures. Both formation of defects and enrichment of PE domains may finally lead to physical membrane disruption.

2.2. Membrane Thinning as a Precursor of Pore Formation

If a peptide has bound to a membrane, the consequences for the lipid bilayer can be diverse. The two extreme situations, with the peptide being oriented either perpendicular or parallel to the membrane surface, are reflected in the pore and the carpet model, respectively. In the latter case, the peptide will position itself in the interface, thereby occupying space in the head-group region of the outer leaflet and consequently leading to voids and disorder in the hydrophobic core. The extent of this perturbation depends, besides the size and topology of the peptide, on a number of parameters such as charge distribution, hydrophobic angle and hydrophobicity [36]. Furthermore, the perturbation in the hydrophobic core caused by a certain peptide also strongly depends on the phospholipid matrix, as demonstrated very recently for the human host-defense peptide LL-37, PGLa as well as melittin [59] and discussed later in this contribution (see Section 7). Upto a certain extent, the lipids will be able to fill these voids by e.g., increased *trans*-gauche isomerization of the hydrocarbon chains and/or by moving the interior leaflet towards the peptides resulting in membrane thinning (Figs 5 and 6). However, above a threshold concentration, the voids seem to become energetically unfavorable and the system minimizes its energy by e.g., formation of pores as put forward by the group of Huang [60]. This group conducted extensive X-ray diffraction and neutron scattering experiments on the influence of lipid–peptide interaction on the thickness of the phospholipid bilayer and determined the critical concentration for insertion in a series of systematic studies. Below this concentration, antimicrobial peptides (magainin 2, protegrin-1 and melittin) are aligned parallel to the bilayer plane (surface state or S state), while above this concentration they are oriented perpendicularly

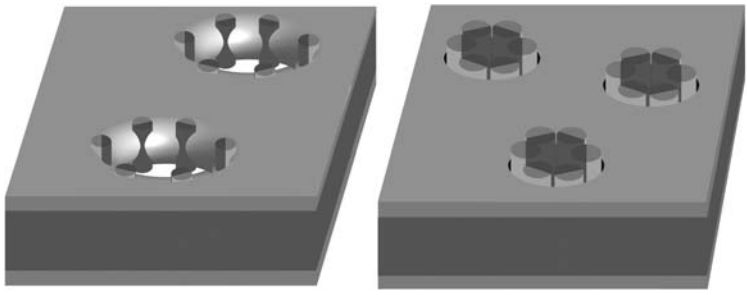

Figure 5 Model of the toroidal (left) and barrel-stave (right) pore; for details see text.

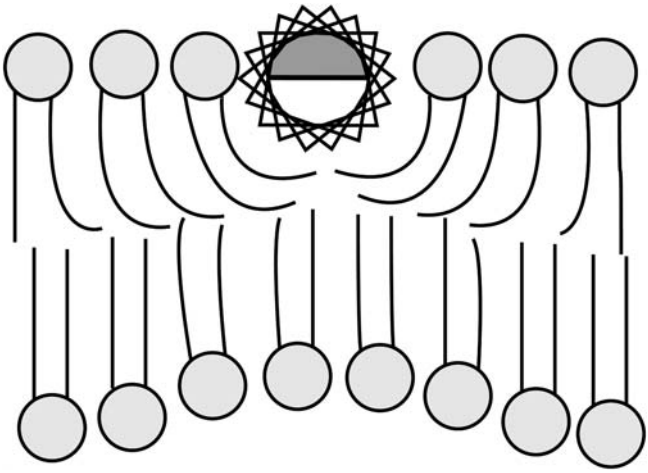

Figure 6 Illustration showing the effect of an amphipatic peptide with a spatial location parallel to the bilayer surface. Neighboring phospholipids will be characterized by increased *trans-gauche* isomerization of the hydrocarbon chains to fill the void in the hydrophobic core resulting in membrane thinning.

(inserted state or I state) [61–65]. The transition from the S state to the I state has a sigmoidal peptide-concentration dependence indicating cooperativity in the peptide–membrane interactions. Data gained on this transition of alamethicin measured in three bilayer conditions were explained by a free energy that took into account the membrane-thinning effect induced by the peptides. This model was extended to melittin that was shown to form toroidal pores, instead of barrel-stave pores as in the case of alamethicin, demonstrating that the membrane thinning effect is a plausible mechanism for the peptide-induced pore formations [66].

The thinning of the bilayer observed is in the range of 2–3 Å and is an average value over local dimple deformation [60]. However, an atomic force microscopy study on the effect of MSI-78, a derivative of magainin, on DMPC bilayers revealed that the bilayer thickness was not reduced uniformly over the entire bilayer area [67]. Instead, upon binding of the peptide distinct domains were formed, where the bilayer thickness was reduced by about 11 Å. Increasing the peptide concentration resulted in a growth of these domains without affecting the reduction of thickness and the parallel orientation of this α-helical peptide to the membrane.

X-ray studies also yielded structural information on the channel forming peptide Gramicidin D. This peptide is known to form well-defined dimeric channels in lipid bilayers [68]. Gramicidin D apparently stretches DLPC bilayers and thins DMPC bilayers toward a common thickness of 32.4 ± 0.3 Å owing to hydrophobic mismatch between the peptide and the hydrophobic core of the individual bilayer [69,70]. However, further studies with the α-helical synthetic WALP peptides, which consist of a hydrophobic sequence of leucine and alanine of varying lengths bordered at both ends by tryptophan as membrane anchors, did not reveal a bilayer thickness adjustment as observed in the presence of Gramicidin D [71]. Since the energy cost of hydrophobic mismatch is greater than the energy cost of membrane

deformation [70], this result is intriguing. The authors suggest that this energy argument is not applicable for single helix since the way the lipids pack around it differs greatly from larger proteins like Gramicidin.

2.3. Detergent-Like Effect – Micellar Lipid–Peptide Disk Formation

Another mechanism by which antimicrobial peptides can destroy their target membrane involves micellization *via* a detergent-like mode of action [37]. The character of particularly linear amphipathic α-helical peptides and their interactions with membranes show analogies to detergent molecules. For example, melittin with its overall amphipathic character composed of a cluster of cationic amino acids at the C-terminus and a stretch of hydrophobic amino acids, resembles the features of many detergents being characterized by a polar/charged head group and a hydrophobic moiety. Melittin was found to exhibit pronounced effects on the phase behavior of DPPC already at very low peptide concentrations (lipid-to-peptide molar ratio of 1000/1) [72,73]. A similar concentration-dependent behavior was reported for the detergent cetyltrimethylammonium chloride [74]. However, at high melittin concentrations (lipid-to-peptide molar ratio of 15/1), disk-shaped particles were found for the DMPC/melittin mixture [75,76], suggesting a detergent-like solubilization of the membrane under these experimental conditions. The idea of gradual membrane disintegration is also supported by data gained from staphylococcal δ-lysin/DMPC multilamellar vesicles [77,78]. Modeling of X-ray data further suggested that the disk-like micelles were surrounded by a ring of peptide of about 1 nm thickness as sketched in Fig. 7 [78]. There has been some debate about the peptide arrangement that surrounds the hydrophobic core, i.e., if the helix axes of the peptide is located normal or parallel to the bilayer plane of the disk-micelle. Evidence for a location parallel to the disk-plane was shown in case of discoidal micelles formed by apolipoproteins [79]. However, as the peptide

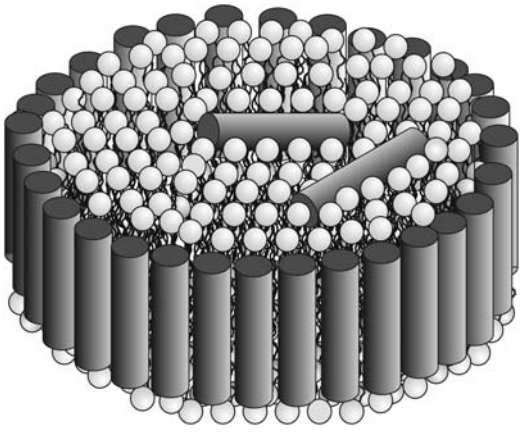

Figure 7 Drawing of a disk-like lipid micelle with the helical peptide surrounding the disk preventing exposure of the hydrophobic core of the lipid micelle. Note that the peptide could be also arranged parallel to the disk surface.

orientation cannot be determined by X-ray, small-angle neutron scattering experiments with deuterated peptide would be necessary to clarify this point.

2.4. Promotion or Prevention of Non-Lamellar Phases

As mentioned above, PE is a major component of bacterial cell membranes. Although PE like PC is zwitterionic, they feature very different molecule geometries. PC is shaped cylindrically, whereas PE is characterized by a truncated cone shape owing to its small head group as compared to the cross-section of its hydrocarbon chains [80,81]. Therefore, PE possesses a large spontaneous curvature making the lipid prone to the formation of non-lamellar structures [82]. The balance between lamellar and non-lamellar phase promoting lipids is thought to be essential for many membrane-associated processes such as function of membrane proteins and membrane fusion [83–85]. Incorporation of small molecules like antimicrobial peptides, which are able to shift this balance to one direction or the other, is therefore bound to have a large impact on membrane function and integrity [36]. Peptides that impose a negative curvature stress on the bilayer can potentiate the intrinsic negative curvature of these bilayers leading to the formation of non-lamellar lipid structures, however, peptides having the contrary effect, i.e., stabilizing the PE bilayer by intercalation into the interfacial region, are also described in the literature [86].

As outlined in Section 1.1, microorganisms such as *E. coli* or *A. laidlawii* have been shown to precisely regulate the amounts of non-lamellar phase preferring lipids such as PE, DPG or monogalactosyl-diglyceride in a narrow window close to a lamellar to non-lamellar phase boundary [7,87,88]. AMPs interfere with the packing constraints arising from the coexistence of lamellar and non-lamellar phase forming lipids and may lower the lamellar to non-lamellar phase boundary leading to membrane rupture. In this regard, X-ray diffraction is a highly convenient technique to detect the presence of non-lamellar phases, with the apparent advantage over e.g., ^{31}P-NMR that the supramolecular structure of the lipid aggregates can be analyzed in all structural details [89].

The cyclic peptide Gramicidin S from *B. brevis*, for example, was shown to disrupt liposomes composed of lipid extracts from *E. coli* and *A. laidlawii* by decreasing the energetic barriers against the formation of cubic phases by promoting negative curvature (Fig. 8) [49].

AMPs were also shown to promote the formation of non-lamellar lipid structures in pure PE model systems. Alamethicin induces a cubic phase, when incorporated in small amounts in dielaidoyl PE [90] and an inverse hexagonal phase in dioleoyl PE liposomes [91]. It was suggested that alamethicin induces such lipid structures by changing the thickness and/or flexibility of the lipid bilayer. In diphytanoyl PC model membranes alamethicin causes membrane thinning with a concomitant increase in chain disorder over a large area [62,92]. Therefore, it was proposed that the decrease in membrane thickness is compensated by an increase of the hydrophobic cross-sectional area of the lipid acyl chains, which in case of PE would further enhance the existing mismatch between the cross-sectional areas of the head group and hydrocarbon chains. This could be a promotive force for the lipid monolayer to curl.

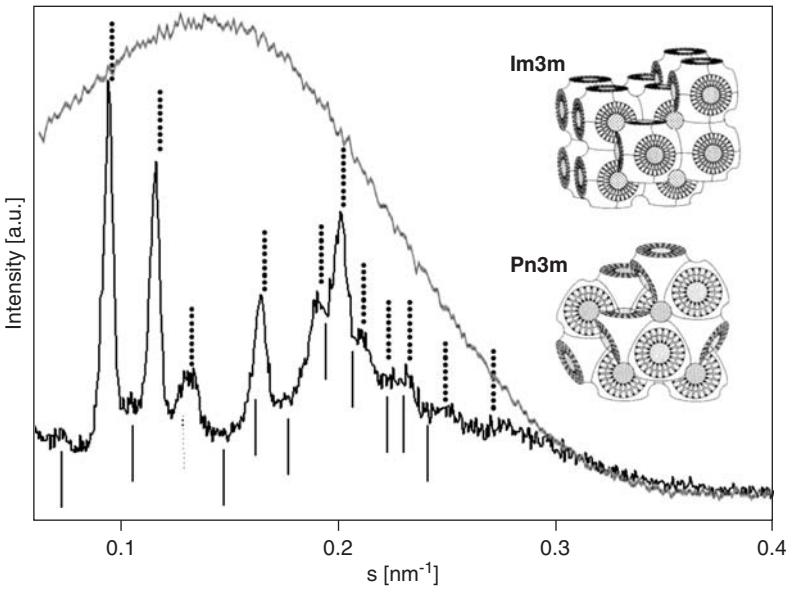

Figure 8 Small-angle X-ray diffractogram of *E. coli* membrane total lipid extract (gray line) showing the typical scattering of uncorrelated bilayers and in the presence of (4 mol%) Gramicidin S (black line) recorded at 25°C. Position of hkl-reflections corresponding to a cubic phase of space group Pn3m (dotted) and Im3m (solid), respectively, are indicated in the diffractogram.

Promotion of an inverse hexagonal phase was observed for nisin in dioleoyl- and palmitoyloleoyl-PE, respectively [50]. The formation of this non-bilayer structure can be explained in analogy to hydrophobic molecules such as squalene that also strongly decrease the phase boundary between fluid lamellar and inverse hexagonal phase [93]. Thus, the insertion of the large hydrophobic section of nisin (segments 1–19) will lead to an increase of the hydrophobic volume in the bilayer interior and in turn promote negative curvature. The role of insertion of a large hydrophobic volume into the bilayer can also be deduced from the synthetic cecropin B analog CB3, which in contrast to the natural cecropin B was composed of two hydrophobic α-helices [94]. Whereas for cecropin B pore formation was proposed, CB3 induced rapid formation of irregularly shaped, non-lamellar structures.

Examples of peptides inducing positive curvature strain in a membrane thereby inhibiting the formation of non-lamellar phases include e.g., δ-lysin [51], LL-37 [95] and magainin [96].

3. General Aspects of Model Membranes

3.1. Global and Local Membrane Properties

Having outlined the need for studying mimetics of biological membranes in the introductory section, it appears obvious to look for novel ways to attain a better and

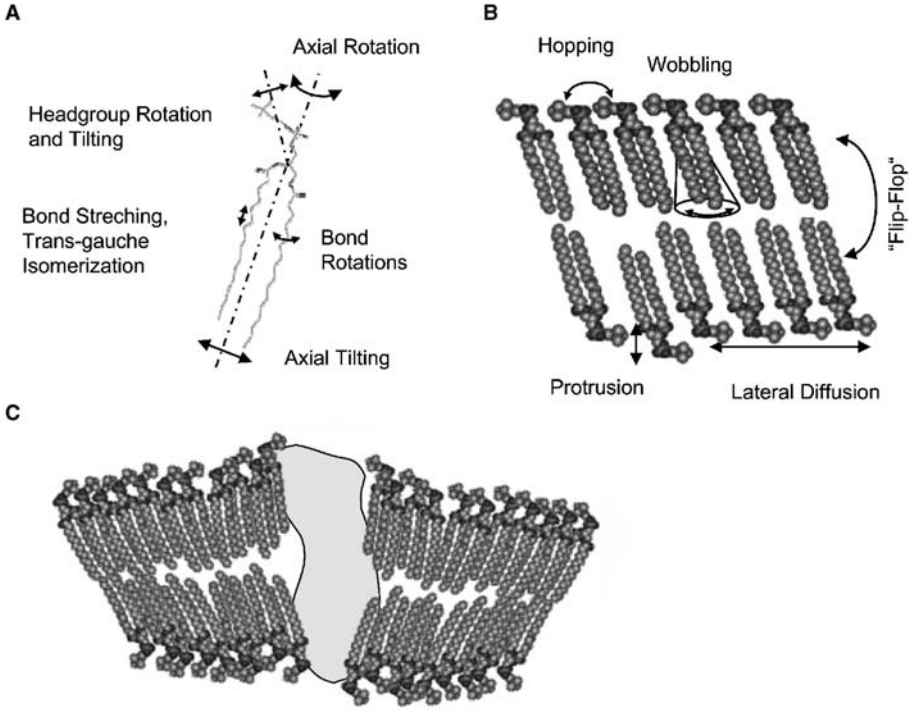

Figure 9 Schematic examples of local bilayer properties including several modes of vibrations and rotations within a single lipid molecule (A), single molecular motions (B) and local membrane perturbation by the inclusion of a membrane protein (C).

characterization of the systems throughout. In doing so, it is important to realize the different time and length scales involved in the problem. With respect to length scales, membrane properties may be divided into local and global features, which are, however, intimately coupled to each other [97,98]. Local membrane properties would be, for example, different modes of molecular motions and vibrations, diffusion, chain tilt, but also any disorder in the vicinity of defects (Fig. 9).

In turn, global membrane properties are the overall bilayer structure, bilayer interactions, elasticity, global curvature, chain packing, to name but a few (Fig. 10). This general distinction between global and local membrane properties is clearly artificial and is due to experimental techniques that address either the one or the other aspect.

Spectroscopic techniques and all-atom molecular dynamics (MD) simulations are traditionally applied to study membrane properties on the local scale. Important distinctions between the different spectroscopic techniques come from the different timescales involved that range from fast bond vibration modes with correlation times on the order of 10^{-14} s to transbilayer diffusion of lipids ("flip-flop"), which may take up to several days. Fourier transform infrared (FTIR) and Raman spectroscopy are the techniques of choice to study the vibrational bands exhibiting

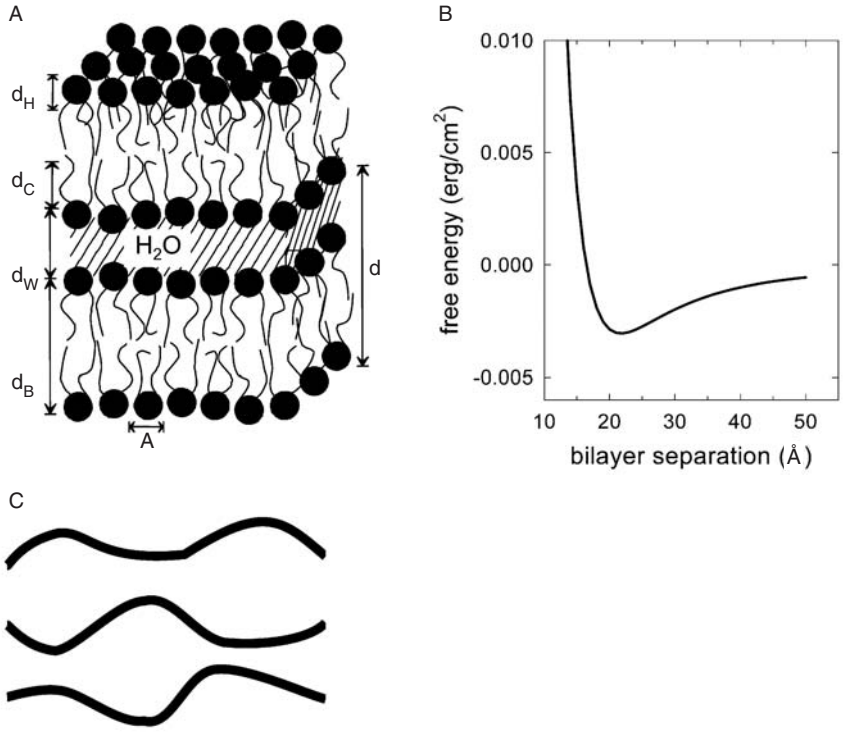

Figure 10 Schematic of some global membrane properties like, the overall structure with the lamellar repeat distance d, membrane thickness d_B, bilayer separation d_W, hydrocarbon chain length d_C, head group thickness d_H and lateral area per lipid molecule (A). Panel B shows a bilayer interaction potential and panel C collective bending fluctuations.

the fastest dynamics, whereas magnetic resonance methods such as electron paramagnetic resonance (EPR) and nuclear magnetic resonance (NMR) cover the "slower" motions, such as, molecular wobbling or axial rotations. Here, EPR is sensitive to faster molecular motions than NMR. On the other hand, EPR requires the incorporation of nitroxide spin-labels in the membrane, whose concentration needs to be kept low in order to avoid effects on the bilayer structure. Of recent interest are also dynamic scattering techniques such as coherent inelastic X-ray and neutron scattering [99–101], neutron backscattering [102] and X-ray photon correlation spectroscopy [103].

Global membrane properties, such as the overall structure can be determined applying elastic X-ray or neutron scattering [104–106], but also H^2NMR spectra can yield information on the hydrocarbon chain length of the lipid bilayer [107]. Bilayer interactions can be measured by the surface force apparatus, atomic force microscopy, pipette aspiration or the osmotic stress method [108,109]. Also bilayer elasticity can be studied by a range of techniques including micropipette aspiration [110], mode-analysis of bending fluctuations [111] and electric-field-induced deformations on large unilamellar vesicles [112], but also others such as, e.g., optical

dynamometry [113], optical force measurements [114] or line-shape analysis of Bragg peaks [115–118] have been applied. Depending on the applied experimental technique, the reported bending rigidity K_C values show some scatter, but are usually in the range of 10^{-20} J-10^{-19} J for phospholipid bilayers.

3.2. Domains-Rafts

Biological membranes are compounds of several lipid components (and proteins, sugars, etc.). Thus, often binary or ternary mixtures of synthetic lipids are studied in order to address the complex lipid composition in natural membranes. The mixtures then have to accommodate the properties of the individual components, which may lead to a demixing or formation of lipid domains. In turn, a demixing of lipid components may also be induced by interactions with membrane active compounds, such as, peptides [36,119]. Lipid domains have been observed in model systems already some time ago [120–123]. However, due their possible implication in several cellular functions in natural membranes, such as endocytosis, protein trafficking and signal transduction [124,125], domains or better "rafts" as they are called these days have recently seen a tremendous increase of research interest. Again it is important to realize the different time and length scales. Domain formation may occur as a dynamic process at short-time and small-length scales, respectively. In this case, the formed domains are small in size and not stable but constantly create and dissipate and are often referred to as micro-domains (Fig. 11A).

On the other hand, lipid molecules may also segregate and form large areas composed of single lipids that are stable over longer timescales. This type of domains is often referred to as macroscopic domains. It is, however, important to note that in the thermodynamic limit only the latter case of domain formation may be called a phase separation. A lack of this strict distinction has led to severe controversies in literature with the most prominent example being binary mixtures of phospholipids with cholesterol. Early phase diagrams [126], based on NMR data [127], show the existence of a miscibility gap within the fluid phase of phospholipid/cholesterol mixtures. This fluid–fluid phase separation has been supported by several further experimental studies such as, [128–131]. Although McMullen and McElhaney [130] criticized using the terminology of phase diagram in the context of lipid/cholesterol binary mixtures, their differential scanning calorimetry (DSC) data clearly showed the co-existence of two phases in a certain composition range, which can be interpreted according to [126] as the L_d (liquid-disordered) and L_o (liquid-ordered) phases, where the latter phase is induced at high cholesterol concentrations due to its rigid character. In contrast, groups using other techniques, such as X-ray diffraction [132] or more recently fluorescent microscopy [133] found no direct evidences for phase-coexistence in such binary mixtures. Only stable and large domains within the fluid phase have been reported in ternary mixtures of lipids with cholesterol, using similar techniques [133–135].

While these more recent results will most likely lead to a revision of the original phase diagrams of binary cholesterol/lipid mixtures, there is another general lesson to learn from this example. Global techniques, such as, X-ray (or neutron) diffraction, or fluorescence microscopy average over a large period in time and hence are

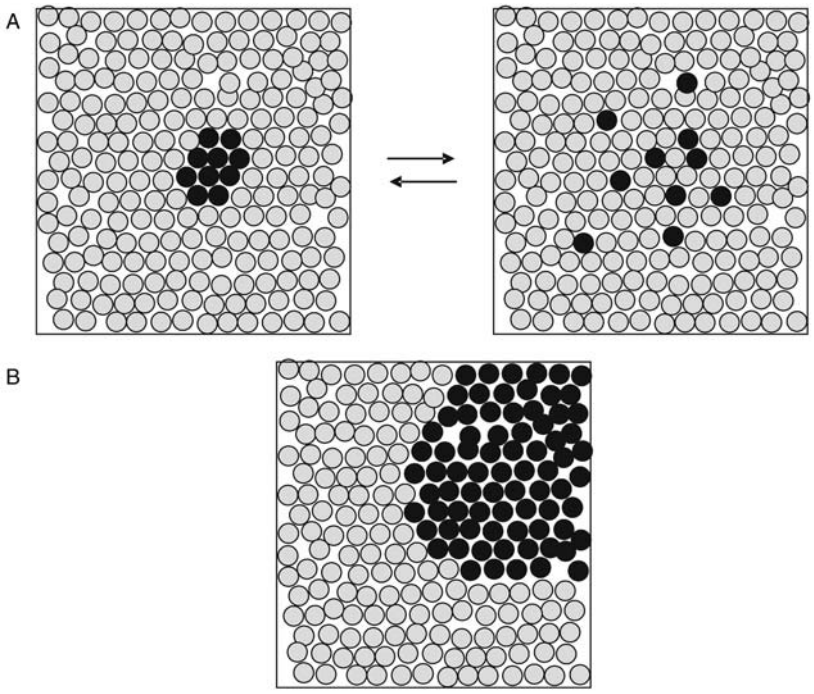

Figure 11 Schematic of microscopic (A) and macroscopic domains (B), where each circle represents a single lipid molecule. Microscopic domains involve only a few lipid molecules and are highly unstable. Macroscopic domains in contrast exhibit sizes upto microns and are stable over an extended time period.

unable to detect the signal from unstable microscopic domains. On the other hand, spectroscopic techniques may also observe density fluctuations from the creation and dissipation of such "nuclei" and DSC seems to be able to detect both. Rather than thinking in advantages and disadvantages of the individual techniques it is more important to realize that only through the application of more than one technique, questions related to domain formation can be addressed adequately, i.e., a technique sensitive to a long timescale should be combined with a technique sensitive to short timescales. In the case of lipid–peptide interactions, the combination of small- and wide-angle X-ray scattering (SWAXS) and DSC has been proven to be particularly useful as described in the previous section.

4. X-ray Diffraction in Combination with a Global Data Analysis

Several recent reviews have dealt with the determination of structural parameters from lipid bilayer systems using SAXS [98,136,137]. We will therefore restrict ourselves here only to the essentials and refer for more details to the above-listed articles.

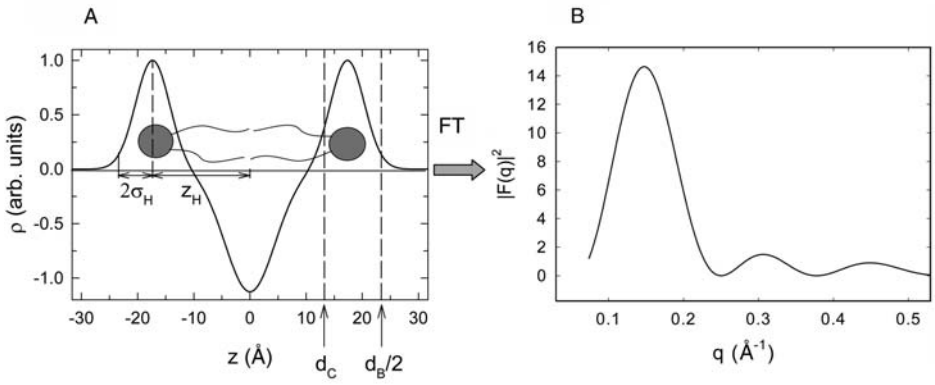

Figure 12 Electron density profile of lipid bilayers across the membrane (panel A) and the absolute square of its Fourier transform given by the form factor (panel B). z_H is the position of the lipid headgroup and σ_H its width. Panel A further shows definitions for the membrane thickness d_B and the hydrocarbon chain thickness d_C.

X-rays are known to interact with the electron cloud of atoms and scatter in the elastic case without loosing or taking up energy from the atoms. The contrast in X-ray scattering experiments comes from the number of electrons per volume (= electron density) and its modulation across the sample. Thus, the real space information that is obtained from scattering experiments is obtained by calculating the electron density from the scattering data. In the case of lamellar lipid phases, the electron density varies only across the lipid bilayer. The corresponding electron density profile can be modeled to sufficient accuracy by the summation of three Gaussian distributions [138–140], two centered at the position of the electron-dense lipid head groups and one of negative amplitude in the middle of the bilayer, where the hydrocarbon chains meet (Fig. 12A).

In order to compare with experimental data, one needs to Fourier transform the electron density profile, which can be calculated analytically. The thereby derived function is called the form factor $F(q)$, which varies as a function of the modulus of the scattering vector q, which is related to the X-ray photon wavelength λ and the scattering angle θ by $q = 4\pi \sin(q)/\lambda$. Figure 12B shows the absolute square of the form factor, which corresponds to the intensity recorded in a diffraction experiment.

Frequently, lipid bilayers self-assemble into a stack of several bilayers. In this case, positional correlations between the bilayers leading to the observation of Bragg peaks in scattering patterns need to be considered. The shape of the peaks is affected due to the significant disorder present in the lipid multibilayers. This is accounted for by two theoretical descriptions. The paracrystalline theory [141,142] takes into account a Gaussian distribution of distances between idealized solid layers, which additionally display some thermal fluctuations (Fig. 13B). This leads in comparison to thermal fluctuations of the layers around regularly distributed distances (Fig. 13A) to an increase of the Bragg peak width with diffraction order. The decrease of peak intensity is also observed in the case of simple thermal fluctuations.

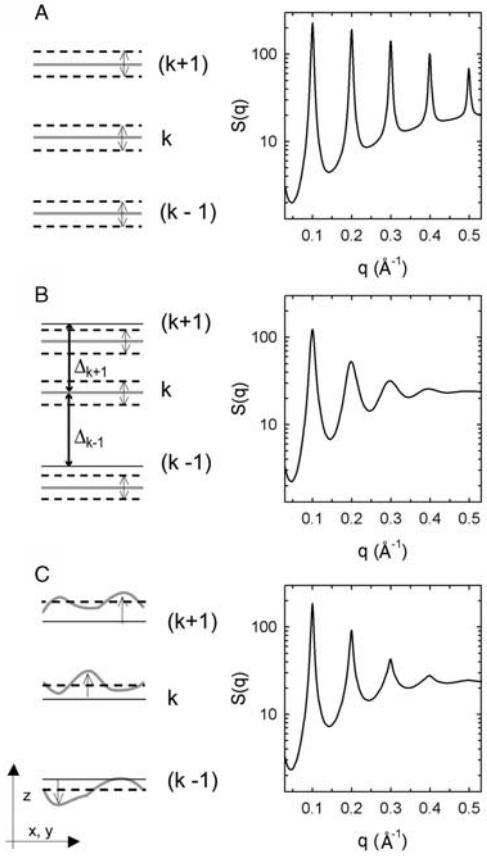

Figure 13 Disorder in lamellar stacking and its consequences on the Bragg peaks. (A) Thermal disorder, (B) paracrystalline theory and (C) Caillé theory.

The second theory, named after Caillé [143,144], considers the flexibility of the bilayers yielding bending fluctuations. This translates into cusp-like diffraction peaks (Fig. 13C), which also broaden with increasing diffraction order. It has been shown experimentally that the Caillé theory accounts for the shape of Bragg peaks of multilamellar vesicles in the fluid L_α phase [145]. In turn, bilayer elasticity decreases by about one order of magnitude upon transforming lipid bilayers into the gel phase. Thus, in the lamellar gel phase the bilayer can be considered as solid, and the paracrystalline theory should apply. Nevertheless, there seem to be some inconsistencies in fitting higher order Bragg peaks [98], which may be due to the simplifying assumption of a Gaussian distribution of bilayer separations. Nevertheless, we have been successful in applying this theory in several cases as will be detailed below.

In X-ray scattering experiments on a liposomal dispersion, one records the scattered intensity as a function of wave vector q. For lipid–peptide interaction it is preferable to work under physiological relevant conditions, i.e., at full hydration and adjusting pH and ionic strength of the buffer solution. In this case, SAXS

patterns of even multilamellar vesicles (MLVs) frequently display only two to three solid orders of diffraction. Then Fourier reconstruction techniques that rely on the observation of many Bragg peaks turn out to be unreliable. It becomes often even worse, when the system self-assembles into oligolamellar vesicles (OLVs) containing only a few layers. This results in only very weak signatures of Bragg peaks. The third case is the formation of unilamellar vesicles (ULVs) or more generally positionally uncorrelated bilayers, for which scattering patterns display no Bragg peaks at all but only a diffuse modulation due to the form factor (Fig. 14).

All three lamellar aggregation forms are observed frequently and the system may transform from one into the other by changes in temperature, pH and ionic strength or upon interacting with membrane active compounds such as peptides. It is therefore a prerequisite to have an analysis technique at hand, which is capable to retrieve structural parameters for all three scenarios. The global analysis technique put forward by our lab [98,138–140] is to date the only existing method that is capable of doing so using one and the same set of parameters to describe the electron density profile. This latter aspect is of particular importance in order to be able to compare the retrieved structural parameters among each other. Figure 14 demonstrates this capability of the analysis technique. Additional examples will be given further below.

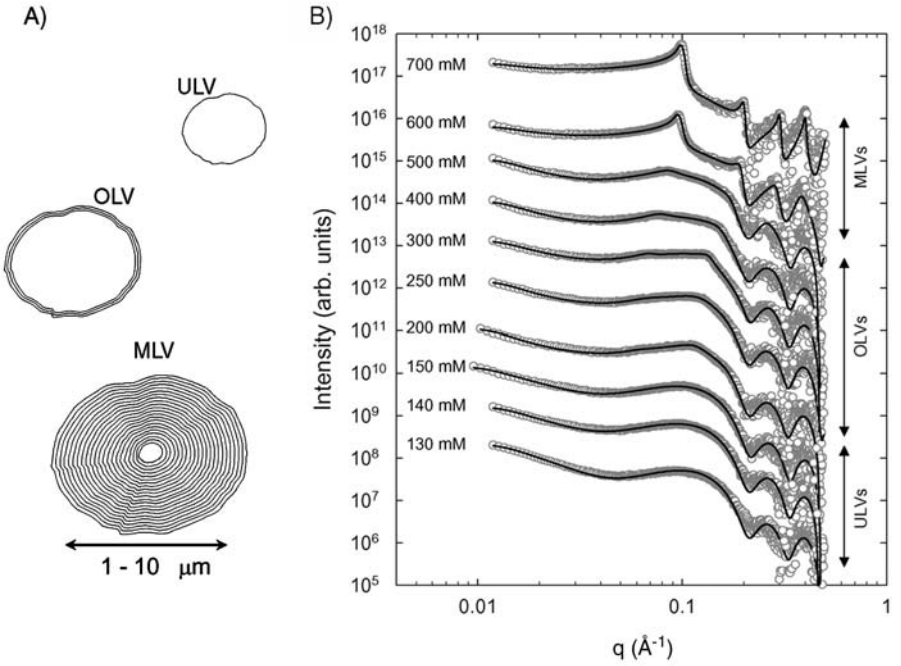

Figure 14 Different lamellar aggregation forms (panel A) lead to distinct scattering patterns (panel B). The scattering data shown corresponds to negatively charged DPPG bilayers at pH 7.4, 20 mM Na-phosphate buffer, containing various amounts of NaCl (concentrations are given in the scattering patterns). The solid lines correspond to fits to the experimental data using the global analysis technique.

5. Bacterial Model Membranes

As outlined in more detail in Section 1, membrane composition can be very diverse, differing not only between species, but also in different membranes in one single cell. Some insight into the nature and function of biological membranes can be gained by studying synthetic bilayers consisting of a single type of phospholipid or mixtures of two or three phospholipids. Such systems are sufficiently simple to permit a systematic analysis of their properties, yet complex enough to retain certain essential properties associated with the biological systems. PCs, SMs and cholesterol are often used to model eukaryotic cell membranes, whereas PGs, PEs and cardiolipin and mixtures of these lipids have been used to mimic cytoplasmic bacterial membranes [30]. The structural and thermodynamic characterization of the model system used is a prerequisite for the understanding of lipid–peptide interaction.

Mixtures of PE and PG lipids are in a first approximation model of bacterial membranes, where systems rich in PE rather mimic the inner membrane of Gram-negative bacteria and PG-rich systems the cytoplasmic membrane of Gram-positive bacteria. Both lipids differ distinctly in their properties, which are briefly summarized below. PEs are zwitterionic and therefore self-assemble in the presence of an aqueous solution into MLVs and are able to form intermolecular hydrogen bonds. Further, due to their molecular shape in the form of a truncated cone, PEs prefer negative surface curvatures, which leads to the formation of non-lamellar structures such as inverted hexagonal and bicontinuous cubic phases at temperatures above the lamellar fluid phase [146]. In turn, the headgroup of PGs bear a single dissociable proton with an apparent pK of ~3 [147,148]. Hence, PGs are neutral at low pH and completely negatively charged for pH >5. At low pH, PGs behave similar to PEs, which is expressed in the thermotropic behavior [149,150] and hydrocarbon chain packing, as observed by X-ray diffraction [150,151]. At high pH, the hydrocarbon chains of disaturated PGs in the lamellar gel phase are tilted with respect to the bilayer normal [151] analogously to PCs, while the hydrocarbon chains of PEs are oriented normal to the bilayer plane [137]. Moreover, their thermotropic properties at neutral pH seem to resemble closely that of PCs [150,152], although some recent results form our lab show an additional transition in PGs, which is most likely due to a change of the head group tilt [153]. Further, the properties of PGs at high pH depend strongly on the electrolyte concentration and composition of the aqueous phase. This is due to the negative charge of the lipid, which is more or less screened by the presence of counter ions. For example, PGs form an intermediate phase that is rich in weakly correlated defect lines (pores) between the lamellar gel and lamellar fluid phase in the absence of salt [154].

Mixtures of PE and PGs have to accommodate the different properties of the individual lipids. It is not surprising that PEs and PGs show almost ideal mixing properties at low pH [149], due to the above mentioned similarities of PGs with PEs in this case. At high pH, however, the different properties come into play, which lead to non-ideal mixing behavior that is largely independent of hydrocarbon chain length and degree of saturation [149,155,156]. Figure 15 shows the phase

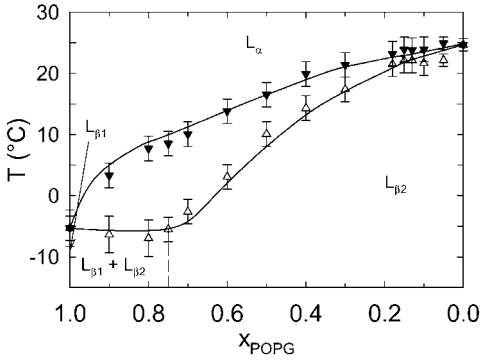

Figure 15 Phase diagram for POPG/POPE mixtures as determined from the heat capacity functions and X-ray diffraction. The coexistence lines (solidus and liquidus curves) are calculated using the four-parameter model for non-ideal, non-symmetric mixing. (△)'s correspond to the experimental T_{on} and (▼)'s to the T_{off} of the main phase transitions. The system displays fluid L_α and L_β phases. The hydrocarbon chain packing at high PG content differs from that at low PG concentrations and we therefore differentiate between the $L_{\beta 1}$ and $L_{\beta 2}$ phases. These two phases are found to coexist at low PE content (regime marked by dashed line). Figure taken from ref. [156].

diagram of POPG/POPE mixtures, which has been determined from a combination of DSC and X-ray scattering data [156].

In brief, the phase diagram is obtained as follows (for detailed description see recent review by Garidel [157]): Onset and offset temperatures T_{on} and T_{off} have been determined from the DSC thermograms using the tangent method. The solidus and liquidus lines are then simulated based on regular solution theory using non-ideality parameters for describing deviations from ideal mixing behavior. Positive non-ideality parameters reflect immiscibility between the lipids, resulting in a lateral phase separation and domain formation of lipids of the same type and in the same phase, whereas negative values reflect a tendency to ordered "chessboard" type mixing of the two lipids in the membrane plane. Finally, the phases are assigned using the signatures of hydrocarbon chain packing observed in the wide-angle regime of X-ray diffraction patterns (see, e.g., [155,156]).

Besides a complex mixing behavior, PE/PG mixtures exhibit also unusual behavior regarding bilayer interactions. This is the domain of SAXS and hence well-suited for the above-described global data analysis model. At high PG content OLVs are formed, while the system displays MLVs at high PE concentration. Thus, the PE/PG mixtures exhibit all possible lamellar aggregation forms discussed in Fig. 15.

Of particular interest is the regime of OLVs. Here, bilayers are positionally correlated in the gel phase and become positionally uncorrelated above the T_m [158]. Experimentally, this is observed by a change of SAXS patterns displaying Bragg peaks at low temperature to patterns that exhibit pure diffuse scattering (Fig. 16A). The global analysis model is able to fit both diffraction patterns, and yields valuable structural information. The loss of positional correlations has been termed a thermal unbinding and has been predicted by theory 20 years ago [159].

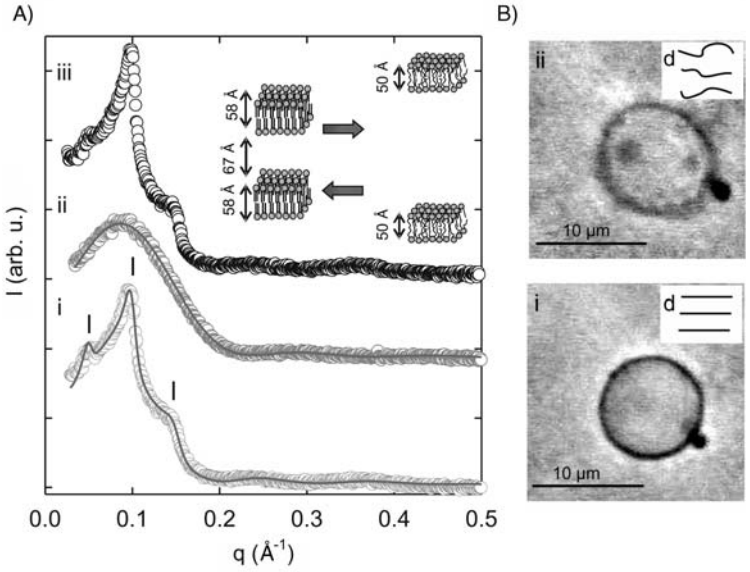

Figure 16 Thermal unbinding of a 87/13 (mol/mol) mixture of POPE/POPG (20 mM Na-phosphate buffer, 130 mM NaCl, pH 7.4) upon heating through the main phase transition $T_m = 23.4^\circ$C. Panel A shows the SAX diffraction patterns, which exhibit Bragg peaks (indicated by dashes) in the gel phases (i, iii) due to positional correlations (bound state). Upon entering the fluid phase the system looses these correlations and exhibits pure diffuse scattering (ii) (unbound state). The system returns to its bound state upon cooling back below the T_m (iii). The inset gives some structural details obtained upon application of the global data analysis (solid line shows corresponding fits). Panel B shows optical microscopy images obtained in phase contrast mode below (i) and above (ii) the T_m. Below the T_m the vesicle exhibits a sharp borderline, which becomes fuzzy upon entering the L_α phase due to the loss of positional correlations. (Data taken from refs. [156,158]).

Interestingly, the system returns into its bound state after cooling back to the initial temperature. The unbinding is caused by the drop of the bending rigidity across the main phase transition [113,114] leading to a significant increase of bilayer undulations. Thereby, the increase of steric repulsion [160] is sufficient to transfer the system from a weakly bound state into an unbound state [158]. Optical microscopy further shows that the OLVs remain intact and do not form ULVs (Fig. 16B).

6. The Antimicrobial Peptide LF11 – Influence of N-Acylation

This section is intended to demonstrate the effects of peptides on the global properties of model membranes. It should be noted though that contributions of the peptides to the electron density profile at the applied peptide concentrations of

$\leqslant$4 mol% are negligible. Hence, X-ray diffraction is – in the studied cases – sensitive only to changes of the overall structural properties. This way bilayers are used as "sensors" to global changes imposed by the peptides. As an example, we choose our recent study on the influence of LF11 and its N-lauryl-derivative C12LF11 on DPPG and DPPC bilayers [161]. DPPG may be regarded as a simple model system for bacterial membranes and DPPC as mimetics for mammalian plasma membranes.

The naturally occurring antimicrobial peptide lactoferricin (LFcin) [162,163] is a pepsin cleavage fragment from lactoferrin (LF), a multifunctional iron-binding glycoprotein originally discovered in bovine milk [164] and later in exocrine secretions of mammals as well as in granules and neutrophiles during inflammatory responses [165,166]. LFcin inhibits growth of a diverse range of microorganisms like Gram-negative bacteria, Gram-positive bacteria and yeast filamentous fungi, including some antibiotic-resistant pathogens and is supposed to kill the target organisms by membrane permeabilization and at the same time suppresses the activation of innate immunity by microbial components such as lipopolysaccharides [167]. LF derivatives have been constructed to gain insight into its mode of antibacterial action [163,168]. One of the strategies to improve antimicrobial activity may be the attachment of a hydrophobic chain in order to compensate for the lack of hydrophobicity [169,170]. However, such strategy usually leads to a higher toxicity toward eukaryotic cells that can result in loss of target cell selectivity [36]. We have, therefore, studied the effect of both LF11s, an 11-residue fragment of human LFcin, and its N-lauryl-derivative, C12LF11, on membrane mimetic systems in order to gain information on the role of hydrophobic attachment for membrane selectivity.

From DSC experiments, we found that the "usual" phase sequence of $L_{\beta'} \rightarrow P_{\beta'} \rightarrow L_{\alpha}$ observed both for PCs and PGs [152,171] is mainly affected by C12LF11, with a decrease of the T_m by 0.7°C, a reduction of the transition enthalpy by about 25% and an abolishment of the pretransition (Fig. 17). LF11 in turn had little effect on the thermotropic behavior of the two lipids and only reduced the pretransition enthalpy of DPPG considerably by about 85%.

In agreement with these results, a global analysis of the small-angle X-ray diffraction patterns shows no significant effects of LF11 on the membrane thickness and bilayer interaction in the case of DPPC, which is also evident from the literally unaffected packing of the hydrocarbon chains (Fig. 18). Small, but significant effects are observed in the case of DPPG. On the other hand, C12LF11 causes strong swelling in DPPC and leads to the formation of positionally uncorrelated bilayers in the case of DPPG, which coincide with a small increase of the membrane thickness [161]. Hence, N-acylation of LF11 allows the peptide to insert readily into charged and non-charged bilayers, whereas "pure" LF11 affects only charged bilayers in a very modest way.

Interestingly, these results correlate well with *in vitro* tests on *S. aureus*, *E. coli*, *P. aeruginos*a and human red blood cells [161]. LF11 was found to exhibit minor antimicrobial activity and no hemolytic activity. C12LF11, on the contrary showed increased antimicrobial activity, but was also lethal to red blood cells. This clearly demonstrates the need for an optimum balance between electrostatic and hydrophobic peptide properties in order to tweak antimicrobial activity. The first characteristic evidently is needed for getting adsorbed to the membrane surface, while

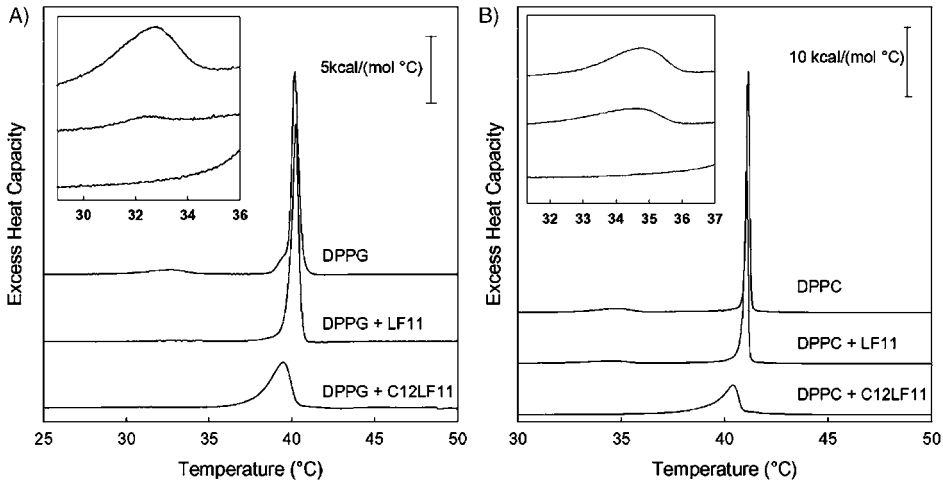

Figure 17 DSC thermograms of DPPG (panel A) and DPPC (panel B) in the presence and absence of LF11 or C12LF11. Insets show an enlargement of the pretransition regime. Pure DPPG exhibits under present conditions (20 mM Na-phosphate buffer 130 mM NaCl pH 7.4) a pretransition at 32.8°C and pure DPPC at 34.8°C. The main transition occurs in the absence of a peptide at 40.2°C for DPPG and 41.1°C for DPPC, respectively. (Data taken from ref. [161]).

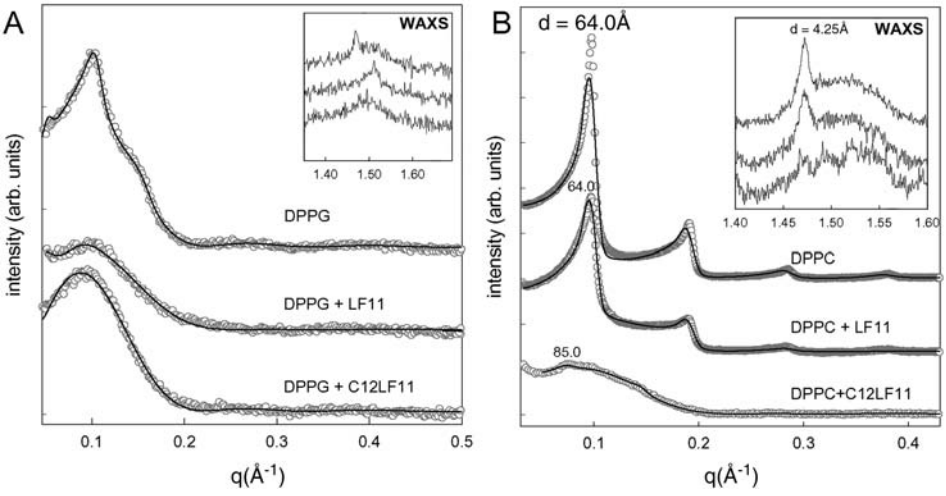

Figure 18 Small- and wide-angle X-ray scattering patterns of DPPG (panel A) and DPPC (panel B) in the presence and absence of LF11 or C12LF11 at 25°C (aqueous phase: 20 mM Na-phosphate buffer 130 mM NaCl pH 7.4). Solid lines give the best fits to the experimental data using the global analysis technique described above. Insets show an enlargement of the WAXS regime. Pure DPPG exhibits positionally, weakly correlated bilayers with a *d*-spacing of 120 Å, which get less correlated in the presence of LF11 and completely uncorrelated upon the addition of C12LF11. Pure DPPC, in turn, is well-known to form MLVs, which are unaffected by adding LF11. C12LF12 leads to a large swelling of the system and a strong perturbation of the hydrocarbon chain packing as evidenced in the WAXS pattern (Data taken from ref. [161]).

the latter is required to penetrate into the hydrophobic core of the bilayer. Revealing this balance is one of the challenges of the future in the field.

7. Structural Information on Coexisting Membrane Domains

Throughout this contribution, we have shown that the effects of antimicrobial peptides on membranes can be quite diverse and strongly depend not only on the nature of the peptides but also on the properties of the lipids forming the matrix of the membrane bilayer. We have also presented evidence that formation of domains due to the interaction of the peptides with specific lipids may lead to membrane dysfunction. Former X-ray studies complemented by microcalorimetric and spectroscopic experiments (see Section 2) yielded already some information on the properties of these domains. However, so far a detailed structural analysis from X-ray data on coexisting domains was limited. Recent work in our laboratory, however, revealed a situation under which the characteristics of individual domains can be deduced from X-ray scattering data.

Our systematic X-ray study on the phase behavior of disaturated PG with a chain length of C14–C18 has brought new insight into the structure of their gel-phase at physiological pH and ionic strength [153]. In this phase, these negatively charged lipids as well as disaturated PCs are characterized by a hydrocarbon chain tilt, which in general can be attributed to the mismatch between the lateral areas of the head group and the hydrocarbon chains [172]. In the case of PGs under the experimental conditions, the electrostatic repulsion between the like-charged head groups is responsible for an effectively larger head-group area that causes the chains to tilt. However, the area per PG molecule obtained from our wide-angle X-ray experiments is smaller than the reported values of the corresponding PC. This can be explained by the tilting of the PG head group out of the bilayer plane, thereby optimizing the van der Waals interaction and thus hydrocarbon chain packing. Another possibility to overcome the packing mismatch between the phospholipid head group and hydrocarbon chains, if it exceeds a critical value, is the formation of an interdigitated phase $L_{\beta I}$, where the terminal methyl groups of one monolayer are located near the polar interface of the other membrane leaflet. This gives each lipid head group four-times the lateral space of a single hydrocarbon chain. Such an interdigitated phase has been reported for pure lipid phases [173–178], in the presence of large ions [179], in mixtures of PCs with small amphiphilic molecules such as anesthetics [180], lysoPC [181] or short-chain alcohols [182–185].

Applying our global data analysis to SAXS obtained from di-C14, C16 and C18 PGs revealed coexisting interdigitated and non-interdigitated domains in the case of distearoyl-PG (C18) (Fig. 19). Here, we draw advantage from the fact that the two phases are stable over time and well-separated unlike in the case of cholesterol/PC mixtures. This gives two distinct scattering signals – in particular, we find additional diffuse scattering that cannot be explained by a single-phase model – which can be separated. No interdigitation was found for the shorter chain PGs. However, very

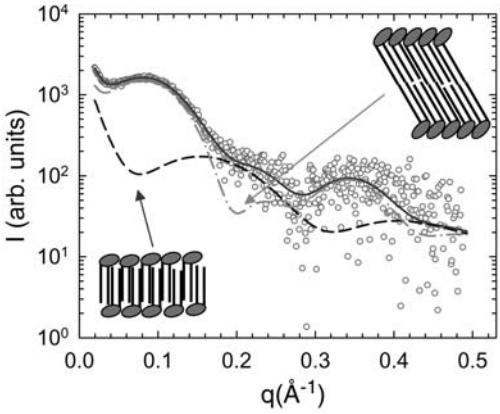

Figure 19 Coexistence of interdigitated and non-interdigitated bilayers in liposomal preparations of distearoylphosphatidylglycerol in 20 mM Na-phosphate buffer, 130 mM NaCl, pH 7.4. Panel A shows the small-angle X-ray scattering data of the lipid–water system, which has been analyzed by a global model (dashed line: interdigitated phase, dashed-dotted line: non-interdigitated phase, solid line: sum of interdigitated and non-interdigitated intensities).

long-chain PCs seems to face a similar problem of packing mismatch between head group and hydrocarbon chains since an interdigitated phase was reported for PCs with more than 20 hydrocarbons per chain [186].

Recent studies on interactions of DPPG and DSPG with various antimicrobial peptides also reveal the formation of an interdigitated phase [59]. Depending on the kind and amount of peptide added, fully interdigitated phases or the coexistence of interdigitated and non-interdigitated phases were observed. The presence of 4 mol% LL-37, a human antimicrobial peptide, yielded fully interdigitated DPPG liposomes. Taking into consideration results from spectroscopic experiments [187,188] the most likely organization of LL-37 is parallel to the bilayer plane shielding the tail ends of the lipids from the interfacial water, thereby forming a quasi-interdigitated structure $L_{\beta Iq}$ as sketched in Fig. 20. Most interestingly, at the same concentration of LL-37, we also found coexisting interdigitated and non-interdigitated phases for the long-chain zwitterionic lipids DSPC and DAPC, whereas at shorter chains, i.e., DPPC and DMPC, disk-like micelles were formed (see also Section 2.3). Thus, LL-37 can exhibit completely different mechanisms of membrane perturbation depending on the nature of the lipid.

The occurrence of the quasi-interdigitated phase at shorter chain-lengths of PG as compared to PC can be explained by the lower penetration depth of the peptide, which is due to the electrostatic interaction between the cationic amino acid residues and the negatively charged phosphate group of PG. This results in larger voids in PG bilayers than in the corresponding PC favoring a structural rearrangement of the bilayer in the form of an interdigitated phase. The balance between peptide penetration depth and hydrocarbon core thickness certainly is a major reason for the different modes of action of LL-37, although the intrinsic property of a given lipid to adopt an interdigitated structure will facilitate its formation. Furthermore, we have also observed coexisting interdigitated and non-interdigitated lipid domains for

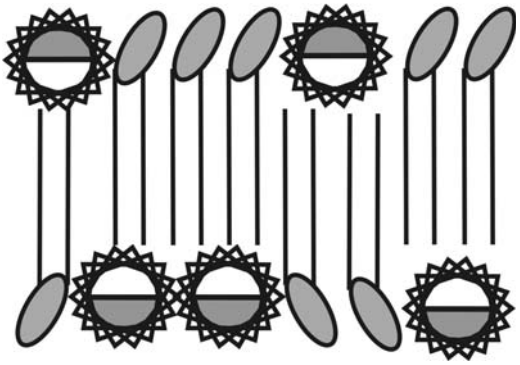

Figure 20 Illustration of a quasi-interdigitated phase induced by amphipathic peptides aligned parallel to the bilayer surface, where the methyl ends of the opposing phospholipid monolayers are protected by the hydrophobic amino acid residues from the aqueous phase.

PGLa (corresponding to the high temperature phase described in Section 2.1) and melittin for certain PGs and PCs. Based on these results, we proposed a general phase diagram suggesting phase regions for the formation of interdigitated lipid–peptide domains and of disk-like lipid–peptide micelles as a function of headgroup charge and hydrocarbon chain length. Moreover, we suggest that this is in principle applicable for other lipid–peptide mixtures, as well, particularly for amphipathic peptides with a spatial orientation parallel to the membrane surface [59].

8. Outlook

Because of the different physical and chemical properties of the lipids found in biological membranes, one can expect that these differences lead to membranes with diverse structural and mechanical properties (often also denoted as global properties), which in turn allows antimicrobial peptides to discriminate between bacterial and mammalian membranes [36]. The studies on liposomes mimicking the more complex biological membranes as described above support this notion. It is therefore a prerequisite to study the global and local properties of pure lipids or lipid mixtures in detail, in order to be able to address the effects observed, when antimicrobial peptides, or, more generally, membrane active compounds interact with the lipid matrix [98]. Further developments with respect to X-ray data analysis will certainly contribute their share to the understanding of lipid–peptide interaction on a molecular level complementing the wealth of data available from thermodynamic and spectroscopic measurements.

REFERENCES

[1] M.A. Yorek, in: G. Cevc, (Ed.), Phospholipids Handbook, Marcel Dekker, New York, 1993, pp. 745–775.

[2] T. Vanden Boom, J.E. Cronan Jr., Annu. Rev. Microbiol. 43 (1989) 317–343.
[3] A. Chopra, G.K. Khuller, Crit. Rev. Microbiol. 11 (1984) 209–271.
[4] A.A. Spector, M.A. Yorek, J. Lipid Res. 26 (1985) 1015–1035.
[5] G. Garab, K. Lohner, P. Laggner, T. Farkas, Trends Plant Sci. 5 (2000) 489–494.
[6] Y. Deng, S.D. Kohlwein, C.A. Mannella, Protoplasma 219 (2002) 160–167.
[7] S. Morein, A. Andersson, L. Rilfors, G. Lindblom, J. Biol. Chem. 271 (1996) 6801–6809.
[8] J.E. Rothman, J. Lenard, Science 195 (1977) 743–753.
[9] E.M. Bevers, P. Comfurius, D.W. Dekkers, M. Harmsma, and R.F. Zwaal, Lupus 7 Suppl 2 (1998) S126–S131.
[10] R.F. Zwaal, A.J. Schroit, Blood 89 (1997) 1121–1132.
[11] E. Prenner, G. Honsek, D. Honig, D. Mobius, K. Lohner, Chem. Phys. Lipids 145 (2007) 106–118.
[12] M. Seigneuret, P.F. Devaux, Proc. Natl. Acad. Sci. USA 81 (1984) 3751–3755.
[13] M.A. Kol, A.I. de Kroon, J.A. Killian, B. de Kruijff, Biochemistry 43 (2004) 2673–2681.
[14] V.A. Fadok, D.R. Voelker, P.A. Campbell, J.J. Cohen, D.L. Bratton, P.M. Henson, J. Immunol. 148 (1992) 2207–2216.
[15] S.J. Martin, C.P. Reutelingsperger, A.J. McGahon, J.A. Rader, R.C. van Schie, D.M. LaFace, D.R. Green, J. Exp. Med. 182 (1995) 1545–1556.
[16] R.F. Zwaal, P. Comfurius, E.M. Bevers, Cell. Mol. Life Sci. 62 (2005) 971–988.
[17] S.M. Hammond, P.A. Lambert, A.N. Rycroft, The Bacterial Cell Surface, Croom Helm, London, 1984.
[18] S.G. Wilkinson, Gram-negative bacteria, in: C. Ratledge, S.G. Wilkinson (Eds.), Microbial Lipids, Academic Press, London, 1988, pp. 299–488.
[19] A. Aspedon, E.A. Groisman, Antimicrobial peptide resistance mechanisms in bacteria, in: K. Lohner, (Ed.), Development of Novel Antimicrobial Agents: Emerging Strategies, Horizon Scientific Press, Norfolk, UK, 2001, pp. 31–44.
[20] R.P. Huijbregts, A.I. de Kroon, B. de Kruijff, Biochim. Biophys. Acta 1469 (2000) 43–61.
[21] C.P. Sparrow, C.R. Raetz, J. Biol. Chem. 260 (1985) 12084–12091.
[22] R.T. Ambron, R.A. Pieringer, Phospholipids in micro-organisms, in: G.B. Ansell, J.N. Hawthorne, R.M.C. Dawson (Eds.), Form and Function of Phospholipids, Elsevier, Amsterdam, 1973, pp. 289–331.
[23] W.M. O'Leary, S.G. Wilkinson, Gram-positive bacteria, in: C. Ratledge, S.G. Wilkinson (Eds.), Microbial Lipids, Academic Press, London, 1988, pp. 117–201.
[24] A. Peschel, M. Otto, R.W. Jack, H. Kalbacher, G. Jung, F. Gotz, J. Biol. Chem. 274 (1999) 8405–8410.
[25] S.D. Shukla, C. Green, J.M. Turner, Biochem. J. 188 (1980) 131–135.
[26] L.I. Barsukov, V.I. Kulikov, L.D. Bergelson, Biochem. Biophys. Res. Commun. 71 (1976) 704–711.
[27] D.G. Bishop, J.A. Op den Kamp, L.L. van Deenen, Eur. J. Biochem. 80 (1977) 381–391.
[28] J.E. Rothman, E.P. Kennedy, J. Mol. Biol. 110 (1977) 603–618.
[29] S.E. Blondelle, K. Lohner, Biopolymers 55 (2000) 74–87.
[30] K. Lohner (Ed.), Development of Novel Antimicrobial Agents: Emerging Strategies, Horizon Scientific Press, Wymondham, Norfolk, UK, 2001.
[31] M.A. Baker, W.L. Maloy, M. Zasloff, L.S. Jacob, Cancer Res. 53 (1993) 3052–3057.
[32] T. Ganz, R.I. Lehrer, Curr. Opin. Immunol. 10 (1998) 41–44.
[33] M. Zasloff, Nature 415 (2002) 389–395.
[34] Y.J. Gordon, L.C. Huang, E.G. Romanowski, K.A. Yates, R.J. Proske, A.M. McDermott, Curr. Eye Res. 30 (2005) 385–394.
[35] D. Avrahami, Y. Shai, Biochemistry 42 (2003) 14946–14956.
[36] K. Lohner, S.E. Blondelle, Comb. Chem. High Throughput Screen. 8 (2005) 241–256.
[37] B. Bechinger, K. Lohner, Biochim. Biophys. Acta 1758 (2006) 1529–1539.
[38] Z. Oren, Y. Shai, Novel Antimicrob. Agents 14 (2001) 184–204.
[39] K. Matsuzaki, Molecular mechanisms of membrane perturbation by antimicrobial peptides, in: K. Lohner, (Ed.), Development of Novel Antimicrobial Agents: Emerging Strategies, Horizon Scientific Press, Wymondham, Norfolk, UK, 2001, pp. 167–181.

[40] K. Matsuzaki, O. Murase, N. Fujii, K. Miyajima, Biochemistry 35 (1996) 11361–11368.
[41] S.J. Ludtke, K. He, W.T. Heller, T.A. Harroun, L. Yang, H.W. Huang, Biochemistry 35 (1996) 13723–13728.
[42] H. Vogel, Biochemistry 26 (1987) 4562–4572.
[43] K. He, S.J. Ludtke, D.L. Worcester, H.W. Huang, Biophys. J. 70 (1996) 2659–2666.
[44] W.T. Heller, A.J. Waring, R.I. Lehrer, T.A. Harroun, T.M. Weiss, L. Yang, H.W. Huang, Biochemistry 39 (2000) 139–145.
[45] L. Yang, T.A. Harroun, T.M. Weiss, L. Ding, H.W. Huang, Biophys. J. 81 (2001) 1475–1485.
[46] Y. Shai, Biopolymers 66 (2002) 236–248.
[47] A. Latal, G. Degovics, R.F. Epand, R.M. Epand, K. Lohner, Eur. J. Biochem. 248 (1997) 938–946.
[48] K. Lohner, A. Latal, R.I. Lehrer, T. Ganz, Biochemistry 36 (1997) 1525–1531.
[49] E. Staudegger, E.J. Prenner, M. Kriechbaum, G. Degovics, R.N. Lewis, R.N. McElhaney, K. Lohner, Biochim. Biophys. Acta 1468 (2000) 213–230.
[50] R. El Jastimi, M. Lafleur, Biochim. Biophys. Acta 1418 (1999) 97–105.
[51] K. Lohner, E.J. Prenner, Biochim. Biophys. Acta 1462 (1999) 141–156.
[52] O. Konovalov, I. Myagkov, B. Struth, K. Lohner, Eur. Biophys. J. 31 (2002) 428–437.
[53] O. Konovalov, S.M. O'Flaherty, E. Saint-Martin, G. Deutsch, E. Sevcsik, K. Lohner, Physica B-Condens. Matter 357 (2005) 185–189.
[54] D. Gidalevitz, Y. Ishitsuka, A.S. Muresan, O. Konovalov, A.J. Waring, R.I. Lehrer, K.Y. Lee, Proc. Natl. Acad. Sci. USA 100 (2003) 6302–6307.
[55] P.M. Abuja, A. Zenz, M. Trabi, D.J. Craik, K. Lohner, FEBS Lett. 566 (2004) 301–306.
[56] W. Jing, E.J. Prenner, H.J. Vogel, A.J. Waring, R.I. Lehrer, K. Lohner, J. Pept. Sci. 11 (2005) 735–743.
[57] R.F. Epand, M.A. Schmitt, S.H. Gellman, R.M. Epand, Biochim. Biophys. Acta 1758 (2006) 1343–1350.
[58] B.B. Bonev, W.C. Chan, B.W. Bycroft, G.C. Roberts, A. Watts, Biochemistry 39 (2000) 11425–11433.
[59] E. Sevcsik, G. Pabst, A. Jilek, K. Lohner. Biochim. Biophys. Acta (2007) doi:10.1016/j.bbamem.2007.06.015.
[60] H.W. Huang, Biochim. Biophys. Acta 1758 (2006) 1292–1302.
[61] S. Ludtke, K. He, H. Huang, Biochemistry 34 (1995) 16764–16769.
[62] K. He, S.J. Ludtke, W.T. Heller, H.W. Huang, Biophys. J. 71 (1996) 2669–2679.
[63] H.W. Huang, F.Y. Chen, M.T. Lee, Phys. Rev. Lett. 92 (2004) 198304.
[64] M.T. Lee, F.Y. Chen, H.W. Huang, Biochemistry 43 (2004) 3590–3599.
[65] M.T. Lee, W.C. Hung, F.Y. Chen, H.W. Huang, Biophys. J. 89 (2005) 4006–4016.
[66] F.Y. Chen, M.T. Lee, H.W. Huang, Biophys. J. 84 (2003) 3751–3758.
[67] A. Mecke, D.K. Lee, A. Ramamoorthy, B.G. Orr, M.M. Banaszak Holl, Biophys. J. 89 (2005) 4043–4050.
[68] A.S. Arseniev, I.L. Barsukov, V.F. Bystrov, A.L. Lomize, Y. Ovchinnikov, FEBS Lett. 186 (1985) 168–174.
[69] T.A. Harroun, W.T. Heller, T.M. Weiss, L. Yang, H.W. Huang, Biophys. J. 76 (1999) 937–945.
[70] T.A. Harroun, W.T. Heller, T.M. Weiss, L. Yang, H.W. Huang, Biophys. J. 76 (1999) 3176–3185.
[71] T.M. Weiss, P.C. van der Wel, J.A. Killian, R.E. Koeppe, H.W. Huang, Biophys. J. 84 (2003) 379–385.
[72] M. Posch, U. Rakusch, C. Mollay, P. Laggner, J. Biol. Chem. 258 (1983) 1761–1766.
[73] A. Collotto, K. Lohner, P. Laggner, Prog. Colloid Polym. Sci. 89 (1992) 334.
[74] K. Müller, G. Lipka, K. Lohner, P. Laggner, Thermochimica Acta 94 (1985) 187–197.
[75] J. Dufourcq, J.-F. Faucon, G. Fourche, J.-L. Dasseux, M. le Maire, T. Gulik-Krzywicki, Biochim. Biophys. Acta 859 (1986) 33–48.
[76] M. Monette, M. Lafleur, Biophys. J. 68 (1995) 187–195.
[77] K. Lohner, P. Laggner, J.H. Freer, J. Solution Chem. 15 (1986) 189–198.
[78] K. Lohner, E. Staudegger, E.J. Prenner, R.N. Lewis, M. Kriechbaum, G. Degovics, R.N. McElhaney, Biochemistry 38 (1999) 16514–16528.

[79] D. Atkinson, D.M. Small, Annu. Rev. Biophys. Biophys. Chem. 15 (1986) 403–456.
[80] P.R. Cullis, B. de Kruijff, Biochim. Biophys. Acta 559 (1979) 399–420.
[81] J.N. Israelachvili, S. Marcelja, R.G. Horn, Q. Rev. Biophys. 13 (1980) 121–200.
[82] S.M. Gruner, J. Phys. Chem. 93 (1989) 7562–7570.
[83] S.M. Gruner, P.R. Cullis, M.J. Hope, C.P. Tilcock, Annu. Rev. Biophys. Biophys. Chem. 14 (1985) 211–238.
[84] M.W. Tate, E.F. Eikenberry, D.C. Turner, E. Shyamsunder, S.M. Gruner, Chem. Phys. Lipids 57 (1991) 147–164.
[85] B. de Kruijff, Nature 386 (1997) 129–130.
[86] R.M. Epand, Biochim. Biophys. Acta 1376 (1998) 353–368.
[87] L. Rilfors, A. Wieslander, G. Lindblom, Subcell. Biochem. 20 (1993) 109–166.
[88] R.N. McElhaney, Membrane structure, in: J. Maniloff, R.N. McElhaney, L.R. Finch, J.B. Baseman (Eds.), Mycoplasma: Molecular Biology and Pathogenesis, American Society for Microbiology, Washington, DC, 1992, pp. 113–155.
[89] J.M. Seddon, Biochim. Biophys. Acta 1031 (1990) 1–69.
[90] S.L. Keller, S.M. Gruner, K. Gawrisch, Biochim. Biophys. Acta 1278 (1996) 241–246.
[91] A. Angelova, R. Ionov, M.H. Koch, G. Rapp, Arch. Biochem. Biophys. 378 (2000) 93–106.
[92] Y. Wu, K. He, S.J. Ludtke, H.W. Huang, Biophys. J. 68 (1995) 2361–2369.
[93] K. Lohner, G. Degovics, P. Laggner, E. Gnamusch, F. Paltauf, Biochim. Biophys. Acta 1152 (1993) 69–77.
[94] H.M. Chen, K.W. Leung, N.N. Thakur, A. Tan, R.W. Jack, Eur. J. Biochem. 270 (2003) 911–920.
[95] K.A. Henzler Wildman, D.K. Lee, A. Ramamoorthy, Biochemistry 42 (2003) 6545–6558.
[96] K. Matsuzaki, K. Sugishita, N. Ishibe, M. Ueha, S. Nakata, K. Miyajima, R.M. Epand, Biochemistry 37 (1998) 11856–11863.
[97] S. Marcelja, Biophys. J. 76 (1999) 593–594.
[98] G. Pabst, Biophys. Rev. Lett. 1 (2006) 57–84.
[99] S.H. Chen, C.Y. Liao, H.W. Huang, T.M. Weiss, M.C. Bellisent-Funel, F. Sette, Phys. Rev. Lett. 86 (2001) 740–743.
[100] T.M. Weiss, P.J. Chen, H. Sinn, E.E. Alp, S.H. Chen, H.W. Huang, Biophys. J. 84 (2003) 3767–3776.
[101] M.C. Rheinstädter, C. Ollinger, G. Fragneto, F. Demmel, T. Salditt, Phys. Rev. Lett. 93 (2004) 108107.
[102] M.C. Rheinstadter, T. Seydel, F. Demmel, T. Salditt, Phys. Rev. E Stat. Nonlin. Soft Matter Phys. 71 (2005) 061908.
[103] G. Brotons, D. Constantin, A. Madsen, T. Salditt, Physica B-Condens. Matter 357 (2005) 61–65.
[104] G. Cevc (Ed.), Phospholipids Handbook, Marcel Dekker, New York, 1993.
[105] R. Lipowsky, E. Sackmann (Ed.), Structure and Dynamics of Membranes. Generic and Specific Interactions, Elsevier, Amsterdam, 1995.
[106] J. Katsaras, T. Gutberlet (Ed.), Lipid Bilayers. Structure and Interactions, Springer, Berlin, 2000.
[107] H.I. Petrache, K. Tu, J.F. Nagle, Biophys. J. 76 (1999) 2479–2487.
[108] V.A. Parsegian, R.P. Rand, Interaction in membrane assemblies, in: R. Lipowsky, E. Sackmann (Eds.), Structure and Dynamics of Membranes, North-Holland, Amsterdam, 1995, pp. 643–690.
[109] T.J. McIntosh, Curr. Opin. Struct. Biol. 10 (2000) 481–485.
[110] R. Kwok, E. Evans, Biophys. J. 35 (1981) 637–652.
[111] H. Engelhardt, H.P. Duwe, E. Sackmann, J. Phys. Lett. (Paris) 46 (1985) 395–400.
[112] M. Kummrow, W. Helfrich, Phys. Rev. A 44 (1991) 8356–8360.
[113] R. Dimova, B. Pouligny, C. Dietrich, Biophys. J. 79 (2000) 340–356.
[114] C.H. Lee, W.C. Lin, J. Wang, Phys. Rev. E 64 (2001) 020901.
[115] H.I. Petrache, N. Gouliaev, S. Tristram-Nagle, R.T. Zhang, R.M. Suter, J.F. Nagle, Phys. Rev. E 57 (1998) 7014–7024.
[116] G. Pabst, H. Amenitsch, D.P. Kharakoz, P. Laggner, M. Rappolt, Phys. Rev. E 70 (2004) 021908.

[117] Y. Liu, J.F. Nagle, Phys. Rev. E 69 (2004) 040901.
[118] T. Salditt, J. Phys. Condens. Matter 17 (2005) R287–R314.
[119] S. May, D. Harries, A. Ben Shaul, Biophys. J. 79 (2000) 1747–1760.
[120] E.J. Shimshick, H.M. McConnell, Biochemistry 12 (1973) 2351–2360.
[121] C. Gebhardt, H. Gruber, E. Sackmann, Z. Naturforsch. 32c (1977) 581–596.
[122] P. Laggner, Nature 294 (1981) 373–374.
[123] O.G. Mouritsen, K. Jorgensen, Chem. Phys. Lipids 73 (1994) 3–25.
[124] M. Edidin, Ann. Rev. Biophys. Biomol. Struct. 32 (2003) 257–283.
[125] K. Simons, J. Mol. Cell. Cardiol. 36 (2004) 759.
[126] J.H. Ipsen, G. Karlstrom, O.G. Mouritsen, H. Wennerstrom, M.J. Zuckermann, Biochim. Biophys. Acta 905 (1987) 162–172.
[127] M.R. Vist, J.H. Davis, Biochemistry 29 (1990) 451–464.
[128] D.J. Recktenwald, H.M. Mcconnell, Biochemistry 20 (1981) 4505–4510.
[129] M.B. Sankaram, T.E. Thompson, Proc. Natl. Acad. Sci. USA 88 (1991) 8686–8690.
[130] T.P. McMullen, R.N. McElhaney, Biochim. Biophys. Acta 1234 (1995) 90–98.
[131] R.F. de Almeida, A. Fedorov, M. Prieto, Biophys. J. 85 (2003) 2406–2416.
[132] M. Rappolt, M.F. Vidal, M. Kriechbaum, M. Steinhart, H. Amenitsch, S. Bernstorff, P. Laggner, Eur. Biophys. J. 31 (2003) 575–585.
[133] S.L. Veatch, S.L. Keller, Biochim. Biophys. Acta 1746 (2005) 172–185.
[134] S.L. Veatch, K. Gawrisch, S.L. Keller, Biophys. J. 90 (2006) 4428–4436.
[135] S. Karmakar, B.R. Sarangi, V.A. Raghunathan, Solid State Commun. 139 (2006) 630–634.
[136] J.F. Nagle, S. Tristram-Nagle, Biochim. Biophys. Acta 1469 (2000) 159–195.
[137] M. Rappolt, P. Laggner, G. Pabst, Structure and elasticity of phospholipid bilayers in the L_α phase: a comparison of phosphatidylcholine and phosphatidylethanolamine membranes, in: S.G. Pandalai, (Ed.), Recent Research Developments in Biophysics, Transworld Research Network, Kerala, 2004, pp. 363–394.
[138] G. Pabst, M. Rappolt, H. Amenitsch, P. Laggner, Phys. Rev. E 62 (2000) 4000–4009.
[139] G. Pabst, J. Katsaras, V.A. Raghunathan, M. Rappolt, Langmuir 19 (2003) 1716–1722.
[140] G. Pabst, R. Koschuch, B. Pozo-Navas, M. Rappolt, K. Lohner, P. Laggner, J. Appl. Crystallogr. 63 (2003) 1378–1388.
[141] R. Hosemann, S.N. Bagchi, Direct Analysis of Diffraction by Matter, North-Holland, Amsterdam, 1962.
[142] A. Guiner, X-ray Diffraction, Freeman, San Francisco, 1963.
[143] A. Caillé, C. R. Acad. Sci. B Paris 274 (1972) 891–893.
[144] R. Zhang, R.M. Suter, J.F. Nagle, Phys. Rev. E 50 (1994) 5047–5060.
[145] R. Zhang, S. Tristram-Nagle, W. Sun, R.L. Headrick, T.C. Irving, R.M. Suter, J.F. Nagle, Biophys. J. 70 (1996) 349–357.
[146] J.M. Seddon, R.H. Templer, Polymorphism of lipid–water systems, in: R. Lipowsky, E. Sackmann (Eds.), Structure and Dynamics of Membranes, North-Holland, Amsterdam, 1995, pp. 97–160.
[147] A. Watts, K. Harlos, W. Maschke, D. Marsh, Biochim. Biophys. Acta 510 (1978) 63–74.
[148] G. Cevc, Biochim. Biophys. Acta 1031 (1990) 311–382.
[149] P. Garidel, A. Blume, Eur. Biophys. J. 28 (2000) 629–638.
[150] B. Tenchov, R. Koynova, G. Rapp, Biophys. J. 80 (2001) 1873–1890.
[151] A. Watts, K. Harlos, D. Marsh, Biochim. Biophys. Acta 645 (1981) 91–96.
[152] Y.P. Zhang, R.N. Lewis, R.N. McElhaney, Biophys. J. 72 (1997) 779–793.
[153] G. Pabst, S. Danner, S. Karmakar, G. Deutsch, V.A. Raghunathan, Biophys. J. 93 (2007) 513–525.
[154] K.A. Riske, L.Q. Amaral, H.G. Döbereiner, M.T. Lamy, Biophys. J. 86 (2004) 3722–3733.
[155] K. Lohner, A. Latal, G. Degovics, P. Garidel, Chem. Phys. Lipids 111 (2001) 177–192.
[156] N.B. Pozo, K. Lohner, G. Deutsch, E. Sevcsik, K.A. Riske, R. Dimova, P. Garidel, G. Pabst, Biochim. Biophys. Acta 1716 (2005) 40–48.
[157] P. Garidel, C. Johann, A. Blume, J. Therm. Anal. Calorim. 82 (2005) 447–455.
[158] B. Pozo-Navas, V.A. Raghunathan, J. Katsaras, M. Rappolt, K. Lohner, G. Pabst, Phys. Rev. Lett. 91 (2003) 028101.

[159] R. Lipowsky, S. Leibler, Phys. Rev. Lett. 56 (1986) 2541–2544.
[160] W. Helfrich, Z. Naturforsch. 33a (1978) 305–315.
[161] D. Zweytick, G. Pabst, P.M. Abuja, A. Jilek, S.E. Blondelle, J. Andra, R. Jerala, D. Monreal, d.T. Martinez, K. Lohner, Biochim. Biophys. Acta 1758 (2006) 1426–1435.
[162] H.J. Vogel, D.J. Schibli, W. Jing, E.M. Lohmeier-Vogel, R.F. Epand, R.M. Epand, Biochem. Cell Biol. 80 (2002) 49–63.
[163] J.L. Gifford, H.N. Hunter, H.J. Vogel, Cell. Mol. Life Sci. 62 (2005) 2588–2598.
[164] M. Sorenson, M.P.L. Sorenson, C. R. Trav. Lab. Carlsberg 23 (1939) 55–59.
[165] P.L. Masson, J.F. Heremans, C.H. Dive, Clin. Chim. Acta 14 (1966) 735–739.
[166] P.L. Masson, J.F. Heremans, E. Schonne, J. Exp. Med. 130 (1969) 643–658.
[167] H. Wakabayashi, M. Takase, M. Tomita, Curr. Pharm. Des. 9 (2003) 1277–1287.
[168] P.M. Hwang, N. Zhou, X. Shan, C.H. Arrowsmith, H.J. Vogel, Biochemistry 37 (1998) 4288–4298.
[169] A. Majerle, J. Kidric, R. Jerala, J. Antimicrob. Chemother. 51 (2003) 1159–1165.
[170] D. Avrahami, Y. Shai, J. Biol. Chem. 279 (2004) 12277–12285.
[171] R. Koynova, M. Caffrey, Biochim. Biophys. Acta 1376 (1998) 91–145.
[172] J.F. Nagle, Ann. Rev. Phys. Chem. 31 (1980) 157–195.
[173] J.L. Ranck, T. Keira, V. Luzzati, Biochim. Biophys. Acta 488 (1977) 432–441.
[174] P. Laggner, K. Lohner, G. Degovics, K. Muller, A. Schuster, Chem. Phys. Lipids 44 (1987) 31–60.
[175] K. Lohner, A. Schuster, G. Degovics, K. Muller, P. Laggner, Chem. Phys. Lipids 44 (1987) 61–70.
[176] P. Laggner, K. Lohner, R. Koynova, B. Tenchov, Chem. Phys. Lipids 60 (1991) 153–161.
[177] I. Winter, G. Pabst, M. Rappolt, K. Lohner, Chem. Phys. Lipids 112 (2001) 137–150.
[178] S. Tristram-Nagle, R.N. Lewis, J.W. Blickenstaff, M. Diprima, B.F. Marques, R.N. McElhaney, J.F. Nagle, J.W. Schneider, Chem. Phys. Lipids 134 (2005) 29–39.
[179] B.A. Cunningham, P.J. Quinn, D.H. Wolfe, W. Tamura-Lis, L.J. Lis, O. Kucuk, M.P. Westerman, Biochim. Biophys. Acta 1233 (1995) 68–74.
[180] T. Hata, H. Matsuki, S. Kaneshina, Biophys. Chem. 87 (2000) 25–36.
[181] J.Z. Lu, Y.H. Hao, J.W. Chen, J. Biochem. (Tokyo) 129 (2001) 891–898.
[182] T.J. McIntosh, R.V. McDaniel, S.A. Simon, Biochim. Biophys. Acta 731 (1983) 109–114.
[183] E.S. Rowe, Biochim. Biophys. Acta 813 (1985) 321–330.
[184] T. Adachi, H. Takahashi, K. Ohki, I. Hatta, Biophys. J. 68 (1995) 1850–1855.
[185] T.J. McIntosh, H. Lin, S. Li, C. Huang, Biochim. Biophys. Acta 1510 (2001) 219–230.
[186] W.J. Sun, S. Tristram-Nagle, R.M. Suter, J.F. Nagle, Biochim. Biophys. Acta 1279 (1996) 17–24.
[187] Z. Oren, J.C. Lerman, G.H. Gudmundsson, B. Agerberth, Y. Shai, Biochem. J. 341 (Pt 3) (1999) 501–513.
[188] K.A. Henzler Wildman, D.K. Lee, A. Ramamoorthy, Biochemistry 42 (2003) 6545–6558.
[189] D.A. White, The phospholipid composition of mammalian tissues, in: G.B. Ansell, J.N. Hawthorne, R.M.C. Dawson (Eds.), Form and Function of Phospholipids, Elsevier, Amsterdam, 1973, pp. 441–482.

This page intentionally left blank

CHAPTER SIX

Application of Spin-Labeling EPR and ATR-FTIR Spectroscopies to the Study of Membrane Heterogeneity

Janez Štrancar*, *and* Zoran Arsov

Contents

1. Introduction 140
2. Experimental Methods to Approach Membrane Heterogeneity 142
   2.1. Membrane Exploration by SL-EPR 144
   2.2. Membrane Exploration by ATR–FTIR Spectroscopy 147
3. Membrane Hydration 149
   3.1. Effect of the Level of Hydration on the Membrane Properties Studied by SL-EPR 149
   3.2. Application of ATR–FTIR Spectroscopy to Distinguish Free and Lipid-Bound Water 150
4. Membrane Heterogeneity Characterization by SL-EPR 152
   4.1. Comparison of Characterization by Different Spin Probes in Model Membranes 152
   4.2. Effect of Spin Probe Partitioning on Membrane Heterogeneity Characterization 155
5. Membrane Heterogeneity Characterization by ATR–FTIR Spectroscopy 157
6. Conclusions 160
Acknowledgements 160
References 161

Abstract

Spectroscopic methods play a major role in understanding of biological membranes. Electron paramagnetic resonance (EPR) together with spin labeling (SL) is one of the most powerful methods to explore the membrane heterogeneity. What makes this method superior is the nanosecond time scale and nanometer spatial scale sensitivity as well as the possibility of *in vitro* and *in vivo* application on various systems, from model to biological membranes. The lateral heterogeneity of membranes is detected through the directional and rotational motion sensitivity that originates in significant anisotropy

* Corresponding author. Tel.: +386-1-477-3254; Fax: +386-1-477-3191
E-mail address: janez.strancar@ijs.si (J. Štrancar).

Jožef Stefan Institute, Department of Solid State Physics, Laboratory of Biophysics, Jamova 39, SI-1000 Ljubljana, Slovenia

Advances in Planar Lipid Bilayers and Liposomes, Volume 6
ISSN 1554-4516, DOI 10.1016/S1554-4516(07)06006-1

of magnetic properties of spin labels. In addition, infrared spectroscopy can gain additional information about the complexity of the interaction patterns through the influence of molecular environment on vibrational bands of the membrane constituent molecules.

In this chapter, the application of SL-EPR and attenuated total reflection Fourier transform infrared (ATR–FTIR) spectroscopy for examination of membrane heterogeneity will be presented. The problems of the level of membrane hydration on the membrane properties will be addressed. In addition, the problem of "biased" reporting of spin probe molecules and partitioning problem in heterogeneous lipid bilayer will be presented. It will be demonstrated that by the ATR–FTIR method it is possible to appreciate the influence of lipid bilayer on the water structure. In the end, the use of ATR-FTIR to distinguish different lipid phases in phosphatidylcholine/cholesterol model membranes will be shown.

1. Introduction

Description of a membrane strongly depends on a reference point in the time and the distance scale [1]. Due to the interactions that stabilize the membrane structure, membrane constituents cannot easily leave a membrane and at the same time the water soluble molecules cannot simply permeate through a membrane. This fact imposes the basic property of the membrane – compartmentalization of space, i.e., separating the interior and exterior. When describing a membrane simply as a two-dimensional object, one does not want to describe any further molecular details of a membrane. The simplification is usually good enough to describe basic mechanical properties of the membrane. However, focusing on a molecular level, the complexity of the structures and interactions makes the description much more difficult.

In the case of real biological membranes the striking complexity involves hundreds of different lipids and several thousands of different proteins with a very diverse chemical structure. Consequently, the interaction scheme between the membrane constituents becomes a very complex one. Charged headgroups induce variations in Coulomb interaction. Then, the charge separation in zwitterionic lipid leads to dipolar interaction. Next, non-additive van der Waals attraction forces strongly influence the ordering of the acyl chains and sterol rings. Not forgetting the hydrogen bonding with which the supramolecular structures are stabilized due to the cooperative effect. And finally, one should not overlook the effect of the hydrophobic interaction resulting from minimization of free energy of a system with water/lipid interface.

Even if we focus on a model system consisting of a single-lipid molecule type, the interaction complexity still remains. For example, in the famous two-dimensional ferromagnetic system of a single type of spin particles involving two interactions with different ranges, the system at certain temperature rearranges itself to form domains and domain walls and the temperature dependence shows a typical phase transition behavior. In analogy, since in the case of a single-lipid type model

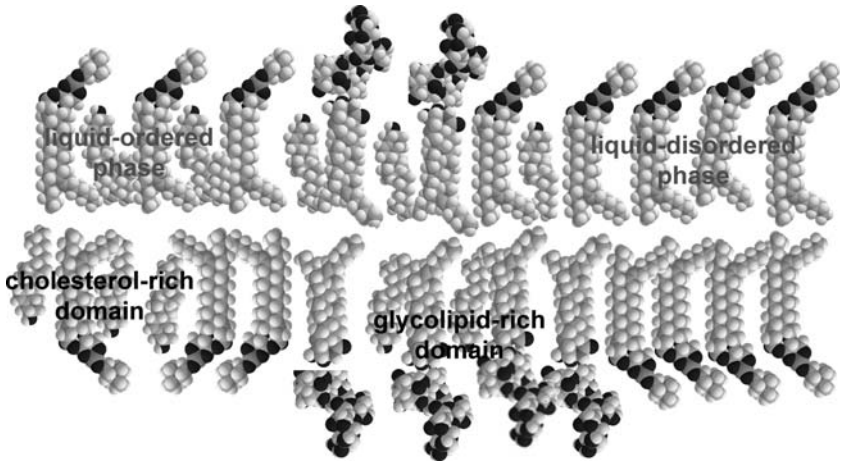

Figure 1 Schematic presentation of lateral heterogeneity that originates in the interaction complexity (gray labels) and in the biochemical complexity (black labels) of membrane. The heterogeneity can be expressed at different levels from acyl-chain region (hydrophobic core) to the glycocalyx region (hydrophilic surface).

membrane Coulomb and dipolar as long-ranged and van der Waals interaction and hydrogen bonding as short-ranged interactions are present, already in such a "simple" membrane the expected behavior is at least as complex as in the mentioned ferromagnetic system. Membrane domains with domain walls are expected to form close to the temperature around phase transitions [2]. If more complex mixtures are used [3,4], usually the lateral domain structure (phase behavior) becomes more complex (Fig. 1), although sometimes molecular composition can cause that membrane constituents are more compatible.

Model membranes composed of different lipid types exhibit lateral phase separation [5]. The exact temperatures and compositions for different phases are described by the shape of the corresponding temperature-composition phase diagrams. An example for the mixture of dimyristoyl-phosphatidylcholine (DMPC) and cholesterol (Chol) is shown in Fig. 2 [6] (for notations of the lipid phases see the caption to Fig. 2). It is important to add that the phase diagram presented in Fig. 2 shows a simplified picture. For example, the so called ripple phase [7] was not taken into account in the presented phase diagram. In addition, different experiments show that beside the phases presented in Fig. 2 also other phases can be present [8,9].

Also biological membranes have heterogeneous structures exhibiting coexistence of different lateral lipid domains in which lipid molecules have different physical properties [10–13]. The liquid phase separation in the presence of cholesterol in model systems (Fig. 2) is interesting, while in biological membranes one of the most important sources of heterogeneity is the coexistence of cholesterol-poor and cholesterol-rich domains, the latter in some cases also called lipid rafts [14–16].

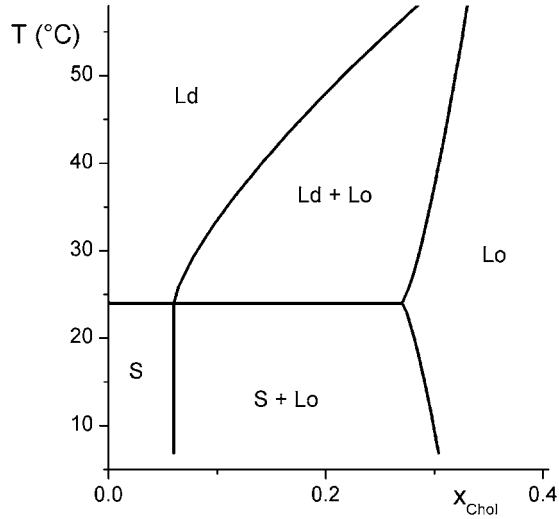

Figure 2 Temperature-composition phase diagram for lipid mixture DMPC/Chol (adapted from [6]). Lipid phases are denoted as gel phase S, liquid-ordered phase Lo and liquid-disordered phase Ld. Two phase coexistence regions are possible: S and Lo phase coexistence (S+Lo) and Ld and Lo phase coexistence (Ld+Lo). Mole fraction of cholesterol is denoted by x_{Chol}. Lines represent phase boundaries between different phase regions. At the horizontal line the main phase transition occurs.

Due to strong amphiphatic character of membrane constituents the lateral heterogeneity evolves at different levels, from acyl-chain region (hydrophobic core) to the glycocalyx region (hydrophilic surface) (Fig. 1) [17]. The steric repulsion and van der Waals attraction are mainly responsible for this behavior in the hydrophobic core, while in the hydrophilic surface the entropic repulsion and hydrogen bonding dominate. In both cases the Coulomb and dipolar interaction always complicate the description.

Since the complex interactions with different ranges induce clustering [18,19], modified dynamics [20,21], surface potential lateral variation [22], etc., they are potentially responsible for many physiological responses in real cells. For example, they can modify the activities of membrane proteins [23–25]. It is therefore of extreme importance to understand the properties of structural complexity, i.e., membrane heterogeneity, in model systems, in order to be able to apply this knowledge to functional studies of the much more complex biological membranes.

2. Experimental Methods to Approach Membrane Heterogeneity

To study the membrane heterogeneity, beside the spatial scale at molecular level also a proper time scale is needed. The latter is suitable, when the diffusion of lipid molecules and the domain lifetime are appropriate so that the averaging does

not occur. The dynamics of molecular lateral diffusion and rotational reorientation occur at sub-nanosecond-to-nanosecond time scale, making three spectroscopic methods the methods of choice for the membrane heterogeneity exploration: electron paramagnetic resonance (EPR) spectroscopy, fluorescence spectroscopy and infrared (IR) spectroscopy.

Both EPR and fluorescence spectroscopies usually require labeling in the membrane studies. In case of EPR, the probability of finding natural stable paramagnetic center that is needed to interact with magnetic field, is very low, therefore one introduces a spin label. To be sensitive to various membrane properties, lipohilic spin labels are usually applied with a nitroxide radical group in the system (Fig. 3, top left) [26]. The sensitivity of SL-EPR to the molecular level comes from molecular interactions with electron molecular orbital of a nitroxide electron modifying its magnetic properties and being highly anisotropic [27]. The time scale of a typical 10-GHz EPR experiment with a nitroxide spin label is in the range of a few nanoseconds.

Similarly, the fluorescence spectroscopy needs an optically resonating chemical structure, which usually means a π-system of coupled aromatic rings. Since these are also not very common in the membranes, one needs again to implement labeling, which in fluorescence case means labeling with fluorophores [28,29]. Again the sensitivity comes from molecular interactions with aromatic ring

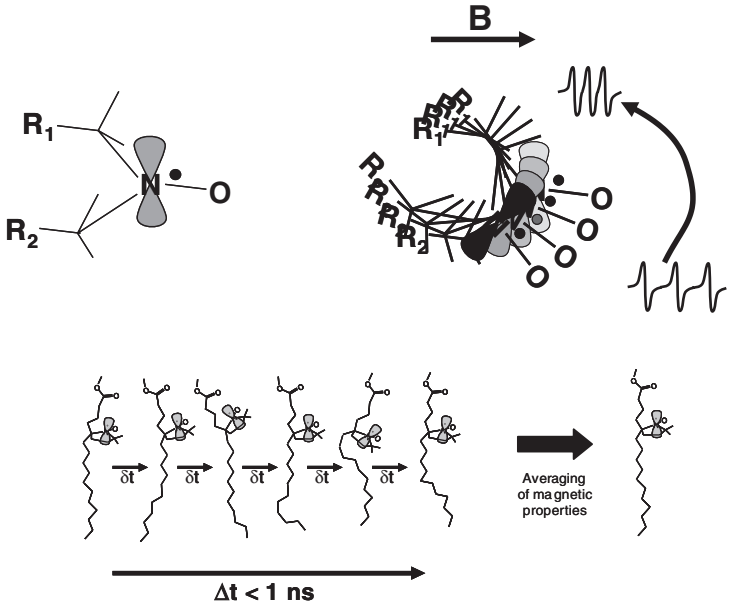

Figure 3 Schematic presentation of nitroxide moiety of a spin label (top left) of the origin of the sensitivity to orientation and rotational motion relative to magnetic field in the EPR experiment (top right) and of the partial averaging due to fast rotational motion of spin probe molecule and thus the nitroxide moiety (bottom).

molecular orbitals by modifying their optical properties. Spatial scale and time scale are very similar to EPR scales.

The advantage of IR spectroscopy is that the spectroscopic probes are not required. It reports on transitions between vibrational states of molecular groups present in the observed system, which depend on molecular conformations and interactions. Since the latter are based on the properties of the environment of the observed molecules, IR spectroscopy can be used to detect heterogeneous structure of a lipid membrane. Beside the molecular spatial scale, also the time scale in the picosecond range is appropriate.

2.1. Membrane Exploration by SL-EPR

Despite the fact that reporter molecules need to be artificially introduced into the membrane with SL-EPR, it is believed that the perturbation to the local molecular environment is small as the nitroxide-stable radical group size is effectively only the size of four methyl groups and the introduced molar concentration is low. Nitroxide group of a spin label has very anisotropic magnetic properties that originate in anisotropic electron probabilities that induce anisotropic magnetic properties of the spin probes. This affects the resonant line positions when the direction of the nitroxide group is changed relative to external magnetic field (Fig. 3, top right). Typical range of the components of the hyperfine coupling tensor is from 0.5 to 3.5 mT, which can induce the 7-fold shrinkage of the nitroxide triplet line when changing the orientation to magnetic field. Similarly, the anisotropy of Zeeman coupling would imply the line shift up to 1 mT when changing the direction to magnetic field.

When a fast rotational motion is introduced, i.e., when rotational reorientation is faster than the EPR time scale of a few nanoseconds, the interaction with magnetic field is partially averaged out according to the orientations allowed by reorientation potential (Fig. 3, bottom). Due to high anisotropy of magnetic tensors SL-EPR is highly sensitive also to molecular reorientation [27]. Note that in the slow motions regime the reorientation is too slow to affect the interaction with external magnetic field in EPR experiments. Note also, that the effect of lateral diffusion (range nm^2/ns) and the rotational motion of a liposome or a cell (also much slower than EPR time scale) also do not average out the local motional anisotropy. This means that the lineshape effect of the reorientation of a spin-label molecule at some position in the membrane is efficiently decoupled from lateral diffusion effect and the effect of the distribution of local membrane normal vectors relative to magnetic field. Therefore, the detection of local motional patterns in model or real membrane systems is allowed. In addition, SL-EPR is sensitive also to polarity and proticity of the local environment of the spin label as well as to local spin–spin interaction that depend also on the local concentrations of spin labels and/or other paramagnetic species [30].

Particular spectral response originates in each group of spin probes that exhibit similar motional properties and other properties of the local environment, i.e., possess a well-defined motional pattern. However, when the complexity is increased as in the case of the laterally heterogeneous sample, more than one

motional pattern should appear after introduction of the spin labels into a membrane, and several spectral components emerge superimposed in the experimental spectrum of a spin-labeled membrane. It is clear that only computer simulations can resolve a complex EPR spectrum defined by a large set of the spectral parameters of the superimposed spectral components [31–33]. By introduction of a special algorithm that helps to determine the complexity without predefining the number of spectral components in advance, the maximal number of motional patterns of four is usually applied. The only model, which can provide the spectral parameters without severe correlations (especially when superposition is added), is the anisotropic-wobbling cone model with fast-restricted partly averaged rotational motion [34], defined by the two anisotropy cone angles ϑ_0 and φ_0, which are multiplied and normalized by $\pi^2/4$ to get the free rotational space Ω. Although there exist much more accurate and generalized simulation models that are based on the generalized Liouville formalism [35], the chosen model managed to compromise the accuracy, the ability of being applied in inverse problem solving as well as the demand on computation time. The implemented simulation model derives resonant line distributions by solving the Hamiltonian equations for each direction to magnetic field with partially averaged magnetic tensors. This distribution is then used with absorption lineshape to calculate complex lineshape that depends on the rate and anisotropy of motion, local polarity, proticity and linewidth parameters. The complexity is taken into account by superposition of different spectral components originating in individual motional patterns/environments.

Since many spectral parameters have to be fitted, multi-run evolutionary optimization dHEO is applied (Fig. 4, 1. loop) [32,36], based on generational genetic (evolutionary) algorithm (EO), a stochastic population-based search

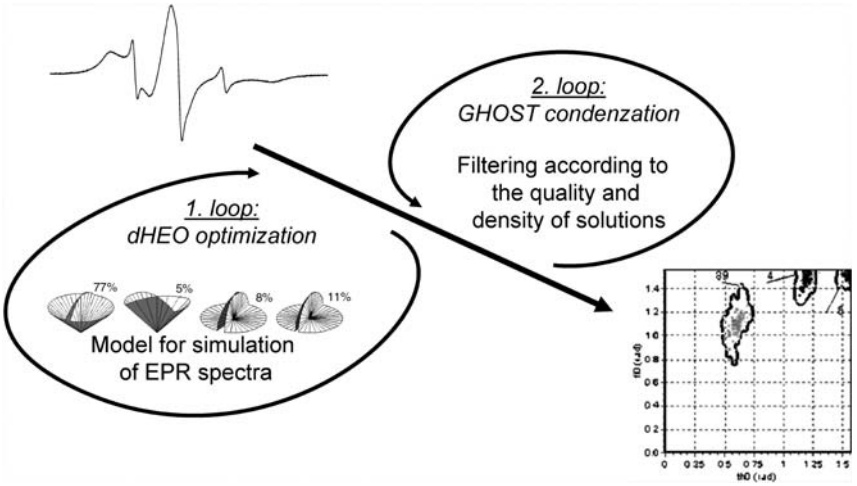

Figure 4 Schematic presentation of the analysis of EPR spectra by spectral simulation, hybrid evolutionary optimization dHEO and subsequent GHOST data condensation methodology resulting in the so called GHOST diagram and detection of spin labels' significant motional patterns.

method. Our implementation combines the benefits of the genetic algorithm and Downhill Simplex and is successful in both finding promising regions of solutions and extracting fine-tuned solutions [36]. In addition, starting population can be generated randomly and thus eliminating human input by enabling an automatic optimization. At the same time the stochastic nature of this optimization allows us to determine the errors in the spectral parameters independently of the covariance matrix analysis. Special shaking operator is implemented to speed up the characterization by maintaining diversity in single runs at the same time keeping the convergence level and in that way enabling extraction of more complex characterization with smaller number of runs [36]. The complete optimization method is implemented in the software package EPRSIM-C [37].

As the dHEO search methodology is stochastic, multiple optimization runs are required. The resulting multiple sets of spectroscopic data are condensed with the GHOST condensation method to extract the significant motional patterns for spin label in a membrane (Fig. 4, 2. loop) [34]. The solutions are smoothly filtered according to the goodness of fit as well as to the solution density defined by the neighborhood principle in the parameter space. These two criteria guarantee that only the good and the frequent solutions are taken into account. Finally, the filtered solutions are grouped together according to the neighborhood principle and thus condensed into a set of significant motional patterns.

Despite the robustness and power of the applied data analysis methodology the user should apply a series of measurements as a multidimensional experiment, in which for example various temperature series are measured at different concentrations of the membrane constituent or buffer properties. This can clarify the interpretation of the described complex data significantly. For example, it can help to decide about the significance of the patterns with smaller proportions as well as to distinguish several groups of solutions very closely in the solution space.

SL-EPR was successfully applied to many membrane systems to detect motional patterns and lateral heterogeneity. Labeling with a variety of possible spin probes (Fig. 5) was used in model membranes of liposomes, eukariotic cell membranes and even in membranes of living tissues. Usually, it is assumed that molecular probes feel macroscopical phase changes. However, they also undergo free energy minimization in their local environment meaning that they can respond differently to different interactions and temperature [38]. Especially, we want to stress that the phase transitions and other phenomena that are observed macroscopically can be differently detected at various levels from the interface region of lipid headgroups and sugar moieties of glycolipids to the lipophilic region of alkyl chains of the lipids. When membrane is constituted from more than one type of lipid, the lateral variation of the probe partitioning almost always appears in addition to lateral aggregation and domain formation. This does not only point to the properties of the spin probe molecules in the local lipid environment but also reminds the researcher that any molecule that will dissolve and partition in the lipid bilayer can spread in a very complicated manner. Consequently, it may become difficult to conclude about the biological relevance of such a molecule type especially in a complex environment of real cell membrane.

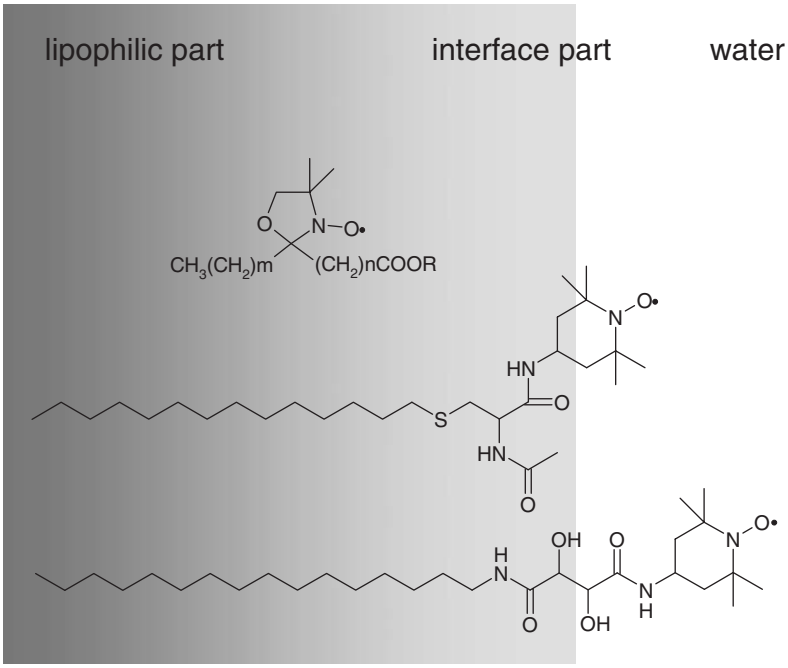

Figure 5 Schematic presentation of some typical spin labels applied for membrane research. Oxazolidine type of nitroxides -R-FASL m,n (top) and amphiphilic piperidine nitroxides (center and bottom) are presented. Approximate average location of the nitroxide group relative to lipophilic part, interface region or water environment is depicted with gray shades.

2.2. Membrane Exploration by ATR–FTIR Spectroscopy

The most commonly used infrared method in biophysical studies is transmission Fourier transform infrared (FTIR) spectroscopy. However, some problems can be encountered with this technique when using liquid samples. Water is an extremely strong absorber, so a high thickness of sample can lead to signal saturation. Even when very small sample cell spacers are used, the absorbance for dilute samples can be too high and subsequently the detector is no longer working in its linear regime. An alternative method is attenuated total reflection (ATR) FTIR [39]. In this method a solid or a liquid sample must be brought into contact with an internal reflection element (IRE), and the infrared beam is focused into the IRE. The light travels inside the IRE by means of a series of internal reflections from one surface of the IRE to the other, creating an exponentially decaying evanescent field outside the IRE. Absorption of the energy of the evanescent field by the sample provides ATR–FTIR spectra. For a schematic presentation of the ATR setup, see Fig. 6. The effective path length for this interaction depends on several parameters and is typically in the order of 1 μm (see below). Because of the small light penetration depth the ATR method is ideal for highly absorbing samples, for surfaces, and for thin film measurements.

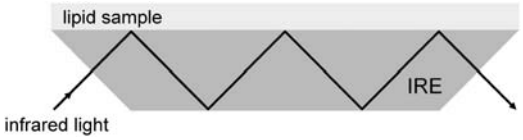

Figure 6 Schematic presentation of ATR–FTIR experimental setup. Lipid sample (either dried or hydrated) is prepared in a form of a membrane stack. Infrared light in the internal reflection element (IRE) is attenuated by the interaction of the sample with the evanescent field.

The penetration depth of infrared light in the sample is defined by properties of the sample and the IRE. It holds

$$d = \lambda / \left(2\pi n_{\mathrm{IRE}} \sqrt{\sin^2\theta - (n/n_{\mathrm{IRE}})^2} \right) \tag{1}$$

where d is the penetration depth, λ the wavelength of incident light, n_{IRE} the real refractive index of the internal reflection element (IRE), θ the angle of incidence and n the real refractive index of the sample. In our case the IRE was a trapezoidal germanium plate ($50 \times 10 \times 2$ mm) with an incidence angle of 45° yielding 25 internal reflections. Therefore, the penetration depth for lipid samples is between 0.2 and 0.7 μm for wavenumbers between 4000 and 800 cm^{-1} and can be estimated from equation (1) ($n_{\mathrm{IRE}} = 4.0$, $\theta = 45^\circ$, $n = 1.4$).

In ATR–FTIR studies of lipid samples an IRE is covered with lipid layer(s). A stack of oriented planar lipid bilayers (lipid multibilayers) is usually formed by placing lipids dissolved in chloroform on the IRE and evaporating the solvent [40]. In our case an alternative method was used, where a small amount of liposome suspension in water (at a lipid concentration of 20 mg/ml) was added onto the IRE and spread over the whole area. Thin stacks of lipid multibilayers were obtained by evaporating water. Experiments can either be conducted on dried or hydrated lipid multibilayers. By controlling the level of hydration lyotropic and other hydration-dependent properties of the system can be studied [41,42]. Additional information becomes available when polarized infrared light is used [40]. Infrared dichroism is a useful tool because the spectral information about molecular conformations and interactions is supplemented by information about molecular orientation.

Lately, more and more focus is put on the studies of single-lipid monolayers and bilayers, while solid supported membranes can be successfully used as models of cellular membranes [43]. A variety of techniques have been devised for preparation of supported membranes. Most of them include spreading of vesicles either directly on a solid surface or on a preformed lipid monolayer [43]. Lipid monolayers are conventionally deposited on the internal reflection plate by the Langmuir–Blodgett technique [44]. In such experiments the lipid packing density, the lipid phase, the orientational order parameter, the thickness of the water layer trapped between the membrane and the substrate and the number of trapped water molecules per lipid can be determined [45].

3. Membrane Hydration

Lipid hydration is of great importance in the studies of the lyotropic phase behavior of lipid/water systems and in the studies of the hydration forces between lipid bilayers [46,47]. The arrangement of the lipid headgroups perturbs the ordering and the dynamics of water molecules compared with the properties of bulk water [48]. This perturbed water is usually referred to as bound or interfacial water. The primary hydration layer of surface-adsorbed water differs from the subsequent layers of water (referred to as free water) because the polar surface strongly interacts with this first layer of water molecules *via* relatively strong water–substrate (solvent–solute) interactions [49]. Due to the small size of water molecules they fit well into the free volumes of the bilayer forming clusters of water molecules in a complex network of hydrogen bonds, which include also the phosphate and carbonyl groups of the lipid.

3.1. Effect of the Level of Hydration on the Membrane Properties Studied by SL-EPR

Effect of membrane hydration can be nicely detected on oriented membrane stack due to orientation/rotational sensitivity of EPR spectroscopy [50]. At the same time types of defects (unaligned membranes, pores, necks, passages, edges, cylinders, etc.) and modified motional patterns (ordered, disordered) can be detected (Fig. 7). It is interesting to note that even purely hydrated membranes

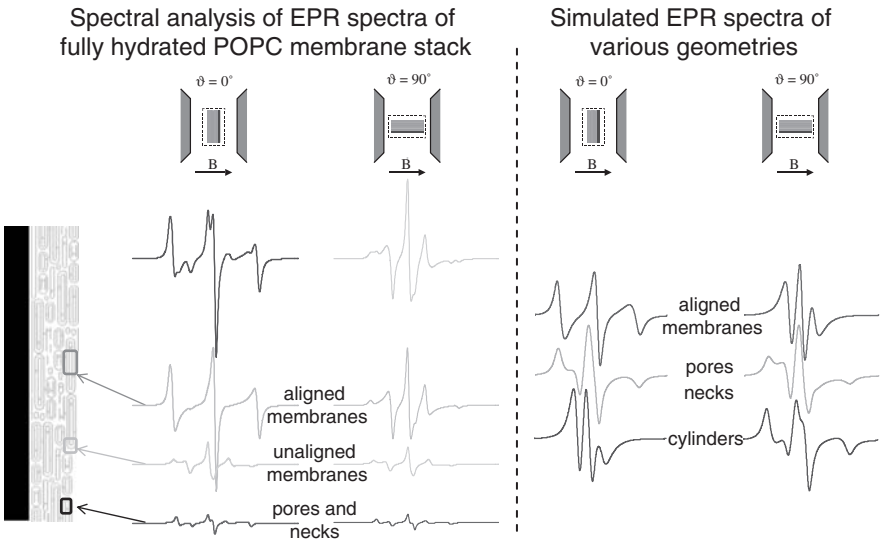

Figure 7 Comparison of EPR spectra of fully hydrated POPC membrane stack is shown for both orientations of oriented membranes relative to magnetic field (left). In addition, spectral lineshapes of typical defects in membrane stack are shown for both orientations to magnetic field (right).

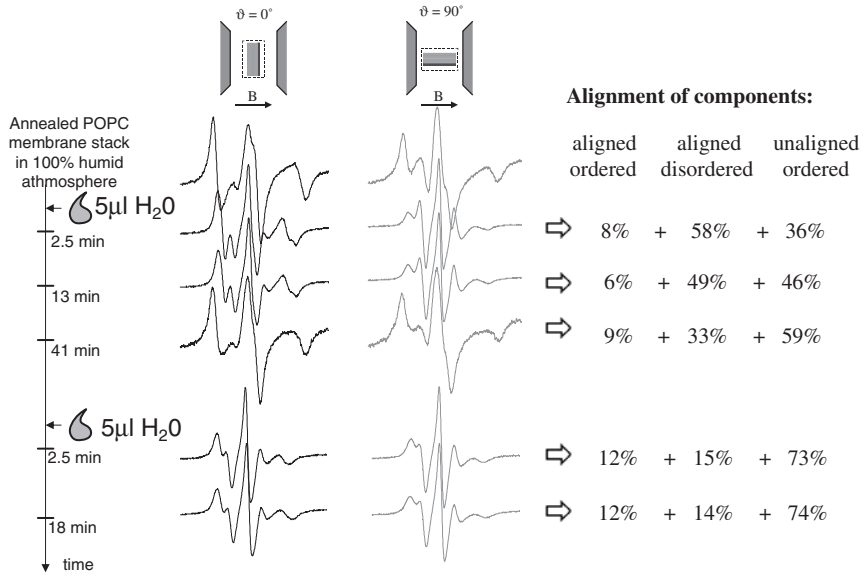

Figure 8 Time dependence of experimental EPR spectra of spin-labeled oriented membrane stack after addition of water to the POPC sample of stacked membranes that was previously annealed in 100% humid atmosphere for 24 h (left). The proportions of aligned (ordered and disordered) component as well as the unaligned component are shown as derived from EPR spectral simulations (right).

(annealed at 100% humidity) at temperature above the main phase transition reveal ordered phase, similar to the fully hydrated membranes prepared in excess water below temperature of the main phase transition.

The rigidifying membrane effect is not only limited to a membrane stack that is not accompanied by the excess of free water, but to some extent also to the supported membranes. If the support is very strong and very dense in lateral direction, it can drastically influence the fluid character of the lipid bilayer changing the lateral heterogeneity significantly. Forcing a membrane into a partially dehydrated state (without excess of free water) or supporting it solidly, such a membrane goes into non-natural state introducing numerous defects (pore, neck, linear edge effect, passage, etc.) due to constrained free-energy minimization. Since the local geometry of molecular distribution strongly affects EPR spectra it can be used to elucidate this effect. Moreover, the influence of the level of hydration of a membrane stack on the alignment can be traced with time (Fig. 8).

3.2. Application of ATR–FTIR Spectroscopy to Distinguish Free and Lipid-Bound Water

IR spectroscopy is suitable to study the structure of water surrounding lipid bilayers, while it is capable to characterize water properties on the molecular level. This method was extensively used to characterize the hydration sites of lipids [41,51,52]

and the properties of water molecules that bind to the headgroups [53,54]. Despite this extensive work, experimental data about the structure of water and the network of hydrogen bonds at the polar interface of lipid bilayers are relatively rare.

When lipid multibilayers were prepared for our ATR–FTIR experiments, the amount of lipids deposited on the IRE suffices to fill the whole penetration depth of the evanescent field with hydrated lipid multibilayers. Therefore, the bands in ATR–FTIR spectra of lipid samples hydrated in excess deuterated water (D_2O) corresponding to D_2O-stretching mode are not due to bulk water, but due to interlayer water trapped between subsequent lipid bilayers. Beside water molecules with bulk-like properties (free water), the interlayer water includes also bound water. It is demonstrated in Fig. 9A that the presence of bound water can be appreciated in ATR–FTIR spectra through comparison of D_2O-stretching modes for bulk deuterated water and for a hydrated lipid sample of DMPC. The change in the shape of the D_2O-stretching mode is in accordance with the change seen for hydrated reverse micelles with small diameters and indicates a strong perturbation of the hydrogen-bond network [55].

In addition, a comparison between the D_2O-stretching mode spectral region for DMPC and DMPC/Chol 0.4 samples is shown in Fig. 9B. The first interesting feature of this comparison is that the thickness of the water layer trapped between subsequent bilayers in DMPC/Chol 0.4 sample is significantly smaller than in the case of DMPC as judged from the lower intensity of the D_2O-stretching mode (see the inset of Fig. 9B). Moreover, when spectra are normalized to the same D_2O-stretching mode intensity, a difference in the shape of this mode can be appreciated (Fig. 9B). A few reasons might cause this difference to occur, e.g., a relatively higher amount of bound water for the DMPC/Chol 0.4 and/or perturbation of the hydrogen-bond network between water and DMPC by cholesterol.

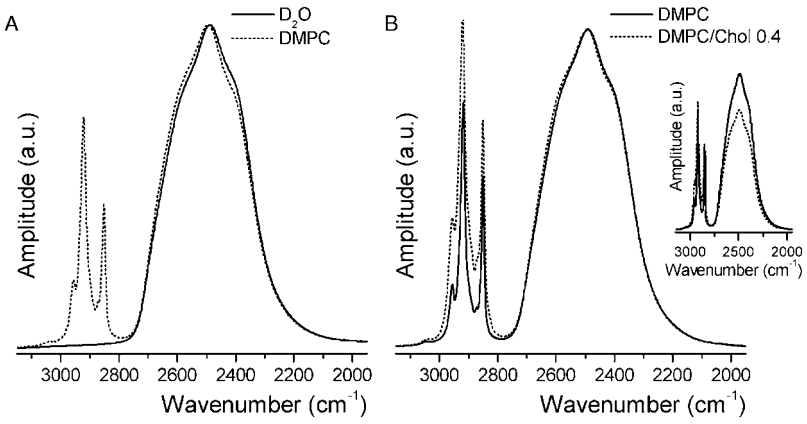

Figure 9 Comparison of the shape of D_2O-stretching mode for different samples. (A) Comparison of bulk D_2O and of interlayer D_2O in a stack of DMPC bilayers on IRE, $T = 24\ ^{\circ}C$. Spectra were normalized to the same amplitude. (B) Comparison between spectra of DMPC and DMPC/Chol 0.4 normalized to the same amplitude, $T = 9\ ^{\circ}C$. Inset shows spectra without normalization.

4. Membrane Heterogeneity Characterization by SL-EPR

4.1. Comparison of Characterization by Different Spin Probes in Model Membranes

The "biased" reporting of the spin probes originates in the fact that spin probes are not infinitesimally small and they interact with the surrounding molecules. Although it is thought that spin labels copy the major motional patterns from natural molecular analogs, distribute similarly as their natural molecular analogs and have only a little influence on the local molecular arrangements when low concentrations are used, the interpretation of the experimental data has to be done with great care.

In the following example a small segment of a comparative study of reporting of different spin probes about the same model systems is presented. Here the simplicity of the model membrane is a precondition to detect "biased" reporting. First, single-lipid membranes were used, prepared from distearoyl-phosphatidylcholine (DSPC), dipalmitoyl-phosphatidylcholine (DPPC), dimyristoyl-phosphatidylcholine (DMPC), palmitoyl-oleoyl-phosphatidyl choline (POPC) and dioleoyl-phosphatidylcholine (DOPC). These lipids were chosen to represent different lengths and saturation of alkyl chains but the same headgroup. Next, cholesterol was added to induce different interactions and consequently different motional patterns. Spin probes based on palmitic acid derivatives with different headgroups and nitroxide positions were applied: MeFASL 10,3, MeFASL 2,11, HFASL 10,3 and HFASL 2,11. For all the samples the temperature series were acquired in the interval crossing the main phase transition. Spectra of a typical temperature series are shown in Fig. 10. The steps of typical spectral analysis are schematically presented in Fig. 11 for one temperature series. All the samples were analyzed in a similar way. The "biased" reporting was searched among the differences in the

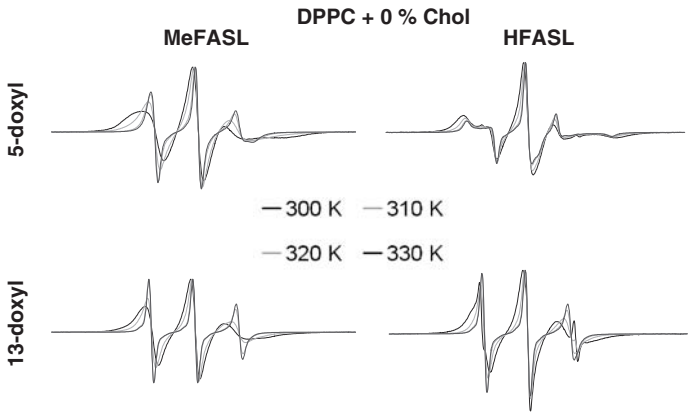

Figure 10 Examples of EPR spectra for 5-doxyl and 13-doxyl MeFASL and HFASL spin probes in DPPC membranes in the 300–330 K temperature range.

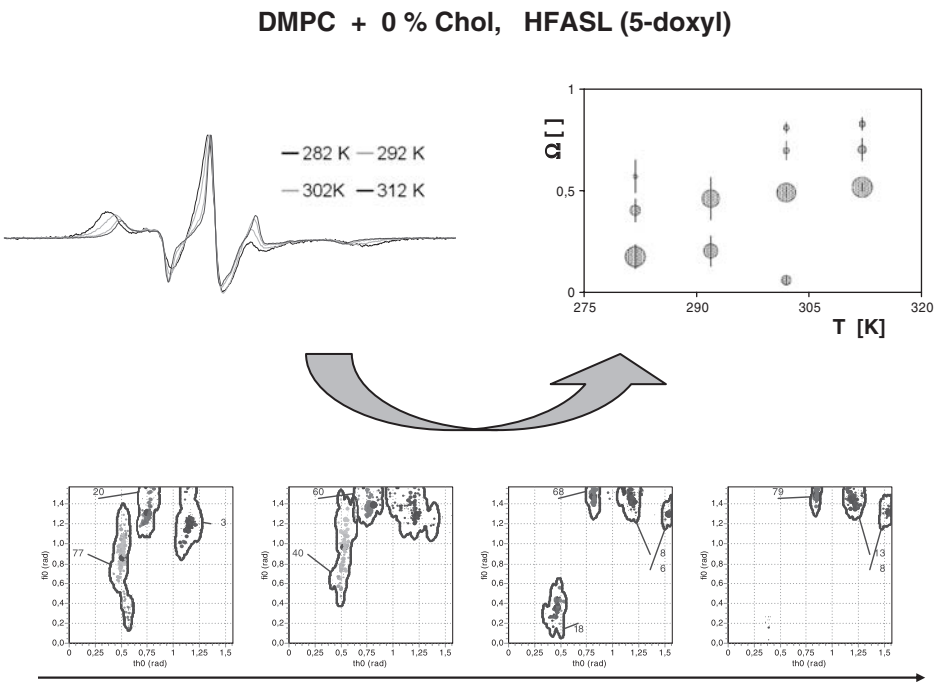

Figure 11 An example of spectral analysis and the GHOST condensation procedure. Individual steps (spectra acquisition, GHOST condensation and final condensed results in terms of the free rotational space $\Omega = \vartheta_0\varphi_0/(\pi/2)^2$) are shown for temperature series of 5-doxyl HFASL in DMPC. Other spectra were analyzed in a similar way.

temperature and composition series. Such differences if any should emerge in different ways for limited conditions for each probe.

The data series were carefully compared and interpreted to explain the interactions at molecular level taking into account two details specifically: dissociation of the headgroup in case of HFASL and weak vertical anchoring in the case of MeFASL spin labels. The non-dissociated form of HFASL acts like MeFASLs headgroup as seen in Fig. 12. The dissociated form of HFASL 10,3 is vertically fixed or pushed from the membrane and dissolved in water by forming the micelles, as seen in the case of HFASL 2,11 in the presence of cholesterol (Fig. 13). Note that for the same label in the bilayer without cholesterol (Fig. 12), the partitioning to the water is much weaker, indicating that the dissociation is less probable. One can even speculate that the spin probe molecule with nitroxide group placed at the end of the fatty acid chain sunk inside the membrane and thus prevents dissociation as seen in Fig. 13 by lower amounts of completely unrestricted motional patterns. On the contrary, the anchoring effect of MeFASL family is weaker especially at low temperatures.

Taking these details into account we can detect the conditions where differences in reporting about the membrane heterogeneity will occur for different types of spin probes. At the same time, the sensitivity of particular spin probes to the

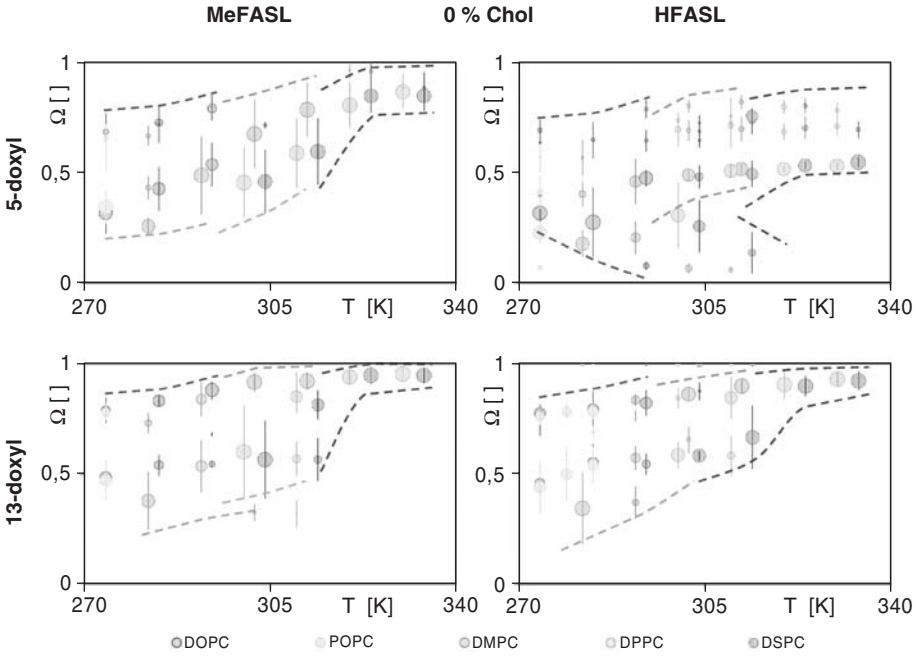

Figure 12 Condensed results of the significant motional patterns of the 5-doxyl and 13-doxyl MeFASL and HFASL spin probes in DSPC, DPPC, DMPC, POPC and DOPC membranes without cholesterol. The temperature range was from 20 K below to 20 K above the main phase transition temperature of the corresponding lipid. The free rotational space Ω is shown on the *y*-axis, as the main characteristics of the rotational restriction and a measure of anisotropy of rotational motion of a spin probe (please see plate no. 3 in the color section).

variation of the local composition at certain temperature can be checked. The latter is physiologically relevant since the same happens when spin probe or any other membrane-soluble substance diffuses laterally through the regions with different local compositions.

The most striking effect seen in Figs. 12 and 13 is the absolute character of motional patterns that are available at certain temperature independently on the local lipid composition. The most unrestricted and the most restricted patterns follow the quasi-linear temperature dependence indicated with dashed colored lines following the same color legend as in the presentation of the solutions in the same graph. This fact is very surprising since the possible motional patterns are the same at certain temperature for the lipids with long saturated acyl chains forming the S phase or for the lipids with short or unsaturated chains that are in the Ld phase. However, it is then exactly the composition which is responsible of the range of patterns realized by a molecule embedded in the lipid bilayer. It should be stressed that the lines of the most restricted motional patterns for all labels end up abruptly just above the physiological temperatures without merging with the lines of the most unrestricted motional patterns. It seems that this reflects the real molecular picture since it does not depend on the type of spin probe.

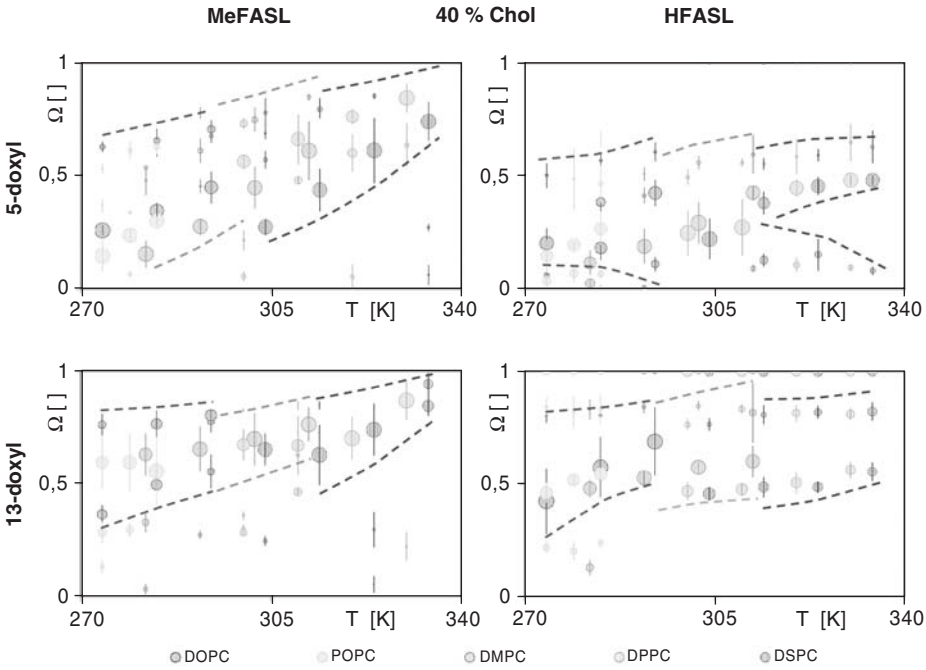

Figure 13 Condensed results of the significant motional patterns of the 5-doxyl and 13-doxyl MeFASL and HFASL spin probes in DSPC, DPPC, DMPC, POPC and DOPC membranes with 40 molar% of cholesterol. The temperature range was from 20 K below to 20 K above the main phase transition temperature of the corresponding lipid (without cholesterol). The free rotational space Ω is shown on the *y*-axis, as the main characteristics of the rotational restriction and a measure of anisotropy of rotational motion of a spin probe (please see plate no. 4 in the color section).

In addition, one can also see the well-known phenomena that the order of the acyl chain, i.e., the restrictions of the rotational motion, decreases with the position as detected in the cases of all the spin probes. This difference is even more striking for the lipid bilayers with cholesterol as indicated by the line of the allowed most restricted motional patterns (Fig. 13).

4.2. Effect of Spin Probe Partitioning on Membrane Heterogeneity Characterization

The proportion of a particular spectral component, determined by EPR spectra decomposition [13], is not necessarily the same as the fraction of a corresponding lipid phase in a membrane, due to the partitioning properties of spin probe between different lipid phases [56]. The DMPC/Chol system was studied. Spin probe MeFASL(10,3) (methyl ester of 5-doxyl palmitate) was used.

From known phase diagrams fractions of particular lipid phases can be determined at certain temperature and composition by the so called lever rule [56]. For temperatures above the temperature of the main phase transition T_m ($T > T_m$), at which the system is in the phase coexistence region Ld+Lo, it holds for the fraction

of lipids in the Ld phase

$$f^{\mathrm{Ld}}(T) = \frac{x^{\mathrm{Lo}}_{\mathrm{Chol}}(T) - x^{0}_{\mathrm{Chol}}}{x^{\mathrm{Lo}}_{\mathrm{Chol}}(T) - x^{\mathrm{Ld}}_{\mathrm{Chol}}(T)} \tag{2}$$

where $x^{\mathrm{Lo}}_{\mathrm{Chol}}(T)$ and $x^{\mathrm{Ld}}_{\mathrm{Chol}}(T)$ represent cholesterol mole fractions at the corresponding phase boundaries, and x^{0}_{Chol} the mole fraction of cholesterol in the sample.

A spectrum $I(B)$ is decomposed into a different number of spectral components $I_i(B)$ related to the lipid phases (domain types)

$$I(B) = \sum_i w^i I_i(B) \tag{3}$$

where w^i is proportion of spectral component i and B the magnetic field. Since phase diagrams for DMPC/Chol shows coexistence of two lipid phases at most (Fig. 2), EPR spectra were decomposed into two spectral components ($i = 1, 2$).

It can be seen from Fig. 14A that we can qualitatively describe a spectrum from a two phase coexistence region, e.g., a spectrum of DMPC/Chol 0.2 sample, which is at $T > T_{\mathrm{m}}$ in the Ld+Lo coexistence region, as a superposition of spectra from DMPC/Chol 0.1 and DMPC/Chol 0.4 samples that correspond to single-phase regions. In order to make this procedure more precise, the spectra of samples with composition corresponding to the mole fraction of cholesterol at the phase boundary would have to be taken into account. An example of EPR spectra decomposition of the same experimental spectrum to two spectral components corresponding to the population of spin probes in disordered and ordered lipid environment is shown in Fig. 14B.

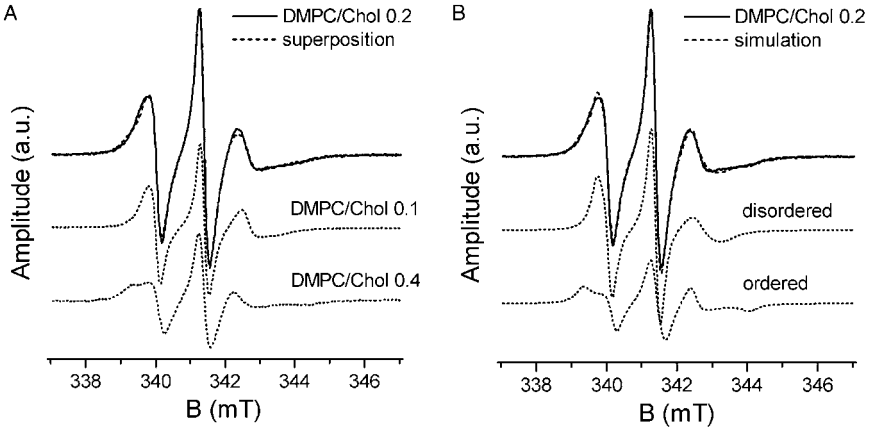

Figure 14 Comparison of experimental and calculated EPR spectra. (A) Comparison of the experimental spectrum of spin-labeled DMPC/Chol 0.2 liposomes at temperature 33 °C ($T > T_{\mathrm{m}}$), corresponding to the coexistence region Ld+Lo, with a superposition of the spectra corresponding to the single-lipid phase regions DMPC/Chol 0.1 (the Ld phase) and DMPC/Chol 0.4 (the Lo phase). (B) Comparison of the experimental EPR spectrum of DMPC/Chol 0.2 ($T = 33$ °C K, $T > T_{\mathrm{m}}$) compared with simulated (fitted) spectrum. The fitted spectrum is decomposed into two spectral components corresponding to the coexisting population of disordered (the Ld phase) and ordered lipids (the Lo phase).

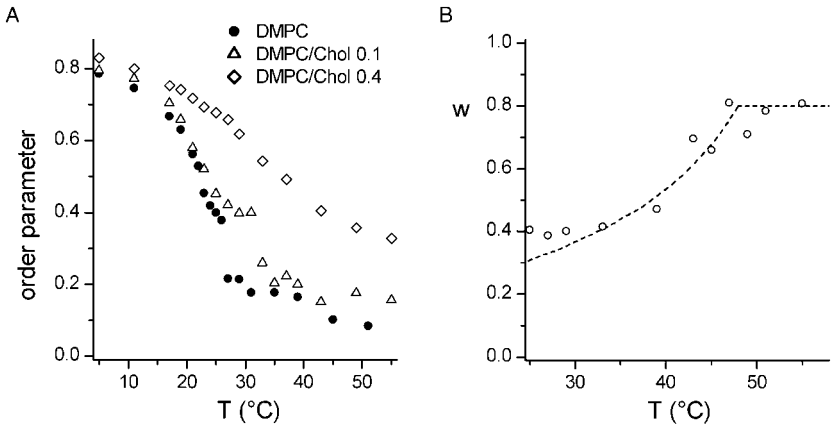

Figure 15 Temperature dependence of parameters obtained by EPR spectra decomposition for different DMPC/Chol samples. (A) Order parameter of the spectral component corresponding to the population of ordered lipids. Estimate of uncertainty in order parameter is ± 0.02. (B) Measured proportions of the spectral component corresponding to the population of disordered lipids (points) and calculated fraction of lipids in the Ld phase (line) for the mixture DMPC/Chol 0.2. Estimate of uncertainty in measured values of proportion is ± 0.05.

The temperature dependence of order parameter, reporting about the time-averaged angular fluctuation of the acyl-chain segment where spin label (in our case nitroxide radical) is attached to the spin probe molecule, was extracted from the recorded EPR spectra by spectral simulations (Fig. 15A). Above $T_m = 24\,^{\circ}C$ for pure DMPC [57] order parameter drops discontinuously as expected due to the phase transition S→Ld. Similarly for DMPC/Chol 0.1 samples order parameter shows a discontinuous drop close to the temperature corresponding to the completion of the phase separation Ld+Lo→Ld (Fig. 2). On the contrary, only a steady decrease can be observed in the order parameter for DMPC/Chol 0.4, in accordance with the presence of only one lipid phase for all temperatures (Fig. 2).

In Fig. 15B for DMPC/Chol 0.2 sample (at $T > T_m$) the comparison between the temperature dependence of experimentally determined proportion of spectral component corresponding to the population of disordered lipids according to equation (3) and calculated values of fraction for the Ld phase according to equation (2) is shown. The temperature at which proportion increases to the maximum value agrees well with the temperature corresponding to the completion of phase separation Ld+Lo→Ld (Fig. 2). Since proportions agree relatively well with the calculated fractions, it seems that our spin probe partitions approximately uniformly between the Ld and the Lo phase [56].

5. Membrane Heterogeneity Characterization by ATR–FTIR Spectroscopy

The IR spectral features most sensitive to phospholipid molecular structure and interactions arise from the vibrations of the acyl chains. There are several modes

sensitive to chain conformation and interaction. The methylene stretching frequencies qualitatively monitor both lipid conformational order and acyl-chain packing [58]. As these modes are among the most intense in the IR spectra of lipids and membranes, they have been widely used for lipid conformational studies.

As an example, the temperature dependence of the methylene antisymmetric stretching band peak position is shown in Fig. 16 for DMPC/Chol system. For pure DMPC results show a strong jump in the peak frequencies above T_m (Fig. 16). For samples with Chol 0.2 the increase of the peak position with temperature becomes steeper above T_m and then less steep again close to the temperature corresponding to the completion of phase separation Ld+Lo→Ld (Fig. 2). Samples with Chol 0.4 show a linear increase in frequency (Fig. 16), due to the presence of only one lipid phase, i.e., the Lo phase, for all temperatures (Fig. 2).

A potentially interesting region of the IR spectrum for studying properties of different lipid phases is the carbonyl absorption band arising from the stretching vibrations of ester carbonyl groups of glycerolipids. The band is strong and occurs in a region essentially free of significant absorptions by groups. Carbonyl bands are conformationally sensitive, reflect the level of hydration at the membrane interface and are influenced by hydrogen bonding [59]. It was noted before that the band shape changes, if the lipid undergoes the main phase transition [60].

To highlight differences in the shape of the carbonyl band for samples with different amounts of cholesterol, overlaid spectra normalized to the same area are presented in Fig. 17A. The most obvious difference is the increased asymmetry in the shape of the carbonyl band for samples with cholesterol and a much larger carbonyl bandwidth for samples with Chol 0.4 compared to samples without cholesterol. The increased asymmetry in the presence of cholesterol [61] and broadening [62] was already noted before for the DPPC/Chol system.

Similarly to EPR spectra of spin-labeled liposomes, also ATR–FTIR spectra of lipid multibilayers at appropriate temperature and composition are expected to

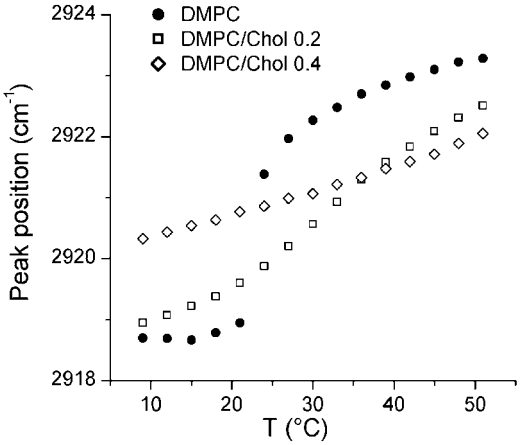

Figure 16 Temperature dependence of methylene antisymmetric stretching band peak position for DMPC/Chol samples with different mole fractions of cholesterol. Samples were prepared in excess D_2O. Estimate of the uncertainty in the peak position is ± 0.1 to $\pm 0.2\ cm^{-1}$.

reflect the coexistence of different lipid phases. As shown in Fig. 17B a spectrum from a sample exhibiting phase coexistence can be qualitatively described as a superposition of spectra from samples that correspond to single phases. If the ATR–FTIR spectra of samples with composition corresponding to the mole fraction of cholesterol at the phase boundary were taken into account, the agreement between experimental and calculated spectrum should be better.

The temperature dependence of the carbonyl band peak position for samples with different mole fractions of cholesterol is shown in Fig. 18A. For pure DMPC

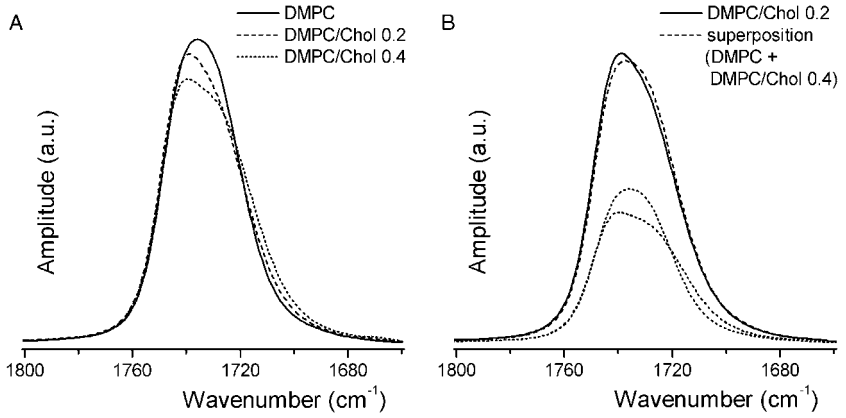

Figure 17 Dependence of carbonyl band shape in DMPC/Chol samples on mole fraction of cholesterol. Samples were prepared in excess D_2O, $T = 9\ ^{\circ}C$ ($T < T_m$). (A) Comparison of the carbonyl band shape for samples with different amount of cholesterol. Absorption bands were normalized to the same area. (B) Comparison of the carbonyl band shape of DMPC/Chol 0.2, corresponding to the coexistence region S+Lo, with a superposition of the carbonyl bands corresponding to the single-lipid phase regions DMPC (the S phase) and DMPC/Chol 0.4 (the Lo phase).

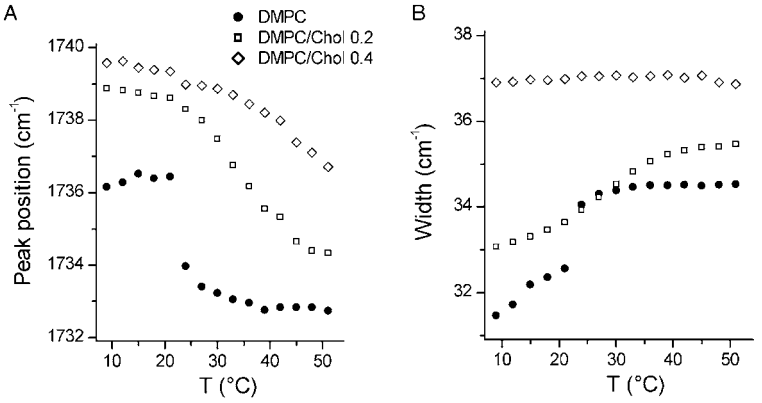

Figure 18 Temperature dependence of carbonyl band (A) peak position and (B) half-bandwidth for DMPC/Chol samples with different mole fractions of cholesterol. Samples were prepared in excess D_2O. Estimate of the uncertainty for both parameters is around $\pm 0.3\ cm^{-1}$.

a jump of the peak position to lower frequencies occurs near the temperature of the main phase transition T_m (Fig. 18A). For DMPC/Chol 0.2 samples the slope changes its steepness above T_m again (Fig. 18A). Samples with Chol 0.4 show more or less steady decrease of the peak position with temperature (Fig. 18A). Similar lipid-phase-specific behavior can also be observed for the temperature dependence of the half-bandwidth of carbonyl band (Fig. 18B). It can be concluded from comparison of Figs. 16 and 18 that the shapes of the curves of the temperature dependence of the peak position and of the half-bandwidth of the carbonyl band report on the lipid phase of the sample and reflect conformational changes in the bilayer.

6. Conclusions

It was shown that SL-EPR in combination with sophisticated simulations and data analysis techniques developed in the recent decade became a powerful methodology for membrane exploration. In addition, ATR–FTIR method was demonstrated to be suitable for examining hydrated lipid bilayers.

The results obtained by SL-EPR on supported membranes or dehydrated membranes indicate that the generalization to the biological membranes has to be done carefully. Full interaction scheme at the local molecular level has to match the one in fully hydrated lipid bilayer system prepared in excess free water to enable direct predictions in the more complex environments like biological membranes. Furthermore, the ATR–FTIR spectroscopy can be used to examine water structure adjacent to lipid bilayers, while it is possible to appreciate the presence of bound water.

It can be concluded that the molecular picture of lipid bilayer is more complex than a simple classification to different lipid phases. The molecular probing by SL-EPR reveals much more, from the local interactions to partitioning and composition, making this technique a powerful tool in exploration of membrane heterogeneity. Moreover, also ATR–FTIR spectroscopy is appropriate and complementary for this purpose. It was shown that in mixtures of phosphatidylcholines and cholesterol beside the acyl-chain modes also the carbonyl band is useful to reveal the presence of different lipid phases.

ACKNOWLEDGEMENTS

The authors acknowledge the financial support from the state budget by the Slovenian Research Agency (programme no. P1-0060, project no. J1-6581 and Z1-9502). The part of the work dealing with the ATR–FTIR spectroscopy was carried out with the financial support of the Sincrotrone Trieste. We thank Prof. Peter Laggner and Dr. Heinz Amenitsch for valuable suggestion regarding the work on SL-EPR on oriented membranes. We thank Iztok Urbančič and Nace Zidar for carrying out the experimental work concerning detection of biased spin probe reporting. We thank Dr. Luca Quaroni for the help on the research conducted with infrared spectroscopy. Some of the work was done in collaboration with different research groups enabled by the financial support from EC COST D22 and COST P15 Actions.

REFERENCES

[1] M. Bloom, J.L. Thewalt, Time and distance scales of membrane domain organization, Mol. Membr. Biol. 12 (1995) 9–13.
[2] K. Jorgensen, J.H. Ipsen, O.G. Mouritsen, M.J. Zuckermann, The effect of anaesthetics on the dynamic heterogeneity of lipid membranes, Chem. Phys. Lipids 65 (1993) 205–216.
[3] K. Jørgensen, O.G. Mouritsen, Phase separation dynamics and lateral organization of two-component lipid membranes, Biophys. J. 69 (1995) 942–954.
[4] C. Leidy, W.F. Wolkers, K. Jørgensen, O.G. Mouritsen, J.H. Crowe, Lateral organization and domain formation in a two-component lipid membrane system, Biophys. J. 80 (2001) 1819–1828.
[5] E.J. Shimshick, H.M. McConnell, Lateral phase separation in phospholipid membranes, Biochemistry 12 (1973) 2351–2360.
[6] P.F.F. Almeida, W.L.C. Vaz, T.E. Thompson, Lateral diffusion in the liquid phases of dimyristoylphosphatidylcholine/cholesterol lipid bilayers: a free volume analysis, Biochemistry 31 (1992) 6739–6747.
[7] B.R. Copeland, H.M. McConnell, The rippled structure in bilayer membranes of phosphatidylcholine and binary mixtures of phosphatidylcholine and cholesterol, Biochim. Biophys. Acta 599 (1980) 95–109.
[8] T.P.W. McMullen, R.N. McElhaney, New aspects of the interaction of cholesterol with dipalmitoylphosphatidylcholine bilayers as revealed by high-sensitivity differential scanning calorimetry, Biochim. Biophys. Acta 1234 (1995) 90–98.
[9] S. Karmakar, V.A. Raghunathan, Cholesterol-induced modulated phase in phospholipid membranes, Phys. Rev. Lett. 91 (2003) 098102.
[10] R. Welti, M. Glaser, Lipid domains in model and biological membranes, Chem. Phys. Lipids 73 (1994) 121–137.
[11] M. Edidin, Lipid microdomains in cell surface membranes, Curr. Opin. Struct. Biol. 7 (1997) 528–532.
[12] F.R. Maxfield, Plasma membrane microdomains, Curr. Opin. Cell Biol. 14 (2002) 483–487.
[13] Z. Arsov, M. Schara, J. Štrancar, Quantifying the lateral lipid domain properties in erythrocyte ghost membranes using EPR-spectra decomposition, J. Magn. Reson. 157 (2002) 52–60.
[14] M. Ge, K.A. Field, R. Aneja, D. Holowka, B. Baird, J.H. Freed, Electron spin resonance characterization of liquid ordered phase of detergent-resistant membranes from RBL-2H3 cells, Biophys. J. 77 (1999) 925–933.
[15] D.A. Brown, E. London, Structure and function of sphingolipid- and cholesterol-rich membrane rafts, J. Biol. Chem. 275 (2000) 17221–17224.
[16] G.J. Schütz, G. Kada, V.P. Pastushenko, H. Schindler, Properties of lipid microdomains in a muscle cell membrane visualized by single molecule microscopy, EMBO J. 19 (2000) 892–901.
[17] J. Štrancar, M. Schara, S. Pečar, New EPR method for cellular surface characterization, J. Membr. Biol. 193 (2003) 15–22.
[18] F.J. Sharom, C.W.M. Grant, A model for ganglioside behaviour in cell membrane, Biochim. Biophys. Acta 507 (1978) 280–293.
[19] M.W. Peters, K.R. Barber, C.W.M. Grant, Lateral distribution of gangliosides in bilayer membranes: lipid and ionic effects, J. Neurosci. Res. 12 (1984) 343–353.
[20] L.A. Bagatolli, E. Gratton, G.D. Fidelio, Water dynamics in glycosphingolipid aggregates studied by LAURDAN fluorescence, Biophys. J. 75 (1998) 331–341.
[21] E. Bertoli, M. Masserini, S. Sonnino, R. Ghidoni, B. Cestaro, G. Tettamanti, Electron paramagnetic resonance studies on the fluidity and surface dynamics of egg phospatidylcholine vesicles containing gangliosides, Biochim. Biophys. Acta 467 (1981) 196–202.
[22] H. Beitinger, V. Vogel, D. Möbius, H. Rahmann, Surface potentials and electric dipole moments of ganglioside and phospholipid monolayer: contribution of the polar headgroup at the water/lipid interface, Biochim. Biophys. Acta 984 (1989) 293–300.
[23] M. Shinitzky, Membrane fluidity and cellular functions, in: M. Shinitzky, (Ed.), Physiology of Membrane Fluidity, Vol. 1, CRC Press, Boca Raton, 1984, pp. 1–51.

[24] D. Marsh, Lipid-protein interactions and heterogeneous lipid distribution in membranes, Mol. Membr. Biol. 12 (1995) 59–64.
[25] Z. Arsov, M. Schara, M. Zorko, J. Štrancar, The membrane lateral domain approach in the studies of lipid-protein interaction of GPI-anchored bovine erythrocyte acetylcholinesterase, Eur. Biophys. J. 33 (2004) 715–725.
[26] H. Schindler, J. Seelig, EPR spectra of spin labels in lipid bilayers, J. Chem. Phys. 59 (1973) 1841–1850.
[27] S.P. Van, G.B. Birelli, O.H. Griffith, Rapid anisotropic motion of spin labels: models for motion averaging of the ESR parameters, J. Magn. Reson. 15 (1974) 444–459.
[28] J.R. Lakowicz, Fluorescence spectroscopic investigations of the dynamic properties of proteins, membranes and nucleic acids, J. Biochem. Biophys. Methods 2 (1980) 91–119.
[29] C. Ho, B.W. Williams, C.D. Stubbs, Analysis of cell membrane micro-heterogeneity using the fluorescence lifetime of DPH-type fluorophores, Biochim. Biophys. Acta 1104 (1992) 273–282.
[30] H.J. Steinhoff, A. Savitsky, C. Wegener, M. Pfeiffer, M. Plato, K. Möbius, High-field EPR studies of the structure and conformational changes of site-directed spin labeled bacteriorhodopsin, Biochim. Biophys. Acta 1457 (2000) 253–262.
[31] J. Štrancar, M. Šentjurc, M. Schara, Fast and accurate characterization of biological membranes by EPR spectral simulations of nitroxides, J. Magn. Reson. 142 (2000) 254–265.
[32] B. Filipič, J. Štrancar, Tuning EPR spectral parameters with a genetic algorithm, Appl. Soft Comput. 1 (2001) 83–90.
[33] J. Štrancar, T. Koklič, Z. Arsov, Soft picture of lateral heterogeneity in biomembranes, J. Membr. Biol. 196 (2003) 135–146.
[34] J. Štrancar, T. Koklič, Z. Arsov, B. Filipič, D. Stopar, M.A. Hemminga, Spin label EPR-based characterization of biosystem complexity, J. Chem. Inf. Model. 45 (2005) 394–406.
[35] D.J. Schneider, J.H. Freed, Calculating slow motional magnetic resonance spectra: a user's guide, in: L.J. Berliner, J. Reuben (Eds.), Biological Magnetic Resonance, Vol. 8: Spin Labeling, Theory and Applications, Plenum Press, New York, 1989, pp. 1–76.
[36] A.A. Kavalenka, B. Filipič, M.A. Hemminga, J. Štrancar, Speeding up a genetic algorithm for EPR-based spin label characterization of biosystem complexity, J. Chem. Inf. Model. 45 (2005) 1628–1635.
[37] J. Štrancar, EPRSIM-C Version 6.2., 1996–2007, http://www.ijs.si/ijs/dept/epr/EPRSIMC_overview.htm.
[38] J. Mravljak, J. Konc, M. Hodošček, T. Šolmajer, S. Pečar, Spin-labeled alkylphospholipids in a dipalmitoylphosphatidylcholine bilayer: molecular dynamics simulations, J. Phys. Chem. B Condens. 110 (2006) 25559–25561.
[39] N.J. Harrick, Internal Reflection Spectroscopy, John Wiley & Sons, New York, 1967.
[40] U.P. Fringeli, The structure of lipids and proteins studied by attenuated total reflection (ATR) infrared spectroscopy, II. Oriented layers of a homologous series: phosphatidylethanolamine to phosphatidylcholine, Z. Naturforsch. 32c (1977) 20–45.
[41] J. Grdadolnik, J. Kidric, D. Hadzi, Hydration of phosphatidylcholine reversed micelles and multilayers – an infrared spectroscopic study, Chem. Phys. Lipids 59 (1991) 57–68.
[42] H. Binder, The molecular architecture of lipid membranes – new insights from hydration-tuning infrared linear dichroism spectroscopy, Appl. Spectrosc. Rev. 38 (2003) 15–69.
[43] E. Sackmann, Supported membranes: scientific and practical applications, Science 271 (1996) 43–48.
[44] S.A. Tatulian, Structural effects of covalent inhibition of phospholipase A2 suggest allosteric coupling between membrane binding and catalytic sites, Biophys. J. 84 (2003) 1773–1783.
[45] S.A. Tatulian, Attenuated total reflection Fourier transform infrared spectroscopy: a method of choice for studying membrane proteins and lipids, Biochemistry 42 (2003) 11898–11907.
[46] J. Milhaud, New insights into water-phospholipid interactions, Biochim. Biophys. Acta 1663 (2004) 19–51.
[47] S. Leikin, V.A. Parsegian, D.C. Rau, R.P. Rand, Hydration forces, Annu. Rev. Phys. Chem. 44 (1993) 369–395.

[48] K. Gawrisch, D. Ruston, J. Zimmerberg, V.A. Parsegian, R.P. Rand, N. Fuller, Membrane dipole potential, hydration forces, and the ordering of water at membrane surfaces, Biophys. J. 61 (1992) 1213–1223.
[49] J.N. Israelachvili, H. Wennerström, Role of hydration and water structure in biological and colloidal interactions, Nature 376 (1996) 219–225.
[50] M. Rappolt, H. Amenitsch, J. Štrancar, C.V. Teixeira, M. Kriechbaum, G. Pabst, M. Majerowicz, P. Laggner, Phospholipid mesophases at solid interfaces: in-situ X-ray diffraction and spin-label studies, Adv. Colloid Interface Sci. 111 (2004) 63–77.
[51] J.L.R. Arrondo, F.M. Goni, J.M. Macarulla, Infrared spectroscopy of phosphatidylcholines in aqueous suspensions. A study of the phosphate group vibrations, Biochim. Biophys. Acta 794 (1984) 165–168.
[52] L. Ter-Minassian-Saraga, E. Okamura, J. Umemura, T. Takenaka, Fourier transform infrared-attenuated total reflection spectroscopy of hydration of dimyristoylphosphatidylcholine multibilayers, Biochim. Biophys. Acta 946 (1988) 417–423.
[53] J. Grdadolnik, J. Kidric, D. Hadzi, An FT-IR study of water hydrating dipalmitoylphosphatidylcholine multibilayers and reversed micelles, J. Mol. Struct. 322 (1994) 93–103.
[54] H. Binder, Water near lipid membranes as seen by infrared spectroscopy, Eur. Biophys. J., DOI:10.1007/s00249-006-0110-6.
[55] D. Cringus, J. Lindner, M.T.W. Milder, M.S. Pshenichnikov, P. Vöhringer, D.A. Wiersma, Femtosecond water dynamics in reverse micellar nanodroplets, Chem. Phys. Lett. 408 (2005) 162–168.
[56] Z. Arsov, J. Štrancar, Determination of partition coefficient of spin probe between different lipid membrane phases, J. Chem. Inf. Model. 45 (2005) 1662–1671.
[57] J.M. Holopainen, J. Lemmich, F. Richter, O.G. Mouritsen, G. Rapp, P.K.J. Kinnunen, Dimyristoylphosphatidylcholine/C16:0-ceramide binary liposomes studied by differential scanning calorimetry and wide- and small-angle X-ray scattering, Biophys. J. 78 (2000) 2459–2469.
[58] R. Mendelsohn, D.J. Moore, Vibrational spectroscopic studies of lipid domains in biomembranes and model systems, Chem. Phys. Lipids 96 (1998) 141–157.
[59] R.N.A.H. Lewis, R.N. McElhaney, W. Pohle, H.H. Mantsch, Components of the carbonyl stretching band in the infrared spectra of hydrated 1,2-diacylglycerolipid bilayers: a revaluation, Biophys. J. 67 (1994) 2367–2375.
[60] H.L. Casal, H.H. Mantsch, Polymorphic phase behaviour of phospholipid membranes studied by infrared spectroscopy, Biochim. Biophys. Acta 779 (1984) 381–401.
[61] J. Umemura, D.G. Cameron, H.H. Mantsch, A Fourier transform infrared spectroscopic study of the molecular interaction of cholesterol with 1,2-dipalmitoyl-sn-glycero-3-phosphocholine, Biochim. Biophys. Acta 602 (1980) 32–44.
[62] O. Reis, R. Winter, T.W. Zerda, The effect of high external pressure on DPPC-cholesterol multilamellar vesicles: a pressure-tuning Fourier transform infrared spectroscopy study, Biochim. Biophys. Acta 1279 (1996) 5–16.

This page intentionally left blank

CHAPTER SEVEN

Electroporation of Planar Lipid Bilayers and Membranes

Mojca Pavlin, Tadej Kotnik, Damijan Miklavčič, Peter Kramar, *and* Alenka Maček Lebar[1,*]

Contents

1. Introduction 167
2. Experimental Investigation of Electroporation on Planar Lipid Bilayers 169
   2.1. Breakdown Voltage 170
   2.2. Capacitance 173
   2.3. Conductance/Resistance 174
3. Attempts of Theoretical Explanation of Electroporation 175
   3.1. The Hydrodynamic Model 177
   3.2. The Elastic Model 178
   3.3. The Hydroelastic Model 179
   3.4. The Viscohydroelastic Model 181
   3.5. The Phase Transition Model 183
   3.6. The Domain-Interface Breakdown Model 186
   3.7. The Aqueous Pore Formation Model 187
   3.8. Extensions of the Aqueous Pore Formation Model 192
4. Electroporation of Cells-Experimental Observations and Analysis of Underlying Phenomena 194
   4.1. Induced Transmembrane Voltage and Forces on the Cell Membrane 195
   4.2. Maxwell Stress Tensor and Forces Acting on a Cell in an External Field 198
   4.3. Transport of Molecules Across Permeabilized Membrane 199
   4.4. Experimental Studies and Theoretical Analysis of Cell Electroporation *in vitro* 201
5. Comparison between Planar Lipid Bilayers and Cell Electroporation 211
Appendix A 213
   A.1. The Instability in the Hydrodynamic Model 213
   A.2. The Instability in the Elastic Model 213

* Corresponding author. Tel.: +386 1 4768 770; Fax: +386 1 4264 658
E-mail address: alenka.maceklebar@fe.uni-lj.si (A. Maček Lebar).

[1] University of Ljubljana, Faculty of Electrical Engineering, Tržaška 25, SI-1000 Ljubljana, Slovenia

Advances in Planar Lipid Bilayers and Liposomes, Volume 6
ISSN 1554-4516, DOI 10.1016/S1554-4516(07)06007-3

A.3. The Instability in the Hydroelastic Model 214
A.4. The Instability in the Viscohydroelastic Model 215
A.5. The Energy of a Hydrophilic Pore 216
Appendix B 217
B.1. Calculation of the Fraction of Surface Area of Transient Pores 217
B.2. Quantification of Ion Diffusion and Long-Lived Pores 218
References 219

Abstract

Strong external electric field can destabilize membranes and induce formation of pores thus increasing membrane permeability. The phenomenon is known as membrane electroporation, sometimes referred to also as dielectric breakdown or electropermeabilization. The structural changes involving rearrangement of the phospholipid bilayer presumably lead to the formation of aqueous pores, which increases the conductivity of the membrane and its permeability to water-soluble molecules which otherwise are deprived of membrane transport mechanisms. This was shown in variety of experimental conditions, on artificial membranes such as planar lipid bilayers and vesicles, as well as on biological cells *in vitro* and *in vivo*. While studies of electroporation on artificial lipid bilayers enabled characterization of the biophysical processes, electroporation of biological cells led to the development of numerous biomedical applications. Namely, cell electroporation increases membrane permeability to otherwise nonpermeant molecules, which allows different biological and medical applications including transfer of genes (electrogene transfer), transdermal drug delivery and electrochemotherapy of tumors. In general, the key parameter for electroporation is the induced transmembrane voltage generated by an external electric field due to the difference in the electric properties of the membrane and the external medium, known as Maxwell–Wagner polarization. It was also shown that pore formation and the effectiveness of cell electroporation depend on parameters of electric pulses like number, duration, repetition frequency and electric field strength, where the later is the crucial parameter since increased transmembrane transport due to electroporation is only observed above a certain threshold field. Two main theoretical approaches were developed to describe electroporation. The electromechanical approach considers membranes as elastic or viscoelastic bodies, and applying principles of electrostatics and elasticity predict membrane rupture above critical membrane voltage. A conceptually different approach describing formation and expansion of pores is based on energy consideration; it is assumed that external electric field reduces the free energy barrier for formation of hydrophilic pores due to lower polarization energy of water in the pores compared to the membrane. Combined with stochastic mechanism of pores expansion it can describe experimental data of bilayer membranes. Still, the molecular mechanisms of pore formation and stabilization during electroporation are not fully understood and rigorous experimental conformation of different theories is still lacking.

The focus of this chapter is to review experimental and theoretical data in the field of electroporation and to connect biophysical aspects of the process with the phenomenological experimental observations obtained on planar lipid bilayers, vesicles and cells.

1. Introduction

Biological membranes play a crucial role in living organisms. They are soft condensed matter structures that envelope the cells and their inner organelles. Biological membranes maintain relevant concentration gradients by acting as selective filters toward ions and molecules. Besides their passive role, they also host a number of metabolic and biosynthetic activities [1].

The interaction of electric fields with biological membranes and pure phospholipid bilayers has been extensively studied in the last decades [2,3]. Strong external electric field can destabilizes membranes and induce changes in their structure. The key parameter is the induced-transmembrane voltage generated by an external electric field due to the difference in the electric properties of the membrane and the external medium, known as Maxwell–Wagner polarization. According to the most plausible theory until now the lipids in the membrane are rearranged to form aqueous pores which increases the conductivity of the membrane and its permeability to water-soluble molecules which otherwise are deprived of membrane transport mechanisms. Therefore this phenomenon is known as electroporation, sometimes referred to also as dielectric breakdown or electropermeabilization of membranes.

Reversible "electrical breakdown" of the membrane has first been reported by Stampfli in 1958 [4], but for some time this report has been mostly unnoticed. Nearly a decade later, Sale and Hamilton reported on nonthermal electrical destruction of microorganisms using strong electric pulses [5]. In 1972, Neumann and Rosenheck showed that electric pulses induce a large increase of membrane permeability in vesicles [6]. Following these pioneering studies three important works have motivated a series of further investigations. First, Neumann *et al.* showed in 1982 that genes can be transferred into the cells by using exponentially decaying electric pulses [7]. A few years later, in 1987, Okino and Mohri and, in 1988, Mir *et al.* showed that definite amounts of molecules are introduced into the cells in either *in vivo* or *in vitro* conditions, by using electric pulses [8,9]. Most of the early work was done on isolated cells in conditions *in vitro*, but it is now known that many applications are also successful in *in vivo* situation. It was showed that using electroporation, small and large molecules can be introduced into cells and extracted from cells, and proteins can be inserted into the membrane and cells can be fused. As a result of its efficiency, electroporation has rapidly found its applications in many fields of biochemistry, molecular biology and medicine.

By applying an electric field of adequate strength and duration, the membrane returns into its normal state after the end of the exposure to the electric field – electroporation is reversible. However, if the exposure to electric field is too long or the strength of the electric field is too high, the membrane does not reseal after the end of the exposure, and electroporation is irreversible in such a case. According to the type of electroporation (i.e. reversible or irreversible), two groups of applications exist: functional, where functionality of cells, tissues or microorganisms must be sustained; and destructive, where electric fields are used to destroy plasma membranes of cells or microorganisms [10].

Irreversible electroporation can be used for nonthermal food and water preservation, where permanent destruction of microorganisms is required [11–13].

Functional applications are currently more widespread and established in different experimental or practical protocols. Probably, the most important functional application is the introduction of a definite amount of small or large molecules to the cytoplasm through the plasma membrane [14,15]. Electrochemotherapy (ECT) is a therapeutic approach in cancer treatment that combines chemotherapy and electroporation. The delivery of electric pulses at the time when a chemotherapeutic drug reaches its highest extracellular concentration considerably increases the transport through the membrane toward the intracellular targets and cytotoxicity of a drug is enhanced. In several preclinical and clinical studies, either on humans or animals, it was demonstrated that ECT can be used as the treatment of choice in local cancer treatment [16–18]. Application of electroporation for transfer of DNA molecules into the cell is referred to as electrogenetransfection (EGT) and has not yet entered clinical trials [15]. Another application of electroporation is insertion of molecules into the cell membrane. As the membrane reseals, it entraps some of the transported molecules, and if these molecules are amphipathic (constituted of both polar and nonpolar regions), they can remain stably incorporated in the membrane [19,20]. Under appropriate experimental conditions, delivery of electric pulses can lead to the fusion of membranes of adjacent cells. Electrofusion has been observed between suspended cells [21,22], and even between cells in tissue [23]. For successful electrofusion in suspension, the cells must previously be brought into close contact, for example, by dielectrophoresis [21]. Electrofusion has proved to be a successful approach in production of vaccines [24] and antibodies [25].

Application of high-voltage pulses to the skin causes a large increase in ionic and molecular transport across the skin [26]. This has been applied for transdermal delivery of drugs [27] and also works for larger molecules, for example, DNA oligonucleotides [28].

In spite of successful use of electroporation in biomedical applications, the molecular mechanisms of the involved processes are still not fully explained and there is lack of connection between experimental data and theoretical descriptions of pore formation [2,29–32]. It was shown that pore formation and the effectiveness of cell electroporation depend on parameters of electric pulses like number (N), duration (T), repetition frequency (f) and electric field strength (E). The later is the crucial parameter since increased transmembrane transport due to electroporation is only observed above a certain threshold field. It was also shown [33,34] that neither electrical energy nor charge of the electric pulses alone determine the extent of electroporation consequences and that the dependency on E, N and T is more complex [35].

Electroporation has been observed and studied in many different systems, i.e. artificial planar lipid bilayers, giant lipid vesicles, cells *in vitro* and *in vivo*. Cell membranes are much more complicated than artificial lipid structures, with respect to geometry, composition and the presence of active processes. The problem associated with the complexity of natural cell membranes can be avoided by investigating synthetic liposomes or vesicles which mimic the geometry and the size of cell membranes, but are void of ion channels and the multitude of other embedded

components. Artificial planar lipid bilayer is the simpliest modeling lipid system that also has the geometric advantage of providing electrical and chemical access to both sides of a membrane.

In the following, we shall review experimental and theoretical data in the field of electroporation and connect biophysical aspects of the process with the phenomenological experimental observations obtained on planar lipid bilayers, vesicles and cells.

2. Experimental Investigation of Electroporation on Planar Lipid Bilayers

The planar lipid bilayer can be considered as a small fraction of total cell membrane. As such has often been used to investigate basic aspects of electroporation; especially because of its geometric advantage of allowing chemical and electrical access to both sides of a membrane. Planar lipid bilayers can generally be formed by three different techniques: painting technique, folding technique or tip-dip technique [36]. In either case a thin bi-molecular film composed of specified phospholipids and organic solvent is formed on a small aperture in a hydrophobic partition separating two aqueous compartments. Electrodes plunged in the aqueous compartments permit the measurement of currents and voltages across the membrane. By reason of that two measuring principles of planar lipid bilayer's properties are commonly used (Fig. 1): voltage clamp method [37–48] and current clamp method [49,50,51–59]. From an electrical point of view a planar lipid bilayer can be regarded as a nonconducting capacitor, therefore two electrical properties, capacitance (C) and resistance (R), mostly determine its behavior.

When voltage clamp method is used the voltage signal is applied to the planar lipid bilayer; either a step change [47], pulse [37,41,44], linear rising [60] or some other shape of the voltage signal. The simplest as well as mostly used shape of the voltage signal is a square voltage pulse [37,41]. It is commonly used for

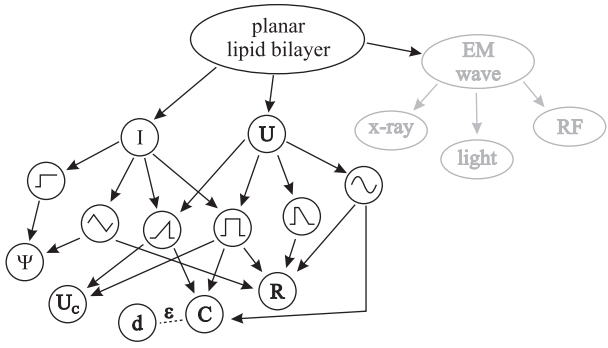

Figure 1 Electrical properties of planar lipid bilayer: resistance (R), capacitance (C), thickness (d), voltage breakdown (U_c) and mass fluctuation (Ψ) are measured with application of current (I) or voltage (U).

determination of planar lipid bilayer breakdown voltage (U_c) and capacitance [44]. Some experiments were done by two sinus-shaped voltage signals: the first with low frequency and large amplitude and the second with high frequency and low amplitude that was added to the first one. In this way lipid bilayer conductance and capacitance were determined at the same time [59]. When current clamp method is used, the current is applied to the lipid bilayer. Usually this method is appropriate for measuring resistance of a planar lipid bilayer and mass flow through it as a consequence of increased membrane permeability. It is believed that during this kind of measurements the lipid bilayer is more stable due to less voltage stress [50,53]; therefore, also small changes in membrane structure and the occurrence of fluctuating defects can be observed [45,50,54]. Scalas *et al.* [54], for example, reported on time course of voltage fluctuations that followed an increase of the membrane conductance due to the opening and closing hydrophilic pores.

Combination of electrical recording techniques with different kinds of high frequency electromagnetic fields offers additional investigations of structure–function relationships of planar lipid bilayer and of membrane interacting peptides [61–64]. For structure elucidation of lipid–water mesophases, small- and wide-angle X-ray scattering method were used [61]. Hanyu *et al.* [62] have presented an experimental system which allows measurement of current (function) and fluorescence emission (structural change) of an ion channel in planar lipid bilayer while membrane potential is controlled [62]. Rapid and reversible changes in photo responsive planar lipid bilayers electrical properties when irradiated with light were studied by Yamaguchi *et al.* [63]. Planar lipid bilayers have been also exposed to RF-field of about 900 MHz according to GSM standards and authors have revealed that temperature oscillations due to the pulsed radio frequency fields are too small to influence planar lipid bilayer's low frequency behavior [64].

2.1. Breakdown Voltage

Breakdown voltage (U_c) is one of the most important properties of a lipid bilayer when biomedical and biotechnological applications of electroporation are under consideration. It has been measured either by voltage clamp or current clamp method using rectangular, triangular or step shape of the signal (Fig. 1). Mostly, the breakdown voltage of the planar lipid bilayer is determined by a rectangular voltage pulse (10 μs–10 s). The amplitude of the voltage pulse is incremented in small steps until the breakdown of the bilayer is obtained [37]. First the voltage pulse charges up the planar lipid bilayer. Above a critical voltage (breakdown voltage U_c) defects are created in the planar lipid bilayer allowing an increase of the transmembrane current. Usually membrane collapses then after.

The influence of various factors, such as lipid composition [37,38,55], organic solvent [41], temperature [44] and electrolyte composition [43,44], on the absolute value of U_c has been studied. Benz *et al.* have measured U_c by presence of various salts in the electrolyte bathing the membranes [44] and shown that presence of Li^+, Na^+, K^+, Rb^+ or Cs^+ ions do not change U_c. It was also proved that ionic strength of bathing solution had no influence on U_c [40,43]. Experiments have demonstrated that with increasing temperature U_c of planar lipid bilayer decrease. [44].

Table 1 U_c of planar lipid bilayer composed if lipid molecules of a single type. All measurements have been done using 0.1 M KCl as a bathing solution.

BLM	U_c (mV)	Method	Reference
Azolecitin	423	Voltage clamp – 100 μs pulse	[38]
POPC	450	Voltage clamp – 100 μs pulse	[37,39,40]
POPS	480	Voltage clamp – 100 μs pulse	[39,40]
Egg PC	280	Current clamp – triangle (1.6–2.5 mHz)	[52,55]
DPh PC	390	Current clamp – triangle (1.6–2.5 mHz)	[52,55]
	527	Voltage clamp – 10 μs pulse	[39,40]
DPh PS	525	Voltage clamp – 10 μs pulse	[39,40]
PS	500	Current clamp – triangle (2.5 mHz)	[55]
GM	170	Current clamp – triangle (2.5 mHz)	[55]

Table 2 U_c of planar lipid bilayer composed from two lipid molecules or lipid molecules and surfactants. All measurements have been done using 0.1 M KCl as a bathing solution.

BLM	U_c (mV)	Method	Reference
Azolecitin+Poloxamer 188	448	Voltage clamp – 10 μs pulse	[38]
POPC+0.1 μM $C_{12}E_8$	383	Voltage clamp – 10 μs pulse	[37]
POPC+1 μM $C_{12}E_8$	333	Voltage clamp – 10 μs pulse	[37]
POPC+10 μM $C_{12}E_8$	333	Voltage clamp – 10 μs pulse	[37]
Egg PC/Ch 4:1	270	Current clamp – triangle (2.5 mHz)	[55]

U_c depends on a type of hydrophilic chain of the lipids (Table 1). Meier has reported that palmitoyl-oleoyl (PO) membrane require ~100 mV smaller breakdown voltages compared to diphytanoyl (DPh) membranes [39].

Incorporation of nonphospholipid substances into planar lipid bilayer changes the intensity and duration of the electrical stimulus needed for breakdown. Such effect is a consequence of the surfactant molecular shape acting to change the spontaneous curvature of the membrane, which is especially important during the defects formation process. Troiano *et al.* [37] performed a quantitative study on the effect of $C_{12}E_8$ on planar lipid bilayer made of 1-palmitoyl 2-oleoyl phosphatidylcholine (POPC). Their results and results of some other studies are gathered in Table 2.

Using voltage pulse protocol the number of applied voltage pulses is not known in advance and each bilayer is exposed to voltage stress many times. Such a pretreatment of the lipid bilayer affects its stability and consequently the determined breakdown voltage of the lipid bilayer [47]. Another approach for the breakdown voltage determination was suggested by our group [60]. Using linear rising signal the breakdown voltage is determined by a single voltage exposure.

Our system for following up electroporation of planar lipid bilayers consists of a signal generator, a Teflon chamber and a device, which is used for measurements of membrane current and voltage (Fig. 2).

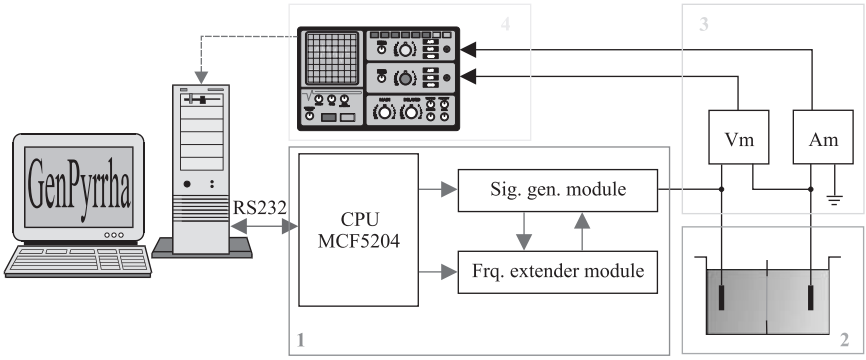

Figure 2 System for electroporation of planar lipid bilayer. (1) The microprocessor board with MCF5204 processor and two modules. One module generates arbitrary signals and the other that is realized in Xillinx, is used for frequency extension. (2) Chamber for forming lipid bilayers and two Ag–AgCl electrodes. (3) Modules for current and voltage amplification. (4) Digital oscilloscope for data storing [60].

Signal generator is a voltage generator of an arbitrary type that provides voltage amplitudes from −5 to +5 V. It is controlled by costume written software (Genpyrrha), specially designed for drawing the voltage signal that is used for membrane electroporation.

Two Ag–AgCl electrodes, one on each side of the planar lipid bilayer are plunged into the salt solution. Transmembrane voltage is measured via a LeCroy differential amplifier 1822. The same electrodes are used to measure transmembrane current. Both signals are stored in oscilloscope LeCroy Waverunner-2 354 M in Matlab format and processed offline.

Chamber is made out of Teflon. It consists of two cubed reservoirs with volume of 5.3 cm^3 each. In the hole between two reservoirs a thin Teflon sheet with a round hole (105 μm diameter) is inserted. Lipid bilayer is formed by the folding method [36,65].

Measurement protocol consists of two parts: capacitance measurement (Fig. 3A) and lipid bilayer breakdown voltage measurement (Fig. 3B). Capacitance of each planar lipid bilayer is measured by discharge method [60].

Breakdown voltage (U_c) of the lipid bilayer is measured then after by the linear rising signal. The slope of the linear rising signal (k) and the peak voltage of the signal have to be selected in advance. Breakdown voltage is defined as the voltage at the moment t_{br} when sudden increase of transmembrane current is observed. Time of breakdown t_{br} was defined as a lifetime of the lipid bilayer at a chosen slope of the linear rising signal (Fig. 3). Owing to already known experimental evidence that lipid bilayer lifetime is dependent on the applied voltage [37,66] and that the lipid bilayer breakdown voltage is dependent on the lipid bilayer pre-treatment [47], U_c and t_{br} are measured at six or seven different slopes. Indeed lifetime of lipid bilayer depends on the slope of linear rising voltage signal and also the breakdown voltage is a function of the slope of the linear rising voltage signal; it increases with increasing slope. Therefore, using nonlinear regression, *a* two parameters curve is

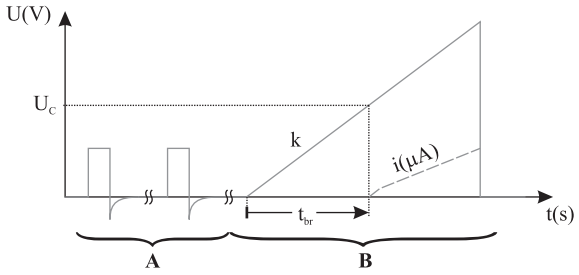

Figure 3 **Measurement protocol: (A) capacitance measurement of lipid bilayer was measured in two steps. In the first step, we measured capacitance of the electronic system without lipid bilayer. Second step was measuring capacitance of electronic system with lipid bilayer and salt solution. (B) Voltage breakdown measurement with linear rising signal [60].**

fitted to the data

$$U = \frac{a}{1 - e^{-t/b}} \tag{1}$$

where U is U_c measured at different slopes, t the corresponding $t_{br,}$ and a and b the parameters. Parameter a is an asymptote of the curve which corresponds to minimal breakdown voltage U_{cMIN} for specific bilayer. Parameter b governs the inclination of the curve.

The results obtained with described measuring protocol are presented in Fig. 4. U_c and t_{br} of POPC, POPC+1 μM $C_{12}E_8$ and palmitoyl-oleoyl phosphatidylserine (POPS):POPC (3:7) planar lipid bilayers have been measured and U_{cMIN} for each bilayer has been calculated. Computed parameter that corresponds to U_{cMIN} for specific bilayer is 0.49, 0.58 and 0.55 V, respectively.

Evans *et al.* used similar approach in their experiments on lipid vesicles [67]. They applied tension at different loading rates and they found out that tension needed for membrane rupture increases with increasing loading rate. As in our case the loading rate dependence of rupture events implies a kinetic process of defect formation (see theoretical explanations in the next chapter). It has to be noted that measuring protocol mentioned offers also better reproducibility and lower scattering of measured data due to the fact that each bilayer is exposed to electroporation treatment only once.

2.2. Capacitance

The capacitance (C) is a parameter that is considered to be the best tool for probing the stability and formal goodness of the planar lipid bilayer. It can be determined by various methods. Most common and simple method for measuring planar lipid bilayer capacitance is discharge pulse [38,41]. Galluci *et al.* have described a measurement system where two sinus signals with frequencies 1 Hz and 1 kHz are mixed and applied to planar lipid bilayer. Amplitude and phase of both signals governs planar lipid bilayer's capacitance and resistance simultaneously [68]. Such continuous monitoring of C may prove useful in tracking planar lipid bilayer electrical properties that depend on the lipids composition and incorporated

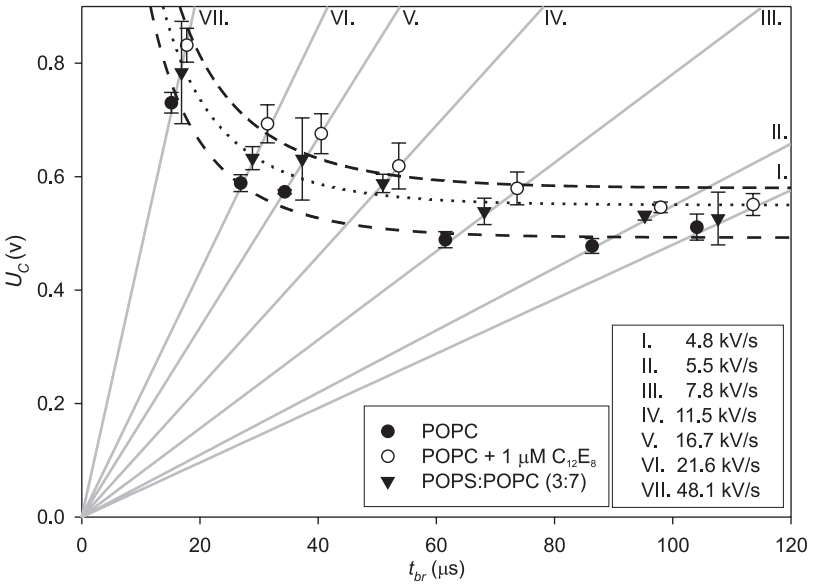

Figure 4 The breakdown voltage (U_c) (dots) of lipid bilayers as a function of lifetime t_{br}. The gray lines show seven different slopes (k) of applied liner rising voltage signal. Dash, dotted and dash–dotted curves represent two parameters curve fitted to data (1). Asymptotes of the curves (a) correspond to minimal breakdown voltage U_{cMIN} for lipid bilayers made of POPC, POPC+1 μM $C_{12}E_8$ and POPS:POPC (3:7) (Table 3).

nonphospholipids substances. Capacitance of planar lipid bilayer can also be determined by triangular voltage signal [49], that is controlled by the regulation system including charged planar lipid bilayer as a part. Therefore the period of the triangular voltage signal is related to capacitance of planar lipid bilayer. When current clamp method is used, capacitance of planar lipid bilayer can be measured with ramp signal [52,53,69].

Gallucci *et al.* have observed that the capacitance of planar lipid bilayer is dependent of concentration of salt solution. Capacitance measured in higher concentration of salt solution is lower than in lower concentration of salt solution [68]. Capacitances of planar lipid bilayers measured by various methods in different salt solutions are gathered in Table 3.

2.3. Conductance/Resistance

Resistance (R) or conductance (G) as electrical property of nonpermeablized planar lipid bilayer can be measured only during application of voltage or current signal. Galluci *et al.* [68] have developed the system for measuring G and C simultaneously and continuously as a function of time. This method allows measuring of electrical properties of nonpermeabilized planar lipid bilayer as well as during the process of defect formation and electroporation.

Melikov *et al.* [45] monitored fluctuations in planar lipid bilayer conductance induced by applying a voltage step of sufficiently high amplitude. They showed that

Table 3 Capacitance of planar lipid bilayers measured by various methods in dierent salt solutions.

BLM	C (μF/cm^2)	Salt solution	Method	Reference
Azolecitin	0.59	0.1 M KCl	Discharge pulse	[38]
	0.3–0.4	–	Current ramp	[69]
DOPC		0.1 M NaCl	Discharge pulse	[41]
DOPE		0.1 M NaCl	Discharge pulse	[41]
DPh PC	0.60–0.75	0.1 M KCl		[51–53,55]
	0.76–1.13	1 M KCl		[51,54]
	0.36	1 M NaCl	Discharge pulse	[41]
Ox Ch	0.555	1 M KCl	Discharge pulse	[41]
	0.5		Current ramp	[69]
	0.41	1 M KCl	Muxd sin wave	[59]
	0.45	0.1 M KCl	Muxd sin wave	[68]
	0.47	0.5 M KCl	Muxd sin wave	[68]
	0.40	1 M KCl	Muxd sin wave	[68]
PC	0.75	0.1 M KCl	Current clamp triangular	[52,55]
PI	0.25	1 M KCl	Muxd sin wave	[59]
	0.30	0.1 M KCl	Muxd sin wave	[68]
	0.27	0.5 M KCl	Muxd sin wave	[68]
	0.25	1 M KCl	Muxd sin wave	[68]
POPC	0.59	0.1 M KCl	Discharge pulse	[37]

the amplitude of fluctuations varied in a rather broad interval (form 150 to 1500 pS) and they related them with the formation of local conductive defects (see theoretical explanations in the next chapter).

Robello *et al.* [52] observed a sharp increase in conductance induced by external electric field obtained under current clamp conditions. They related it with creation of hydrophilic paths that increase the planar lipid bilayer conductance by one order of magnitude.

Similarly Kalinowski *et al.* [70] presented chronopotentiometric method for following planar lipid bilayer conductance during local conductive defects creation that also allows observing of their dynamical behavior. The voltage fluctuations reported in their work are consistent with theoretical models that predict formation of temporary aqueous pathways across the membrane.

3. Attempts of Theoretical Explanation of Electroporation

A number of theoretical models have been put forward as possible explanations of electroporation. Here, an attempt will be made to present these models roughly in their chronological order of appearance, and to review them critically,

Table 4 Values of the quantities used in the evaluation of the models.

Parameter	Notation	Value	Reference or explanation
Membrane			
Electric conductivity	σ_m	$\sim 3 \times 10^{-7}$ S/m	[71]
Dielectric permittivity	ε_m	4.4×10^{-11} F/m	[71]
Elasticity module	Y	$\sim 1 \times 10^{8}$ N/m^2	[72]
Viscosity	μ	0.6 Ns/m^2	[73]
Surface tension	Γ	$\sim 1 \times 10^{-3}$ J/m^2	[32]
Edge tension	γ	$\sim 1 \times 10^{-11}$ J/m	[32]
Thickness (undistorted)	d_0	5×10^{-9} m	[1]
Cytoplasm			
Electric conductivity	σ_i	0.3 S/m	[74,75]
Dielectric permittivity	ε_i	7.1×10^{-10} F/m	Set at the same value as ε_e
Extracellular medium			
Electric conductivity	σ_e	1.2 S/m	[76] (blood serum at 35°C)
Dielectric permittivity	ε_e	7.1×10^{-10} F/m	[77] (physiological saline at 35°C)

comparing their properties and abilities to those that the complete theoretical description of electroporation should provide:

- A physically realistic picture of both the nonpermeabilized and the permeabilized membrane. Unlike a true breakdown process, electroporation does not lead to a total disintegration of the system, but is localized and often even reversible.
- Limited reversibility. Based on the amplitude and duration of electric pulses, the permeabilized state is either reversible or irreversible.
- Dependence on pulse duration and the number of pulses. With longer pulses, a lower amplitude suffices for achieving the permeabilized state.
- A realistic value of the minimal transmembrane voltage ("critical voltage") at which permeabilization occurs. Most of the presented models provide an expression for this voltage, typically a function of several quantities. By inserting the typical values of these quantities into the expressions, we assess their agreement with experimentally measured critical voltage, which is in the range of a few hundred millivolts. These values are given in Table 4, where those which are either known only up to an order of magnitude, or can vary considerably, are marked by a tilde.
- Stochasticity. Variability of the critical pulse amplitude in experiments on cells can largely be attributed to the variability of cell size within the treated population. However, a certain degree of stochasticity is also observed in electropermeabilization of pure lipid vesicles and planar bilayers. Some authors view the ability of a model to account for this as crucial [32].

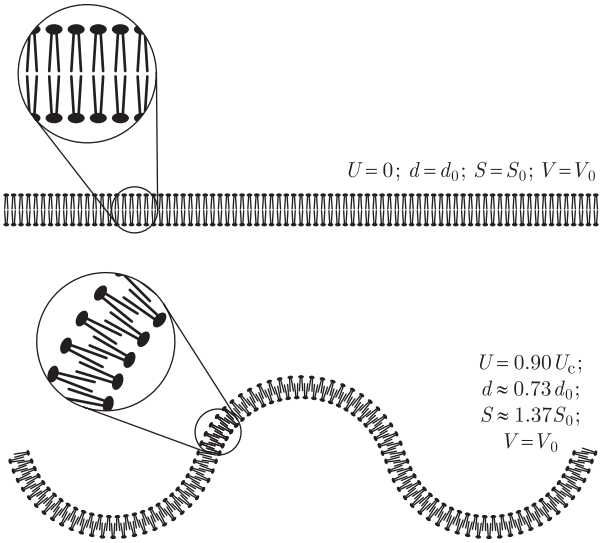

Figure 5 Membrane deformation according to the hydrodynamic model.

3.1. The Hydrodynamic Model

The hydrodynamic model, developed in the early 1970s [78,79], describes the membrane as a charged layer of a nonconductive and noncompressible liquid separating two conductive liquids. The transmembrane voltage exerts a pressure on this layer, and as it is assumed noncompressible in volume, the decrease in its thickness leads to an increase in its surface area. If either the volume enveloped by the membrane (in vesicles) or the perimeter of the membrane (in planar bilayers) is assumed to remain constant, the membrane thus becomes rippled (Fig. 5).

As the membrane surface area increases, so does its surface tension and thereby the pressure opposing the compression. At sufficiently low voltages, the two pressures reach an equilibrium at which the membrane thickness stabilizes. However, as shown in Appendix A.1, this equilibration is only possible up to the critical voltage given by

$$U_c = \sqrt{\frac{\Gamma d_0}{2\varepsilon_m}} \tag{2}$$

where Γ is the surface tension of the membrane, d_0 its uncompressed thickness and ε_m its dielectric permittivity. Above U_c an instability occurs: the compressive pressure prevails, causing a breakdown of the membrane. Applying typical parameter values from Table 4 to the above expression, we get $U_c \approx 0.24\,\mathrm{V}$, which is in good agreement with the experimental data. The equations in Appendix A.1 also describe the membrane thickness as a function of the transmembrane voltage (Fig. 6).

The hydrodynamic model has several shortcomings. First, it applies to liquids with isotropic fluidity, which is not true for lipid bilayers, where transverse movement of molecules is very restricted. Second, it fails at the very first requirement listed at the beginning of this chapter, as it does not describe the permeabilized

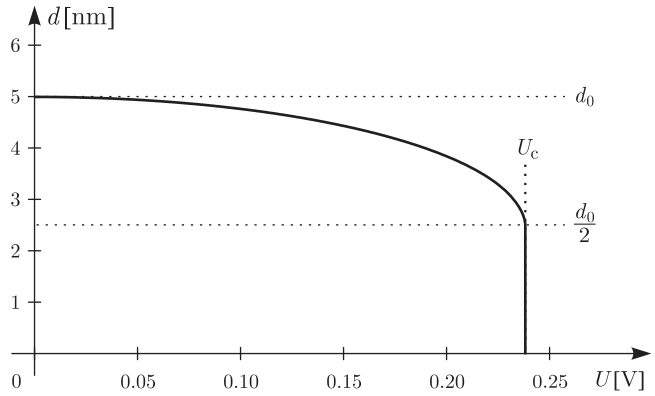

Figure 6 Membrane thickness as a function of the transmembrane voltage in the hydrodynamic model, using parameter values from Table 4.

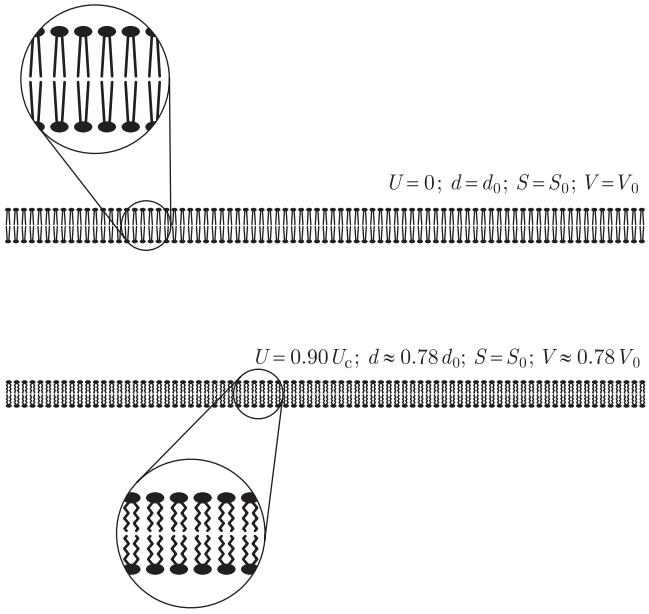

Figure 7 Membrane deformation according to the elastic model.

membrane. Of the other requirements, only the prediction of a realistic critical transmembrane voltage is met.

3.2. The Elastic Model

In contrast to the hydrodynamic model, which assumes a membrane with a constant volume and a variable surface, the elastic model, presented soon afterwards [80], assumes a variable volume and a constant surface (Fig. 7). In the elastic model,

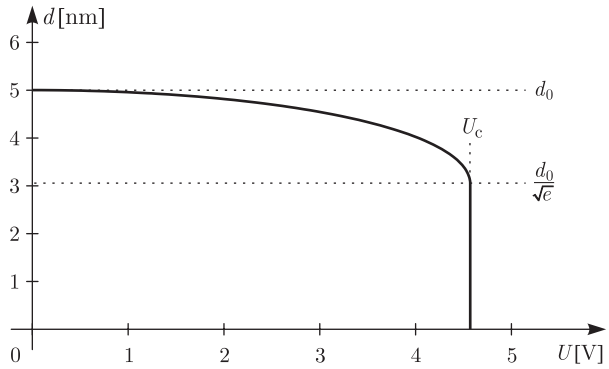

Figure 8 **Membrane thickness as a function of the transmembrane voltage in the elastic model, using parameter values from Table 4.**

the pressure exerted by the transmembrane voltage leads to a decrease in the volume of the membrane and an increase of elastic pressure opposing the compression. Also here, the equilibrium becomes impossible above a critical voltage (see Appendix A.2) given by

$$U_c \approx 0.61\ d_0 \sqrt{\frac{Y}{\varepsilon_m}} \tag{3}$$

where Y is the elasticity module of the membrane, d_0 its uncompressed thickness and ε_m its dielectric permittivity. Above U_c, there is an instability similar to the one in the hydrodynamic model.

Applying typical parameter values (Table 4) to the expression above, we get $U_c \approx 4.57$ V, which is roughly an order of magnitude too large. With the equations in Appendix A.2, we can also plot the membrane thickness as a function of the transmembrane voltage (Fig. 8).

In addition to the unrealistic prediction of critical voltage, the model assumes that Y does not vary with deformation, which is certainly false at 39% compression of the membrane at the point of instability (Fig. 8). This model also offers no description of the permeabilized membrane, and fails to meet any other requirement listed at the beginning of this chapter.

3.3. The Hydroelastic Model

The assumptions on which the hydrodynamic and the elastic model are built are mutually excluding as well as unrealistic. By treating the membrane as a liquid with both surface tension and elasticity, one obtains the more realistic hydroelastic model, in which both the volume and the surface of the membrane vary, and the charged membrane both compresses in volume and forms ripples (Fig. 9).

Similarly to the two models described previously, the hydroelastic model predicts a compressive instability (see Appendix A.3). With typical parameter values (Table 4) it yields $U_c \approx 0.34$ V, which is in good agreement with experimental data.

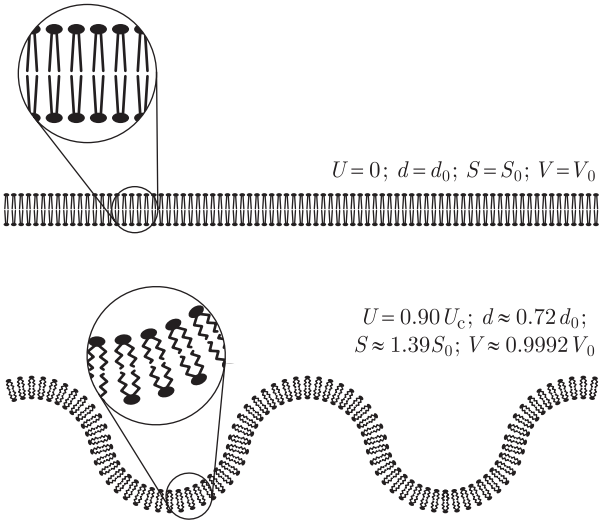

Figure 9 Membrane deformation according to the hydroelastic model.

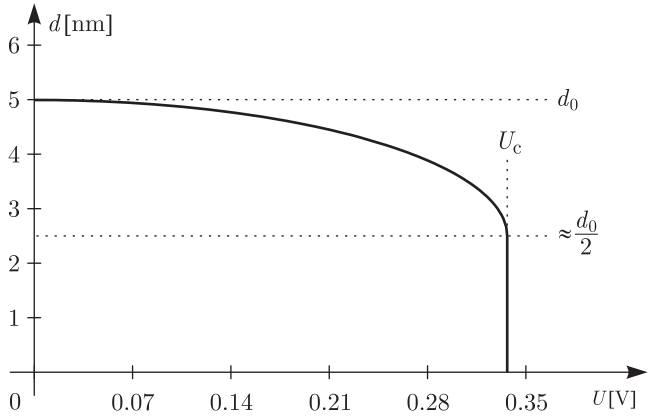

Figure 10 Membrane thickness as a function of the transmembrane voltage in the hydroelastic model, using parameter values from Table 4.

According to the hydroelastic model, at U_c the membrane thickness is reduced to 50% of the initial value (Fig. 10), its surface is enlarged to almost 200% of the initial value (Fig. 11) and the volume is reduced to 99.8% of the initial value (Fig. 12).

As Fig. 12 shows, according to the hydroelastic model the volume compression is very small, and even at the critical voltage the membrane volume is reduced by only 0.2% with respect to the initial value. Therefore, in this model the assumption of constant value of the elasticity module is much more reasonable than in the elastic model, in which the membrane breakdown is associated with a volume reduction of almost 39%. While the description of the compressive instability provided by the hydroelastic model is more realistic than those of the hydrodynamic

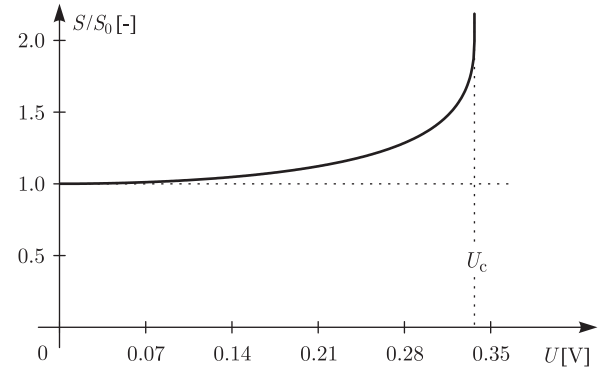

Figure 11 Membrane surface area as a function of the transmembrane voltage in the hydroelastic model, using parameter values from Table 4.

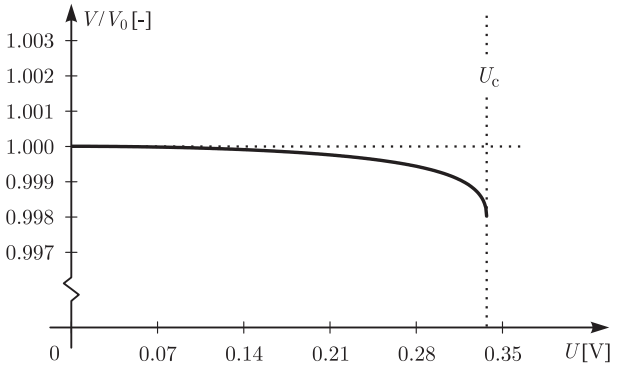

Figure 12 Membrane volume as a function of the transmembrane voltage in the hydroelastic model, using parameter values from Table 4.

and the elastic model, it has the same general drawback – it gives a nonsensical picture of the electropermeabilized membrane: a uniform, infinitely thin layer, only this time a rippled one. With the exception of a realistic prediction of the critical transmembrane voltage, the model also fails to meet any other requirement given in the list at the beginning of this chapter.

3.4. The Viscohydroelastic Model

Making another step toward complexity, the viscohydroelastic model (referred to by its authors as viscoelastic) expands the hydroelastic model by adding to it the membrane viscosity [81,82]. As in the hydroelastic model, in this model the charged membrane is both compressed and rippled. However, the viscosity impedes the molecular flow, and thus the compression is not instantaneous, but follows the onset of the transmembrane voltage gradually.

During the compression and rippling of the membrane, the impeded molecular flow leads to the thinning of the membrane at those locations where the flow would

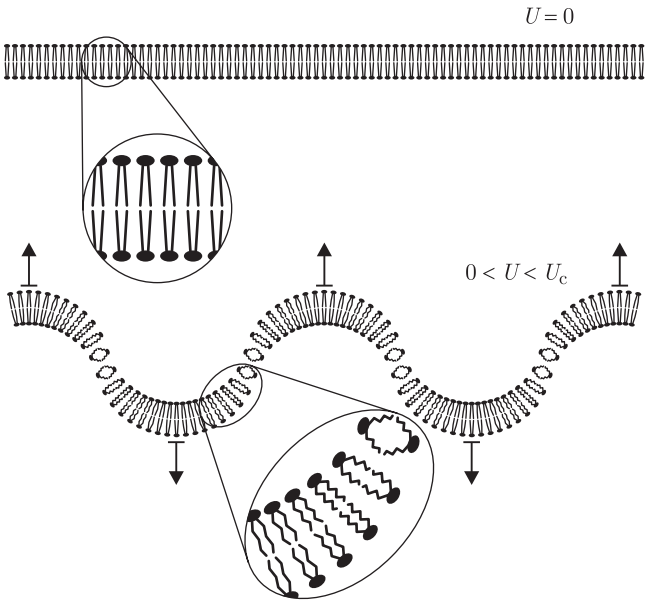

Figure 13 Membrane deformation according to the viscohydroelastic model.

have to be the most rapid to maintain the uniform thickness (Fig. 13). Up to a certain voltage, the membrane still reaches a state of equilibrium, but at higher voltages, the integrity of the membrane cannot be sustained and discontinuities form at the locations of the highest thinning. The analysis of such instability is elaborate and is described in more detail elsewhere [73,83], while Appendix A.4 gives a short outline of its results. This analysis shows that in the viscohydroelastic model, the instability occurs if the transmembrane voltage exceeds the critical amplitude given by

$$U_c = \sqrt[4]{\frac{8\,\Gamma Y d_0^3}{\varepsilon_m^2}} \tag{4}$$

and lasts longer than the critical duration,

$$\tau_c = \frac{24\mu}{\frac{\varepsilon_m^2 U^4}{\Gamma d_0^3} - 8Y} \tag{5}$$

where μ is membrane viscosity, the rest of the notation being the same as in the previously described models. Applying typical parameter values (Table 4), we get $U_c \approx 2.68$ V, so in this aspect the viscohydroelastic model performs worse than both the hydroelastic and the hydrodynamic model. However, it also offers a principal advantage over any of the previously described models, as the requirement of an above-critical voltage is linked to that of above-critical duration, providing a possible explanation of the dependence of permeabilization on the duration of electric

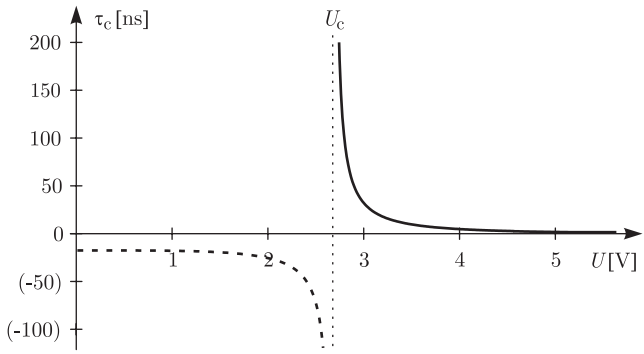

Figure 14 Critical duration of the transmembrane voltage as a function of its amplitude in the viscohydroelastic model, using parameter values from Table 4.

pulses. This is elucidated by Fig. 14, which shows the relation between the amplitude and the critical duration of the transmembrane voltage. At $U = 1.01 \times U_c \approx 2.71\,\text{V}$, the critical duration τ_c of the transmembrane voltage is approximately 450 ns, which is in close agreement with the sub-microsecond imaging experiments [84,85]. Still, the critical duration in the model decreases extremely rapidly, and at $U = 1.20 \times U_c \approx 3.12\,\text{V}$ we already have $\tau_c \approx 17\,\text{ns}$, while experimentally this decrease is much slower. Also, according to the viscohydroelastic model, the permeabilized membrane is torn along the ripples, but no such disconnections have so far been observed, making this description of the permeabilized membrane questionable.

3.5. The Phase Transition Model

According to the models presented up to this point, electropermeabilization is a modification of the supramolecular membrane structure. In contrast, the phase transition model describes this phenomenon as a conformational change of membrane molecules [72]. On the molecular scale, the pressures are replaced by molecular energies, and the pressure equilibrium corresponds to the state of minimum free energy. With several minima of free energy, several stable states are possible, each corresponding to a distinct phase. In lipid bilayers, there are in general two such phases, solid (gel) and liquid phase.

The phase transition model of electropermeabilization is an extension of the statistical mechanical model of lipid membrane structure [86,87]. According to this model, the free energy of the membrane at a temperature T and an average molecular surface area S is given by an expression of a general form

$$W(T,S) = W_\text{f}(S) + W_\text{c}(T,S) + W_\text{ic}(T,S) + W_\text{ih}(T,S) \tag{6}$$

where W_f is the flexibility energy (from continuous deformations, e.g. compression), W_c is the conformational energy (from discrete deformations, e.g. *trans–cis* transitions), W_ic is the energy of interactions between the hydrocarbon chains and W_ih is the energy of interactions between the polar heads of the lipids. Regrettably,

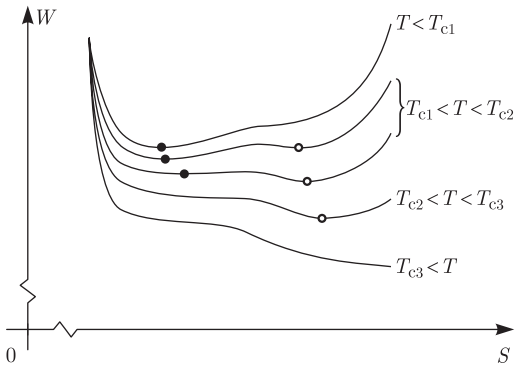

Figure 15 Free energy of a lipid molecule in the bilayer as a function of the molecular area, at five different temperatures. The units on both axes are arbitrary.

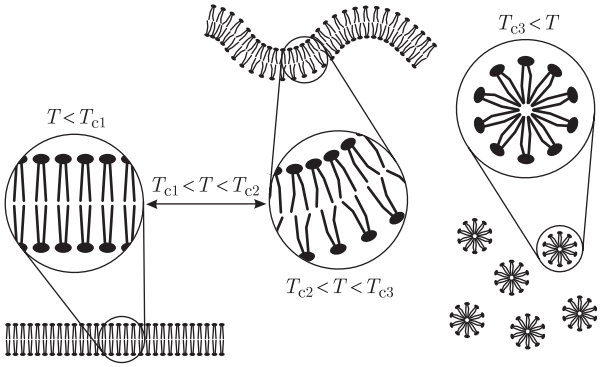

Figure 16 Membrane deformation and breakdown according to the phase transition model.

in the statistical mechanical model of Jacobs and co-workers, only $W_f(S)$ is an expression with a genuine physical basis, while the rest are polynomial regressions to the experimental data. In addition, the model contains several parameters with completely unknown actual values, and by adapting these one gets an arbitrarily good agreement with the experimental data. The specific formulae of the phase transition model are thus of little interest here, so we henceforth focus on the qualitative description it provides. Figure 15 illustrates this description by plotting the free energy per molecule as a function of the average area occupied per molecule, with the temperature serving as a parameter, and with arbitrary units on both axes.

As shown in Fig. 15, at temperatures below T_{c1}, the dependence of free energy on molecular area has a single minimum, which corresponds to the solid (gel) phase, which is the only possible stable state (Fig. 16, left). Between T_{c1} and T_{c2}, a second minimum occurs on the curve, corresponding to the liquid phase. In this temperature range, both phases can exist, but the one corresponding to the global minimum is more frequent. Above T_{c2}, the first minimum disappears, and the membrane can only persist in the liquid phase (Fig. 16, center). Finally, at

temperatures above T_{c3}, the remaining minimum also vanishes, and the membrane dissolves in the surrounding water, forming small micelles (Fig. 16, right). As an example, for a DPPC bilayer, $T_{c1} \approx 25^{\circ}\mathrm{C}$, $T_{c2} \approx 40^{\circ}\mathrm{C}$ and $T_{c3} \approx 165^{\circ}\mathrm{C}$ [1].

In the presence of a transmembrane voltage, the model described above has to be expanded by an additional component of the free energy, the electrical energy W_e, and the total free energy now becomes

$$W(T, S, U) = W_f(S) + W_c(T, S) + W_{ic}(T, S) + W_{ih}(T, S) + W_e(T, S, U) \quad (7)$$

where we assume that the electrical energy depends not only on the transmembrane voltage, but also on the temperature and the molecular surface area. In his model [72], Sugár derived the following approximation for $W_e(T, S, U)$:

$$W_e(T, S, U) = kT \log \frac{YS}{l\pi kT} - \frac{\varepsilon_m^2 S}{128 l^3 Y} U^4 \quad (8)$$

where k is the Boltzmann constant, T the absolute temperature, Y the elasticity module of the molecules in the direction of their hydrocarbon chains, S the average area of the molecules, l is the length of the hydrocarbon chains, ε_m is the dielectric permittivity of the molecules and U the transmembrane voltage. From this formula it is evident that at a sufficiently high transmembrane voltage, W_e becomes negative, shifting the entire free energy curve down, and this shift is more pronounced at higher molecular areas. Figure 17 shows this effect at a physiological temperature $T_{c1} < T < T_{c2}$ (for reasons described above, we again use arbitrary units for both axes). At a voltage U_{c1}, the first minimum of the free energy disappears, forcing the membrane into the liquid phase state. At a somewhat higher voltage U_{c2}, the remaining minimum also ceases to exist, leading to the breakdown of the membrane. The phases of the lipid membrane at various voltages are thus analogous to those at various temperatures presented in Fig. 16. Using numerical values for all the parameters of his model, Sugár calculated that for a DPPC bilayer, $U_{c1} \approx 260\,\mathrm{mV}$ and $U_{c2} \approx 280\,\mathrm{mV}$.

Comparison between Figs. 15 and 17 shows that according to the phase transition model, the presence of transmembrane voltage has an effect similar to

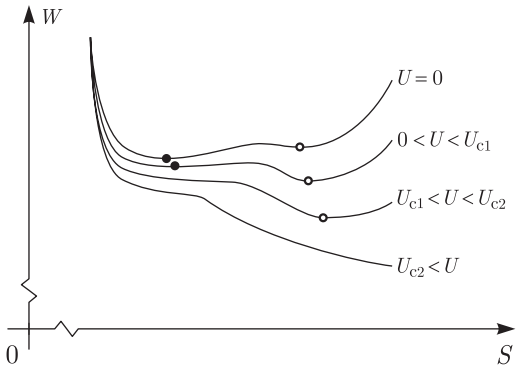

Figure 17 Free energy of a lipid molecule in the bilayer as a function of the molecular area, at four different transmembrane voltages. The units on both axes are arbitrary.

heating, causing a transition to the liquid phase, and eventually to decomposition similar to a high-temperature disintegration. Such a description is very unrealistic, since the permeabilized membrane is far from complete disintegration, and often returns to the nonpermeabilized state.

For an impartial evaluation of the predicted value of the critical transmembrane voltage, the parameters of the model which are at present arbitrary will have to be determined experimentally. In addition, this model is only provisional until the polynomial expressions obtained by regression are replaced by physical laws.

Still, the phase transition model meets several requirements at which all the previous models fail. The permeabilized state is the minimum of free energy, and the return to the nonpermeable state requires a sufficient input of energy, which offers a possible explanation of the observed durability of the permeabilized state. Similarly, the transition to this state requires a sufficient input of energy, which could explain the dependence on pulse duration. Above the second critical voltage, the downward slope of the free energy is never reversed, leading to a breakdown and explaining the limited reversibility of electropermeabilization. Except for the explanation of the dependence on the number of pulses, this model thus meets all the qualitative requirements from the list at the beginning of this chapter. This suggests that the approach based on the free energy could be a promising one.

3.6. The Domain-Interface Breakdown Model

The domain-interface breakdown model takes into account the fact that cell membranes can consist of distinct domains which differ in their lipid structure, particularly in their content of cholesterol. According to this model, electropermeabilization is localized to the boundaries between the domains [88,89], as Fig. 18 schematically shows.

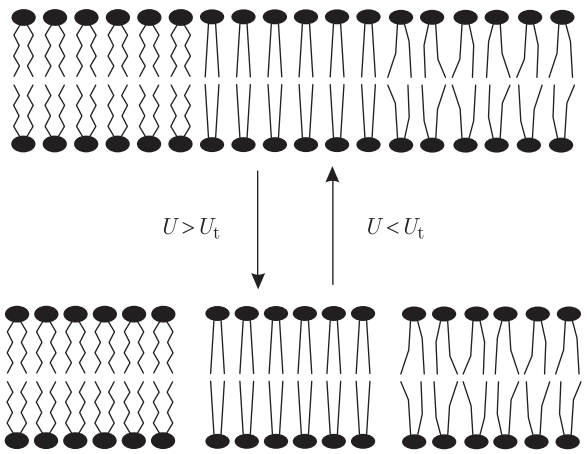

Figure 18 Membrane breakdown according to the domain-interface breakdown model.

Similarly to the viscohydroelastic model, in the domain-interface breakdown model the increased permeability is a result of fractures, with the difference that in the former model they occur along the ripples, while in the latter they form along the domain interfaces. As with the viscohydroelastic model, this description remains questionable, as such fractures have never been observed. In addition, while the model describes permeabilization as localized to the domain interfaces, the phenomenon is also observed experimentally in bilayers and vesicles with homogeneous lipid structure. Thus the domain-interface breakdown can only serve as an additional mechanism, perhaps enhancing permeabilization in cell membranes with respect to that in artificial bilayers and vesicles.

3.7. The Aqueous Pore Formation Model

The first four models treated here – the hydrodynamic, the elastic, the viscoelastic and the viscohydroelastic model – view electroporation as a large scale phenomenon, in which the molecular structure of the membrane plays no direct role.[1] The next two – the phase transition model and the domain-interface breakdown model – represent the other extreme, trying to explain the phenomenon by the properties of individual lipid molecules and interactions between them.

A compromise between these two approaches is offered by the model of pore formation, according to which electropermeabilization is caused by formation of transient aqueous pores (electroporation) in the lipid bilayer. In this model, each pore is formed (surrounded) by a large number of lipid molecules, but the shape, size and stability of the pore are strongly influenced by the structure of these molecules and their local interactions.

The model of pore formation is the last one to be described here, and in its present form, it is considered by many as the most convincing explanation of electropermeabilization. Therefore, in the following paragraphs an attempt will be made to follow its development rather comprehensively, from the first designs up to its current appearance.

The possibility of spontaneous pore formation in lipid bilayers was first analyzed in 1975, independently by two groups [90,91]. According to this analysis (which did not yet account for the effects of transmembrane voltage) formation of a cylindrical pore of radius r changes the free energy of the membrane by

$$\Delta W(r) = 2\gamma\pi r - \Gamma\pi r^2 \tag{9}$$

where γ is the edge tension and Γ the surface tension of the membrane. The first term, often termed the edge energy, is positive, since a pore creates an edge in the membrane, with a length corresponding to the circumference of the pore. The second term, the surface energy, is negative, as a pore reduces the surface area of the membrane. According to the above expression, the change of free energy is positive for small pores, and negative for sufficiently large pores. This implies that

[1] This point should not be obscured by the figures accompanying the models, in which separate lipid molecules are depicted. However, these figures combine the macroscopical description, which is actually provided by these models, with the existing knowledge of molecular structure of the lipid membrane.

spontaneous pore formation is inhibited by an energy barrier, explaining the stability of the membrane in the physiological conditions. The critical radius at which the energy barrier reaches a peak and the height of this peak are given by

$$r_c = \frac{\gamma}{\Gamma}, \quad \Delta W_c = \Delta W(r_c) = \frac{\pi\gamma^2}{\Gamma}. \tag{10}$$

Typical parameter values (Table 4) give $r_c \approx 10\,\text{nm}$. If a larger pore is artificially created (e.g. by piercing the membrane), this energy barrier is overcome, and since no stable state exists at larger pore radii, the membrane breaks down.

In the presence of a transmembrane voltage, formation of a pore also affects the capacitive energy of the system. By accounting for this Abidor and co-workers obtained a more general expression for the change of the free energy [47],

$$\Delta W(r, U) = 2\gamma\pi r - \Gamma\pi r^2 - \frac{(\varepsilon_e - \varepsilon_m)\pi r^2}{2d} U^2. \tag{11}$$

where U is the transmembrane voltage, while ε_e and ε_m are the dielectric permittivities of the aqueous medium (in approximation, that of water) in the pore and the membrane. The transmembrane voltage reduces both the critical radius of the pore and the energy barrier, which are now given by

$$r_c(U) = \frac{\gamma}{\Gamma + \frac{\varepsilon_e - \varepsilon_m}{2d} U^2}, \quad \Delta W_c(U) = \Delta W(r_c, U) = \frac{\pi\gamma^2}{\Gamma + \frac{\varepsilon_e - \varepsilon_m}{2d} U^2}. \tag{12}$$

Applying parameters values from Table 4, Fig. 19 shows the free energy curves in absence and in presence of transmembrane voltage (solid) The voltage reduces the critical radius from $r_c \approx 10\,\text{nm}$ (outside the graph range) to $r_c \approx 1.93\,\text{nm}$, i.e. to less than 20% of the value in the absence of transmembrane voltage, and the energy barrier is decreased in the same proportion.

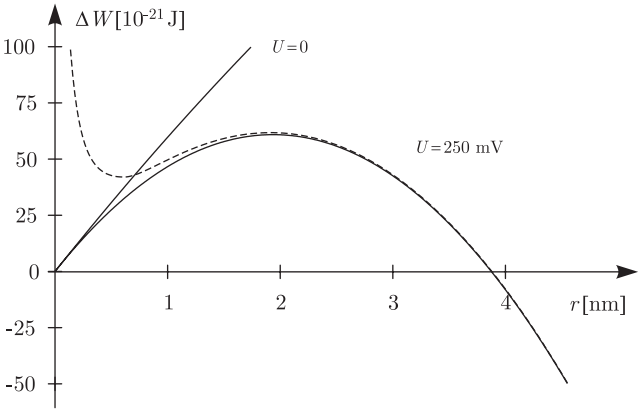

Figure 19 Free energy change due to the occurrence of a hydrophilic pore in the lipid bilayer, plotted as a function of the pore radius. The solid curves show the case of a constant edge tension, and the dashed curve the case where the edge tension increases as the pore radius decreases.

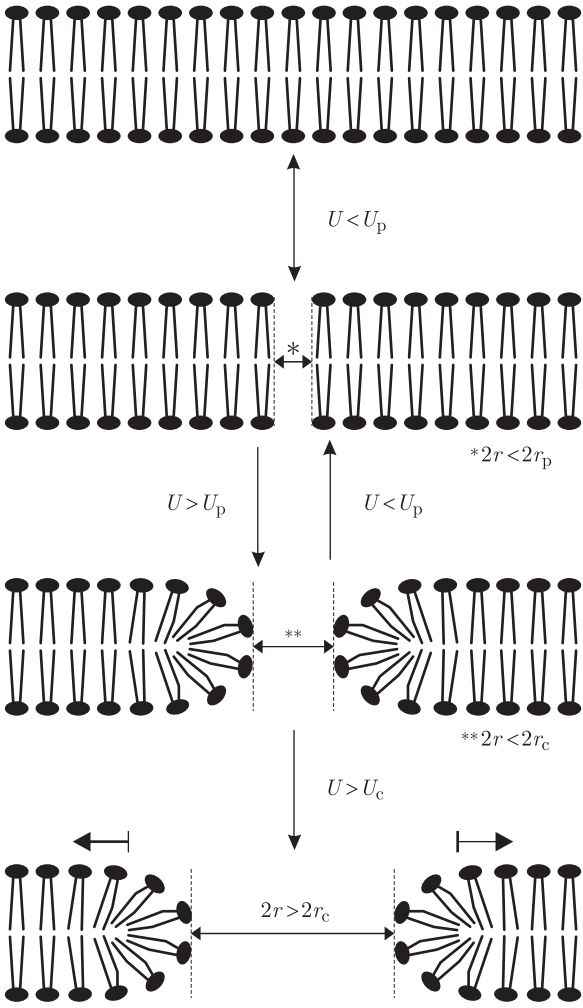

Figure 20 Formation of an aqueous pore according to the model of electroporation. From top to bottom: the intact bilayer; the formation of a hydrophobic pore; the transition to a hydrophilic pore and a limited expansion of the pore radius corresponding to a reversible breakdown; unlimited expansion of the pore radius corresponding to an irreversible breakdown.

Like many of the models presented before, this version of the model of pore formation fails to describe a permeabilized membrane, since according to it, an above-critical voltage causes a complete breakdown of the membrane. Another shortcoming of this model becomes evident from the structure of an aqueous pore (Fig. 20, bottom), where the lipids adjacent to the aqueous inside of the pore are reoriented in a manner that their hydrophilic heads are facing the pore, while their hydrophobic tails are hidden inside the membrane. Weaver and Mintzer argued that such a reorientation requires an input of energy which is larger for smaller pores [92], correspondingly increasing the free energy of the membrane at small pore radii

(Fig. 19, dashed). They suggested that this effect can be accounted for by treating the edge energy as a function $\gamma(r)$ the value of which becomes larger as the pore radius decreases,

$$\Delta W(r, U) = 2\gamma(r)\pi r - \Gamma\pi r^2 - \frac{(\varepsilon_e - \varepsilon_m)\pi r^2}{2d} U^2, \tag{13}$$

but they did not provide an expression for $\gamma(r)$.

The next step in the revision of the model of pore formation was a crucial one, as it described the stable state of a pore [46]. The argument that led to this revision is again illustrated in Fig. 20, where the hydrophilic structure of the pore is reached through a transition from an initial, hydrophobic state, in which the lipids still have their original orientation. The expressions for ΔW given so far do not deal with this transition, and at all radii they treat the pore as fully formed, i.e. hydrophilic. Glaser and co-workers argued that up to the pore radius r_p at which the hydrophilic state forms, the free energy change due to a hydrophobic pore must be analyzed instead, for which they derived the expression (see Appendix A.5)

$$\Delta W(r, U) = 2\pi d r \Gamma_h \frac{I_1(r/\lambda)}{I_0(r/\lambda)}, \tag{14}$$

where Γ_h is the surface tension at the interface of the hydrophobic internal surface of the pore and water, λ is the characteristic length of hydrophobic interactions, and I_k denotes the modified Bessel function of k-th order. As in the hydrophilic case, the total change of free energy also reflects the decrease of the membrane surface and the electric energy. The change of free energy of the membrane accompanying electroporation can thus be described by the system of two equations

$$\Delta W(r, U) = \begin{cases} 2\pi d r \Gamma_h \dfrac{I_1(r/\lambda)}{I_0(r/\lambda)} - \Gamma\pi r^2 - \dfrac{(\varepsilon_e - \varepsilon_m)\pi r^2}{2d} U^2; & r < r_p \\ 2\pi r\gamma(r) - \Gamma\pi r^2 - \dfrac{(\varepsilon_e - \varepsilon_m)\pi r^2}{2d} U^2; & r > r_p \end{cases} \tag{15}$$

The pore radius r_p at which the transition from the hydrophobic to the hydrophilic state occurs corresponds to the intersection of the hydrophilic and the hydrophobic branch of ΔW, but as $\gamma(r)$ is not defined, it is also impossible to give an explicit formulation of r_p.

Using $\lambda = 1$ nm [93], $\Gamma_h = 0.05$ N/m [46] and other values as in Table 4, we can plot both branches of ΔW on the same graph, as shown in Fig. 21. For transmembrane voltages of 250 and 350 mV, the solid lines give the curve into which the hydrophobic and the hydrophilic branch combine, and the dashed lines are the extrapolations of these two branches beyond their actual domains. Regrettably, a local minimum of free energy only occurs if the hydrophilic branch contains a suitable form of the (unknown) function $\gamma(r)$.

The model of pore formation as illustrated by Figs. 20 and 21 represents what is today referred to as the aqueous pore formation model (or simply as "the standard model of electroporation"), where the phenomenon is defined as formation of aqueous pores in the presence of transmembrane voltage. In this model,

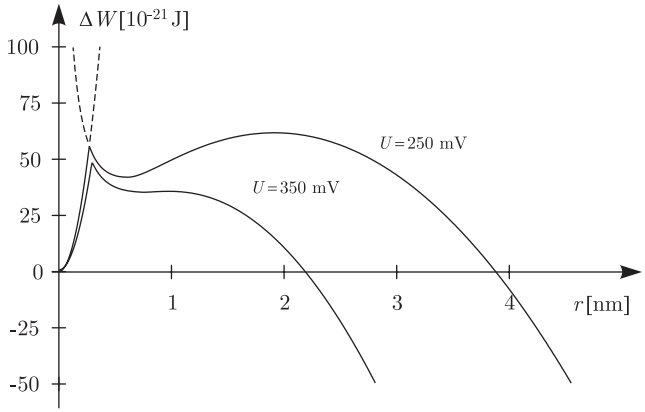

Figure 21 **Free energy change due to the formation of an aqueous pore, plotted as a function of the pore radius. The initial increase corresponds to the formation and expansion of a hydrophilic pore, the local maximum to the transition to a hydrophilic pore, and the subsequent local minimum corresponds to the radius of a (semi-) stable hydrophilic pore. At sufficiently high transmembrane voltages, this minimum transforms into a monotonic decrease, which corresponds to an irreversible breakdown.**

transmembrane voltage decreases the energy input necessary to induce a transition from the hydrophobic[2] to the hydrophilic state. The hydrophilic pores correspond to a local minimum of free energy, and are thus stable, which could possibly explain the experimentally observed durability of the permeabilized state. Reversibility of this state is limited as at voltages above the critical value there is an irreversible breakdown of the membrane. Qualitatively, also the dependence of electropermeabilization on pulse duration is explained, since pore formation requires a sufficient input of energy for the transition to the hydrophilic state. In the models of pore formation, including the aqueous pore formation model of electroporation, the transmembrane voltage does not cause, but only facilitates the formation of hydrophilic pores, which can account for the stochasticity of electropermeabilization. As Figs. 19 and 20 testify, the values at which this facilitating effect becomes pronounced are in hundreds of millivolts, and thus in relatively good agreement with the experiments.

Still, the aqueous pore formation model of electroporation has two significant shortcomings. The first is clearly observable in Fig. 21; namely, with realistic parameter values applied, the transmembrane voltage reduces the energy barrier of the hydrophobic–hydrophilic transition, but it reduces the barrier of an irreversible breakdown to a much larger extent. For example, a transmembrane voltage above 361 mV reduces the energy barrier of aqueous pore formation by only several percent, but once the pore is formed, this voltage imminently leads to the breakdown. This effect is independent of the choice of the arbitrary function $\gamma(r)$, since it is governed exclusively by the contribution of the electric energy. Nonetheless, the

[2] Because of the lateral thermic fluctuations of the lipid molecules, hydrophobic pores, with lifetimes in the picosecond range, are in certain extent always present in the membrane.

undefined functional form of $\gamma(r)$ is the second shortcoming of the aqueous pore formation model of electroporation. In absence of its definition, the expressions for the energy barrier that impedes the hydrophobic–hydrophilic transition, as well as the minimum radius of a hydrophilic pore r_p also remain undefined. This shortcoming will probably be addressed in the future, either theoretically, by a derivation of a physical law which would define $\gamma(r)$, or experimentally, by a measurement of its values. On the long term, the former alternative is definitely preferred.

Subsequent paragraphs contain a short overview of various extensions of the aqueous pore formation model that have been proposed by different authors.

3.8. Extensions of the Aqueous Pore Formation Model

Several approaches have been proposed for improving the aqueous pore formation model presented in the preceding section. Two of these [94,95] addressed its dubious prediction that transmembrane voltage strongly facilitates an irreversible breakdown. Barnett and Weaver accounted for the fact that a pore alters not only the capacitive, but also the conductive energy of the membrane, and reformulated the electric energy as[3]

$$\Delta W_e = -\frac{(\varepsilon_e - \varepsilon_m)\pi}{d} U^2 \int_0^r \frac{\rho \, d\rho}{(1+\lambda(\rho))^2} \tag{16}$$

with

$$\lambda(\rho) = \frac{\pi \rho \sigma_p}{2 d \sigma_e} \tag{17}$$

where σ_e and σ_p are the electric conductivities of the aqueous medium outside and inside the pore. The exact value of σ_p depends on the properties of the lipid headgroups forming the surface of the pore, as well as on the properties of the aqueous medium inside the pore, but in the first approximation it is reasonable to assume that $\sigma_p \approx \sigma_e$, so that

$$\lambda(\rho) = \frac{\pi \rho}{2d} \tag{18}$$

and the electric energy is given by

$$\Delta W_e = -(\varepsilon_e - \varepsilon_m)\, U^2 \left(\frac{4d \log\left(1 + \frac{\pi r}{2d}\right)}{\pi} - \frac{2r}{1 + \frac{\pi r}{2d}} \right). \tag{19}$$

Figure 22 compares, for a transmembrane voltage of 350 mV, the free energy change as a function of pore radius with (solid) and without (dashed) the described modification of the electric energy. The revised curve of free energy change shows a significantly broadened range of stable pore radii. The voltage which leads to an irreversible breakdown is shifted up to $\approx$458 mV, which is an improvement with respect to the previous value of $\approx$361 mV, but is still rather low. Also in the revised

[3] Note that using $\lambda(\rho) = 0$, we get ΔW_e of the standard model (i.e. the result derived by Abidor and co-workers).

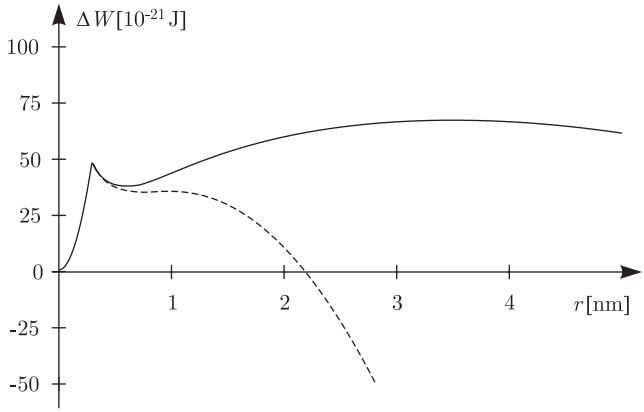

Figure 22 Free energy change as a function of the pore radius, without (dashed) and with (solid) the modification of the conductive electric energy as formulated by Barnett and Weaver [94].

model, the facilitating effect of transmembrane voltage on formation of aqueous pores remains very weak.

Freeman and co-workers [95] made an attempt to enhance this model further by accounting for the energy needed by charged particles to traverse the pore (the Born energy), which led them to a more complicated expression for $\lambda(\rho)$ expressed as a polynomial regression of experimental data.

Another study has addressed the effect of the difference between the osmolarities of the extracellular medium and the cytoplasm [32]. To address this effect, the change of free energy must incorporate the change of osmotic energy caused by the pore formation,

$$\Delta W_{\mathrm{osm}} = -\frac{|p_{\mathrm{e}} - p_{\mathrm{i}}|R}{2}\pi r^2 \tag{20}$$

where p_{e} and p_{i} are the osmotic pressures in the extracellular medium and inside the vesicle or cell, respectively, and R is the radius of the vesicle or cell. The osmotic energy thus acts similarly to the surface energy and the electric energy – it reduces the free energy of the membrane, and is proportional to r^2. This implies that a difference between the osmolarities makes the membrane more susceptible to the effects of the transmembrane voltage, which seems to be in agreement with experiments [96,97].

Finally, it was also analyzed how electroporation is affected by the curvature of the membrane [98]. Unlike in planar bilayers, in vesicles and cells the membrane is inherently curved, with the curvature increasing with a decreasing cell radius. According to the calculations by Neumann and co-workers, the change of curvature energy caused by the pore formation is

$$\Delta W_{\mathrm{crv}} = -\frac{64Y}{Rd}\pi^2 r^2 \tag{21}$$

where Y is the elasticity module of the membrane and R the radius of the cell. This also shows that the curvature reduces the free energy of the membrane and implies that, at a given transmembrane voltage, electroporation is more intense in smaller cells.[4]

Today, many consider the aqueous pore formation model to be the most convincing explanation of electroporation. If in the future it preserves this status, then further research, especially measurements of the relevant physical quantities, should gradually result in the improvement of the current form of the aqueous pore formation model. It is reasonable to expect that some of the tentative extensions described above will soon be incorporated into the model, while revisions and entirely new propositions will continue to appear. It is also reasonable to expect that an explicit formulation of the function $\gamma(r)$ should be given in the near future. The insights obtained by molecular dynamics simulations, and perhaps by an advanced method of visualization or another type of detection, should also yield a clearer picture of the electropermeabilized membrane on a nanometer scale, thereby providing the final verdict on the validity of the concept of electroporation.

4. Electroporation of Cells-Experimental Observations and Analysis of Underlying Phenomena

The electroporation of cells is sometimes also referred to as electropermeabilization, which stresses the crucial observation that increased permeability of the cell membrane is observed above a certain critical (threshold) applied electric field. It was shown by several independent studies that electroporation of cells is closely related to electroporation of lipid bilayer membranes, referred to also as dielectric breakdown, and that the structural changes in the membrane are formed in the lipid part of the cell membrane. Still the exact molecular mechanisms of the formation, structure and stability of these permeable structures (pores) are not completely understood [32,99]. On one hand the theoretical descriptions that were developed for lipid bilayers do not include cell structures such as cytoskeleton and proteins. In addition non of the existing theories can describe permeable structures or pores which could be stable for minutes and hours after pulse application. On the other hand, the increased permeability after the pulses, which enables delivery of molecules (drugs, DNA molecules …) is crucial for application of cell electroporation in biotechnology in biomedicine [2,100,101]. Therefore, phenomenological observations and quantification of cell electroporation can lead to some conclusions enabling evaluation of electroporation theories when applying them to such complex systems as cells and helps to understand the underlying mechanisms.

For this reason, we will present the theoretical and experimental data on the electroporation of cells. We will focus on the experimental evidence of cell

[4] This is true for a given transmembrane voltage, but not for a given pulse amplitude, since the transmembrane voltage induced by the pulse is proportional to the cell radius.

electroporation *in vitro* and on related theoretical interpretations. First, we briefly present theoretical descriptions of phenomena involved in cell electroporation: the induced transmembrane potential, forces which act on the cell and the transport which occurs through permeabilized cell membrane. Then we will overview several experimental studies, which studied different involved phenomena (imaging, conductivity, transport of molecules …), and finally we discuss how the theoretical description of pore formation presented in previous section can be applied to experimental observations of cell electroporation.

4.1. Induced Transmembrane Voltage and Forces on the Cell Membrane

Even though the exact physical–chemical mechanisms of cell electroporation are not clear and several theoretical models exist, it is generally accepted that one of the key parameters for successful permeabilization is the induced transmembrane voltage. This voltage is generated by an external electric field due to the difference in the electric properties of the membrane and the external medium, known as the Maxwell–Wagner polarization [102,103]. If the induced transmembrane voltage is large enough, i.e. above the critical value, electroporation is observed – a cell membrane becomes permeabilized in a reversible process allowing easier transport of ions and entrance of molecules that otherwise cannot easily cross the cell membrane [2,6,7,29,32,101].

4.1.1. The induced transmembrane voltage on a spherical cell

We consider a spherical cell exposed to an external homogeneous electric field E_0, as schematically shown in Fig. 23, where R denotes radius of the cell, d thickness of the membrane, conductivities σ and ε permittivities of the cell membrane, cytoplasm and exterior (Table 5).

The Laplace equation holds for all three regions: e – external medium, m – membrane and i – the cell interior. The respective potentials satisfying Laplace's

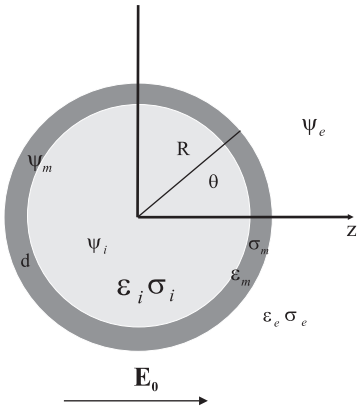

Figure 23 A spherical cell in external electric field.

Table 5 Typical values of conductivity and permittivities of a cell [104].

	Conductivity	Permittivity
External medium	[a]$\sigma_e = 1.2\,\mathrm{S/m}$	$\varepsilon_e = 7.1 \times 10^{-10}\,\mathrm{As/Vm}$
Cytoplasm	$\sigma_i = 0.5\,\mathrm{S/m}$	$\varepsilon_i = 7.1 \times 10^{-10}\,\mathrm{As/Vm}$
Membrane	$\sigma_m = 10^{-7}\,\mathrm{S/m}$	$\varepsilon_m = 4.4 \times 10^{-11}\,\mathrm{As/Vm}$
Membrane thickness	$d = 5 \times 10^{-9}\,\mathrm{m}$	
Cell radius	$R = 10^{-5}\,\mathrm{m}$	

[a]Physiologycal saline

equation are given by following expressions [105]:

$$\Psi_e = E_0 r\cos\theta - \frac{a}{r^2}E_0\cos\theta \tag{22}$$

$$\Psi_m = AE_0 r\cos\theta - \frac{B}{r^2}E_0\cos\theta \tag{23}$$

$$\Psi_i = CE_0 r\cos\theta \tag{24}$$

where r and θ are spherical coordinates. The boundary conditions at two borders-inner radius (R_1) and outer radius (R), representing the conservation of the current:

$$\sigma_e\frac{\partial\psi_e}{\partial r}\Big|_R = \sigma_m\frac{\partial\psi_m}{\partial r}\Big|_R, \quad \sigma_m\frac{\partial\psi_m}{\partial r}\Big|_{R_1} = \sigma_i\frac{\partial\psi_i}{\partial r}\Big|_{R_1} \tag{25}$$

and potential:

$$\psi_e\big|_R = \psi_m\big|_R, \quad \psi_m\big|_{R_1} = \psi_i\big|_{R_1} \tag{26}$$

define a set of four linear equations for the constants a, A, B and C. By solving the above set of equations [2] and taking into account that for cells $d \ll R$ we obtain the expression for the induced transmembrane voltage:

$$U_m = \Delta\Psi = \frac{3}{2}E_0 R\cos\theta\frac{3\frac{d}{R}\sigma_i\sigma_e}{(\sigma_m + 2\sigma_e)\left(\sigma_m + \frac{1}{2}\sigma_i\right) - \left(1 - \frac{3d}{R}\right)(\sigma_e - \sigma_m)(\sigma_i - \sigma_m)} \tag{27}$$

which can be further simplified if the membrane conductivity is much smaller than external and internal conductivity (true for physiological conditions):

$$U_m = \Delta\Psi = \frac{3}{2}E_0 R\cos\theta. \tag{28}$$

The induced transmembrane voltage has maximum at both cell poles and is proportional to the external electric field and cell diameter. From the transmembrane voltage we can obtain the electric field inside the membrane $E_m = U_m/d$, which is amplified for a factor of $R/d(\sim 10^3)$. And predominately this strong electric field inside the cell membrane is crucial for structural changes inside the lipid bilayer.

Most of the authors agree [29,106–108] that the induced transmembrane voltage is superimposed on the resting transmembrane voltage, resulting in an asymmetric transmembrane voltage. The above equation gives the induced transmembrane voltage for a spherical cell, which is valid for cells for most of the conditions present in experiments and is widely used in the literature. However, there are some cases where this simplified equation leads to considerable errors: for very low-conductive media $\sigma_e < 0.01$ S/m [109,110] the original equation has to be used where all three conductivities influence the induced transmembrane voltage. The above derivation follows from Laplace equation, which is valid only if the electroneutrality condition is satisfied (no net charges in any of the regions). This is not true for a biological cell where surface charge is present in a layer with thickness of a Debye length. Thus, instead of the Laplace equation the Poisson equation should be solved. The difference between the solutions of both equations is significant only for very low-conductive media and can be neglected otherwise [2,111].

Schwan derived the time dependent solution [109] for the induced transmembrane voltage on a spherical cell for a step turn-on of a DC electrical field:

$$\Delta\Psi = \frac{3}{2} E_0 R \cos\theta \left(1 - e^{-t/\tau}\right) \frac{3\frac{d}{R}\sigma_i\sigma_e}{(\sigma_m + 2\sigma_e)\left(\sigma_m + \frac{1}{2}\sigma_i\right) - \left(1 - \frac{3d}{R}\right)(\sigma_e - \sigma_m)(\sigma_i - \sigma_m).} \quad (29)$$

The time constant τ also depends on the dielectric properties of the membrane:

$$\tau = \frac{\varepsilon_m}{\frac{d}{R}\frac{2\sigma_e\sigma_i}{2\sigma_e + \sigma_i} + \sigma_m} \quad (30)$$

where ε_m denotes permittivity of the membrane. The time constant τ represents a typical time needed for charging of a cell membrane, which behaves as a capacitor. It is directly related to the frequency of beta dispersion observed in impedance spectra of cells. For a typical biological cell we obtain a time constant around a microsecond, which represents the time that is needed for the induced transmembrane voltage to build up on the cell membrane and for electroporation to occur. For times shorter than microsecond the cell interior is also exposed to an electric field, resulting in the induced transmembrane voltage across the membrane of the cellular organelles. Thus for very short high-voltage pulses cell organelles can be permeabilized [112]. The above equation is valid for the response of a cell to a square pulse, however, for other pulse shapes the responses differs from the exponential [113].

4.1.2. Dense cell systems

In case of dense cell systems (dense suspension and tissue) with high cell volume fraction ($f > 0.1$) [114,115] the local electric field E is lower than the applied electric field E_0 due to the effect of neighboring cells. In Fig. 24 it can be seen that in case when $f = 0.5$ normalized induced transmembrane voltage is decreased from 1.5 to 1.3 for cells organized in fcc lattice, which is the most realistic representation of cell ordering in dense suspension. Therefore in dense cell suspensions and tissue the decrease in the local field should be taken into account.

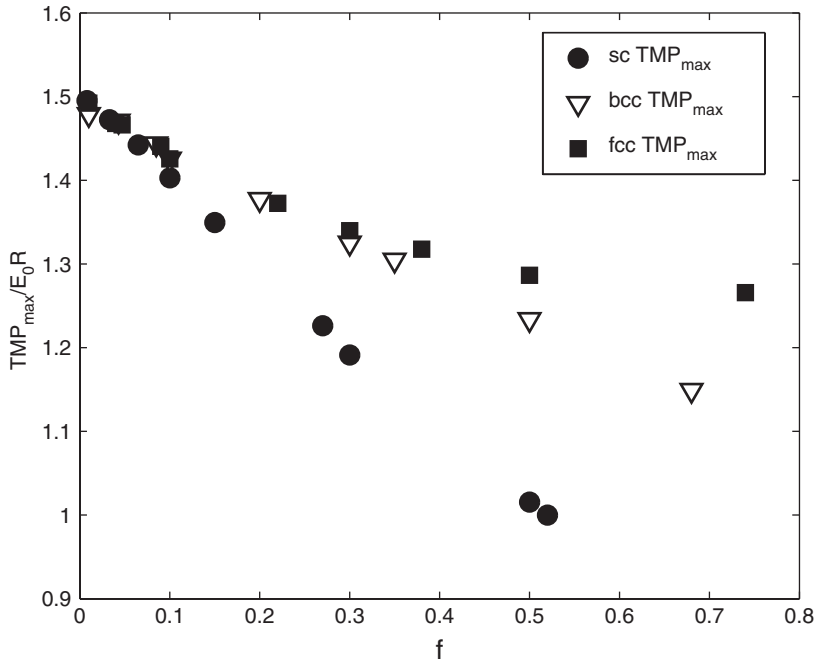

Figure 24 The normalized maximal ($\phi = 0^\circ$) induced transmembrane voltage-TMP$_{max}/E_0R$ in dense cell suspension (*f*-cell volume fraction) for three different cubic lattices (simple cubic – sc, body centered cubic – bcc and face centered cubic lattice – fcc).

4.2. Maxwell Stress Tensor and Forces Acting on a Cell in an External Field

The cell membrane experiences different forces in the presence of an external electrical field, which can be derived from Maxwell stress tensor:

$$T_{ij} = \varepsilon\left(E_i E_j - \tfrac{1}{2}E^2\delta_{ij}\right). \tag{31}$$

From the solution of a Laplace equation for a cell in an external field E_0 (equations (22–24)) we can calculate the electric fields in the cytoplasm, membrane and outside the cell [2]. For the average radial component of the field inside the membrane we obtain:

$$E_{rm} = \frac{3}{2}\frac{R(1-2d/R)}{d}E_0\cos\theta \approx \frac{3}{2}\frac{R}{d}E_0\cos\theta \tag{32}$$

and for radial components inside and outside the cell:

$$E_{ri}(R_1) = 3E_0\frac{\sigma_m\sigma_e}{(2\sigma_m\sigma_e + \sigma_m\sigma_i) + 2\sigma_i\sigma_e d/R}\cos\theta \approx 3E_0\frac{\sigma_m R}{\sigma_i\, d}\cos\theta \tag{33}$$

$$E_{re}(R) = 3E_0\frac{\sigma_m\sigma_i\left(1-2d/R\right)}{(2\sigma_m\sigma_e + \sigma_m\sigma_i) + 2\sigma_i\sigma_e d/R}\cos\theta \approx 3E_0\frac{\sigma_m R}{\sigma_e\, d}\cos\theta. \tag{34}$$

If we insert the above equations into the expression for Maxwell stress tensor:

$$T_{ij} = \varepsilon\left(E_i E_j - \tfrac{1}{2}E^2\delta_{ij}\right) \tag{35}$$

we obtain the compression force in the membrane:

$$T_{rr}^{m} = \varepsilon_m E_{rm}^2/2 = \frac{9}{8}\left(\frac{R}{d}\right)^2 \varepsilon_m E_0^2 \cos^2\theta. \tag{36}$$

Additionally, each surface experiences slightly different pressure yielding a net outward-directed force which tends to elongate the cell in the direction of the field:

$$T_{rr}^{e} - T_{rr}^{i} = \frac{9}{2}\frac{R}{d}\varepsilon_m E_0^2 \cos^2\theta. \tag{37}$$

The elongation due to Maxwell stress tensor can be observed for giant vesicles under the microscope [116] for electric fields used in electroporation, however for cells the cytoskeleton prevents cells to deform. Only in case of extremely strong electric fields (above 10 kV/cm) that are used for electroporation of organelles with nanosecond pulses, some deformation of cells can be observed [117,118].

4.3. Transport of Molecules Across Permeabilized Membrane

In this section, we discuss the underlying mechanisms which contribute to the increased transport for ions, molecules and macromolecules across an electropermeabilized membrane. There are several possible transmembrane transport mechanisms of which most important are diffusion, electrophoresis, electroosmosis and osmosis. Which mechanism is dominant depends on the type of the object (ion, molecule), the length of the pulses, electric field strength, concentration gradients and other physical parameters. However, general observation in different experimental studies was that transport of ions and molecules occurs only through the permeabilized area.

4.3.1. Diffusion

The flux of a given neutral molecule through the permeable membrane can be described by diffusion equation:

$$\frac{dn_e(t)}{dt} = -\frac{c_e(t) - c_i(t)}{d}\, D f_{per}(t, E, t_E, N)\, S_0 \tag{38}$$

where f_{per} represents the fraction of pores in the cell membrane which is a complex function of time (t) (mostly due to resealing process), electric field strength (E), pulse duration (t_E) and number of pulses (N). Additionally, the diffusion constant for a given molecule depends on the size of permeable structures (pores), leading to an equation which in real experimental observations of molecular uptake can be used only approximately. The above equation can also describe diffusion of ions or charged molecules through the permeabilized region since diffusion is a relatively slow process which occurs mainly after the pulse application and thus the Nernst–Planck equation (see equation (90)) simplifies to the above equation.

4.3.2. Electrophoresis

Electrophoresis is another mechanism of transport which was shown to be the most important for the transport of charged macromolecules, especially for DNA molecules. The electrophoretic driving force acts on the charged molecules in the electric field, thus, unlike diffusion, is present only during the pulse. For this reason protocols for gene transfection use much longer pulses (a few to tens of milliseconds) than pulses used for uptake of smaller molecules, or combination of short high-voltage and long low-voltage pulses [119–121]. Electrophoretic force is the driving force for all charged molecules:

$$F = e_{\text{eff}} E_{\text{loc}} \tag{39}$$

where e_{eff} is the effective charge of a given molecule and E_{loc} the local electric field. The effective charge depends on the charge of a given molecule and on the ionic strength of the solution. The velocity of a given molecule depends on its mobility and viscosity of the medium.

4.3.3. Osmosis and electroosmosis

The osmotic flow is driven by the difference in the osmotic pressure inside and outside of the cell:

$$\Phi(t) \propto c(t)\, \Delta p \tag{40}$$

depending also on the permeability of the membrane. In most experimental conditions isoosmolar media are used, however, when a cell membrane is permeabilized, ions and smaller molecules are free to move due to diffusion, whereas macromolecules are bound inside the cell. Consequently, the cell interior is not in osmotic equilibrium with the exterior and thus water flowing into the cell causes its swelling. This swelling, also named colloid-osmotic swelling, is observed in electroporation experiments on cells [122–125]. Together with the flow of water also the molecules are driven into the cell.

Electroosmosis is the transport of bulk liquid through a pore under the influence of an electric field. In an electric field ions migrate together with their sheath of water molecules, which induces the flow of water through the pore.

4.3.4. The permeabilized surface area

Independently on the process it was shown that the transport of ions and molecules during electroporation occurs only through the permeabilized area S_c, i.e. the area which is exposed to above-critical voltage [84,126–128]. From the expression for the induced transmembrane voltage for an isolated spherical cell (equation (28)) we can define the critical angle θ_c where the induced voltage equals the critical voltage U_c:

$$\Delta U_c = \Delta\Psi = 1.5\, ER \cos\theta_c. \tag{41}$$

If we neglect the resting transmembrane voltage we obtain the formula for the area of two spherical caps (see Fig. 25) where $\Delta\Psi > U_c$:

$$S_c = 2 \times 2\pi R^2 (1 - \cos\theta_c). \tag{42}$$

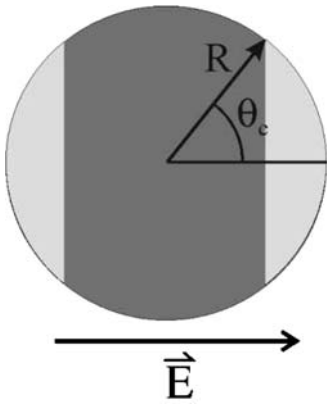

Figure 25 Schematical representation of permeabilized area of cell membrane.

Now, we define the critical field as the electric field when $\theta_c = 0 : E_c = U_c/1.5$ and thus obtain the total area exposed to above-threshold transmembrane voltage:

$$S_c = S_0(1 - E_c/E). \tag{43}$$

When considering the flow of molecules and ions across the permeabilized membrane above equation has to be incorporated in order to determine total flow across the membrane. Therefore, part of electric field dependence of pore fraction f_{per} is due to the increased permeabilized surface.

4.4. Experimental Studies and Theoretical Analysis of Cell Electroporation *in vitro*

Different studies analyzed cell electroporation *in vitro* either on single cells as well as on attached cells, cells in suspensions or multicell spheroids. Common observation is that electroporation is a threshold phenomenon and that it is governed by pulse parameters (duration, number and repetition frequency). Sometimes the critical voltage (or applied field) above which the transport is observed is defined as the reversible threshold since the changes are reversible and the cell membrane reseals after a given time lasting from minutes to hours. The value of the critical (threshold) transmembrane voltage at the room temperature was reported to be between 0.2 and 1 V [29,31,85,108] depending on pulse parameters and experimental conditions [129]. Further increase of the electric field causes irreversible membrane permeabilization and cell death due to direct physical loss of membrane integrity or due to excessive loss of the cell interior content.

4.4.1. Imaging of the transmembrane voltage during electroporation

Kinosita, Hibino and co-workers [84] used fast video imaging on a microsecond time scale to measure transmembrane voltage of sea urchin eggs during and after the

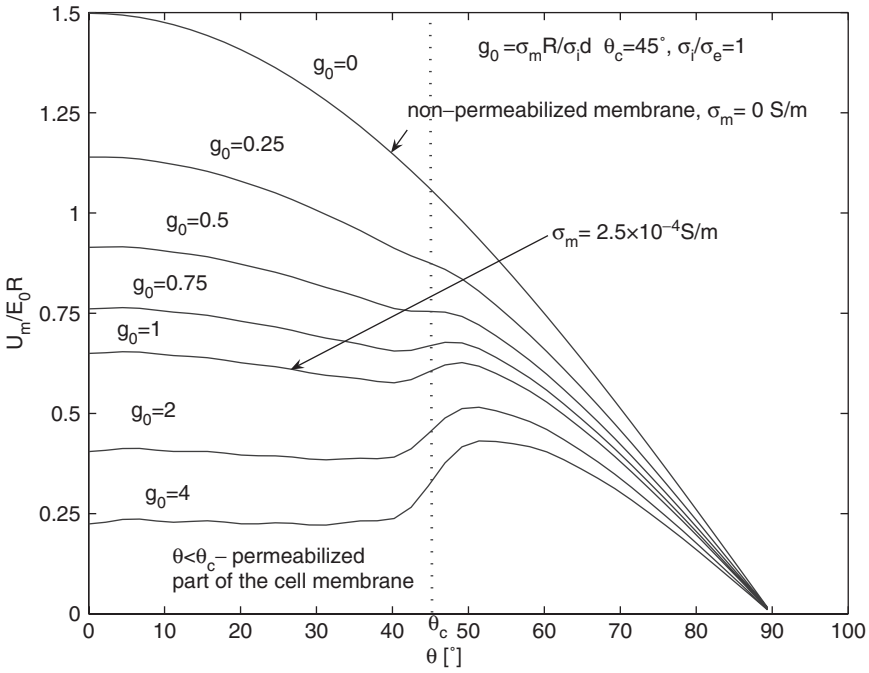

Figure 26 Analytically calculated normalized induced transmembrane voltage (TMP/E_0R) on a permeabilized cell for different maximum membrane conductivities g_0, $v = \sigma_i/\sigma_e$ [130]. Note that $g_0 = 1$ corresponds to $\sigma_m = 2.5 \times 10^{-4}$ S/m, a value of a permeabilized cell and $g_0 = 0$ to nonpermabilized membrane.

electric pulses. They observed a decrease of a cosine profile due to the increased specific membrane conductance, which they estimated to be around few S/cm^2. In the same study the authors also studied the kinetics of resealing and obtained two time constants: one of a few microseconds and the second time constant around a millisecond. This was compared to analytical model of an electroporated cell which also predicts a decrease in induced transmembrane voltage on a electroporated cell of which the membrane at the two pole caps has increased conductivity (see Fig. 26). The parameter g_0 is the normalized maximal membrane conductance at the two poles of the cell, defined as:

$$g_0 = \frac{\sigma_m}{\sigma_i}\frac{R}{d}. \tag{44}$$

Their experiments and analysis clearly showed that there exist conductive pathways during cell electroporation, which increase conductivity and decrease the induced transmembrane voltage in the area that is permeabilized. In the following study [85] they further showed that there exist at least two mechanisms for membrane resealing, where the slower process in the order of minutes enables a successful uptake of molecules following the application of pulses.

4.4.2. Measurements of conductivity in cell suspensions and pellets – quantification of short-lived pores

The first measurements of electrical properties of cells in a suspension during electroporation were done by Kinosita and Tsong [122,131,132], who measured electric properties of the isotonic suspension of erythrocytes. They observed an increase in the conductivity for electric fields around kV/cm and explained it with the increased membrane permeability for the ions due to formation of pores in a cell membrane. The initial step of pore formation was governed by the magnitude of the transmembrane voltage. From the measured changes of conductivity using their theoretical model they calculated the membrane conductivity and estimated the number of pores and ion flux through the permeabilized membrane. They determined that conductivity increased in two steps: a fast step in the range of one microsecond and a slower step which takes around 100 s. Specific membrane conductance increased up to 100 S/cm^2 but, in general, depended on pulse duration and electric field strength. After the end of the pulse the conductivity of the cell suspension returned to its initial value in a few seconds, but later on again increased due to the ion efflux. These observations were confirmed by the experiments of Abidor and co-authors [123,124] on cell pellets of different cell types, where an increase in the pellet conductance during the pulses above the critical electric field for electroporation was observed. After the pulse the conductance returned to the initial level in several stages: the first stage lasted milliseconds, the second a few seconds and the complete resealing was observed after minutes. They also observed changes of conductance due to the osmotic swelling of cells. Using microsecond and nanosecond pulses, several following studies observed increased conductivity during electroporation *in vitro* and *in vivo* [133,134] which suggested that measurement of conductivity could enable on-line observation and control of tissue electroporation [125,135,136].

Recently we made an extensive *in vitro* study of conductivity during cell electroporation of cell (B16F1 cells) suspensions. Figure 27 represents transient conductivity changes $\Delta\sigma_{tran}{}^{N}/\sigma_0$ during the N-th pulse for $E_0 = [0.4–1.8]$ kV/cm. An increase in transient conductivity changes is observed above 0.5 kV/cm, which is in agreement with the threshold for permeabilization of B16 cells obtained for molecular uptake. Interestingly, the number of pulses does not influence the transient conductivity [125,137].

From the measured conductivity changes fraction of the surface area of pores can be determined. Detailed derivation is presented in Appendix B.1. The fraction of transient pores f_p can be estimated as:

$$f_p = \frac{S_{por}}{S_0} \approx \frac{(1 - E_c/E)\,\sigma_m}{\rho\,\sigma_{0por}} \tag{45}$$

where σ_{0por} is the average conductivity between inside the cell and extracellular medium and parameter ρ is:

$$\rho = \frac{1}{\left(1 + \frac{n\beta U_m}{w_0 - n\beta U_m}\right)\exp(w_0 - n\beta U_m) - \frac{n\beta U_m}{w_0 - n\beta U_m}}. \tag{46}$$

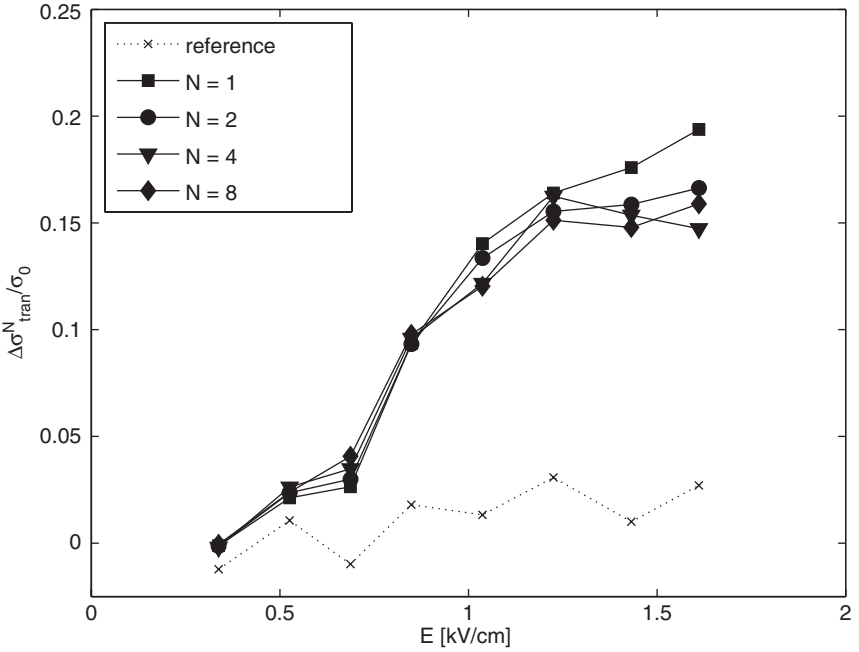

Figure 27 Transient conductivity changes during N-th pulse of the train of $8 \times 100\,\mu s$ pulses are shown. $\Delta\sigma^N_{tran}$ is normalized to the initial conductivity. Solid line-cells in medium, dotted line-reference measurement on medium without cells during the first pulse.

Table 6 Calculation of conductivity inside the aqueous pore – values of used parameters.

N	e/kT	σ_i	U_m	R	D
0.15	$40\,V^{-1}$	0.5 S/m	900 mV	9.5 μm	5 nm
E	E_c	W_0	ρ	σ_m	D
0.84 kV/cm	0.5 kV/cm	2.5–5	0.22–0.57	$1.4–3.5 \times 10^{-5}$S/m	$2.5 \times 10^{-5}\,cm^2/s$

The parameters are defined in Appendix B.1, the values used are presented in Table 6. For the membrane conductivity $\sigma_m = [1.4 - 3.5] \times 10^{-5}$ and inserting values of parameters (see Table 6) we obtain for fraction of transient pores after 100 s pulse being $f_p = 10^{-5} - 10^{-4}$. Conductivity changes calculated theoretically taking into account the nonohmic behavior of the conductivity inside the pore using equation (46) are in good agreement with measured increase in conductivity during the pulses [125].

In Fig. 28, it is demonstrated that the conductivity changes relax almost to initial level in ten milliseconds (100 Hz) and after 1 s the following pulses have almost identical shape as the first pulse. This indicates that during electric pulses short-lived structural changes are formed which transiently increase ion permeation, but have very short lifetime after the pulses.

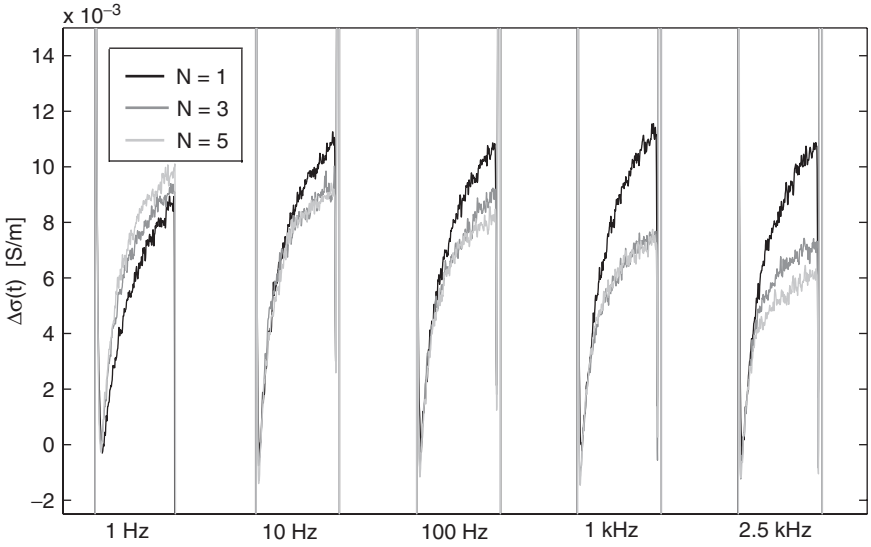

Figure 28 Effect of the repetition frequency on the conductivity changes. Pulses $8 \times 100\,\mu s$ with repetition frequencies from 1 Hz–2.5 kHz were used, $E =$ 0.84 kV/cm. The time-dependent conductivity changes $\Delta\sigma(t)$ of the first, third and the fifth pulse with respect to the first pulse (all initial levels are set to zero) are compared for different frequencies. Obtained from Ref. [125] with permission of Biophysical Society.

Altogether the conductivity measurements enable detection of short-lived permeable structures which are formed during the pulses. However since the conductivity drops to initial level in milliseconds after the pulses, these "pores" do not represent long-lived permeable structures which enable transport of molecules after the pulses.

4.4.3. Experimental studies of the effect of different parameters on molecular transport

The transport, which governs the uptake of molecules and leakage of cytoplasm contents, depends on experimental conditions, pulse parameters and the test molecule. The extensive studies of Teissié, Rols and colleagues, [30,96,120,138–141] examined the effect of different parameters (electric field strength, number of pulses, duration) on the extent of permeabilization uptake of exogenous molecules, cell survival, release of intracellular ATP and resealing. With these measurements it was shown that the critical parameter is the electric field strength and that the extent of permeabilization is governed by both duration and number of pulses. The authors define phenomenological electropermeabilization threshold E_p below which no transport is observed for given pulse parameters. However, they also define "limit" or real threshold E_s [30] which is the threshold below which no permeabilization occurs no matter how long the pulses are or how many are used. This threshold can be interpreted as the value of the electric field where critical transmembrane voltage is reached.

Two other extensive studies of electroporation *in vitro* were made [33,34], where authors studied uptake and viability for different electric field strength, duration, number of pulses and also different cell volume fractions. Data indicated that neither electrical energy nor charge determines the extent of permeabilization and that the dependency is more complex. The results of these two studies also suggest that by increasing number and duration of pulses a certain "limit" threshold for permeabilization is reached, or in other words, the permeabilization curves start at the same electric field strength but the slope is electric field dependent. Even though some studies suggested [3] that pulse shape affects efficiency of electroporation our extensive study [142] of different pulse shapes showed that this is not crucial parameter.

The general observation on the resealing kinetics of cell electroporation is that resealing of the membrane lasts for minutes and is strongly dependent on the temperature. Together with the fact that a colloid-osmotic effect is also present it is obvious that complete resealing of the cell membrane is governed by slow biological processes, which was shown that is ATP dependant.

4.4.4. Osmotic cell swelling

It was shown in several experiments that cells swell during electroporation [123–125,132]. Swelling of permeabilized cells is caused due to the difference in the permeabilities of ions and larger molecules (macromolecules) which results in an osmotic pressure that drives water into the cells and leads to cell swelling. The dynamics and the extent of cell swelling can be observed using imaging of cells during and after pulse application. The results of the measurements of the cell sizes during and after the pulses are shown in Fig. 29. The time constant of colloid osmotic swelling is few tens of seconds which is in agreement with the time constant for efflux of ions, which is between 10 and 20 s.

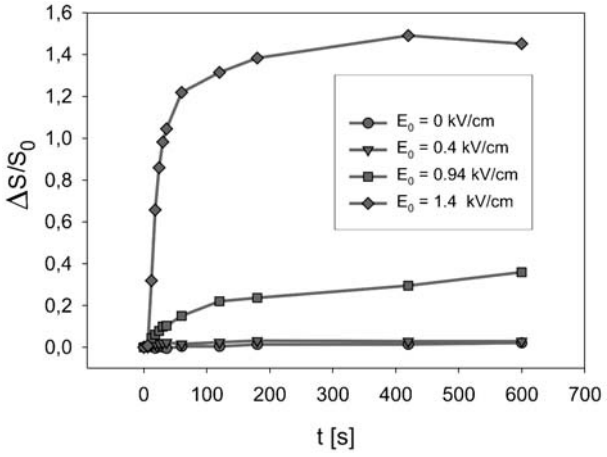

Figure 29 The effect of colloid-osmotic swelling – relative changes of the surface area $\Delta S/S_0$ of cells for different applied electric field strengths E_0 of the electric pulses ($8 \times 100\,\mu s$, 1 Hz) and control ($E_0 = 0$ kV/cm), time $t = 0$ s – start of the first pulse, $t = 7$ s end of pulsation.

4.4.5. Quantification of ion diffusion and the fraction of long-lived pores

The process of ion transport during electroporation is similarly as transport of molecules governed mostly by diffusion. An increase in conductivity between the pulses due to ion efflux can be therefore used to determine the permeability coefficient and fraction of stable pores, which enable molecular transport which is crucial for successful application of electroporation.

The diffusion of ions is a slow process compared to the duration of the electric pulses thus we can assume that the major contribution to efflux of ions occurs without the presence of the electric field:

$$\frac{dc_e(t)}{dt} = -\frac{D\,S(E,N)}{d\;VF(1-F)}(c_e(t) - Fc_i(t)). \tag{47}$$

Definition of parameters and more detailed derivation is presented in Appendix B.2. The solution of above equation for $c_e(t)$ gives exponential rise to maximum, from which it follows that the conductivity between the pulses also increases as an exponential due to ion efflux. Form this it follows that the permeability coefficient k_N after the N-th pulse can be determined from the measured conductivity at N-th pulse ($\Delta\sigma_N$) and at N+1-th pulse ($\Delta\sigma_{N+1}$):

$$k_N = \frac{1}{\Delta t_N}\ln\left[1 - \frac{\Delta\sigma_N}{\Delta\sigma_{\max}}\Big/1 - \frac{\Delta\sigma_{N+1}}{\Delta\sigma_{\max}}\right] \tag{48}$$

The permeability coefficient is directly proportional to the fraction of long-lived pores – f_{per}:

$$f_{per}^N \approx k_N\frac{dRF(1-F)}{3D'}, \quad D' = D\exp(-0.43w_0). \tag{49}$$

In Fig. 30 relative changes of the initial level of conductivity due to ion diffusion at the start of the N-th pulse $\Delta\sigma/\sigma_0 = (\sigma_0^N - \sigma_0)/\sigma_0$ for consecutive pulses are shown. Similarly as in Fig. 27 the initial level starts to increase for above the threshold $E > 0.5$ kV/cm, which can be explained with the efflux of ions (mostly K^+ ions) from the cytoplasm through membrane pores. For higher electric fields ions efflux increases up to 1.6 kV depending also on the number of applied pulses. From measured $\Delta\sigma/\sigma_0 = (\sigma_0^N - \sigma_0)/\sigma_0$ using equation (48) we calculated permeability coefficients k_N which are proportional to fraction of long-lived pores (f_{per}). It can be seen (see Fig. 31) that k_N approximately linearly increases with number of pulses, and as expected increases also with the electric field strength.

4.4.6. The effect of electric field on long-lived pore formation and stabilization

Previously we have obtained the equation (see equation (43)) that determines how the electric field governs the area of the cell membrane, which is exposed to the above-critical transmembrane voltage U_c and has increased permeability: $S_c(E) = S_0\big((1 - E_c)/E\big)$. Furthermore, we can assume that pore formation in the area where $U > U_c$ is governed by the free energy of the pore, where the electrostatic term also includes the square of the electric field $\Delta W_e = aE^2$ [32,46]. Based on this we can assume that the most simplified equation, which describes the field

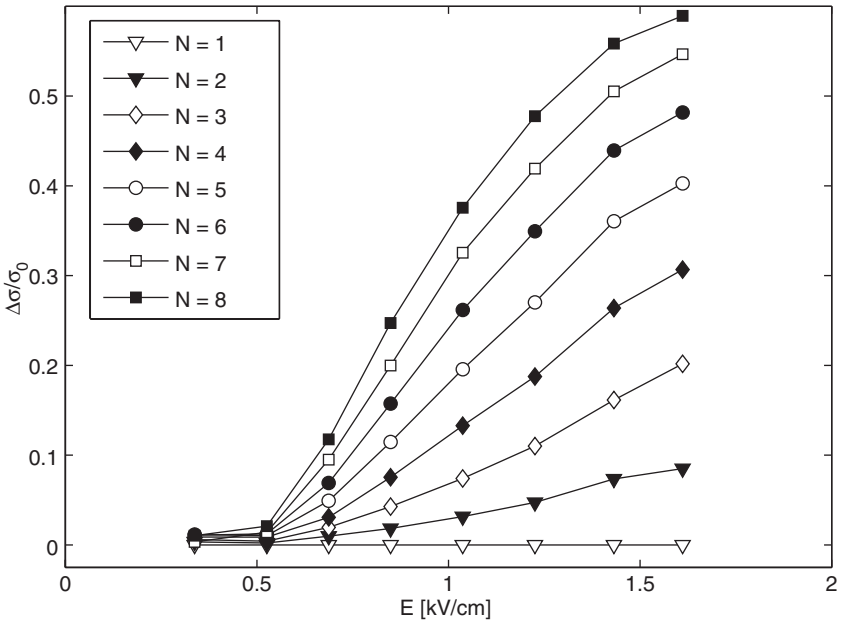

Figure 30 Relative conductivity changes between the pulses due to ion diffusion – $\Delta\sigma/\sigma_0 = (\sigma_0^N - \sigma_0)/\sigma_0$, where σ_0^N is the initial level at the start of the Nth pulse. $8 \times 100\,\mu s$ pulses were used with repetition frequency 1 Hz.

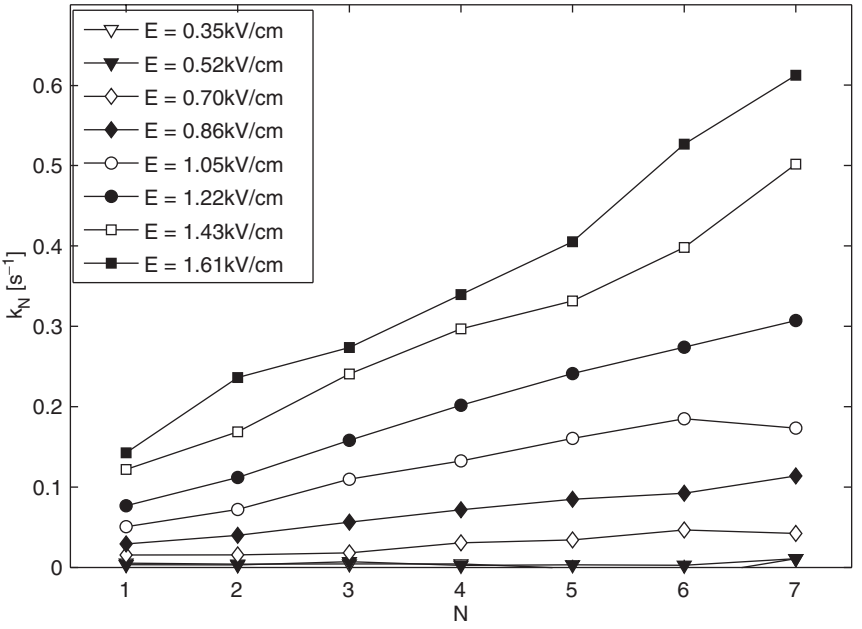

Figure 31 The permeability coefficients k_N for N pulses obtained after the N-th pulse calculated using equation (48) from the conductivity changes $\Delta\sigma/\sigma_0$ using $8 \times 100\,\mu s$ pulses. Obtained from Ref. [137] with permission of Elsevier.

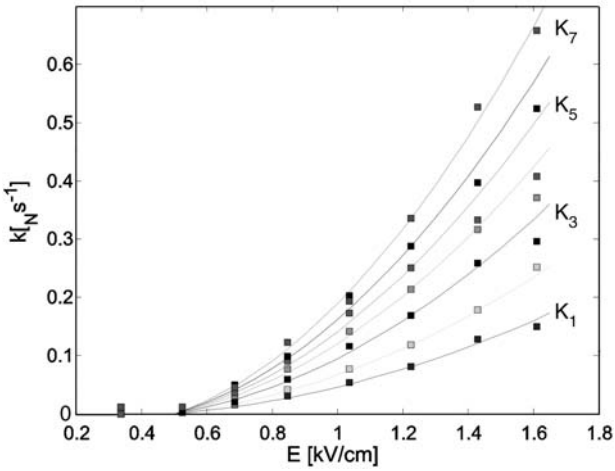

Figure 32 The permeability coefficients k_N for N pulses obtained after the N-th pulse calculated using equation (48) from the conductivity changes $\Delta\sigma/\sigma_0$ using 8×100 μs pulses. Comparison of the prediction of the model according to equation (50) (lines) and the measured permeability coefficients (symbols) is shown [137], with permission of Elsevier.

dependent permeability, can be written as [137]:

$$k_N(E) = C_N(1 - E_c/E)E^2. \tag{50}$$

where C_N are constants that depend on the size of the pores and their growth, and are thus dependent also on the number of pulses. The above equation takes into account the increase of the area of the cell exposed to the above critical voltage and the quadratic field dependence in the permeabilized region.

In Fig. 32 we compare the field dependence of the experimental permeability coefficient with the theoretical model. As expected, the permeability coefficient k_N and with this fraction of "transport" pores (see equation (48)) increases above the threshold electric field. More interestingly, this simple model (equation (50)) can very accurately describe the measured values, as can be seen in Fig. 32. This demonstrates that long-lived pore formation is governed also by the energy of the pores as well as by the number of pulses.

4.4.7. General experimental observations of cell electroporation

To summarize different phenomenological observations of cell electroporation (electropermeabilization)

- The state of transiently increased membrane conductivity indicates the existence of short-lived membrane structures which enable ion permeation. In the aqueous pores formation model of electroporation this corresponds to conductive hydrophilic pores [32]. An alternative explanation of these permeable structures was that they are structural mismatches in the lipid organization [143]. The membrane conductivity drops to the initial level in a range of a millisecond after

the pulses. This could be explained only with the existence of many small pores transient during the electric pulses, which close very rapidly (milliseconds) after the pulse. The number of these short-lived pores does not depend on the number of applied pulses but solely on the electric field strength and pulse duration.

- The state of increased permeability can last for tens of minutes after pulse application. Therefore, it is clear that in contrast to transient pores which reseal in milliseconds some pores are stabilized enabling transport across the membrane in minutes after the pulses. The quantification of ion efflux shows that in contrast to transient short-lived pores these stable pores are governed both by electric field strength as well as the number of pulses. The fraction of long-lived stable pores increases with higher electric field due to larger area of the cell membrane exposed to above critical voltage and due to higher energy which is available for pores formation. Moreover, each pulse increases the probability for the formation of the stable pores.
- The resealing of the cell membrane is a biologically active ATP-dependant process which strongly depends on the temperature and lasts from minutes to hours after pulse application. This clearly shows that long-lived pores are thermodynamically stable.

This and other observations lead to conclusion that the nature of long-lived "transport" pores is different than that of transient pores, which are present only during the pulses.

4.4.8. Possible theoretical explanations of long-lived pores

As shown in previous section there exist two types of pores (structural changes) of which nature, duration and number differs significantly. Hydrophilic pores are not stable after pulse application therefore some additional process must be involved in formation of stable pores. In Fig. 33 possible inter-relations between structural changes, conductivity changes and permeabilization (increased transport of molecules) are shown.

As shown in figure above the nature of long-lived pores and the relation between short-lived structural changes and long-lived is still not completely understood. In literature several explanations for the existence of these stable long-lived pores can be found. It was proposed that larger pores are formed by coalescence of smaller pores (defects) which travel in the membrane [144]. Some authors suggested that pores (defects) migrate along the membrane surface [32] and are grouped around inclusions. Altogether, there are no direct experimental observations which would confirm the hypothesis of a coalescence of pores.

There is general agreement that proteins are involved in stabilization of larger pores [32,46]. Authors speculated that cytoskeleton structure could act similarly to the macroscopic aperture of planar membrane experiments leading to rupture of limited portions of a cell membrane but not of the entire membrane [32]. Other authors suggested [139] that disintegration of the cytoskeleton network could affect electroporation where specific sites in the membrane would be more susceptible to

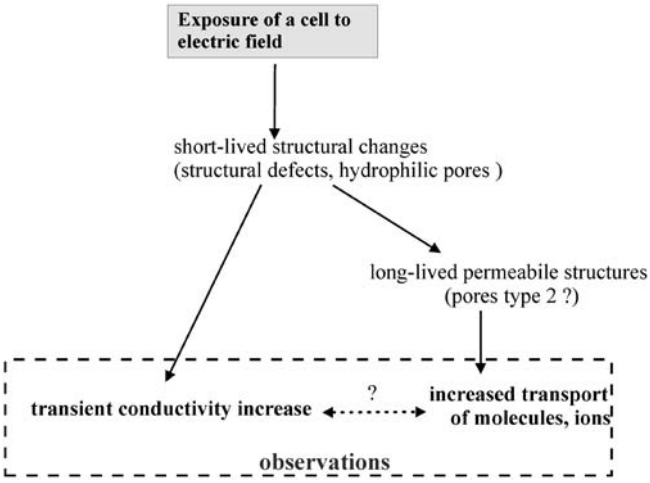

Figure 33 Possible inter-relations between structural changes, conductivity changes and permeabilization (increased transport of molecules).

pore formation. Some experiments suggest that only a few large pores contribute to increased permeability [145], whereas other suggests a contribution from a larger number of small defects due to the structural mismatches in the lipid membrane or due to structural discontinuities at borders between the domains. Recently it was also shown that anisotropic inclusions can stabilize pores in the membrane [146].

Altogether, there is still no definite explanation for the long-lived permeable structures in the cell membrane [99]. Whatever these structures are, they have long resealing times and are large enough to facilitate transport of larger molecules.

5. Comparison between Planar Lipid Bilayers and Cell Electroporation

We have to stress that the described theories were developed for planar bilayer membranes which differ from cell membranes where membrane proteins and cytoskeleton are present. However, several experiments demonstrated that the structural changes probably occur in the lipid region of the cell membrane [29,32,147] and thus these theories can be applied to cell membranes as well.

Both in planar bilayer membranes and cell membranes the authors obtained a gradual increase of conductivity in high electric fields. The time interval preceding the irreversible breakdown and the rate of increase of conductivity are determined by the strength of the applied electric field [147]. The greatest observed difference is that the reversible electroporation in cells is much more common than in planar

bilayer membranes and that resealing of artificial bilayer membranes takes milliseconds whereas resealing of cells can last for several minutes. And specifically this long-lasting increased permeability of cell membrane is crucial for biotechnological and biomedical applications. This shows clearly that for a complete description of cell electroporation the role of the curvature, colloid osmotic swelling and specially cell structures, such as cytoskeleton, domains and membrane proteins have to be discussed and examined.

Altogether from theoretical model of aqueous pore formation can relatively good describe experimental observations on lipid bilayers: critical transmembrane voltage and stochastic nature of the process. However, up to now there is no theoretical description which could completely describe all observable phenomena present during cell electroporation and the underlying physical mechanism: the formation of structural changes in the membrane on a molecular level during the electric pulse, stochastic nature of electroporation, the observed dependency of molecular uptake on pulse duration and number of pulses, field strength, repetition frequency, the strong nonlinear transmembrane current-voltage characteristics with the critical transmembrane voltages between 0.2–1 V and the stability of "pores" after the pulses as well as the resealing dynamics.

Altogether, the model of an aqueous pore formation offers a plausible explanation for its stochastic nature and dependence on the pulse duration. The local minimum in the free energy could represent stable hydrophilic pores, which could explain the state of increase conductivity and permeability during the electric pulses. However, as it can be seen from Fig. 21, by using the realistic parameters a minimum in free energy is obtained only for very specific values of parameters usually suggesting that electroporation would immediately lead to irreversible electroporation. Thus as already discussed in the review of Weaver and Chizmadzhev, some additional processes/structures have to be included to obtain a realistic theoretical model of stable pores which could explain long-lived permeability of the cell membrane after electroporation. It is also clear that this theoretical description should incorporate proteins and cytoskeleton which can be crucial factors that enables pore stabilization and prevent breakdown of the cell membrane thus enabling the most important applications of cell electroporation: electrogene transfer and electrochemotherapy.

Strong support for the existence of pores was given recently by Marrink and colleagues in a molecular dynamics simulation of a lipid bilayer without [148] and in the presence [149] of an external electric field. Owing to thermal energy the lipid molecules constantly fluctuate and sometimes form short-lived states, with a structure similar to that of a small hydrophilic pore. By this, the assumption of the existence of small pores in the membrane before the application of the electric pulse is justified. The dynamic simulation in the presence of an external electric field [149] further showed existence of hydrophilic pores for the induced transmembrane voltage above 2.5 V, which is much higher than experimentally observed critical transmembrane voltage (0.2–1 V), however, these studies are important since they present calculations of the possible lipid states by taking into account forces on a molecular level. Future studies will probably enable building more realistic models.

Appendix A

A.1. The Instability in the Hydrodynamic Model

In this model, the membrane is a layer of nonconductive liquid with permittivity ε_m and surface tension Γ. Its volume V is constant, while both its surface S and thickness d are variable, with initial values denoted by S_0 and d_0. The pressure exerted on the membrane by the transmembrane voltage U is given by

$$p_1 = \frac{\varepsilon_m U^2}{2d^2} \tag{A.1}$$

and is opposed by the pressure due to the increase of membrane surface, which is given by

$$p_2 = -\frac{\Gamma}{V}\int_{S_0}^{S} \mathrm{d}S = -\frac{\Gamma(S - S_0)}{dS}. \tag{A.2}$$

Since in this model the volume is constant, $dS = d_0 S_0$, and we can write

$$p_2 = -\frac{\Gamma(S - S_0)}{d_0 S_0} = -\frac{\Gamma}{d_0}\left(\frac{S}{S_0} - 1\right) = -\frac{\Gamma}{d_0}\left(\frac{d_0}{d} - 1\right) = -\Gamma\left(\frac{1}{d} - \frac{1}{d_0}\right). \tag{A.3}$$

The equilibrium is obtained at a value of d at which $p_1 + p_2 = 0$:

$$\frac{\varepsilon_m U^2}{2d^2} - \Gamma\left(\frac{1}{d} - \frac{1}{d_0}\right) = 0 \tag{A.4}$$

We rewrite this expression as

$$\frac{1}{d_0}d^2 - d + \frac{U^2\varepsilon_m}{2\Gamma} = 0. \tag{A.5}$$

This is a quadratic equation and thus has two solutions, but since at $U = 0$ the membrane thickness is by definition $d = d_0$, only one has a physical meaning, namely

$$d = \frac{d_0}{2}\left(1 + \sqrt{D}\right), \quad \text{where} D = 1 - \frac{2U^2\varepsilon_m}{\Gamma d_0}. \tag{A.6}$$

Real solutions then exist only for $D \geq 0$, and the equilibrium is only reached at voltages below the critical value given by

$$U_c = \sqrt{\frac{\Gamma d_0}{2\varepsilon_m}}. \tag{A.7}$$

A.2. The Instability in the Elastic Model

We represent the membrane as an elastic layer with permittivity ε_m and elasticity module Y_m. We assume that the membrane surface S is constant, while its volume V and its thickness d are variable, with initial values V_0 and d_0. The pressure caused

by the voltage U is again

$$p_1 = \frac{\varepsilon_m U^2}{2d^2} \tag{A.8}$$

and is opposed by the pressure due to the compression of the membrane volume,

$$p_2 = \int_{V_0}^{V} \frac{Y(V)}{V} \mathrm{d}V. \tag{A.9}$$

Assuming that Y does not vary with the deformation, we get

$$p_2 = Y \int_{V_0}^{V} \frac{\mathrm{d}V}{V} = -Y \ln \frac{V_0}{V} = -Y\left(\ln \frac{d_0}{d} + \ln \frac{S_0}{S}\right). \tag{A.10}$$

Since we assume a constant surface, $S = S_0$, the second logarithm is zero, and we have

$$p_2 = -Y \ln \frac{d_0}{d}. \tag{A.11}$$

The equilibrium is obtained at a value of d which gives $p_1 + p_2 = 0$:

$$\frac{\varepsilon_m U^2}{2d^2} - Y \ln \frac{d_0}{d} = 0 \tag{A.12}$$

which we rewrite as

$$\frac{\varepsilon_m U^2}{Yd^2} = \ln \frac{d_0^2}{d^2}. \tag{A.13}$$

Let $\chi = d_0^2/d^2$; then

$$K\chi = \ln \chi, \quad \text{where} K = \frac{\varepsilon_m U^2}{Y d_0^2}. \tag{A.14}$$

This equation is not solvable analytically, but it is easily verified that real solutions exist only for $K \leq 1/e$. The equilibrium is thus only reached below the critical voltage given by

$$U_c = d_0 \sqrt{\frac{Y}{e\varepsilon_m}} \approx 0.61 d_0 \sqrt{\frac{Y}{\varepsilon_m}}. \tag{A.15}$$

A.3. The Instability in the Hydroelastic Model

We assign to the membrane a permittivity ε_m, surface tension Γ and elasticity module Y, and we assume that the volume V, surface S and thickness d of the membrane are all variable, with initial values of the latter two denoted by S_0 and d_0. The pressure generated by the transmembrane voltage is opposed by the pressures due to the membrane surface tension and elasticity (see Appendices A.1 and A.2),

with the equilibrium given by

$$\frac{\varepsilon_m U^2}{2d^2} - \frac{\Gamma(S - S_0)}{dS} - Y \ln\frac{d_0}{d} - Y \ln\frac{S_0}{S} = 0. \tag{A.16}$$

We rewrite this expression as

$$\frac{\varepsilon_m U^2}{2Yd^2} + \frac{\Gamma S_0}{YdS} - \frac{\Gamma}{Yd} = \ln\frac{d_0}{d} + \ln\frac{S_0}{S} \tag{A.17}$$

and substitute $\psi = d_0/d$, $\xi = S_0/S$, to get

$$K_1\psi^2 - K_2\psi(1 - \xi) = \ln\psi + \ln\xi \tag{A.18}$$

where $K_1 = \varepsilon_m U^2/2Yd_0^2$ and $K_2 = \Gamma/Yd_0$. While in the direction perpendicular to the membrane surface, the pressures due to the elasticity and surface tension are co-oriented, in the direction parallel to the membrane they oppose each other, so in the equilibrium

$$\frac{\Gamma(S - S_0)}{dS} - Y \ln\frac{d_0}{d} - Y \ln\frac{S_0}{S} = 0. \tag{A.19}$$

With the same notation as above, this gives

$$K_2\psi(1 - \xi) = \ln\psi + \ln\xi. \tag{A.20}$$

Subtracting this equation from the first equilibrium equation, we get

$$K_1\psi^2 - 2K_2\psi(1 - \xi) = 0 \tag{A.21}$$

and hence

$$1 - \xi = \frac{K_1}{2K_2}\psi. \tag{A.22}$$

Inserting this result into the second equilibrium equation, we finally get

$$\frac{K_1\psi^2}{2} = \ln\psi + \ln\left(1 - \frac{K_1}{2K_2}\psi\right). \tag{A.23}$$

This equation does not have a solution expressible as an elementary function, and to determine U_c, we insert actual parameter values and calculate ψ numerically for increasing values of U, until we reach the point $U = U_c$ for which no real solutions exist.

A.4. The Instability in the Viscohydroelastic Model

In a membrane with permittivity ε_m, surface tension Γ, elasticity module Y and viscosity μ, discontinuities occur after the transmembrane voltage U has been present for the critical duration given by

$$\tau_c = \frac{24\mu}{2\varepsilon_m U^2 k^2 - 8Y - \Gamma d_0^3 k^4} \tag{A.24}$$

where k is the wave number (the reciprocal of the length of the ripples on the membrane). Note that at low values of U, we would obtain a negative value of τ_c, which is physically meaningless; this means that the membrane is stable, and the discontinuities cannot occur at any τ_c. If the ripples can form freely (i.e. if there are no fixed points on the membrane), for a given U the wave number takes a value at which the value of τ_c is minimal

$$\frac{d\tau_c}{dk} = \frac{96\mu(\varepsilon_m U^2 k - \Gamma d_0^3 k^3)}{(2\varepsilon_m U^2 k^2 - 8Y - \Gamma d_0^3 k^4)^2}. \tag{A.25}$$

The solution $k = 0$ is meaningless as it would imply that the ripples are infinitely large, so we have

$$k^2 = \frac{\varepsilon_m U^2}{\Gamma d_0^3}. \tag{A.26}$$

Inserting this value into the expression for the critical duration, we get

$$\tau_c = \frac{24\mu}{\frac{\varepsilon_m^2 U^4}{\Gamma d_0^3} - 8Y}. \tag{A.27}$$

This expression takes a positive value only at voltages above the critical amplitude given by

$$U_c = \sqrt[4]{\frac{8\Gamma Y d_0^3}{\varepsilon_m^2}} \tag{A.28}$$

and the discontinuities occur if a voltage $U > U_c$ lasts longer than the critical duration at this voltage (see Fig. 14).

A.5. The Energy of a Hydrophilic Pore

At a distance ρ from the center of a cylindrical pore with a radius r, the strength of hydrophobic interaction is given by

$$\eta(\rho) = \eta_0 \frac{I_0(\rho/\lambda)}{I_0(r/\lambda)} \tag{A.29}$$

where η_0 is the value of $\eta(\rho)$ directly at the surface, λ the characteristic length of hydrophobic interaction and I_k the modified Bessel function of k-th order. Simultaneously, the total energy of this interaction is described as

$$W = 2\pi d \int_0^r \left[\eta^2(\rho) + \lambda^2 \left(\frac{d\eta(\rho)}{d\rho}\right)^2\right] \rho d\rho \tag{A.30}$$

where d is the height of the pore (the thickness of the membrane). By joining these expressions, we obtain

$$W = 2\pi dr\lambda\eta_0^2 \frac{I_1(r/\lambda)}{I_0(r/\lambda)}. \tag{A.31}$$

At $r \gg \lambda$, the ratio of the two Bessel functions approaches 1, and W is proportional to the pore surface $S = 2\pi rd$,

$$W = S\lambda\eta_0^2 \tag{A.32}$$

which shows that $\lambda\eta_0^2$ corresponds to the surface tension Γ_h at the interface of the hydrophobic surface and water. Since Γ_h is measurable, it is then sensible to rewrite the energy of the pore as

$$W = 2\pi dr\Gamma_h \frac{I_1(r/\lambda)}{I_0(r/\lambda)}. \tag{A.33}$$

Appendix B

B.1. Calculation of the Fraction of Surface Area of Transient Pores

Here, we present the estimation of the fraction of the surface area of pores in the cell membrane from the increased membrane conductivity (similar derivation was first presented by Hibino [84]). We assume that the specific conductance of the permeabilized area of a cell is approximately the sum of the conductance of N_p pores having radius r_p

$$G_p = N_p\pi r_p^2 \frac{\sigma_{por}}{d} = S_{por}\frac{\sigma_{por}}{d} \tag{B.1}$$

where we neglect the very small conductance of nonpermeabilized cell membrane and S_{por} represents the surface of all conducting pores. On the other hand, this conductance is equal to the average membrane conductance of the permeabilized area as obtained from our measurement and from the theoretical model $G_p = G_{meas}$, thus

$$S_{por}\frac{\sigma_{por}}{d} = S_c\frac{\sigma_m}{d} \tag{B.2}$$

where S_c represents the total permeabilized surface of one cell (the area exposed to above-threshold transmembrane voltage – $S_c = S_0\big((1 - E_c)/E\big)$ and σ_m the average membrane conductivity of permeabilized area as defined in the theoretical model. From this it follows that the fraction of pores is

$$f_p = \frac{S_{por}}{S_0} = \frac{S_c\sigma_m}{S_0\sigma_{por}} \approx \frac{\big((1 - E_c)/E\big)\sigma_m}{\sigma_{por}} \approx \frac{\big((1 - E_c)/E\big)\sigma_m}{\rho\sigma_{0por}} \tag{B.3}$$

where parameter ρ takes into account that conductivity inside the pores differs from bulk. Namely, conductance of the pore in an 1:1 electrolyte is given by [46]

$$G_{\mathrm{por}} = G_0 \frac{\exp(\beta U_{\mathrm{m}}) - 1}{\frac{\beta U_{\mathrm{m}}}{d} \int_0^d \exp\left[\beta U_{\mathrm{m}} \frac{d-x}{d} + w(x)\right] dx} = G_0 \rho, \quad G_0 = N_{\mathrm{p}} \pi r_{\mathrm{p}}^2 \frac{\sigma_{0\mathrm{por}}}{d} \tag{B.4}$$

where $\beta = e/kT$ and $w(x) = W(x)/kT$ where e is the electron charge, U_{m} the transmembrane voltage and $W(x)$ the energy of an ion inside the pore due to the interactions of the ion with the pore walls [46,150]. Parameter ρ is a scaling factor, which reduces the conductivity of the ions inside the pores (σ_{por}), compared to the bulk approximation $\sigma_{0\mathrm{por}} \approx (\sigma_{\mathrm{e}} + \sigma_{\mathrm{i}})/2$ in the limit of very large pores when interactions are negligible. For a trapezoid shape of $w(x)$ we obtain from equation (B.4) that when the transmembrane voltage is small $n\beta U_{\mathrm{m}} \ll w_0$:

$$\rho = \exp[-0.43(w_0 - n\beta U_{\mathrm{m}})] \tag{B.5}$$

which is true for physiological conditions where resting transmembrane voltage is between 50 and 100 mV. When we apply external electric field typical for electroporation the transmembrane voltage is large and thus we can use approximation $n\beta U_{\mathrm{m}} \gg w_0 (U_E \gg 25\ \mathrm{mV})$ and we obtain

$$\rho = \frac{1}{\left(1 + \frac{n\beta U_{\mathrm{m}}}{w_0 - n\beta U_{\mathrm{m}}}\right) \exp(w_0 - n\beta U_{\mathrm{m}}) - \frac{n\beta U_{\mathrm{m}}}{w_0 - n\beta U_{\mathrm{m}}}} \tag{B.6}$$

where n is the relative size of the entrance region of the pore and was estimated to be approximately 0.15 [46]. W_0 is the energy of an ion inside center of a pore and was estimated to be few kT [46,151,152].

B.2. Quantification of Ion Diffusion and Long-Lived Pores

Here we analyze theoretically the changes of conductivity on the time scale of seconds, where diffusion of ions dominates. The transport of ions through the membrane is governed by Nernst–Planck equation:

$$\frac{dn_{\mathrm{e}}(x,t)}{dt} = -DS\frac{dc(x,t)}{dx} - \frac{zF}{RT} DSc(x,t)\frac{d\Psi(x,t)}{dx} \tag{B.7}$$

where n_{e} is the number of moles in the external medium, D the diffusion constant ($\approx 2 \times 10^{-5}\mathrm{cm}^2/\mathrm{s}$), c the molar concentration, S the total transport surface $S = N_{\mathrm{c}} S_{\mathrm{por}}$ of N_{c} permeabilized cells and Ψ the electric potential. In general D and S depend on time, pulse duration, electric field strength and number of pulses. Here we will first analyze the ion efflux after the N pulses so only S will depend on N, and D will be constant. The diffusion of ions is a slow process compared to the duration of the electric pulses thus we can assume that the major contribution to efflux of ions occurs without the presence of the electric field. When there is no external electric field present $\Delta\Psi$ is small since only the imbalance of the electric charges due to concentration gradient contributes. Therefore the second term in equation (B.7) can be neglected. By replacing the concentration gradient with $(c_{\mathrm{e}} - c_{\mathrm{i}})/d$ and by taking into account that the sum of ions inside and outside

remains constant, the equation further simplifies:

$$\frac{dc_e(t)}{dt} = -\frac{DS(E,N)}{dVF(1-F)}\left(c_e(t) - Fc_i^0\right) \tag{B.8}$$

where c_i^0 is the initial internal concentration of K^+ ions, V_e represent the external volume and function $S(E,N)$ describes the field dependent surface of pores. If we further neglect the volume fraction changes and assume that S is approximately constant, we obtain that the solution of the above equation is an exponential increase to maximum $c_e^{max} = Fc_i^0$

$$c_e(t) = c_e^{max}\left[1 - \exp\left(-\frac{t}{\tau}\right)\right] \tag{B.9}$$

with a time constant τ and permeability coefficient k being dependent on the fraction of transport pores f_{per}:

$$\tau = \frac{1}{f_E}\frac{3D}{dRF(1-F)}, \quad k = 1/\tau. \tag{B.10}$$

By measuring current and voltage during the train of successive pulses we obtain the change of the initial level of the conductivity, i.e. conductivity increase due to the ion efflux. Taking into account that the permeability coefficient depends on the number of pulses we can express the measured change of conductivity with [137]:

$$\frac{\Delta\sigma(t)}{\sigma_0} = \sum_N A_N\left[1 - \exp(-k_N t)\right]. \tag{B.11}$$

From this it follows that the permeability coefficient after the N-th pulse can be determined from the measured conductivity at N-th pulse ($\Delta\sigma_N$) and at N+1-th pulse ($\Delta\sigma_{N+1}$):

$$k_N = \frac{1}{\Delta t_N}\ln\left[1 - \frac{\Delta\sigma_N}{\Delta\sigma_{max}}\Big/1 - \frac{\Delta\sigma_{N+1}}{\Delta\sigma_{max}}\right] \tag{B.12}$$

where Δt_N is the time difference between N-th and N+1-th pulse and $\Delta\sigma_{max}$ is the maximum value of the conductivity, i.e. the saturation point when the concentrations inside and outside the cell are equal. From the permeability coefficient k_N the fraction of "transport" pores can be estimated using equation (B.10):

$$f_E^N \approx k_N\frac{dRF(1-F)}{3D'} \quad , \quad D' = D\exp(-0.43w_0) \tag{B.13}$$

where we take into account that the effective diffusion constant D' of K^+ ions inside the pore differs from that in the bulk [46,151,152].

REFERENCES

[1] R.B. Gennis, Biomembranes, Molecular Structure and Function, Springer, New York, 1989.
[2] E. Neumann, A. Sowers, C. Jordan, Electroporation and Electrofusion in Cell Biology, Plenum, New York, 1989.

[3] D.C. Chang, B.M. Chassey, J.A. Saunders, A.E. Sowers, Guide to Electroporation and Electrofusion, Academic Press, New York, 1992.
[4] R. Stampfli, Reversible electrical breakdown of the excitable membrane of a Ranvier node, Ann. Acad. Brasil. Ciens. 30 (1958) 57–63.
[5] A.J.H. Sale, A. Hamilton, Effects of high electric fields on microorganisms: I. Killing of bacteria and yeasts, Biochem. Biophys. Acta 148 (1967) 781–788.
[6] E. Neumann, K. Rosenheck, Permeability changes induced by electric impulses in vesicular membranes, J. Membr. Biol. 10 (1972) 279–290.
[7] E. Neumann, M.S. Ridder, Y. Wang, P.H. Hofschneider, Gene transfer into mouse lyoma cells by electroporation in high electric fields 1 (1982) 841–845.
[8] M. Okino, H. Mohri, Effects of high-voltage electrical impulse and an anticancer drug on in vivo growing tumors, Jpn. J. Cancer Res. 78 (1987) 1319–1321.
[9] L.M. Mir, H. Banoun, C. Paoletti, Introduction of definite amounts of nonpermeant molecules into living cells after electropermeabilization: direct access to the cytosol, Exp. Cell Res. 175 (1988) 15–25.
[10] D. Miklavčič, M. Puc, Electroporation, Wiley Encyclopedia of Biomedical Engineering, Wiley, New York, 2006.
[11] J. Teissié, N. Eynard, M.C. Vernhes, A. Benichou, V. Ganeva, B. Galutzov, P.A. Cabanes, Recent biotechnological developments of electropulsation. A prospective review, Bioelectrochemistry 55 (2002) 107–112.
[12] C.N. Haas, D.N. Aturaliye, Kinetics of electroporationassisted chlorination of giardia muris, Water Res. 33 (1999) 1761–1766.
[13] N.J. Rowan, S.J. MacGregor, J.G. Anderson, R.A. Fouracre, O. Farish, Pulsed electric field inactivation of diarrhoeagenic *Bacillus cereus* through irreversible electroporation, Lett. Appl. Microbiol. 31 (2000) 110–114.
[14] L.M. Mir, Therapeutic perspectives of in vivo cell electropermeabilization, Bioelectrochemistry 53 (2001) 1–10.
[15] J. Gehl, Review: electroporation: theory and methods, perspectives for drug delivery, gene therapy and research, Acta Physiol. Scand. 177 (2003) 437–447.
[16] L.M. Mir, S. Orlowski, J. Belehradek, J. Teissié, M.P. Rols, G. Serša, D. Miklavčič, R. Gilbert, R. Heller, Biomedical applications of electric pulses with special emphases on antitumor electrochemotherapy, Bioelectrochem. Bioenerg. 38 (1995) 203–207.
[17] G. Serša, B. Štabuc, M. Čemažar, B. Jančar, D. Miklavčič, Z. Rudolf, Electrochemotherapy with cisplatin: potentiation of local cisplatin antitumor effectiveness by application of electric pulses in cancer patients, Eur. J. Cancer 34 (1998) 1213–1218.
[18] R. Heller, R. Gilbert, M.J. Jaroszeski, Clinical application of electrochemotherapy, Adv. Drug Deliv. Rev. 35 (1999) 119–129.
[19] Y. Mouneimne, P.F. Tosi, R. Barhoumi, C. Nicolau, Electroinsertion of full length recombinant CD4 into red blood cell membrane, Biochim. Biophys. Acta 1027 (1990) 53–58.
[20] S. Raffy, J. Teissié, Electroinsertion of glycophorin A in interdigitation-fusion giant unilamellar lipid vesicles, J. Biol. Chem. 272 (1997) 25524–25530.
[21] I.G. Abidor, A.E. Sowers, Kinetics and mechanism of cell membrane electrofusion, Biophys. J. 61 (1992) 1557–1569.
[22] A.E. Sowers, Membrane electrofusion: a paradigm for study of membrane fusion mechanisms, Methods Enzymol. 220 (1993) 196–211.
[23] H. Mekid, L.M. Mir, In vivo cell electrofusion, Biochim. Biophys. Acta 1524 (2000) 118–130.
[24] T.H. Scott-Taylor, R. Pettengell, I. Clarke, G. Stuhler, M.C. La Barthe, P. Walden, A.G. Dalgleish, Human tumour and dendritic cell hybrids generated by electrofusion: potential for cancer vaccines, Biochim. Biophys. Acta 1500 (2000) 265–267.
[25] E. Schmidt, U. Leinfelder, P. Gessner, D. Zillikens, E.B. Brocker, U. Zimmermann, CD19+ B lymphocytes are the major source of human antibody-secreting hybridomas generated by electrofusion, J. Immunol. Methods 255 (2001) 93–102.
[26] M.R. Prausnitz, V.G. Bose, R. Langer, J.C. Weaver, Electroporation of mammalian skin: a mechanism to enhance transdermal drug delivery, Proc. Natl. Acad. Sci. U.S.A. 90 (1993) 10504–10508.

[27] R. Vanbever, N. Lecouturier, V. Preat, Transdermal delivery of metoprolol by electroporation, Pharmacol. Res. 11 (1994) 1657–1662.
[28] T.E. Zewert, U. Pliquett, R. Langer, J.C. Weaver, Transport of DNA antisense oligonucleotides across human skin by electroporation, Biochem. Biophys. Res. Commun. 212 (1995) 286–292.
[29] U. Zimmermann, Electric field-mediated fusion and related electrical phenomena, Biochim. Biophys. Acta 694 (1982) 227–277.
[30] M.P. Rols, J. Teissié, Electropermeabilization of mammalian cells. quantitative analysis of the phenomenon, Biophys. J. 58 (1990) 1089–1098.
[31] T.Y. Tsong, Electroporation of cell membranes, Biophys. J. 60 (1991) 297–306.
[32] J.C. Weaver, Y.A. Chizmadzhev, Theory of electroporation: a review, Bioelectrochem. Bioenerg. 41 (1996) 135–160.
[33] P.J. Canatella, J.F. Karr, J.A. Petros, M.R. Prausnitz., Quantitative study of electroporation-mediated molecular uptake and cell viability, Biophys. J. 80 (2001) 755–764.
[34] A. Maček-Lebar, D. Miklavčič, Cell electropermeabilization to small molecules in vitro: control by pulse parameters, Radiol. Oncol. 35 (2001) 193–202.
[35] D. Miklavčič, T. Kotnik, Electroporation for electrochemotherapy and gene therapy, in: P.J. Rosch, M.S. Markov (Eds.), Bioelectromagnetic Medicine, Marcel Dekker, New York, 2004, pp. 637–656.
[36] M. Smeyers, M. Leonetti, E. Goormaghtigh, F. Homble, Structure and function of plant membrane ion channels reconstituted in planar lipid bilayers, in: H.T. Tien, A. Ottova-Leitmannova (Eds.), Planar Lipid Bilayers (BLMs) and Their Applications, Elsevier, New York, 2003, pp. 449–478.
[37] G.C. Troiano, L. Tung, V. Sharma, K.J. Stebe, The reduction in electroporation voltages by the addition of surfactant to planar lipid bilayer, Biophys. J. 75 (1998) 880–888.
[38] V. Sharma, K. Uma Maheswari, J.C. Murphy, L. Tung, Poloxamer 188 decreases susceptibility of artificial lipid membranes to electroporation, Biophys. J. 71 (1996) 3229–3241.
[39] W. Meier, A. Graff, A. Diederich, M. Winterhalter, Stabilization of planar lipid membranes: a stratified layer approach, Phys. Chem. Chem. Phys. 2 (2000) 4559–4562.
[40] A. Diederich, G. Bahr, M. Winterhalter, Influence of surface charges on the rapture of black lipid membranes, Phys. Rev., E 58 (1998) 4883–4889.
[41] R. Benz, K. Janko, Voltage-induced capacitance relaxation of lipid bilayer membranes; effects on membrane composition, Biochim. Biophys. Acta 455 (1976) 721–738.
[42] J. Vargas, J.M. Alarcon, E. Rojas, Displacement currents associated with the insertion of Alzheimer disease amyloid (beta)-peptide into planar bilayer membranes, Biophys. J. 79 (2000) 934–944.
[43] C. Wilhelm, M. Winterhalter, U. Zimmermann, R. Benz, Kinetics o pore size during irreversible electrical breakdown of lipid bilayer membranes, Biophys. J. 64 (1993) 121–128.
[44] R. Benz, F. Beckers, U. Zimmermann, Reversible electrical breakdown of lipid bilayer membranes: a charge-pulse relaxation study, J. Membr. Biol. 48 (1979) 181–204.
[45] K.C. Melikov, V.A. Frolov, A. Shcherbakov, A.V. Samsonov, Y.A. Chizmadzhev, L.V. Chernomordik, Voltage-induced nonconductive pre-pores and metastable single pores in unmodified planar lipid bilayer, Biophys. J. 80 (2001) 1829–1836.
[46] R.W. Glaser, S.L. Leikin, L.V. Chernomordik, V.F. Pastushenko, A.I. Sokirko, Reversible electrical breakdown of lipid bilayers: formation and evolution of pores, Biochim. Biophys. Acta 940 (1988) 275–287.
[47] I.G. Abidor, V.B. Arakelyan, L.V. Chernomordik, Y.A. Chizmadzhev, V.F. Pastushenko, M.R. Tarasevich, Electric breakdown of bilayer membranes: I. The main experimental facts and their qualitative discussion, Bioelectrochem. Bioenerg. 6 (1979) 37–52.
[48] A.N. Chanturiya, Detection of transient capacitance increase associated with channel formation in lipid bilayers, Biochim. Biophys. Acta 1026 (1990) 248–250.
[49] S. Kalinowski, Z. Figaszewski, A new system for bilayer lipid membrane capacitance measurements: method apparatus and applications, Biochim. Biophys. Acta 1112 (1992) 57–66.
[50] S. Koronkiewicz, S. Kalinowski, K. Bryl, Programmable chronopotentiometry as a tool for the study of electroporation and resealing of pores in bilayer lipid membranes, Biochim. Biophys. Acta 1561 (2002) 222–229.

[51] A. Ridi, E. Scalas, M. Robello, A. Gliozzi, Linear response of a fluctuating lipid bilayer, Thin Solid Films 327–329 (1998) 796–799.
[52] M. Robello, A. Gliozzi, Conductance transition induced by an electric field in lipid bilayers, Biochim. Biophys. Acta 982 (1989) 173–176.
[53] A. Ridi, E. Scalas, A. Gliozzi, Noise measurements in bilayer lipid membranes during electroporation, EPJ E 2 (2000) 161–168.
[54] E. Scalas, A. Ridi, M. Robello, A. Gliozzi, Flicker noise in bilayer lipid membranes, Europhys. Lett. 43 (1998) 101–105.
[55] I. Genco, A. Gliozzi, A. Relini, M. Robello, E. Scalas, Electroporation in symmetric and asymmetric membranes, Biochim. Biophys. Acta 1149 (1993) 10–18.
[56] E. Pescio, A. Ridi, A. Gliozzi, A picoampere current generator for membrane electroporation, Rev. Sci. Instrum. 71 (2000) 1740–1744.
[57] M. Robello, M. Fresia, L. Maga, A. Grasso, S. Ciani, Permeation of divalent cations trough (alpha)-latrotoxin channels in lipid bilayers: steady-state current-voltage relationship, J. Membr. Biol. 95 (1987) 55–62.
[58] S. Kalinowski, Z. Figaszewski, A four-electrode potentiostat-galvanostat for studies of bilayer lipid membranes, Meas. Sci. Technol. 6 (1995) 1050–1055.
[59] S. Micelli, E. Gallucci, V. Ricciarelli, Studies of mitochondrial porin incorporation parameters and voltage-gated mechanism with different black lipid membranes, Bioelectrochemistry 52 (2000) 63–75.
[60] P. Kramar, D. Miklavčič, A. Maček-Lebar, Determination of the lipid bilayer breakdown voltage by means of a linear rising signal, Bioelectrochemistry 70 (2007) 23–27.
[61] A. Blume, Lipids, in: D. Waltz, J. Teissié, G. Milazzo (Eds.), Bioelectrochemistry of membranes, Birkhauser, Basel-Boston-Berlin, 2004, pp. 24–61.
[62] Y. Hanyu, T. Yamada, G. Matsumoto, Simultaneous measurement of spectroscopic and physiological signals from a planar bilayer system: detecting voltage-dependent movement of a membrane-incorporated peptide, Biochemistry 37 (1998) 15376–15382.
[63] H. Yamaguchi, H. Nakanishi, Characterization of the preparation process and photochemical control of electrical properties of bilayer lipid membranes containing azobenzene chromophores, Biochim. Biophys. Acta 1148 (1993) 179–184.
[64] T.F. Eibert, M. Alaydrus, F. Wiczewski, V.W. Hansen, Electromagnetic and thermal analysis for lipid bilayer membranes exposed to R.F fields, IEEE Trans. Biomed. Eng. 46 (1999) 1013–1021.
[65] N. Montal, P. Mueller, Formation of bimolecular membranes from lipid monolayers and a study of their electrical properties, Proc. Natl. Acad. Sci. U.S.A. 69 (1972) 3561–3566.
[66] A. Maček Lebar, G.C. Troiano, L. Tung, D. Miklavcic, Inter-pulse interval between rectangular voltage pulses affects electroporation threshold of artificial lipid bilayers, IEEE Trans. Nanobioscience 1 (2002) 116–120.
[67] E. Evans, V. Heinrich, F. Ludwig, W. Rawicz, Dynamic tension spectroscopy and strength of biomembranes, Biophys. J. 85 (2003) 2342–2350.
[68] E. Gallucci, S. Micelli, G. Monticelli, Pore formation in lipid bilayer membranes made of phosphatidylinositol and oxidized cholesterol followed by means of alternating current, Biophys. J. 71 (1996) 824–831.
[69] L.V. Chernomordik, S.I. Sukharev, I.G. Abidor, Yu.A. Chizmadzhev, Breakdown of lipid bilayer membranes in an electric field, Biochim. Biophys. Acta 736 (1983) 203–213.
[70] S. Kalinowski, G. Ibron, K. Bryl, Z. Figaszewski, Chronopotentiometric studies of electroporation of bilayer lipid membranes, Biochim. Biophys. Acta 1396 (1998) 204–212.
[71] P.R.C. Gascoyne, R. Pethig, J.P.H. Burt, F.F. Becker, Membrane changes accompanying the induced differentiation of Friend murine erythroleukemia cells studied by dielectrophoresis, Biochim. Biophys. Acta 1146 (1993) 119–126.
[72] I.P. Sugár, A theory of the electric field-induced phase transition of phospholipid bilayers, Biochim. Biophys. Acta 556 (1979) 72–85.
[73] D.S. Dimitrov, R.K. Jain, Membrane stability, Biochim. Biophys. Acta 779 (1984) 437–468.

[74] C.M. Harris, D.B. Kell, The radio-frequency dielectric properties of yeast cells measured with a rapid automated, frequency-domain dielectric spectrometer, Bioelectrochem. Bioenerg. 11 (1983) 15–28.
[75] R. Hlzel, I. Lamprecht, Dielectric properties of yeast cells as determined by electrorotation, Biochim. Biophys. Acta 1104 (1992) 195–200.
[76] F.W. Sunderman, Measurement of serum total base, Am. J. Clin. Pathol. 15 (1945) 219–222.
[77] K. Nrtemann, J. Hilland, U. Kaatze, Dielectric properties of aqueous NaCl solutions at microwave frequencies, J. Phys. Chem. A 101 (1997) 6864–6869.
[78] D.H. Michael, M.E. O'Neill, Electrohydrodynamic instability in plane layers of fluid, J. Fluid Mech. 41 (1970) 571–580.
[79] G.I. Taylor, D.H. Michael, On making holes in a sheet of fluid, J. Fluid Mech. 58 (1973) 625–639.
[80] J.M. Crowley, Electrical breakdown of bimolecular lipid membranes as an electro-mechanical instability, Biophys. J. 13 (1973) 711–724.
[81] C. Maldarelli, R.K. Jain, I.B. Ivanov, E. Rckenstein, Stability of symmetric and unsymmetric, thin liquid films to short and long wavelength perturbations, J. Colloid Interface Sci. 78 (1980) 118–143.
[82] A. Steinchen, D. Gallez, A. Sanfeld, A viscoelastic approach to the hydrodynamic stability of membranes, J. Colloid Interface Sci. 85 (1982) 5–15.
[83] D.S. Dimitrov, Electric field-induced breakdown of lipid bilayer and cell membranes: a thin viscoelastic film model, J. Membr. Biol. 78 (1984) 53–60.
[84] M. Hibino, M. Shigemori, H. Itoh, K. Nagayama, K. Kinosita, Membrane conductance of an electroporated cell analyzed by sub-microsecond imaging of transmembrane potential, Biophys. J. 59 (1991) 209–220.
[85] M. Hibino, H. Itoh, K. Kinosita, Time courses of electroporation as revealed by submicrosecond imaging of transmembrane potential, Biophys. J. 64 (1993) 1789–1800.
[86] R.E. Jacobs, B.S. Hudson, H.C. Andersen, A theory of the chain melting phase transition of aqueous phospholipid dispersions, Proc. Natl. Acad. Sci. U.S.A. 72 (1975) 3993–3997.
[87] R.E. Jacobs, B.S. Hudson, H.C. Andersen, A theory of phase transitions and phase diagrams for one- and two-component phospholipid bilayers, Biochemistry 16 (1977) 4349–4359.
[88] L. Cruzeiro-Hansson, O.G. Mouritsen, Passive ion permeability of lipid membranes modelled via lipid-domain interfacial area, Biochim. Biophys. Acta 944 (1988) 63–72.
[89] L. Cruzeiro-Hansson, J.H. Ipsen, O.G. Mouritsen, Intrinsic molecules in lipid membranes change the lipid-domain interfacial area: cholesterol at domain interfaces, Biochim. Biophys. Acta 979 (1989) 166–176.
[90] J.D. Litster, Stability of lipid bilayers and red blood cell membranes, Phys. Lett. 53A (1975) 193–194.
[91] C. Taupin, M. Dvolaitzky, C. Sauterey, Osmotic pressure induced pores in phospholipid vesicles, Biochemistry 14 (1975) 4771–4775.
[92] J.C. Weaver, R.A. Mintzer, Decreased bilayer stability due to transmembrane potentials, Phys. Lett. 86A (1981) 57–59.
[93] J.N. Israelachvili, R.M. Pashley, Measurement of the hydrophobic interaction between two hydrophobic surfaces in aqueous electrolyte solutions, J. Colloid Interface Sci. 98 (1984) 500–514.
[94] A. Barnett, J.C. Weaver, Electroporation: a unified quantitative theory of reversible electrical breakdown and rupture, Bioelectrochem. Bioenerg. 25 (1991) 163–182.
[95] S.A. Freeman, M.A. Wang, J.C. Weaver, Theory of electroporation for a planar bilayer membrane: predictions of the fractional aqueous area, change in capacitance and pore-pore separation, Biophys. J. 67 (1994) 42–56.
[96] M.P. Rols, J. Teissié, Modulation of electrically induced permeabilizaiton and fusion of Chinese hamster ovary cells by osmotic pressure, Biochemistry 29 (1990) 4561–4567.
[97] M. Golzio, M.P. Mora, C. Raynaud, C. Delteil, J. Teissié, M.P. Rols, Control by osmotic pressure of voltage-induced permeabilization and gene transfer in mammalian cells, Biophys. J. 74 (1998) 3015–3022.

[98] E. Neumann, S. Kakorin, K. Tönsing, Fundamentals of electroporative delivery of drugs and genes, Bioelectrochem. Bioenerg. 48 (1999) 3–16.
[99] J. Teissié, M. Golzio, M.P. Rols, Mechanisms of cell membrane electropermeabilization: a minireview of our present (lack of č) knowledge, Biochim. Biophys. Acta 1724 (2005) 270–280.
[100] S. Orlowski, L.M. Mir, Cell electroporation: a new tool for biochemical and pharmacological studies, Biochim. Biophys. Acta 1154 (1993) 51–62.
[101] M.J. Jaroszeski, R. Heller, R. Gilbert, Electrochemotherapy, Electrogenetherapy and Transdermal Drug Delivery: Electrically Mediated Delivery of Molecules to Cells, Humana Press, Totowa, NJ, 1999.
[102] J.C. Maxwell, Treatise on Electricity and Magnetism, Oxford University Press, London, 1873.
[103] K.S. Cole, Membrane, Ions and Impulses, University of California Press, Los Angeles, 1968.
[104] K.R. Foster, H.P. Schwan, Dielectric properties of tissues, in: C. Polk, E. Postow (Eds.), Handbook of Biological Effects of Electromagnetic Fields, CRC Press, Florida, 1986, pp. 28–96.
[105] J.D. Jackson, Classical Electrodynamics, Wiley, New York, 1999.
[106] U. Zimmermann, The effect of high-intensity electric pulses on eukaryotic cell membranes, in: U. Zimmermann, G.A. Neil (Eds.), Electromanipulation of Cells, CRC press, London, 1996, pp. 1–105.
[107] E. Tekle, R.D. Astumian, P.B. Chock, Electro-permeabilization of cell membranes: effect of the resting membrane potential, Biochem. Biophys. Res. Commun. 172 (1990) 282–287.
[108] J. Teissié, M.P. Rols, An experimental evaluation of the critical potential difference inducing cell membrane electropermeabilization, Biophys. J. 65 (1993) 409–413.
[109] V.H. Pauly, H.P. Schwan, ber die Impendanz einer Suspension von kugelfrmigen Teilchen mit einer Schale, Z. Naturforsch. 14b (1959) 125–131.
[110] T. Kotnik, F. Bobanović, D. Miklavčič, Sensitivity of transmembrane voltage induced by applied electric fields: a theoretical analysis, Bioelectrochem. Bioenerg. 43 (1997) 285–291.
[111] S. Takashima, Electrical Properties of Biopolimers and Membranes, Adam Hilger, Bristol, 1989.
[112] K.H. Schoenbach, S.J. Beebe, E.S. Buescher, Intracellular effect of ultrashort electrical pulses, Bioelectromagnetics 22 (2001) 440–448.
[113] T. Kotnik, D. Miklavčič, T. Slivnik, Time course of transmembrane voltage induced by time-varying electric fields-a method for theoretical analysis and its application, Bioelectrochem. Bioenerg. 45 (1998) 3–16.
[114] R. Susil, D. Šemrov, D. Miklavčič, Electric field-induced transmembrane potential depends on cell density and organization, Electro Magnetobiol. 17 (1998) 391–399.
[115] M. Pavlin, N. Pavšelj, D. Miklavčič, Dependence of induced transmembrane potential on cell density arrangement and cell position inside a cell system, IEEE Trans. Biomed. Eng. 49 (2002) 605–612.
[116] M. Kummrow, W. Helfrich, Deformation of giant lipid vesicles by electric fields, Phys. Rew. A 44 (1991) 8356–8360.
[117] K.J. Müller, V.L. Sukhorukov, U. Zimmermann, Reversible electropermeabilization of mammalian cells by high-intensity, ultra-short pulses of submicrosecond duration, J. Membr. Biol. 184 (2001) 161–170.
[118] R.P. Joshi, Q. Hu, K.H. Schoenbach, H. P. Hjalmarson, Theoretical predictions of electromechanical deformation of cells subjected to high voltages for membrane electroporation, Phys. Rev. E, 65 (2002) 021913.
[119] S.I. Sukharev, V.A. Klenchin, S.M. Serov, L.V. Chernomordik, Y.A. Chizmadzhev, Electroporation and electrophoretic DNA transfer into cells. The effect of DNA interaction with electropores, Biophys. J. 63 (1992) 1320–1327.
[120] M.P. Rols, C. Delteil, M. Golzio, P. Dumond, S. Cros, J. Teissié, In vivo electrically mediated protein and gene transfer in murine melanoma, Nat. Biotechnol. 16 (1998) 168–171.
[121] S. Satkauskas, M.F. Bureau, M. Puc, A. Mahfoudi, D. Scherman, D. Miklavčič D, L.M. Mir, Mechanisms of in vivo DNA electrotransfer: respective contributions of cell electropermeabilization and DNA electrophoresis, Mol. Ther. 5 (2002) 133–140.

[122] K. Kinosita, T.Y. Tsong, Voltage-induced conductance in human erythrocyte, Biochim. Biophys. Acta 554 (1979) 479–497.
[123] I.G. Abidor, A.I. Barbul, D.V. Zhelev, P. Doinov, I.N. Bandarina, E.M. Osipova, S.I. Sukharev, Electrical properties of cell pellet and cell fusion in a centrifuge, Biochim. Biophys. Acta. 115 (1993) 207–218.
[124] I.G. Abidor, L.-H. Li, S.W. Hui, Studies of cell pellets: II. Osmotic properties, electroporation, and related phenomena: membrane interactions, Biophys. J. 67 (1994) 427–435.
[125] M. Pavlin, M. Kandušer, M. Reberšek, G. Pucihar, F.X. Hart, R. Magjarević, D. Miklavčič, Effect of cell electroporation on the conductivity of a cell suspension, Biophys. J. 88 (2005) 4378–4390.
[126] K. Schwister, B. Deuticke, Formation and properties of aqueous leaks induced in human erythrocytes by electrical breakdown 816 (1985) 332–348.
[127] B. Gabriel, J. Teissié, Fluorescence imaging in the millisecond time range of membrane electropermeabilization of single cells using a rapid ultra-low-light intensifying detection system, Eur. Biophys. J. 27 (1998) 291–298.
[128] B. Gabriel, J. Teissié, Time courses of mammalian cell electropermeabilization observed by millisecond imaging of membrane property changes during the pulse, Biophys. J. 76 (1999) 2158–2165.
[129] D. Miklavčič, D. Šemrov, H. Mekid, L.M. Mir, A validated model of in vivo electric field distribution in tissues for electrochemotherpy and for DNA electrotransfer for gene therapy, Biochim. Biophys. Acta 1519 (2000) 73–83.
[130] M. Pavlin, D. Miklavčič, Effective conductivity of a suspension of permeabilized cells: a theoretical analysis, Biophys. J. 85 (2003) 719–729.
[131] K. Kinosita, T.Y. Tsong, Voltage-induced pore formation and hemolysis of human erytrocytes, Biochim. Biophys. Acta 471 (1977) 227–242.
[132] K. Kinosita, T.Y. Tsong, Formation and resealing of pores of controlled sizes in human erythrocyte membrane, Nature 268 (1977) 438–441.
[133] A.L. Garner, N.Y. Chen, J. Yang, J. Kolb, R.J. Swanson, K.C. Loftin, S.J. Beebe, R.P. Joshi, K.H. Schoenbach, Time domain dielectric spectroscopy measurements of HL-60 cell suspensions after microsecond and nanosecond electrical pulses, IEEE Trans. Plasma Sci. 32 (2004) 2073–2084.
[134] M. Schmeer, T. Seipp, U. Pliquett, S. Kakorin, E. Neumann, Mechanism for the conductivity changes caused by membrane electroporation of CHO cell-pellets, Phys. Chem. Chem. Phys. 6 (2004) 5564–5574.
[135] R.V. Davalos, B. Rubinsky, D.M. Otten, A feasibility study for electrical impedance tomography as a means to monitor tissue electroporation for molecular medicine, IEEE Trans. Biomed. Eng. 49 (2002) 400–403.
[136] U. Pliquett, R. Elez, A. Piiper, E. Neumann, Electroporation of subcutaneous mouse tumors by rectangular and trapezium high voltage pulses, Bioelectrochemistry 62 (2004) 83–93.
[137] M. Pavlin, V. Leben, D. Miklavčič, Electroporation in dense cell suspension-Theoretical and experimental analysis of ion diffusion and cell permeabilization, Biochim. Biophys. Acta 1770 (2007) 12–23.
[138] M.P. Rols, J. Teissié, Ionic-strength modulation of electrically induced permeabilization and associates fusion of mammalian cells, Eur. J. Biochem. 179 (1989) 109–115.
[139] M.P. Rols, J. Teissié, Experimental evidence for involvement of the cytoskeleton in mammalian cell electropermeabilization, Biochim. Biophys. Acta 1111 (1992) 45–50.
[140] M.P. Rols, J. Teissié, The time course of electropermeabilization, in: M. Blank, (Ed.), Electricity and Magnetism in Biology and Medicine, San Francisco Press, San Francisco, 1993, pp. 151–154.
[141] M.P. Rols, J. Teissié, Electropermeabilization of mammalian cells to macromolecules: control by pulse duration, Biophys. J. 75 (1998) 1415–1423.
[142] T. Kotnik, G. Pucihar, M. Reberšek, L.M. Mir, D. Miklavčič, Role of pulse shape in cell membrane electropermeabilization, Biochim. Biophys. Acta 1614 (2003) 193–200.

[143] J. Teissié, C. Ramos, Correlation between electric field pulse induced long-lived permeabilization and fusogenicity in cell membranes, Biophys. J. 74 (1998) 1889–1898.
[144] I.P. Sugár, E. Neumann, Stochastic model for electric field-induced membrane pores electroporation, Biophys. Chem. 19 (1984) 211–225.
[145] D.C. Chang, T.S. Reese, Changes in membrane structure induced by electroporation as revealed by rapid freezing electron microscopy, Biophys. J. 58 (1990) 1–12.
[146] M. Fosnarič, V. Kralj-Iglič, K. Bohinc, A. Iglič, S. May, Stabilization of pores in lipid bilayers by anisotropic inclusions, J. Phys. Chem. B 107 (2003) 12519–12526.
[147] L.V. Chernomordik, S.I. Sukarev, S.V. Popov, V.F. Pastushenko, A.V. Sokirko, I.G. Abidor, Y.A. Chizmadzev, The electrical breakdown of cell and lipid membranes: the similarity of phenomenologies, Biochim. Biophys. Acta 902 (1987) 360–373.
[148] S.J. Marrink, E. Lindahl, O. Edholm, A.E. Mark, Simulation of the spontaneous aggregation of phospholipids into bilayers 123 (2001) 8638–8639.
[149] D.P. Tieleman, H. Leontiadou, A.E. Mark, S.J. Marrink, Simulation of pore formation in lipid bilayers by mechanical stress and electric fsields, J. Am. Chem. Soc. 125 (2003) 6282–6383.
[150] A. Parsegian, Energy of an ion crossing a low dielectric membrane: Solutions to four relevant electrostatic problems 221 (1969) 844–846.
[151] K.A. DeBruin, W. Krassowska, Modeling electroporation in a single cell. I. Effects of field strength and rest potential, Biophys. J. 77 (1999) 1213–1223.
[152] K.A. DeBruin, W. Krassowska, Modeling electroporation in a single cell. II. Effects of ionic concentrations, Biophys. J. 77 (1999) 1225–1233.

CHAPTER EIGHT

Cytoskeletal Proteins at the Lipid Membrane

Wolfgang H. Goldmann[1,2,*], Burkhard Bechinger[3], *and* Tanmay Lele[4]

Contents

1. Introduction 228
2. Stopped-Flow Spectrophotometer 229
   2.1. 'Slow' Temperature Jump Apparatus 230
   2.2. Results 231
   2.3. Binding Affinity of Myosin II (Associated/Inserted-Lipid) to Actin 232
3. Differential Scanning Calorimetry (DSC) 233
   3.1. Results 237
4. Solid-State NMR Spectroscopy 238
   4.1. Theory: The Anisotropy of Interactions Measured in Solid-State NMR Spectroscopy 240
   4.2. Experimental Considerations 241
   4.3. Results and Discussion 243
5. Fluorescence Recovery after Photobleaching (FRAP) 244
   5.1. Focal Adhesions and the Plasma Membrane 246
   5.2. Quantifying Protein–Protein Binding Kinetics Inside Living Cells 246
   5.3. Method and Setup of FRAP 246
   5.4. Results 247
   5.5. Quantitative Analysis of FRAP Experiments 249
Acknowledgements 251
References 251

Abstract

The interface at the cell membrane and cytosol offers a wealth of possibilities for intermolecular interactions. Molecular anchors, -bridges, -transmembrane connectors as well as cascades of proteins inside the cell regulate the bidirectional exchange of

* Corresponding author. Tel: +49 (0)9131-85-25605; Fax: +49 (0)9131-85-25601
E-mail address: wgoldmann@biomed.uni-erlangen.de (W.H. Goldmann).

[1] Massachusetts General Hospital, Harvard Medical School, Charlestown, MA 02129, USA
[2] Center for Medical Physics and Technology, Biophysics Group, Friedrich-Alexander-University of Erlangen-Nuremberg, Henkestrasse 91, 91052 Erlangen, Germany
[3] Université Louis Pasteur Strasbourg, CNRS, Institut de Chimie, UMR 7177-LC3, 4, rue Blaise Pascal, 67070 Strasbourg, France
[4] Department of Chemical Engineering, University of Florida, Museum Road, Bldg. 723, Gainesville, FL 32611, USA

Advances in Planar Lipid Bilayers and Liposomes, Volume 6
ISSN 1554-4516, DOI 10.1016/S1554-4516(07)06008-5

information between the cell and extracellular environment. Previously, little attention has been given to lipids that are essential for the membrane architecture and for the regulation and function of membrane-associated cytoskeletal proteins. The emergence of new biophysical techniques has spurred rapid acceleration in the ability of researchers to investigate and understand protein–lipid membrane interactions in artificial systems as well as in cells. Stopped-flow kinetics, differential scanning calorimetry (DSC), solid-state nuclear magnetic resonance (NMR) spectroscopy as well as fluorescence recovery after photobleaching (FRAP) will be described and their application will be discussed.

1. Introduction

Proteins that interface between the cytoskeleton and the plasma membrane control cell shape and tension, and stabilize attachments to other cells and to extracellular substrates. Signals that reach the cell surface and induce intracellular responses may be hormonal, chemical or mechanical. Similarly, signals from inside the cell can give rise to changes in cell membrane architecture, whilst signals, transmitted laterally, within the plane of the lipid membrane may have long-range effects on the cell surface [1–6].

Many proteins exist in soluble forms in the cytoplasm and fractions may associate transiently with the boundary of the lipid membrane. In an aggregate form, proteins (and their complexes) are likely to interact in a two-step mechanism: an initial electrostatic attraction is followed by some form of lipid insertion, which may be associated with protein refolding events. Conformational changes only occur when the lipid membrane finds compatible and complementary configurations such as exposed combinations like α-helices or β-strands on the protein. The assumption is that surface binding to polar lipid head groups is achieved by exposing amphipathic secondary structures, predominantly α-helices. Insertion into one-half of the hydrophobic bilayer requires β-barrels or hydrophobic α-helices. Even when only the amino acid sequence is known, the predictive methods to describe these lipid-binding structures are often accurate. A hydrophobicity index based on physio-chemical properties for each amino acid and the probability, that a protein is membrane spanning or inserting, is derived by hydrophobic plots. We used purpose-written computer matrices to discriminate between liquid surface-seeking and transmembrane configurations of α-helices [7]. By applying this method, we are able to predict potential lipid-binding motifs for several proteins with high accuracy including Cap-Z, filamin, α-actinin, PR3 and other membrane-associated proteins [7–11].

Since new physical techniques have become available, investigating the lipid membrane interface has gained more interest among biochemists and cell biologists. In this chapter, we describe in Section 2 the stopped-flow, in Section 3 differential scanning calorimetric (DSC) and in Section 4 solid-state nuclear magnetic resonance (NMR) measurements to study interactions between proteins and lipid membranes. We further summarize in Section 5 fluorescence recovery after

photobleaching (FRAP) studies aimed at elucidating events accompanying protein binding in cells.

2. Stopped-Flow Spectrophotometer

The principle of this method is to mix two reactant solutions by rapid flow, to stop the flow and to observe the change continuously in an observation cell. The application and limitations are discussed in detail by Gutfreund [12], Bernasconi [13] and Goldmann *et al.* [14].

All experiments that are described here were carried out on an SF 61 stopped-flow spectrophotometer supplied by Hi-Tech-Scientific, Salisbury, UK. A schematic representation of the unit is shown in Fig. 1. The unit consists of two 1 ml Hamilton drive syringes, which can be filled from reservoirs. Syringes are driven simultaneously by compressed air from a pressure-driven ram mounted upon the base unit. At 3 bar normal operating pressure, the dead time is measured to be around 1.5 ms. Solutions are rapidly mixed in a quartz observation/reaction cell that can be controlled thermostatically. The cell is set in light scatter mode with 10 nm path length. Light is transmitted to the cell *via* a quartz fiber optic light guide. Emitted light from the reaction/observation cell is sent *via* a silvered quartz rod to the photomultiplier. The flow is stopped using another 1 ml Hamilton syringe. A micro-switch is pressed by the stopping syringe to give a trigger pulse. The temperature is indicated by a thermocouple placed in the fluid-handling unit and maintained by an external heating device.

A purpose-built stabilized power supply is the energy source for the 100 W high-pressure mercury or Xenon lamp. Light is monochromated with a band pass width of 5 nm by a M300 monochromator. Light scatter measurements of protein–protein and/or protein–lipid interactions are followed at 355 nm and light is passed through a Schott UG11 filter to cut higher order deflections. Emitted light is

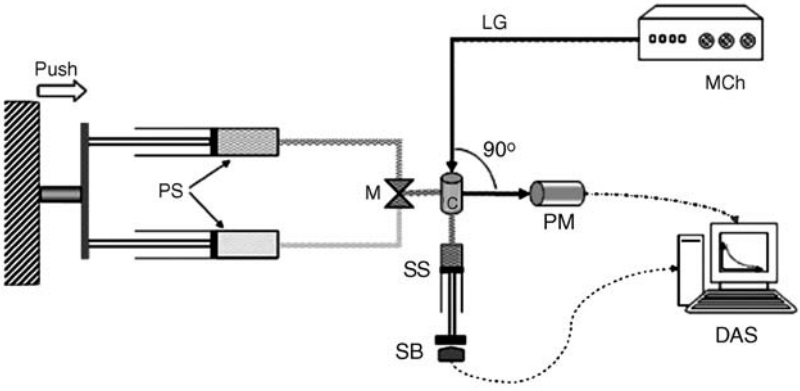

Figure 1 Schematic representation of the stopped-flow apparatus. PS, Probe syringe; M, Mixer; C, Reaction/observation cell; SS, Stopping syringe; SB, Stopping block/micro-switch; PM, Photomultiplier; LG, Light guide; MCh, Monochromator; DAS, Data acquisition system.

detected at 90° for light scatter measurements through a Schott KV 393 filter. The signal is electronically filtered by an unit gain amplifier. The time constant is normally 5% of the half time of an observed protein–protein reaction. High-tension power to drive the photomultiplier is adjusted so that the output is between −1.0 V and −5.0 V depending on the reaction. The signal is then offset to zero voltage, using the backing off on the unity gain amplifier. Transient recorders are triggered by a 5.0 V pulse opening the micro-switch on the stopping block of the stopped-flow machine. The analogue signal from the photomultiplier is then digitized before being transferred to a computer for further analysis. The data are analyzed either as single or averaged traces.

2.1. 'Slow' Temperature Jump Apparatus

Stopped-flow for a temperature jump has been modified according to Goldmann and Geeves [15] (Fig. 2). This method is capable of measuring temperature differences larger than 10°C in less than 150 ms and is sensitive and reliable for measuring myosin II–lipid insertion events.

In this example, a myosin II−lipid solution is held in a single syringe 15°C (T_1). A driving mechanism operated by compressed air pushes the sample into the observation cell. The tubing and the cell are immersed at 30°C (T_2). Temperature regulation is provided by an external heater and an internal thermocouple. A micro-switch is triggered by a front stop that initiates signal detection. The system is designed to allow the solution to equilibrate to the new temperature (T_2)

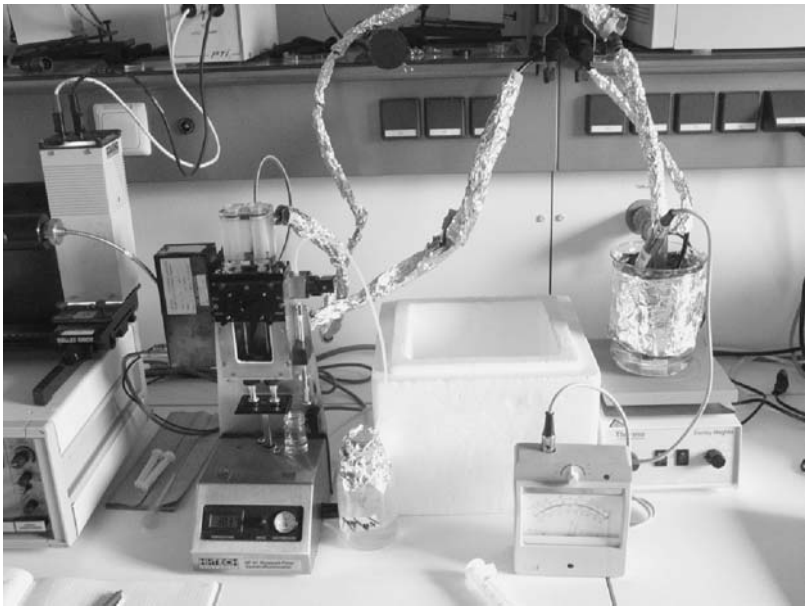

Figure 2 Water circulation at the stopped-flow apparatus. From left to right: electronics unit; sample-handling unit; ice container for cooling and hot plate for heating the circulating solution.

in the cell. Changes in light scatter signal at 355 nm and at a 90° angle are recorded with time. The optical and detection systems are discussed in the stopped-flow spectrophotometer chapter.

2.2. Results

Using the modified stopped-flow apparatus we can show that light scattering can be applied to measure the affinity of myosin II to lipid vesicles. This method is a development for experimental work by Goldmann *et al.* [16] and the analysis by Michel *et al.* [17]. In brief, a solution of 120 µl myosin II–lipid is prepared and prior to experimentation is exposed to 10 cycles of 'freeze-thaw', i.e., cooling of samples to 5°C and warming to 37°C. Then it is filled into the reservoir syringe of the stopped-flow (kept at 10°C) and injected into the reaction/observation chamber (kept at 37°C). Over time, as the solution warms, the light scatter signal (355 nm) is followed at the phase transition (T_M, *melting*) point of dimyristoylphosphatidylcholine (DMPC) and dimyristoylphosphatidylglycerol (DMPG) lipids and molar ratio of 50:50.

As shown in Fig. 3, the light scatter signal for pure lipids is the largest and with increasing myosin II concentrations (0.25 → 3.50 µM) the signal decreases. Based on the relationship

$$\ln(I - I_0/I_0) = A - KxC \tag{1}$$

where, I_0 is the scatter signal before and I after the phase transition, A the intercept of the y-axis, K (association constant) the molar affinity of myosin II to lipids and C the concentration of myosin II. Since the values of I and I_0 are not very accurate, the Boltzmann-Regression curve was used,

$$y = \frac{A_1 - A_2}{1e^{(x-x_0)/\Delta x} + A_2} \tag{2}$$

where, A_1 and A_2 are I and I_0, respectively, and x_0 the center of the distribution, Δx the width of the slope at point x_0. Plotting the curves in Fig. 3 using the linear

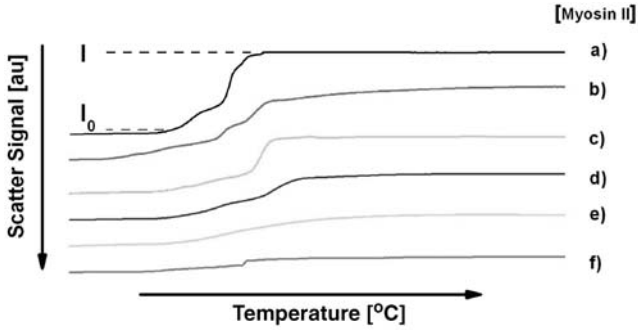

Figure 3 Light scatter signals. Temperature-induced light scatter changes between 20°C and 25°C at 355 nm. Conditions: Lipid and myosin II concentrations: 1.82 mM and (a) 0 µM, (b) 0.25 µM, (c) 0.5 µM, (d) 1.5 µM, (e) 2.5 µM and (f) 3.5 µM, respectively.

relationship, a molar affinity was determined for myosin II to lipid vesicles of K (association constant) $= 0.59 \times 10^6\,\mathrm{M}^{-1}$. The affinity of protein association/insertion into lipid membranes is comparable to other membrane-associated proteins like talin ($K = 2.9 \times 10^6\,\mathrm{M}^{-1}$) and vinculin ($K = 0.33 \times 10^6\,\mathrm{M}^{-1}$) [16]. For a control bovine serum albumin (BSA) was used.

2.3. Binding Affinity of Myosin II (Associated/Inserted-Lipid) to Actin

The binding affinity of actin to myosin II (bound to lipid vesicles) at a constant temperature using the stopped-flow method was assayed and compared to myosin II and actin. Fig. 4 is a typical trace of myosin II binding to actin. A double exponential fit shows a rate of association for $k_{+1} = 3.86\,\mathrm{s}^{-1}$ and for $k_{+2} = 0.72\,\mathrm{s}^{-1}$ at 1 μM actin and 5 μM myosin II concentration at 355 nm. The binding kinetics measured for actin and myosin II bound to lipids also showed a similar value. Unfortunately, the noise level between 0 and 0.2 s was higher and difficult to fit. To circumvent this problem, the method of 'stationary titration' was employed using the stopped-flow apparatus. The light scatter signal at 355 nm was measured using actin concentrations between $0.25 \rightarrow 4\,\mu\mathrm{M}$ and at constant myosin II concentration (5 μM) in the presence/absence of lipids after 1 s of injection into the reaction/observation chamber at 4 bar. The data were analyzed according to Hiromi [18], using the following equation:

$$[A]_0/\alpha = \left([M]_0 + K_\mathrm{d}\right) + \left([A]_0 - \alpha[M]_0\right) \tag{3}$$

where $[A]_0$ = actin and $[M]_0$ = myosin II concentration at $t = 0$ s; K_d = binding (dissociation) constant ($K_\mathrm{d} = 1/K$), and $\alpha =$ the fractional saturation of myosin II

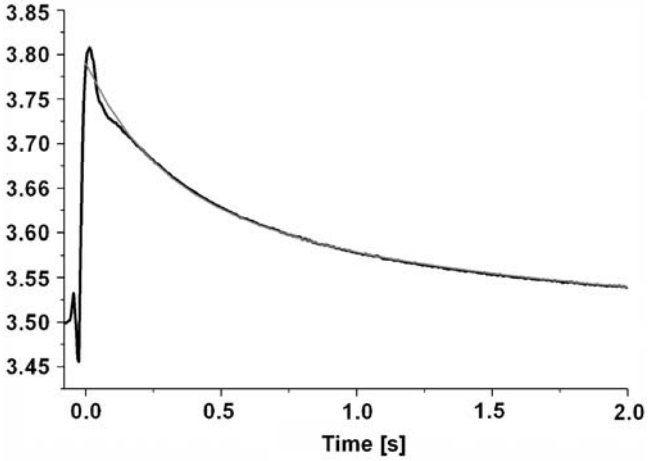

Figure 4 Stopped-flow experiments. Averaged stopped-flow traces of myosin II binding to actin ($n = 3$) with a super-imposed double exponential fit. Rates of association, $k_{+1} = 3.86\,\mathrm{s}^{-1}$ and $k_{+2} = 0.72\,\mathrm{s}^{-1}$. Conditions: actin = 1 μM, myosin II = 5 μM, light scatter signal at 355 nm, and temperature = 23°C.

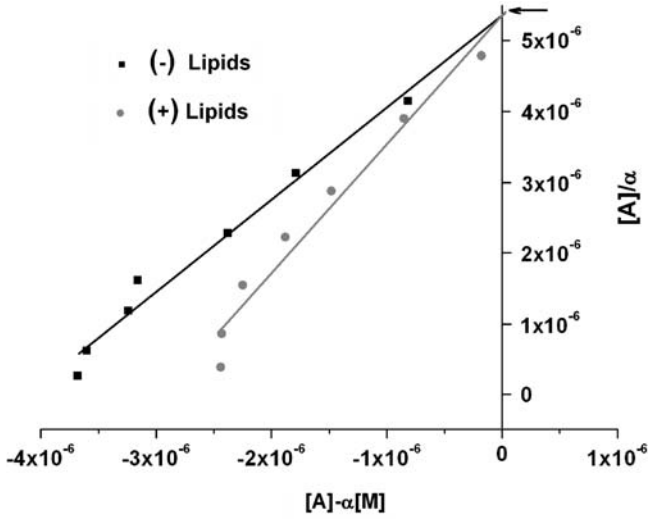

Figure 5 Binding kinetics. A plot of $[A]-\alpha[M]$as a function of $[A]/\alpha$. The linear fit shows an intercept with the y-axis that equals $([M]_0+K_d)$. K_d for myosin II (bound to lipids) and actin = 0.362 μM; K_d for myosin II and actin = 0.357 μM.

by actin. α is defined by the relationship,

$$\alpha = \frac{I_0 - I}{I_0 - I_\infty} \tag{4}$$

where, I_0 = light scatter signal in the absence and I_∞ = at infinitely high-actin concentration. Using these results, $[A]-\alpha[M]$ (x-axis) was plotted against $[A]/\alpha$ (y-axis) to give a linear relationship where, the intercept is the dissociation constant, K_d.

Results from measurements using equation (3) show a K_d for actin–myosin II of 0.357 μM and actin–(myosin II bound to lipid) of 0.362 μM, respectively (Fig. 5). The results are comparable with other membrane-associated proteins [16]. Figure 6 is a schematic representation of actin–myosin II and actin–myosin II–lipid binding.

3. Differential Scanning Calorimetry (DSC)

DSC is the most direct experimental technique to resolve the energy of conformational transitions of biological macromolecules. It provides an immediate access to the thermodynamic mechanism that governs a conformational equilibrium, i.e., between folded and unfolded forms of a protein by measuring the temperature dependence of partial heat capacity, ΔC_p, a basic thermodynamic property. The theory of DSC and the thermodynamic interpretation of the experiment have been the subject of excellent reviews [19–21]. Here, a basic description of the principle of the DSC method will be provided with special

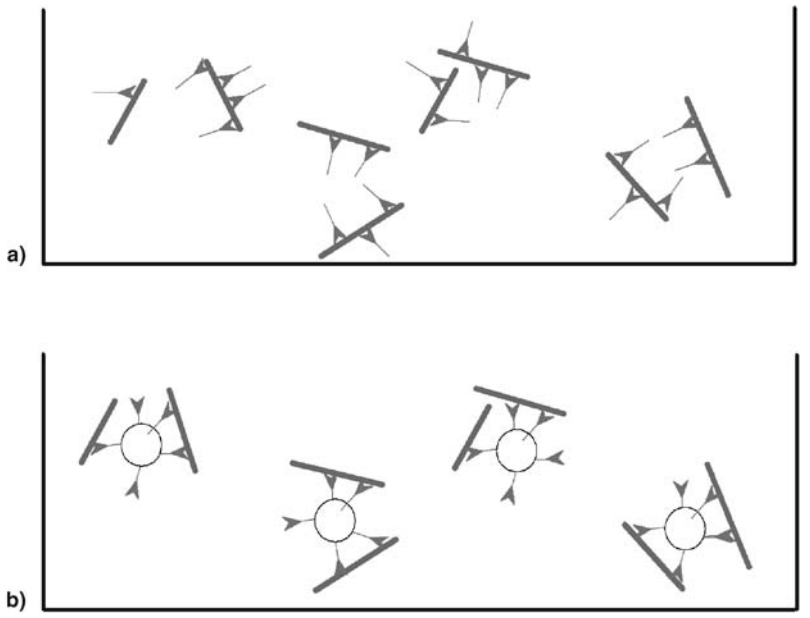

Figure 6 Schematic representation of protein–lipid interaction. Schematic view of (a) myosin II (green) and putative binding to actin (red) and (b) myosin II (bound to lipid vesicles) and actin (please see plate no. 5 in the color section).

emphasis on the potential of DSC to analyze the energetics of protein–lipid association/insertion reactions.

Phospholipids can exist in solvent in a 'gel-like' (*ordered*) as well as 'fluid-like' (*disordered*) phase. The change from a gel to fluid-like phase of a solvated membrane is called its phase transition or (*melting point*). As shown in Fig. 7, this change in specific heat profile has a calorimetric maximum. Before reaching the main phase transition temperature (T_M), some lipids show a pre-transition phase (T_V) at which the 'gel-like' membrane changes from a lamellar ($L_{\beta'}$) to a ripple ($P_{\beta'}$) phase and then proceeds into the fluid phase (L_α).

The saturated covalent bonds in the alkyl chains of lipids can assume many torsion angles. The flexibility of these covalent bonds provides many degrees of freedom. High-energy conformations reduce significantly the *all-trans* configurations and allow any angle of rotation. The phase change from ordered to disordered behavior (*melting*) is regarded as first-order phase transition that follows Gibb's law:

$$\Delta G = \Delta H - T_M \Delta S = 0; \quad \text{or} \quad T_M = \Delta H / \Delta S. \tag{5}$$

where, ΔS = entropy, ΔH = enthalpy and ΔG = free (Gibb's) energy. Using an experimentally determined heat capacity (C_p), it allows the determination of the phase change enthalpy,

$$\Delta H = \int_{\text{gel}}^{\text{fluid}} C_p \Delta T; \quad \Delta S = \Delta H / T_M. \tag{6}$$

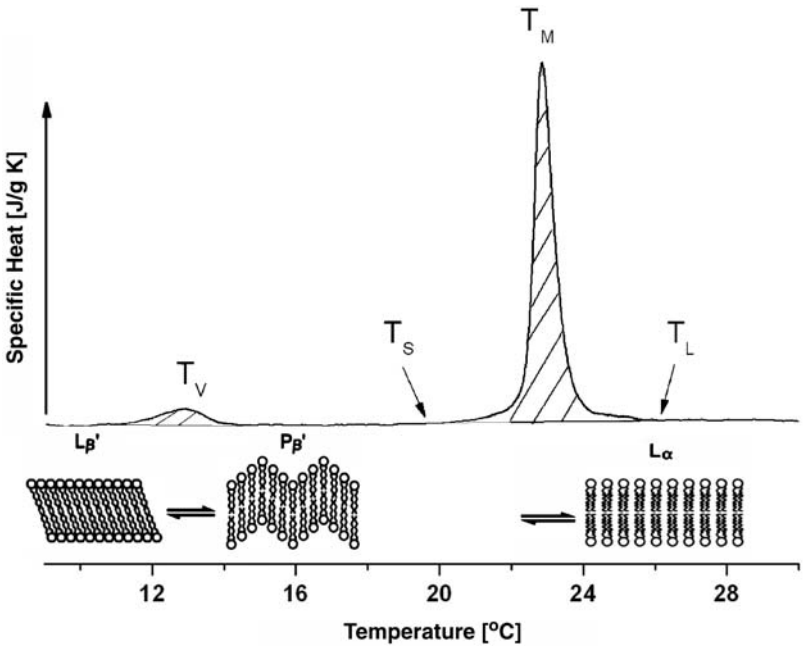

Figure 7 Differential scanning calorimetry. Heat capacity curves and thermotropic phase transitions of DMPC/DMPG vesicles.

From a kinetic view, the melting point is the state where the gel and fluid phase are in equilibrium,

$$K \equiv 1 = \frac{P_{\text{fluid}}(T_{\text{M}})}{P_{\text{gel}}(T_{\text{M}})}. \tag{7}$$

The equilibrium constant, K is determined by the relationship,

$$K = \mathrm{e}^{-\Delta G/RT} = \mathrm{e}^{-(\Delta H - T\Delta S)/RT} \tag{8}$$

where $K = 1$ at $\Delta G = 0$. Since the heat capacity is at a maximum at the phase transition (*melting*) point, the enthalpy fluctuation is therefore also at a maximum. Enthalpy also fluctuates with the surface area, i.e., 'fluid-like' lipids > 'gel-like' lipids and the size, i.e., the volume of lipid molecules is assumed to be constant. The principle of the DSC apparatus is shown in Fig. 8.

The heating of the sample and reference solution is performed at a preset heating rate, $\beta = \Delta T/\Delta t$, where the temperature of the system is determined by $T = T_0 + \beta xt$; (T_0 is the temperature at $t = 0$). The principle of DSC requires the temperature of the sample (probe, T_{P}) and reference (T_{R}) solution to remain constant, i.e., $T = T_{\text{P}} = T_{\text{R}}$. At an endothermic phase transition of the sample solution, this has to be heated to a higher degree compared to the sample solution to keep both temperatures at the same level. The heat output for the sample (P_{P}) will be larger than for the reference (P_{R}), therefore the difference of the heat

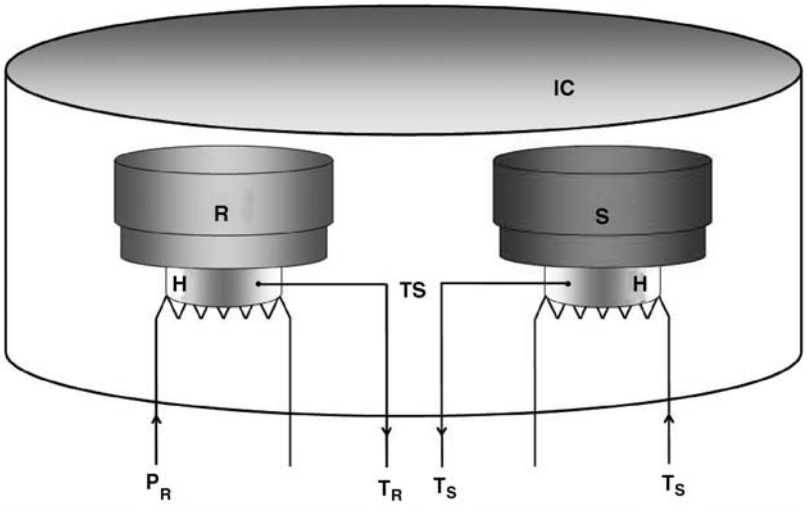

Figure 8 Schematic representation of the DSC apparatus. S, sample cell; R, reference cell; H, heating coil; IC, insulating casing; TS, temperature sensor; T_S and T_R are the currently measured temperatures in sample- and reference cell and (P_R; left) and ($T_S = P_S$; right) are the heat output for the reference and sample cell.

output, ΔP equals P_P–P_R. This is reflected in the heat capacities $\Delta C(T)$ between sample and reference which is proportional to

$$\Delta C(T) = C_p - C_R = \Delta P(T)/\beta. \tag{9}$$

In DSC thermograms, the difference of heat output ΔP is plotted against the temperature T. At the known heat rate, β the heat capacity difference $\Delta C(T)$ between the sample and reference solution as well as the partial dissipation of energy in molar heat capacity can be determined. Figure 7 shows an example of a thermogram for a DMPC and DMPG vesicle solution: pre-transition (T_V) at 13°C and main transition (T_M) at 23°C. Integrating between the start (T_S) and endpoint (T_L) of the DSC temperature signals determine the change in enthalpy

$$\int_{T_L}^{T_S} C_U \Delta T = \Delta_U H \tag{10}$$

A differential scanning calorimeter Q100 from TA Instruments (Fig. 9) was used and the reservoirs for the sample and reference solution are made of stainless steel and to hold a volume of ~100 µl each. Lipid-buffer solutions were placed in the reference cell and the lipid-myosin-II-buffer solutions in the sample cell. Under sealed conditions, both solutions were heated/cooled at a rate, β at 0.5°C/min between +7°C and +35°C in six cycles until the equilibrium of the phase transition enthalpy was reached, using a mixture of DMPC and DMPG at a molar ratio 50:50. A phase transition was observed at ~23°C. Data analysis was performed using the software from *Universal Analysis 2000* (TA Instruments) and *Origin* 7G.

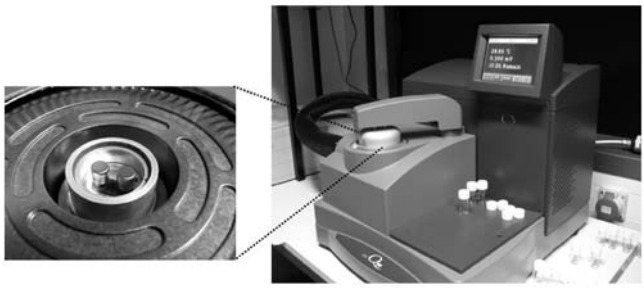

Figure 9 The calorimeter. Image of a calorimeter from TA Instruments (right) and sample and reference cell (arrows, left).

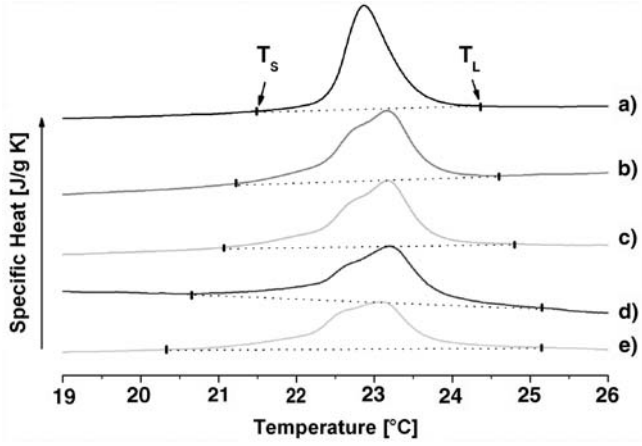

Figure 10 Thermograms. DSC thermogram of DMPC/DMPG without (a) myosin II and with myosin II ($b \rightarrow e$). Conditions: Lipid and myosin II concentration: 14.62 mM, and (b) 0.62 μM, (c) 1.45 μM, (d) 3.12 μM and (e) 6.24 μM, respectively.

3.1. Results

Myosin II insertion into phospholipid membranes was demonstrated using calorimetric measurements. The measurements were performed with multilamellar vesicles (MLVs) at 10 mg/ml consisting of DMPC/DMPG at a molar ratio of 50:50. Using increasing myosin concentrations, the changes in main phase transition were recorded ($P_{\beta'} \leftrightarrow L_{\alpha}$) as shown in Fig. 7. Adding increasing myosin II concentration (traces $b \rightarrow e$; $0.62 \rightarrow 6.24$ μM) to the lipid solution (a; no myosin II), a widening and flattening of the peak curvature was observed (Fig. 10). The start (T_S) and endpoint (T_L) of the phase transition are indicated by the arrows. The relative widening calculated from the relation, $(\Delta T_{1/2} - \Delta T^0_{1/2})/\Delta T^0_{1/2}$ is shown in Fig. 11. For a better comparison of the changes induced by the various myosin II concentrations, the enthalpy changes, ΔH, were normalized to pure lipids, against ΔH_0 (Table 1). Plotting the enthalpy changes $\Delta H/\Delta H_0$ against the molar ratios of myosin II and

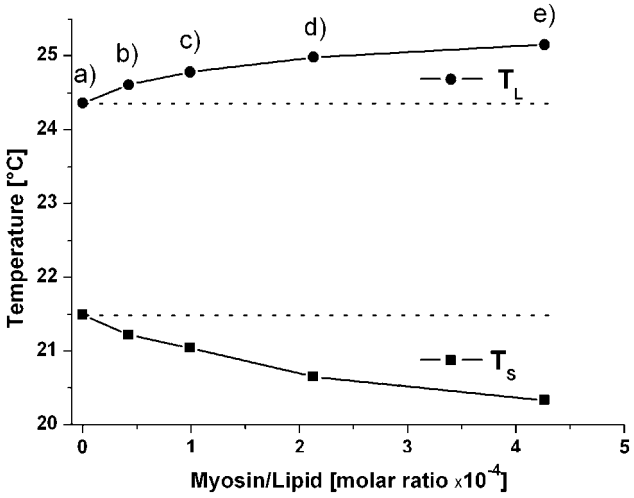

Figure 11 Phase transitions. A plot of T_S (solidus points) and T_L (liquidus points) taken from Fig. 10 as a function of myosin II–lipid molar ratio.

Table 1 Normalizing myosin II concentration against constant lipid concentration and enthalpy changes ΔH against ΔH_o (lipids only).

Lipid	Myosin (μM)	Myosin/Lipid	$\Delta H/\Delta H_0$	Trace
10 mg/ml ≅ 14.62 mM	0	0	1	a
	0.62	1/23580	0.91251	b
	1.45	1/10080	0.86383	c
	3.12	1/4690	0.74985	d
	6.24	1/2345	0.70055	e

lipids, an initial linear relationship followed by a saturation behavior of the lipid vesicles for myosin II was observed. The control protein BSA showed no changes (Fig. 12). Thermodynamic measurements (DSC) proved sufficient to determine the insertion behavior of myosin II into lipid membranes composed of DMPG/DMPC *in vitro* and the light scatter (stopped-flow) method confirmed these findings. The binding affinity of myosin II associated with and without lipids and actin was of a similar order of magnitude, confirming the previous observations of other membrane-interacting proteins [16].

4. Solid-State NMR Spectroscopy

Among the biophysical techniques that allow the investigation of peptides and proteins in bilayer environments solid-state NMR spectroscopy has proven to be a valuable tool. Recently, magic angle sample spinning solid-state NMR has resulted in the first NMR structures in the solid state of proteins in a microcrystalline

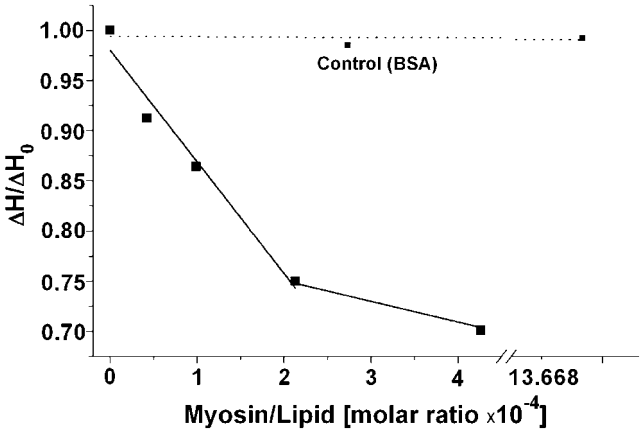

Figure 12 DSC plots. A plot of the changes in enthalpy $\Delta H/\Delta H_0$ against myosin II–lipid molar ratio. Bovine serum albumine (BSA) was used as a control protein.

environment [22] or when exhibiting a highly ordered microenvironment [23]. Furthermore, the technique makes accessible the structure, dynamics and topology of membrane-associated polypeptides (reviewed, e.g., in Refs. [24–27]). Using static-oriented samples, the tilt angles of helices with respect to the bilayer normal have been determined [28], and by measuring a large number of conformational constraints this approach has also been shown to be suitable for the complete structure determination of membrane-bound peptides [23,29]. In this chapter, we demonstrate how the orientation-dependence of NMR interactions is used to extract angular constraints from such static-oriented samples.

Proton-decoupled ^{15}N solid-state NMR spectroscopy of peptides labeled at the backbone amides with ^{15}N has been proven particularly convenient as this method provides the approximate tilt angle of membrane-associated helices in a direct manner [27,28]. Whereas transmembrane helical peptides exhibit ^{15}N chemical shifts around 200 ppm, sequences oriented parallel to the surface resonate at frequencies <100 ppm (Figs. 13A and B).

In a similar manner the deuterium quadrupole splitting of the alanine $-C^2H_3$ groups is dependent on the alignment of the polypeptide relative to the membrane normal [30]. The technique has been used to study the membrane-channel domains of the viral proteins Vpu [31] and M2 [32,33] also in the presence of the channel blocker amantadine [34]. Furthermore antibiotic peptides have been studied in some detail using oriented solid-state NMR spectroscopy, including protegrin 1 [35], pardaxin [36], peptaibols [37–39], melittin [40] or magainins [41]. A family of designed histidine-containing antimicrobial peptides, which is also efficient during the transfection of nucleic acids into cells [42], exhibits transmembrane alignments at neutral pH but reorients to the membrane surface at acidic conditions [43]. By using solid-state NMR spectroscopy it was possible to show that the peptide exhibits its most pronounced antimicrobial properties when oriented parallel to the membrane surface [44] suggesting that the detergent-like properties of amphipathic peptides are essential for membrane permeation [45].

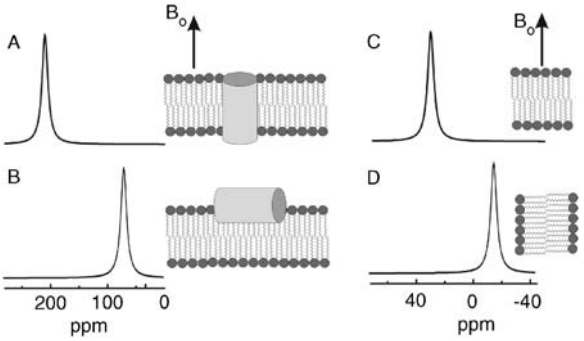

Figure 13 Simulated solid-state NMR spectra. (A) and (B) show simulated ^{15}N solid-state NMR spectra of an α-helical polypeptide oriented with the helix long axis perpendicular (A) or parallel (B) relative to the bilayer surface. The membranes are aligned with their normal parallel to the magnetic field of the NMR spectrometer (B_0). (C) and (D) show ^{31}P solid-state NMR spectra of liquid crystalline phosphatidylcholine membranes oriented with the lipid long axes parallel (C) or perpendicular (D) to B_0.

4.1. Theory: The Anisotropy of Interactions Measured in Solid-State NMR Spectroscopy

The nuclear interactions with the magnetic field are inherently anisotropic and, therefore, dependent on the orientation and conformation of the molecule with respect to the magnetic field direction [46–49]. Whereas in solution fast molecular tumbling ensures isotropic averaging of the nuclear interactions, the reorientational correlation times of molecules that are associated with extended phospholipid bilayers are slow. Therefore, the anisotropic properties of these interactions are reflected in the NMR spectra of membrane-bound peptides or lipids.

The anisotropic chemical shift interaction is mathematically expressed by second rank tensors, which in the principal axis system is described by three orthogonal components σ_{11}, σ_{22} and σ_{33} (for a more detailed explanation see Ref. [28]). This tensor can be transformed into other coordinate systems by successive rotations. The component of the chemical shift tensor in direction of the magnetic field direction (z-direction) corresponds to the measured NMR chemical shift value. When expressed in terms of the Euler angles (Θ and Φ) and the principal elements of the chemical shift tensor σ_{11}, σ_{22} and σ_{33}, the measureable σ_{zz} amounts to

$$\sigma_{ZZ} = \sigma_{11}\sin^2\Theta\cos^2\Phi + \sigma_{22}\sin^2\Theta\sin^2\Phi + \sigma_{33}\cos^2\Theta \qquad (11)$$

Whereas the static ^{15}N chemical shift tensor of the amide bond exhibits σ_{22} and σ_{11} values in the 85 ppm and 65 ppm range, respectively, its σ_{33} component is characterized by a much different value of approximately 230 ppm [50–54]. In α-helical peptides the NH vector and the σ_{33} component cover an angle of about 18° and both are oriented within a few degrees of the helix long axis. Due to the unique size of σ_{33} and its orientation almost parallel to the helix axis it is possible to measure an approximate alignment of the helix within oriented phospholipid bilayers merely by recording the ^{15}N chemical shift interaction. Therefore, in

samples uniaxially oriented with the membrane normal parallel to the magnetic field transmembrane α-helical peptides exhibit ^{15}N resonances >200 ppm (Fig. 13A). In contrast, they resonate in the σ_{11}–σ_{22} range (i.e., <100 ppm) when aligned parallel to the membrane surface (Fig. 13B). To arrive at a detailed structural analysis of solid-state NMR spectra from oriented samples, motional averaging and its effects on the chemical shift anisotropy have to be taken into consideration, however, the above analysis suffices for a semi-quantitative first analysis of polypeptide–membrane interactions.

Furthermore the deuterium spectra of methyl group labeled alanines in oriented membrane polypeptide sample have been analyzed. The methyl group of alanine exhibits fast rotational motions around the C_α–C_β bond. As a result the ^2H tensor is axially symmetric with respect to the C_α–C_β bond vector, and the measured splitting $\Delta\nu_Q$ is directly related to the orientation of the C_α–C_β bond:

$$\Delta\nu_Q = \frac{3}{2}\frac{e^2qQ}{h}\frac{(3\cos^2\Theta - 1)}{2} \tag{12}$$

where Θ is the angle between C_α–C_β bond and the magnetic field direction and e^2qQ/h the static quadrupolar coupling constant [55]. As C_α is an integral part of the polypeptide backbone, the orientation of the C_α–C_β bond also reflects the overall alignment of the peptide.

Due to fast axial rotation of the phospholipids around their long axis the ^{31}P chemical shift is characterized by an averaged symmetric tensor. The singular axis ($\sigma_{||}$) coincides with the rotational axis, i.e., the bilayer normal. In the ^{31}P solid-state NMR spectra of pure liquid crystalline phosphatidylcholine bilayers the signal at 30 ppm is thus indicative of phosphatidylcholine molecules with their long axis oriented parallel to the magnetic field direction (Fig. 13C), whereas a −15 ppm ^{31}P chemical shift is obtained for perpendicular alignments (Fig. 13D). In perfectly aligned samples the phospholipid bilayer spectra consists of a single line. Intensities to the right of this peak can arise from phospholipids with molecular orientations deviating from parallel to the magnetic field direction. In addition, signals in this region (<30 ppm) can be due to local conformational changes of the phospholipid head group, for example due to electrostatic interactions of the ($-HPO_4^-$–CH_2–CH_2–$N^+(CH_3)_3$) dipoles of the phosphocholine head group, hydrogen bonding and/or electric dipole–dipole interactions [56,57]. We routinely record ^{31}P NMR spectra of phospholipid bilayers also of the peptide carrying samples to test for the quality of order and alignment of phospholipid bilayers.

4.2. Experimental Considerations

The peptides investigated by solid-state NMR investigations can be made available either by biochemical overexpression or by chemical solid-phase peptide synthesis. Whereas the former technique is well suited for uniform or selective labeling schemes, the chemical approach allows for specific labeling of one or a few amino acid residues. For example the talin peptide H17 with the sequence GEQIAQ-LIAGYIDIILKKKKSK-amide was prepared using automatic solid-phase peptide synthesis. At the underlined positions the ^{15}N-labeled analogue of alanine was

incorporated. The peptide synthetic products are commonly analyzed and purified using reversed phase high-performance liquid chromatography and their identity confirmed by mass spectrometry.

Typically, 10–15 mg of the polypeptide is reconstituted into about 100–200 mg of phospholipid by co-dissolving the compounds in organic solvents or organic solvent–water mixtures. For sample preparations encompassing the talin peptide hexafluoroisopropanol has proven a good choice. On the other hand, the denaturation of larger proteins should be avoided by the usage of aqueous buffers during the reconstitution process. Typically the mixtures are dried onto 30 ultra-thin cover glasses (9 × 22 mm), where applicable, the organic solvents completely removed and the samples equilibrated at 93% relative humidity. The glass plates are then stacked on top of each other, which results in small brick-shaped samples of 3–4 mm thickness (Fig. 14). These are stabilized and sealed with teflon tape and plastic wrappings. To ensure an optimal filling factor special NMR coils have been developed and tested for these samples [58]. These are flattened in such a manner to reduce the empty space within the coil (Fig. 14). Considerable improvements in signal-to-noise ratio can be achieved by this modification when compared to standard commercial solid-state NMR coils [58]. The membrane normal is aligned parallel to the magnetic field direction but alternative sample alignments have also been investigated, e.g., when the dynamic properties of the membrane-associated peptide are of interest [33,40,59]. Cross-polarization or Hahn echo NMR pulse

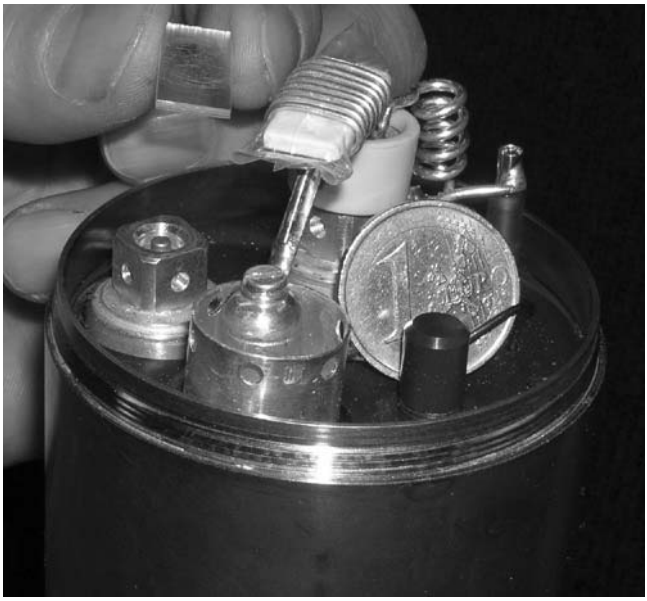

Figure 14 Solid-state NMR probe. The coils geometry has been adapted to the sample geometry. A stack of glass plates with several thousand lipid bilayers in between each pair is shown to the top left. The samples are protected and sealed before insertion into the flattened coil of the NMR probe. Before acquisition the NMR probe is introduced into the NMR magnet with the normal of the glass plates being oriented parallel to the magnetic field direction (Reproduced with permission).

sequences are typically used to acquire ^{15}N, ^{2}H and ^{31}P NMR spectra with the details given in previous publications, for example in Ref. [59,60].

4.3. Results and Discussion

Previous studies indicate the H17 exhibits membrane association predominantly driven by hydrophobic interactions and with partitioning constants in the $10^4\,M^{-1}$ range thereby being comparable to that of posttranslationally attached membrane anchors [61]. During the transfer from the aqueous to the membrane-associated state H17 undergoes a conformational transition from random coil to 86% α-helix [61]. The proton-decoupled ^{15}N solid-state NMR spectrum of the talin peptide H17 labeled with ^{15}N at the alanine-5 position exhibits a chemical shift of 80 ppm (Fig. 15). This value is indicative of an alignment of the peptide helix at the labeled site approximately parallel to the membrane surface [28]. The range of ^{15}N chemical shift values that is obtained from α-helices oriented at tilt angles of 60°, 70°, 80° or 90° (perfect in-plane alignment) are shown below the spectrum (Fig. 15A). This comparison indicates that the peak maximum of the ^{15}N maximum is in agreement with tilt angles of 70°–90°. This slightly oblique alignment is in excellent agreement

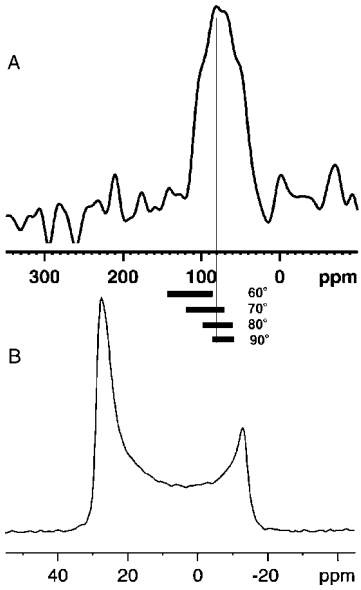

Figure 15 Solid-state NMR spectra of the talin peptide in oriented phospholipid membranes. (A) Proton-decoupled ^{15}N solid-state NMR spectra of 11 mg of the talin peptide reconstituted into 200 mg of 1-palmitoyl-2-oleoyl-*sn*-glycero-3-phosphocholine (POPC) membranes. The mixture has been applied onto glass surfaces, which are oriented with their normal parallel to the magnetic field direction. The bars indicate the calculated ^{15}N chemical shift range for peptides oriented at the indicated tilt angles relative to the membrane normal [27]. For the simulations the static main tensor elements were 223, 75 and 61 ppm with an alignment of the tensor elements as described in Ref. [54]. (B) Proton-decoupled ^{31}P solid-state NMR spectrum of the sample shown in panel A. The ^{31}P NMR line shape represents the distribution of alignments of the phospholipid head group in the sample.

with molecular modeling calculations, which predict a tilt angle of 72° [62] as well as with an area of insertion of 150 $Å^2$, i.e., about 50% of the projection of the helix onto the membrane surface [61].

However, the peak exhibits a considerable line width indicating that other conformations and/or peptide alignments are also present at the labeled site. The signal extends up to 110 ppm, a chemical shift value that is indicative of helix alignments in the 50°–75° range and/or reorientational averaging. At least two different explanations offer themselves to explain the heterogeneity observed at the labeled site. First, the alanine 5 position is relatively close to the N-terminus of the peptide leaving the possibility that the helical structure is not very stable and in conformational exchange. Second, it is possible that the helix as a whole adopts a variety of alignments by slowly wobbling back and forth.

The ^{31}P NMR spectrum of the same sample indicates that the peptide indeed exhibits a pronounced bilayer disordering effect (Fig. 15B). Although a main signal intensity is observed in the 30 ppm region considerable intensities extend throughout the chemical shift anisotropy of a liquid crystalline phosphatidylcholine bilayer. These additional ^{31}P signal intensities indicate that the lipid head group region exhibits a wide distribution of membrane alignments relative to the membrane normal. Interestingly, the H17 peptide from talin has been shown to exhibit fusogenic activities [62], a process that modifies the membrane curvature and requires a high degree of local rearrangements of the membrane.

Although more solid-state NMR experiments would be required to establish a detailed model of the structure and the dynamics of the talin peptide in phospholipid bilayers, the data already demonstrate the basic principles on how oriented solid-state NMR allows one to test not only the topology of membrane-associated peptides but also the polypeptides' influence on the lipid bilayer macroscopic phase properties.

To describe the tilt angle more accurately or to fully determine the structure of membrane-associated polypeptides by solid-state NMR spectroscopy additional angular constraints are accessible. These can be derived, for example, from the ^{15}N or ^{13}C chemical shift positions [40,63,64], ^{15}N–^{1}H dipolar coupling measurements [65–67] or ^{2}H quadrupolar interactions [30]. This latter approach has been particularly valuable as the deuterium NMR measurements provide additional information on the mosaicity of membrane alignment [68] as well as the rotational diffusion rate and thereby the aggregation state of the peptides [69].

It should be noted that the solid-state NMR data develop their full strength when it is possible to combine them with results from other investigations as has been shown for amphipathic peptide antibiotics, transfection peptides [42–44], a peptide from *ras* [70] or the H17 peptide described here [61,62].

5. Fluorescence Recovery after Photobleaching (FRAP)

Anchorage-dependent cells adhere to substrates through the ligation of transmembrane proteins, called integrins to extracellular matrix (ECM) molecules like

fibronectin, collagen and vitronectin [71]. The ligation and clustering of integrins gives rise to the recruitment of a variety of proteins like talin, vinculin and α-actinin [72] that physically connect integrins to the intracellular actin cytoskeleton (Fig. 16), resulting in the formation of a multi-protein complex called the 'focal adhesion' [72]. The focal adhesion forms a physical path for transferring intracellular forces generated in the contractile actin cytoskeleton which are transmitted through integrins onto the ECM substrate. Importantly, mechanical forces generated in the actin cytoskeleton promote adhesion assembly [73,74]. However, the underlying mechanisms are unclear.

Externally applied mechanical forces regulate the composition and the concentration of macromolecules that localize within focal adhesions. Focal adhesion assembly also regulates soluble signaling pathways, including Erk signaling that controls cell growth [75]. A variety of signal transduction pathways that control cell shape, gene expression, differentiation and apoptosis are triggered by integrin ligation [75–81]. Forces applied to beads that are ligated to integrin receptors induce a variety of responses including cAMP signaling [82–85], Ca^{2+} influx (through mechanosensitive ion channels), cytoskeletal remodeling [84], alterations of cell shape [85,86] and changes in nuclear morphology [87]. Thus, the focal adhesion is really a nano-scale mechano-chemical machine that transduces mechanical forces into intracellular biochemical signals, and therefore mediates both

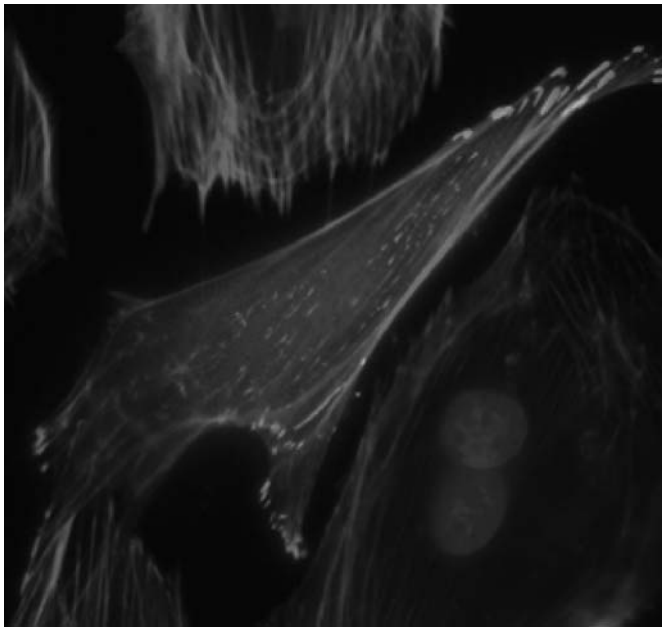

Figure 16 Fluorescence images. Fluorescence image of a single capillary endothelial cell expressing GFP-vinculin (green), stained for F-actin with Alexa phalloidin (red) and nuclei with DAPI (blue). Note: how each actin stress fiber is anchored into focal adhesions at its distal ends (bar = 10 μm). Reproduced with permission from Ref. [103], Copyright (c) 2006, Wiley-Liss, Inc. (please see plate no. 6 in the color section).

chemical and physical control of cellular physiology by ECM and mechanical forces.

5.1. Focal Adhesions and the Plasma Membrane

The formation of focal adhesions causes an increase in the levels of phosphatidylinositol-4,5-bisphosphate (PIP_2) [88,89], while antibodies to (PIP_2) inhibits adhesion assembly [90]. The adhesion protein vinculin interacts with (PIP_2) leading to vinculin activation, which promotes its binding to other adhesion proteins like talin and VASP [90]. Scaffold proteins localized to adhesions like α-actinin and filamin also bind to (PIP_2) [91–93]. Interactions between adhesion proteins and the lipid membranes may expose cryptic-binding sites leading to adhesion assembly, activate the *rho* pathway and promote actin filament assembly through membrane-tethered proteins like N-WASP [94]. The formation of focal adhesions may also regulate the formation of rafts at the lipid membrane; recent studies suggest that adhesion formation results in more order at the lipid membrane than caveolae [95]. Measuring the binding kinetics of proteins anchored to the living plasma membrane and other binding partners in focal adhesions may shed light on membrane-regulated mechanisms of adhesion assembly and regulation. In this chapter, we review our results on measuring the dissociation rate constants of vinculin, a membrane-associated adhesion protein, and zyxin, an adhesion protein that indirectly associates with the lipid membrane through binding interactions with α-actinin [9].

5.2. Quantifying Protein–Protein Binding Kinetics Inside Living Cells

Methods discussed previously in this chapter focused on measuring binding affinities between proteins *in vitro*. Complementary methods that can similarly quantify binding kinetics inside living cells are needed. This may help understand how protein–protein binding interactions may be regulated through intracellular signaling pathways, and how this may influence cellular physiology. For example, mechanical force may alter the binding kinetics of individual adhesion proteins through force-dependent modulation of protein conformation. This may result in net assembly of disassembly of molecules into adhesions. To test this hypothesis, methods that can quantify the binding kinetics of individual proteins inside a living cell are necessary. Such methods in combination with knowledge gained from *in vitro* studies of purified proteins may result in greatly increased insight of how multi-protein complexes are self-assembled, and how they function.

5.3. Method and Setup of FRAP

The diffusion coefficient of proteins inside living cells can be determined using laser photobleaching techniques, such as FRAP [96–98] in conjunction with mathematical models [99–102]. In FRAP, fluorescently labeled molecules within a small region of the surface membrane, cytoplasm or nucleus are exposed to a brief pulse of radiation from a laser beam at the excitation wavelength of the fluorophore (Fig. 17). This irradiation bleaches all the molecules within the path of the beam

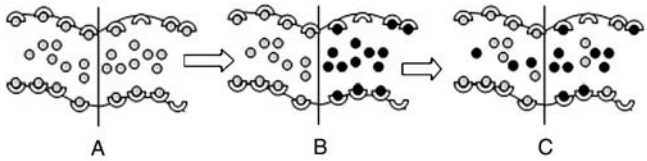

Figure 17 Diagram of molecular behavior during FRAP. (A) Before photobleaching, the bound molecules are in equilibrium with the free molecules. After photobleaching, there are two different modeling assumptions, (B) photobleached molecules are still bound to binding sites, and (C) exchange between fluorescent and bleached bound molecules, along with diffusive mixing leads to recovery (grey circles, fluorescent molecules; black circles, photobleached molecules). Reproduced from Ref. [104] with permission.

without altering their structure or function. Repeated fluorescence images of the bleached zone can be used to measure the rate at which fluorescent molecules redistribute and replace photo-bleached ones. If there is significant binding of molecules to structures in the bleached spot, fluorescence recovery will occur not only from diffusion, but rather from the interplay between binding–unbinding and diffusion. Thus, FRAP data can be potentially employed to make estimates of parameters that characterize the diffusion coefficient, binding rate constant and unbinding rate constant of proteins inside living cells [100]. This provides a significant advantage over biochemical methods that study molecules in solution because it permits analysis of the influence of cellular microenvironments on molecular interactions.

FRAP experiments are typically carried out using laser-scanning confocal microscopes like the Zeiss LSM 510 or the Leica TCS SP2 microscopes. In a laser-scanning confocal microscope, the fluorescence image is created by raster-scanning a highly focused excitation (laser) beam across the sample and recording the emitted fluorescence with a photomultiplier. The image is generated by combining individual pixel data into a computer-generated image. This mode of operation is particularly useful for FRAP experiments, because arbitrary shapes in the sample can be bleached during the raster scan by ramping up laser power selectively in pre-defined areas of the sample, while keeping the incident intensity at zero levels elsewhere. An acousto-optical tunable modulator (AOM) is used to increase the incident laser intensity in very short times (microseconds) in pre-defined bleached spots. Having bleached pre-defined areas, the subsequent recovery in fluorescence can be recorded by capturing fluorescence images over defined time intervals.

5.4. Results

FRAP experiments were performed on the Zeiss LSM 510 META/NLO microscope using a 63X 0.95 NA IR corrected water immersion lens. The 488 nm line of an Argon/2 multiple-lined single-photon laser source (10% of full power) was used for GFP excitation; 100% of the 488 nm line was used for photo-bleaching with 10 iterations corresponding to less than a millisecond. The size of the photo-bleached spot was chosen to be less than a square micron (Fig. 18A). Images were

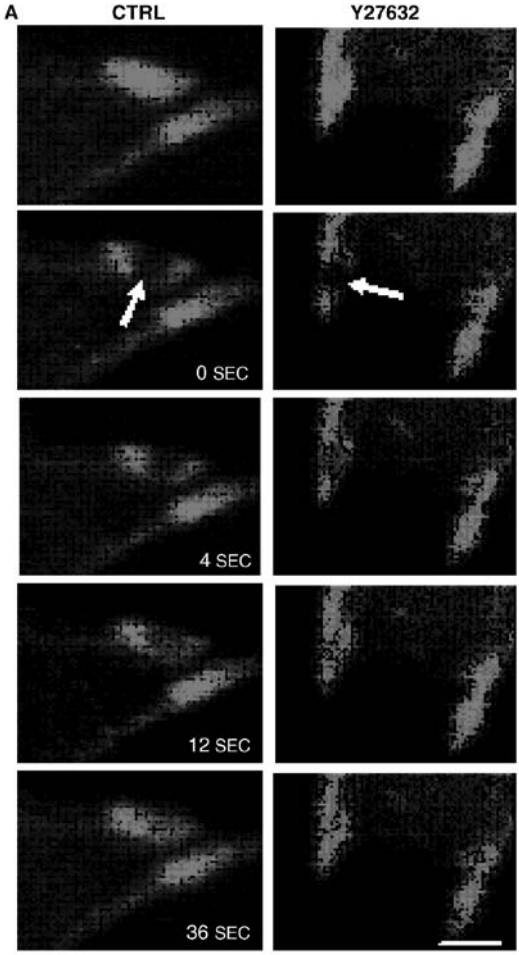
A
CTRL
Y27632
0 SEC
4 SEC
12 SEC
36 SEC

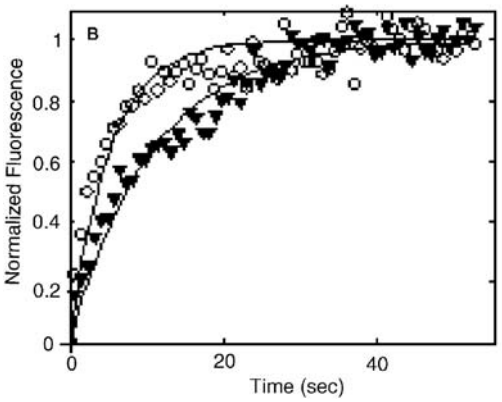
B
Normalized Fluorescence
0
0.2
0.4
0.6
0.8
1
0
20
40
Time (sec)

collected using the Zeiss LSM 510 software (version 3.2). All experiments on microscopes were performed at 37°C using a temperature-controlled stage.

FRAP experiments revealed that zyxin, a focal adhesion protein and putative mechanosensor exchanges with the cytoplasm in several seconds (Fig. 18A). Cells were then treated with Y27632, a small molecule inhibitor that inhibits myosin II phosphorylation, and reduces mechanical force exerted by stress fibers on the focal adhesion. This accelerated the rate of fluorescence recovery of zyxin, while that of vinculin, another adhesion protein remains unchanged. This effect of mechanical force on the exchange rates of zyxin was captured in different types of experiments including laser-severing of individual stress fibers or changing ECM stiffness that ultimately altered the mechanical force exerted on adhesion sites.

5.5. Quantitative Analysis of FRAP Experiments

Fluorescence recovery occurs in the photo-bleached spot (Fig. 18B) because photo-bleached zyxin unbinds from the focal adhesion with a dissociation rate constant k_{OFF}, and is replaced by a fluorescent molecule which rebinds with a rate constant k_{ON}. Fluorescent molecules in the cytoplasm diffuse with a diffusion coefficient D (Fig. 19). Cytoplasmic diffusion coefficients of proteins of the size of zyxin have a diffusion coefficient of a few microns/second. Based on cytoplasmic diffusion coefficients, the diffusion time for zyxin across the 60 nm thickness of the adhesion is on the order of a few milliseconds. Studies of focal adhesion ultrastructure suggest that the interstitial pore size is on the order of 10–30 nm [103]. Given that the size of proteins is on the order of 3–5 nm, the protein size is much smaller than the interstitial size inside focal adhesions. Hence, the interstitial diffusion coefficient of zyxin is not expected to be significantly different from that inside the cytoplasm. To explain the time scales observed for zyxin (Fig. 18A) purely based on diffusion, the interstitial diffusion coefficient would have to be 0.001 square micron/second, a number that is unreasonably low given the difference in protein size and adhesion pore size.

When diffusion is not rate limiting, the recovery of the fluorescence can be described by the differential equation $d\hat{C}_F/dt = k_{ON}SC_F - k_{OFF}\hat{C}_F$ and $\hat{C}_F(0) = \alpha\hat{C}_0$. Here, $\hat{C}_F$ is the concentration of bound fluorescent protein, C_F is the concentration of freely diffusing protein, S is the concentration of available binding sites, $\hat{C}_0 = k_{ON}SC_F/k_{OFF}$ is the pre-bleach concentration in the focal adhesion, and α denotes the fraction of fluorescent molecules that are not bleached in the photo-bleached spot. Making the assumption that C_F is constant (satisfied when

Figure 18 FRAP analysis of GFP zyxin recovery within individual photobleached focal adhesions. (A) Representative images of a FRAP experiment in control *versus* Y27632-treated cells showing that force dissipation accelerates zyxin recovery. Arrows indicate photobleached spots within individual focal adhesions that are analyzed over a period of 36 seconds follow photobleaching (bar = 2 μm). (B) Recovery curve for zyxin in control (open circles) *versus* Y27632-treated cells (closed triangles) from the experiment shown in A; solid lines are curves fit to the data using the method of least squares to estimate the dissociation rate constant k_{OFF} (please see plate no. 7 in the color section).

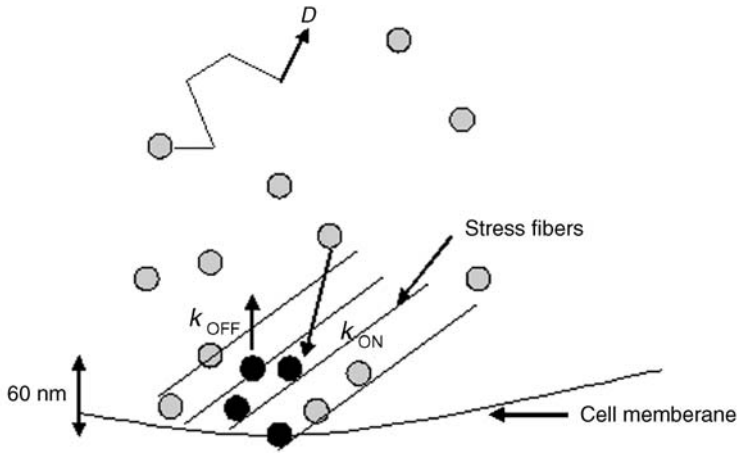

Figure 19 Schematic representation of FRAP. Schematic picture of molecular processes underlying exchange between the cytoplasmic diffusing protein and the adhesion-bound protein during FRAP. The black molecules indicate photobleached molecules, the rest are fluorescent. The vertical dimension of the adhesion is 60 nm, implying that the diffusive length scale is very small and arguing against diffusion being the rate limiting step (see text).

there is minimum photo-bleaching of cytoplasmic diffusing protein, and if the cytoplasmic diffusion is very fast compared to recovery times in the adhesion itself); the solution to the differential equation is $\hat{C}_F - \alpha\hat{C}_0/\hat{C}_0 - \alpha\hat{C}_0 = 1 - e^{-k_{OFF}t}$. Hence, normalized fluorescence recovery in the FRAP experiments yield k_{OFF} in Fig. 18B.

Decreasing the force exerted on the focal adhesions using Y27632 resulted in a continuous time-dependent increase in k_{OFF} of zyxin [103], with the average value of k_{OFF} increasing nearly 2.5-fold [103]. Laser ablation experiments in which individual stress fibers were cut to relax tension showed a similar increase in k_{OFF} in the anchored adhesion. Surprisingly, similar experiments with vinculin revealed that the values of k_{OFF} corresponding to both of its two dynamically distinct subpopulations remained unchanged after treatment with Y27632 [103]. Thus, the molecular-binding kinetics of some, but not all, focal adhesion proteins are selectively sensitive to changes in cytoskeletal tension.

The k_{OFF} measured in these experiments is really an 'effective' rate constant. This is because a protein may bind to multiple binding partners inside cells simultaneously. Further experiments that measure similar properties *in vitro* for protein–protein pairs may be useful in interpreting the intracellular data. FRAP experiments combined with systematic molecular biology experiments (relying on mutagenesis, deletion, etc.) that interfere with specific interactions in cells may also be useful to tease out pair-wise contributions to the time scales. In conclusion, a judicious combination of the *in vitro* methods and *in vivo* methods discussed in this chapter may help yield unprecedented insight into the molecular mechanisms of protein function at the cytoskeletal-lipid interface.

ACKNOWLEDGEMENTS

The authors thank Prof. Gerhard Isenberg, Dr. James Smith, Dipl. Phys. Vitali Schewkunow and Liz Nicholson (MA) for their suggestions and reading and copyediting this manuscript. This work was supported by grants from Deutsche Forschungsgemeinschaft and NATO (to WHG); CNRS, the French Ministry of Research, the European Union, the Université Louis Pasteur, the Region Alsace, the Agence Nationale de la Recherche, Vaincre la Mucoviscidose, the Agence Nationale pour la Recherche contre le SIDA and the Association pour la Recherche sur le Cancer (to BB); (TL) wishes to thank his former mentor Donald E. Ingber, in whose laboratory some of the work reviewed here was performed. For further technical information of the various instruments, please use the websites for stopped-flow: www.hi-techsci.co.uk; www.kintek-corp.com; www.bio-logic.info; www.photophysics.com and for DSC: www.microcal.com; www.tainstruments.com. Figs. 5, 10, 11, 12 and Table 1 were reproduced with permission by BMC Biochemistry.

REFERENCES

[1] G. Isenberg, Actin binding proteins – lipid interactions, J. Muscle Res. Cell Motil. 12 (1991) 136–144; (review).
[2] E.J. Luna, A.L. Hitt, Cytoskeleton–plasma membrane interactions, Science 258 (1992) 955–964; (review).
[3] G. Isenberg, W.H. Goldmann, Actin binding proteins–lipid interactions, in: J.E. Hesketh, I.F. Pryme (Eds.), The Cytoskeleton, Vol. 1, Jai Press Inc., Greenwich, NY, 1995, pp. 169–204.
[4] G. Isenberg, New concepts for signaling perception and transduction by the actin cytoskeleton at cell boundaries, Semin. Cell Dev. Biol. 7 (1996) 707–715.
[5] G. Isenberg, V. Niggli, Interaction of cytoskeletal proteins with membrane lipids, Int. Rev. Cytol. 178 (1998) 73–125. (review).
[6] V. Niggli, Structural properties of lipid-binding sites in cytoskeletal proteins, Trends Biochem. Sci. 26 (2001) 604–611; (review).
[7] J. Smith, G. Diez, A.H. Klemm, V. Schewkunow, W.H. Goldmann, CapZ–lipid membrane interactions: a computer analysis, Theor. Biol. Med. Model. 3 (2006) 30.
[8] W.H. Goldmann, J.M. Teodoridis, C.P. Sharma, B. Hu, G. Isenberg, Fragments from actin binding protein (ABP-280; filamin) insert into reconstituted lipid layers, Biochem. Biophys. Res. Commun. 259 (1999) 108–112.
[9] W.H. Goldmann, J.M. Teodoridis, C.P. Sharma, J.L. Alonso, G. Isenberg, Fragments from alpha-actinin insert into reconstituted lipid bilayers, Biochem. Biophys. Res. Commun. 264 (1999) 225–229.
[10] W.H. Goldmann, J.L. Niles, M.A. Arnaout, Interaction of purified human proteinase 3 (PR3) with reconstituted lipid bilayers, Eur. J. Biochem. 261 (1999) 155–162.
[11] D.L. Scott, G. Diez, W.H. Goldmann, Protein–lipid interactions: correlation of a predictive algorithm for lipid-binding sites with three-dimensional structural data, Theor. Biol. Med. Model. 3 (2006) 17; (review).
[12] H. Gutfreund, Enzymes: Physical Principles, John Wiley & Sons, London, 1972, pp. 1–242.
[13] C.F. Bernasconi, Relaxation Kinetics, Academic Press, New York, 1976, pp. 34–39.
[14] W.H. Goldmann, Z. Guttenberg, R.M. Ezzell, G. Isenberg, The study of fast reactions by the stopped-flow method, in: G. Isenberg, (Ed.), Modern Optics, Electronics, and High Precision Techniques in Cell Biology, Springer-Verlag, Heidelberg, 1998, pp. 159–171.
[15] W.H. Goldmann, M.A. Geeves, A 'slow' temperature jump apparatus build from a stopped-flow machine, Anal. Biochem. 192 (1991) 55–58.
[16] W.H. Goldmann, R. Senger, S. Kaufmann, G. Isenberg, Determination of the affinity of talin and vinculin to charged lipid vesicles: a light scatter study, FEBS Lett. 368 (1995) 516–518.
[17] N. Michel, A.S. Fabiano, A. Polidori, R. Jack, B. Pucci, Determination of phase transition temperatures of lipids by light scattering, Chem. Phys. Lipids 139 (2006) 11–19.

[18] K. Hiromi, Kinetics of Fast Reactions – Theory and Practice, Halsted Press, New York, 1979, pp. 99–104.
[19] J.M. Sturtevant, Biochemical applications of differential scanning calorimetry, Annu. Rev. Phys. Chem. 38 (1987) 463–488.
[20] A. Watts, Protein–lipid interactions, in: A. Neuberger, L.L.M. van Deenen (Eds.), New Comprehensive Biochemistry, Vol. 25, Elsevier, Amsterdam, 1993, pp. 1–379.
[21] I. Jelesarov, H.R. Bosshard, Isothermal titration calorimetry and differential scanning calorimetry as complementary tools to investigate the energetics of biomolecular recognitions, J. Mol. Recognit. 12 (1999) 3–18.
[22] F. Castellani, B. van Rossum, A. Diehl, M. Schubert, K. Rehbein, H. Oschkinat, Structure of a protein determined by solid-state magic-angle-spinning NMR spectroscopy, Nature 420 (2002) 98–102.
[23] A. Lange, K. Giller, S. Hornig, M.F. Martin-Eauclaire, O. Pongs, S. Becker, M. Baldus, Toxin-induced conformational changes in a potassium channel revealed by solid-state NMR, Nature 440 (2006) 959–962.
[24] J.H. Davis, M. Auger, Static and magic angle spinning NMR of membrane peptides and proteins, Prog. NMR Spectrosc 35 (1999) 1–84.
[25] A. Watts, Direct studies of ligand–receptor interactions and ion channel blocking (review), Mol. Membr. Biol. 19 (2002) 267–275.
[26] A. Drechsler, F. Separovic, Solid-state NMR structure determination, IUBMB Life 55 (2003) 515–523.
[27] B. Bechinger, C. Aisenbrey, P. Bertani, Topology, structure and dynamics of membrane-associated peptides by solid-state NMR spectroscopy, Biochim. Biophys. Acta 1666 (2004) 190–204.
[28] B. Bechinger, C. Sizun, Alignment and structural analysis of membrane polypeptides by 15N and 31P solid-state NMR spectroscopy, Concepts Magn. Reson. 18A (2003) 130–145.
[29] T.A. Cross, Solid-state nuclear magnetic resonance characterization of gramicidin channel structure, Meth. Enzymol. 289 (1997) 672–696.
[30] C. Aisenbrey, B. Bechinger, Tilt and rotational pitch angles of membrane-inserted polypeptides from combined 15N and 2H solid-state NMR spectroscopy, Biochemistry 43 (2004) 10502–10512.
[31] B. Bechinger, P. Henklein, Solid-state NMR investigations of Vpu structural domains in oriented phospholipid bilayers: interactions and alignment, in: W. Fischer (Ed.), Viral Membrane Proteins: Structure, Function, Drug Design, Vol. 1, in: M. Zouhair Atassa (Ed.), Series Protein Reviews, Springer-Verlag, Heidelberg, 2005, pp. 177–186, Chapter 13.
[32] Z.Y. Song, F.A. Kovacs, J. Wang, J.K. Denny, S.C. Shekar, J.R. Quine, T.A. Cross, Transmembrane domain of M2 protein from influenza A virus studied by solid-state N-15 polarization inversion spin exchange at magic angle NMR, Biophys. J. 79 (2000) 767–775.
[33] C. Aisenbrey, P. Bertani, P. Henklein, B. Bechinger, Structure, dynamics and topology of membrane polypeptides by oriented ^{2}H solid-state NMR spectroscopy, Eur. Biophys. J. 36 (2007) 451–460.
[34] B. Bechinger, R. Kinder, M. Helmle, T.B. Vogt, U. Harzer, S. Schinzel, Peptide structural analysis by solid-state NMR spectroscopy, Biopolymers 51 (1999) 174–190.
[35] J.J. Buffy, A.J. Waring, R.I. Lehrer, M. Hong, Immobilization and aggregation of the antimicrobial peptide protegrin-1 in lipid bilayers investigated by solid-state NMR, Biochemistry 42 (2003) 13725–13734.
[36] K.J. Hallock, D.K. Lee, J. Omnaas, H.I. Mosberg, A. Ramamoorthy, Membrane composition determines pardaxin's mechanism of lipid bilayer disruption, Biophys. J. 83 (2002) 1004–1013.
[37] C.L. North, M. Barranger-Mathys, D.S. Cafiso, Membrane orientation of the N-terminal segment of alamethicin determined by solid-state ^{15}N NMR, Biophys. J. 69 (1995) 2392–2397.
[38] B. Bechinger, D.A. Skladnev, A. Ogrel, X. Li, N.Y. Swischewa, T.V. Ovchinnikova, J.D.J. O'Neil, J. Raap, ^{15}N and ^{31}P solid-state NMR investigations on the orientation of zervamicin II and alamethicin in phosphatidylcholine membranes, Biochemistry 40 (2001) 9428–9437.

[39] M. Bak, R.P. Bywater, M. Hohwy, J.K. Thomsen, K. Adelhorst, H.J. Jakobsen, O.W. Sorensen, N.C. Nielsen, Conformation of alamethicin in oriented phospholipid bilayers determined by N-15 solid-state nuclear magnetic resonance, Biophys. J. 81 (2001) 1684–1698.
[40] R. Smith, F. Separovic, T.J. Milne, A. Whittaker, F.M. Bennett, B.A. Cornell, A. Makriyannis, Structure and orientation of the pore-forming peptide, melittin, in lipid bilayers, J. Mol. Biol. 241 (1994) 456–466.
[41] B. Bechinger, The structure, dynamics and orientation of antimicrobial peptides in membranes by solid-state NMR spectroscopy, Biochim. Biophys. Acta 1462 (1999) 157–183.
[42] A. Kichler, C. Leborgne, J. März, O. Danos, B. Bechinger, Histidine-rich amphipathic peptide antibiotics promote efficient delivery of DNA into mammalian cells, Proc. Natl. Acad. Sci. U.S.A. 100 (2003) 1564–1568.
[43] B. Bechinger, Towards membrane protein design: pH dependent topology of histidine-containing polypeptides, J. Mol. Biol. 263 (1996) 768–775.
[44] T.C.B. Vogt, B. Bechinger, The interactions of histidine-containing amphipathic helical peptide antibiotics with lipid bilayers: the effects of charges and pH, J. Biol. Chem. 274 (1999) 29115–29121.
[45] B. Bechinger, K. Lohner, Detergent-like action of linear cationic membrane-active antibiotic peptides, Biochim. Biophys. Acta. 1758 (2006) 1529–1539.
[46] U. Haeberlen, High Resolution NMR in Solids, Selective Averaging, Academic Press, New York, 1976.
[47] M. Mehring, Principles of High Resolution NMR in Solids, Springer-Verlag, Berlin, 1983.
[48] T.A. Cross, J.R. Quine, Protein structure in anisotropic environments: development of orientational constraints, Concepts Magn. Reson. 12 (2000) 55–70.
[49] R.G. Griffin, Solid-state nuclear magnetic resonance of lipid bilayers, Meth. Enzymol. 72 (1981) 108–173.
[50] C.J. Hartzell, M. Whitfield, T.G. Oas, G.P. Drobny, Determination of the ^{15}N and ^{13}C chemical shift tensors of L- [^{13}C]alanyl-L-[^{15}N]alanine from the dipole-coupled powder patterns, J. Am. Chem. Soc. 109 (1987) 5966–5969.
[51] D.K. Lee, R.J. Wittebort, A. Ramamoorthy, Characterization of ^{15}N chemical shift and 1H-15N dipolar coupling interactions in a peptide bond of uniaxially oriented and polycrystalline samples by one-dimensional dipolar chemical shift solid-state NMR spectroscopy, J. Am. Chem. Soc. 120 (1998) 8868–8874.
[52] D.K. Lee, Y. Wei, A. Ramamoorthy, A two-dimensional magic-angle decoupling and magic-angle turning solid-state NMR method: an application to study chemical shift tensors from peptides that are nonselectively labeled with ^{15}N isotope, J. Phys. Chem. B 105 (2001) 4752–4762.
[53] T.G. Oas, C.J. Hartzell, F.W. Dahlquist, G.P. Drobny, The amide 15N chemical shift tensors of four peptides determined from 13C dipole-coupled chemical shift powder patterns, J. Am. Chem. Soc. 109 (1987) 5962–5966.
[54] N.D. Lazo, W. Hu, T.A. Cross, Low-temperature solid-state ^{15}N NMR characterization of polypeptide backbone librations, J. Magn. Reson. 107 (1995) 43–50.
[55] J. Seelig, Deuterium magnetic resonance: theory and application to lipid membranes, Q. Rev. Biophys. 10 (1977) 353–418.
[56] P.G. Scherer, J. Seelig, Electric charge effects on phospholipid headgroups. Phosphatidycholine in mixtures with cationic and anionic amphiles, Biochemistry 28 (1989) 7720–7727.
[57] B. Bechinger, J. Seelig, Interaction of electric dipoles with phospholipid head groups. A ^{2}H and ^{31}P NMR study of phloretin and phloretin analogues in phosphatidylcholine membranes, Biochemistry 30 (1991) 3923–3929.
[58] B. Bechinger, S.J. Opella, Flat-coil probe for NMR spectrscopy of oriented membrane samples, J. Magn. Reson. 95 (1991) 585–588.
[59] C.B.B. Aisenbrey, B. Bechinger, Investigations of polypeptide rotational diffusion in aligned membranes by ^{2}H and ^{15}N solid-state NMR spectroscopy, J. Am. Chem. Soc. 126 (2004) 16676–16683.
[60] B. Bechinger, Detergent-like properties of magainin antibiotic peptides: a 31P solid-state NMR study, Biochim. Biophys. Acta 1712 (2005) 101–108.

[61] A. Seelig, X.L. Blatter, A. Frentzel, G. Isenberg, Phospholipid binding of synthetic talin peptides provides evidence for an intrinsic membrane anchor of talin, J. Biol. Chem. 275 (2000) 17954–17961.
[62] G. Isenberg, S. Doerhoefer, D. Hoekstra, W.H. Goldmann, Membrane fusion induced by the major lipid-binding domain of the cytoskeletal protein talin, Biochem. Biophys. Res. Commun. 295 (2002) 636–643.
[63] T.A. Cross, Solid-state nuclear magnetic resonance characterization of gramicidin channel structure, Meth. Enzymol. 289 (1997) 672–696.
[64] V. Wray, R. Kinder, T. Federau, P. Henklein, B. Bechinger, U. Schubert, Solution structure and orientation of the transmembrane anchor domain of the HIV-1 encoded virus protein U (Vpu) by high-resolution and solid-state NMR spectroscopy, Biochemistry 38 (1999) 5272–5282.
[65] B. Bechinger, M. Zasloff, S.J. Opella, Structure and interactions of magainin antibiotic peptides in lipid bilayers: a solid-state NMR investigation, Biophys. J. 62 (1992) 12–14.
[66] A. Ramamoorthy, C.H. Wu, S.J. Opella, Experimental aspects of multidimensional solid-state NMR correlation spectroscopy, J. Magn. Reson. 140 (1999) 131–140.
[67] S.J. Opella, F.M. Marassi, J.J. Gesell, A.P. Valente, Y. Kim, M. Oblatt-Montal, M. Montal, Structures of the M2 channel-lining segments from nicotinic acetylcholine and NMDA receptors by NMR spectroscopy, Nat. Struct. Biol. 6 (1999) 374–379.
[68] C. Aisenbrey, C. Sizun, J. Koch, M. Herget, R. Abele, B. Bechinger, R. Tampe, Structure and dynamics of membrane-associated ICP47, a viral inhibitor of the MHC I antigen-processing machinery, J. Biol. Chem. 281 (2006) 30365–30372.
[69] C. Aisenbrey, B. Bechinger, Investigations of peptide rotational diffusion in aligned membranes by ^{2}H and ^{15}N solid-state NMR spectroscopy, J. Am. Chem. Soc. 126 (2004) 16676–16683.
[70] D. Huster, A. Vogel, C. Katzka, H.A. Scheidt, H. Binder, S. Dante, T. Gutberlet, O. Zschornig, H. Waldmann, K. Arnold, Membrane insertion of a lipidated ras peptide studied by FTIR, solid-state NMR, and neutron diffraction spectroscopy, J. Am. Chem. Soc. 125 (2003) 4070–4079.
[71] R.O. Hynes, Integrins: bidirectional, allosteric signaling machines, Cell 110 (2002) 673–687.
[72] A.D. Bershadsky, N.Q. Balaban, B. Geiger, Adhesion-dependent cell mechanosensitivity, Annu. Rev. Cell Dev. Biol. 19 (2003) 677–695.
[73] N.Q. Balaban, U.S. Schwarz, D. Riveline, P. Goichberg, G. Tzur, I. Sabanay, D. Mahalu, S. Safran, A.D. Bershadsky, L. Addadi, B. Geiger, Force and focal adhesion assembly: a close relationship studied using elastic micropatterned substrates, Nat. Cell Biol. 3 (2001) 466–472.
[74] D. Riveline, E. Zamir, N.Q. Balaban, U.S. Schwarz, T. Ishizaki, S. Narumiya, Z. Kam, B. Geiger, A.D. Bershadsky, Focal contacts as mechanosensors: externally applied local mechanical force induces growth of focal contacts by an mDia1-dependent and ROCK-independent mechanism, J. Cell Biol. 153 (2001) 1175–1186.
[75] Q. Chen, M.S. Kinch, T.H. Lin, K. Burridge, R.L. Juliano, Integrin-mediated cell adhesion activates mitogen-activated protein kinases, J. Biol. Chem. 269 (1994) 26602–26605.
[76] K. Burridge, K. Wennerberg, Rho and Rac take center stage, Cell 116 (2004) 167–179.
[77] A.J. Ridley, M.A. Schwartz, K. Burridge, R.A. Firtel, M.H. Ginsberg, G. Borisy, J.T. Parsons, A.R. Horwitz, Cell migration: integrating signals from front to back, Science 302 (2003) 1704–1709.
[78] K.A. DeMali, K. Wennerberg, K. Burridge, Integrin signaling to the actin cytoskeleton, Curr. Opin. Cell Biol. 15 (2003) 572–582.
[79] S.K. Sastry, K. Burridge, Focal adhesions: a nexus for intracellular signaling and cytoskeletal dynamics, Exp. Cell Res. 261 (2000) 25–36.
[80] K. Burridge, M. Chrzanowska-Wodnicka, Focal adhesions, contractility, and signaling, Annu. Rev. Cell Dev. Biol. 12 (1996) 463–518.
[81] L.H. Romer, K. Burridge, C.E. Turner, Signaling between the extracellular matrix and the cytoskeleton: tyrosine phosphorylation and focal adhesion assembly, Cold Spring Harb. Symp. Quant. Biol. 57 (1992) 193–202.
[82] D.R. Overby, F.J. Alenghat, M. Montoya-Zavala, H.C. Bei, P. Oh, J. Karavitis, D.E. Ingber, Magnetic cellular switches, IEEE Trans. Magn. 40 (2004) 2958–2960.

[83] B.D. Matthews, D.R. Overby, R. Mannix, D.E. Ingber, Cellular adaptation to mechanical stress: role of integrins, Rho, cytoskeletal tension, and mechanosensitive ion channels, J. Cell Sci. 119 (2006) 508–518.
[84] D.R. Overby, B.D. Matthews, E. Alsberg, D.E. Ingber, Novel dynamic rheological behavior of focal adhesions measured within single cells using electromagnetic pulling cytometry, Acta Biomater. 3 (2005) 295–303.
[85] C.S. Chen, J.L. Alonso, E. Ostuni, G.M. Whitesides, D.E. Ingber, Cell shape provides global control of focal adhesion assembly, Biochem. Biophys. Res. Commun. 307 (2003) 355–361.
[86] A. Brock, E. Chang, C.C. Ho, P. LeDuc, X. Jiang, G.M. Whitesides, D.E. Ingber, Geometric determinants of directional cell motility revealed using microcontact printing, Langmuir 19 (2003) 1611–1617.
[87] A.J. Maniotis, C.S. Chen, D.E. Ingber, Demonstration of mechanical connections between integrins, cytoskeletal filaments, and nucleoplasm that stabilize nuclear structure, Proc. Natl. Acad. Sci. U.S.A. 94 (1997) 849–854.
[88] H.P. McNamee, H.G. Liley, D.E. Ingber, Integrin-dependent control of inositol lipid synthesis in vascular endothelial cells and smooth muscle cells, Exp. Cell Res. 224 (1996) 116–122.
[89] H.P. McNamee, D.E. Ingber, M.A. Schwartz, Adhesion to fibronectin stimulates inositol lipid synthesis and enhances PDGF-induced inositol lipid breakdown, J. Cell Biol. 121 (1993) 673–678.
[90] A.P. Gilmore, K. Burridge, Regulation of vinculin binding to talin and actin by phosphatidyl-inositol-4-5-bisphosphate, Nature 381 (1996) 531–535.
[91] K. Fukami, N. Sawada, T. Endo, T. Takenawa, Identification of a phosphatidylinositol 4,5-bisphosphate-binding site in chicken skeletal muscle alpha-actinin, J. Biol. Chem. 271 (1996) 2646–2650.
[92] K. Fukami, K. Furuhashi, M. Inagaki, T. Endo, S. Hatano, T. Takenawa, Requirement of phosphatidylinositol 4,5-bisphosphate for alpha-actinin function, Nature 359 (1992) 150–152.
[93] K. Furuhashi, M. Inagaki, S. Hatano, K. Fukami, T. Takenawa, Inositol phospholipid-induced suppression of F-actin-gelating activity of smooth muscle filamin, Biochem. Biophys. Res. Commun. 184 (1992) 1261–1265.
[94] A.S. Sechi, J. Wehland, The actin cytoskeleton and plasma membrane connection: PtdIns(4,5)P(2) influences cytoskeletal protein activity at the plasma membrane, J. Cell Sci. 113 (2000) 3685–3695.
[95] K. Gaus, S. Le Lay, N. Balasubramanian, M.A. Schwartz, Integrin-mediated adhesion regulates membrane order, J. Cell Biol. 174 (2006) 725–734.
[96] E.D. Salmon, R.J. Leslie, W.M. Saxton, M.L. Karow, J.R. McIntosh, Spindle microtubule dynamics in sea urchin embryos: analysis using a fluorescein-labeled tubulin and measurements of fluorescence redistribution after laser photobleaching, J. Cell Biol. 99 (1984) 2165–2174.
[97] M. Schindler, M.J. Osborn, D.E. Koppel, Lateral diffusion of lipopolysaccharide in the outer membrane of Salmonella typhimurium, Nature 285 (1980) 261–263.
[98] K. Jacobson, Z. Derzko, E.S. Wu, Y. Hou, G. Poste, Measurement of the lateral mobility of cell surface components in single, living cells by fluorescence recovery after photobleaching, J. Supramol. Struct. 5 (1976) 565–576.
[99] D. Axelrod, D. Koppel, J. Schlessinger, E. Elson, W. Webb, Mobility measurement by analysis of fluorescence photobleaching recovery kinetics, Biophys. J. 16 (1976) 1055–1069.
[100] R. Phair, T. Misteli, Kinetic modelling approaches to in vivo imaging, Nat. Rev. Mol. Cell Biol. 2 (2001) 898–907.
[101] Y. Tardy, J. McGrath, J. Hartwig, C. Dewey, Interpreting photoactivated fluorescence microscopy measurements of steady-state actin dynamics, Biophys. J. 69 (1995) 1674–1682.
[102] C.M. Franz, D.J. Muller, Analyzing focal adhesion structure by atomic force microscopy, J. Cell Sci. 118 (2005) 5315–5323.
[103] T.P. Lele, J. Pendse, S. Kumar, M. Salanga, J. Karavitis, D.E. Ingber, Mechanical forces alter zyxin unbinding kinetics within focal adhesions of living cells, J. Cell. Physiol. 207 (2006) 187–194.
[104] T.P. Lele, P. Oh, J.A. Nickerson, D.E. Ingber, An improved mathematical model for determination of molecular kinetics in living cells with FRAP, Mech. Chem. Biosys. 1 (2004) 181–190.

This page intentionally left blank

Subject Index

Actin 232, 233, 234, 238, 245, 246
Algal Toxin 29, 41
Anisotropic Membrane Inclusion 1, 2, 3, 14, 16, 19, 20, 22, 23
Ankyrin 83, 91, 92, 95, 96
  binding domain 90, 91, 92, 93, 94, 95
  PE 92
Antimicrobial peptides 103, 104, 107, 108, 109, 110, 112, 113, 115, 116, 130, 131, 132
Attenuated total reflection (ATR) 140

Baculovirus expression system 33, 34
Bound water 151, 160

Carbonyl band 158, 159, 160
Cell 166, 167, 168, 169, 176, 186, 187, 193, 194, 195, 196, 197, 198, 199, 200, 201, 202, 203, 204, 205, 206, 207, 209, 210, 211, 212, 217, 218, 219
  suspension 197, 198, 203
Cholesterol 140, 141, 142, 151, 152, 153,154, 155, 156, 158, 159, 160
Conductivity 166, 167, 195, 196, 202, 203, 204, 205, 207, 208, 209, 210, 211, 212, 217, 218, 219
Cytoskeleton 50, 51, 52, 58, 59, 60, 61, 62, 64, 65, 66, 67, 68, 69, 72, 73, 74, 75

Detergents 3, 22
  resistant membranes 49, 50, 55
Differential scanning calorimetry 228, 233, 235

Electrolyte solution 1, 6, 9, 10
Electron paramagnetic resonance 139, 143
Electroporation 2, 19, 20, 22
Electrostatic energy 1, 3, 4, 6, 9, 16

Flexible membrane inclusion 12
Flotillin 57, 58, 59, 61, 62, 64
Fluorescence recovery after photobleaching (FRAP) 228, 229, 244 246, 247, 249, 250
FTIR 147

Hydrophilic Pore 1, 2, 3, 5, 7, 9, 11, 13, 15, 17, 19, 20, 21, 22, 23, 25

Immobilised metal affinity chromatography (IMAC) 27, 28, 31, 32, 33, 35, 36, 37
Intrinsic shape of inclusion 11
Ion channel 28, 30, 31, 32, 33, 39, 40, 44

Kinetics 228, 232, 233, 246, 250

Line tension 1, 2, 3, 4, 5, 14, 15, 16, 21, 22
Linear rising signal 171, 172, 173
Lipid
  bilayer 104, 107, 109, 113, 114, 116, 119, 121, 122, 123
  lateral domain 141
  monolayers 87
  phase 140, 141, 142, 148, 155, 156, 157, 158, 159, 160
  rafts 49, 51, 52, 53, 54, 55, 57, 58, 59, 61, 63, 65, 66, 67, 69, 70, 71, 73, 75, 77, 79
  binding sites 82, 89, 91, 95
Liposomes 84, 87, 89, 91, 92, 96

Membrane
  composition 104, 125
  domains 113, 130
  fluidity 100, 104
  free energy 13, 14, 15, 16
  heterogeneity 139, 140, 142, 143, 152, 153, 155, 157, 160
  hydration 140, 149
  proteins 49, 51, 52, 53, 54, 55, 56, 57, 68, 69, 71, 73, 74, 75
  skeletal proteins 81, 82, 84, 95, 97
  skeleton 83, 84, 86, 92, 95,96, 97
Model membranes 104, 112, 116, 117, 125, 127
Myosin II 230, 231, 232, 233, 234, 237, 238, 249

Nonionic surfactant 19, 22

Optimal pore size 1, 17, 18
Optimization method 146
Orientational ordering 2, 3

Phase diagram 141, 142, 155, 156
Phosphatidylcholine 140, 160
Phospholipids 234, 241
Planar bilayer lipid membranes (p-BLM) 30
Planar lipid bilayer 3, 4, 7
Poisson-Boltzmann theory 25
Protein 4.1 83, 95, 96, 97

Small-angle 116, 117, 128, 131
Solid-state NMR spectroscopy 238, 239, 240, 244
Spectral simulation 145, 150, 157
Spectrins 81, 82, 83, 84, 85, 86, 87, 88, 89, 90, 91, 92, 93, 95, 96, 97, 99, 101
  lipid Interactions 89
Spin labeling 139
Stable membrane pores 19
Stomatin 50, 57, 58, 59, 61, 62, 64, 66, 68, 69, 70, 71, 72, 73, 74
Stopped-flow spectrophotometer 229, 231

Talin 232, 241, 242, 243, 244, 245, 246
Theoretical model 175, 195, 203, 209, 212, 217
Thermodynamic 233, 238

Vesiculation 50, 67, 68, 70, 72, 73, 74, 75
Vinculin 232, 245, 246, 249, 250
Voltage-gated sodium channel (VGSC) 28, 29, 30, 31, 32, 33, 34, 35, 36, 38, 39, 40, 41, 43

X-ray scattering 104, 121, 122, 123, 126, 129, 130, 131

Zyxin 246, 249, 250

Color Section

This page intentionally left blank

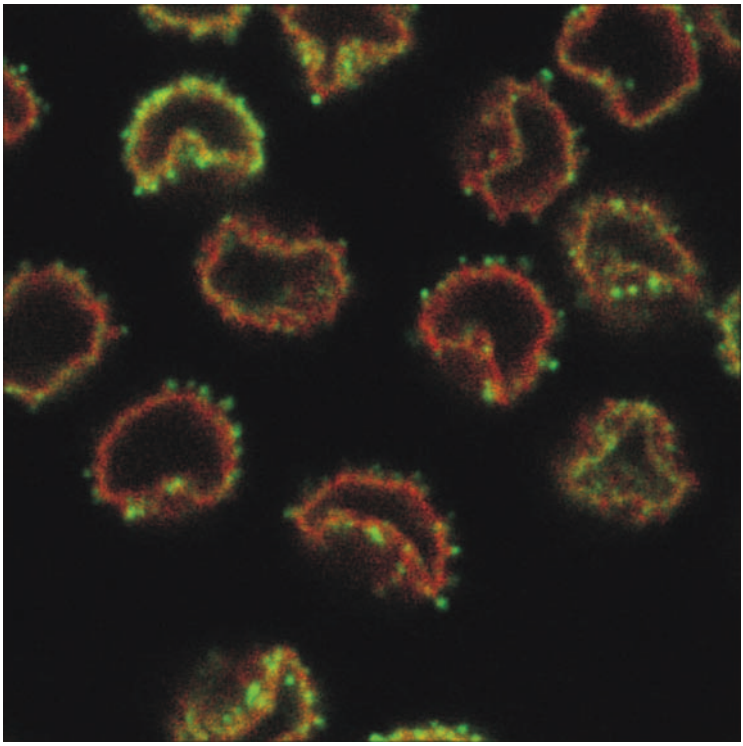

Plate 1 Calcium induces the segregation of stomatin and the cytoskeleton. Erythrocytes were incubated with 1 mM calcium chloride and 5 μM A23187 in TBS at 37°C for 5 minutes, bound to poly-L-lysine coated coverslips, fixed with 4% paraformaldehyde, quenched in 50 mM ammonium chloride and shortly lysed in 0.1% TX-100 at 4°C. The cells were blocked in 5% foetal calf serum, incubated with anti-stomatin monoclonal mouse antibody (GARP50 [46]) for 1 hour, washed and then incubated with rhodamine-labelled phalloidine (red) and fluorescein-labelled anti-mouse antibody (green). A Leica TCS SP microscope was used for confocal laser microscopy. Stomatin is preferentially found at the tips of membrane protrusions, whereas actin is absent therefrom (see page 69 in this volume).

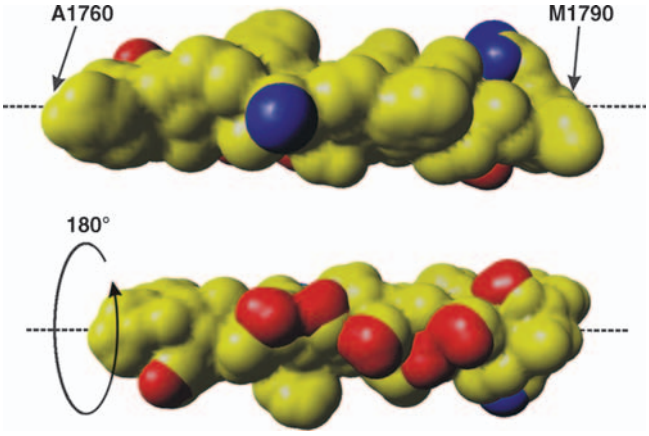

Plate 2 Structural model [78] of the lipid-binding site surface of the ankyrin-binding domain of the β-spectrin (with the permission from the Publisher, Taylor and Francis[R], http://www.informaworld.com). Blue are positively and red are negatively charged residues. Hydrophobic residues are marked yellow (see page 94 in this volume).

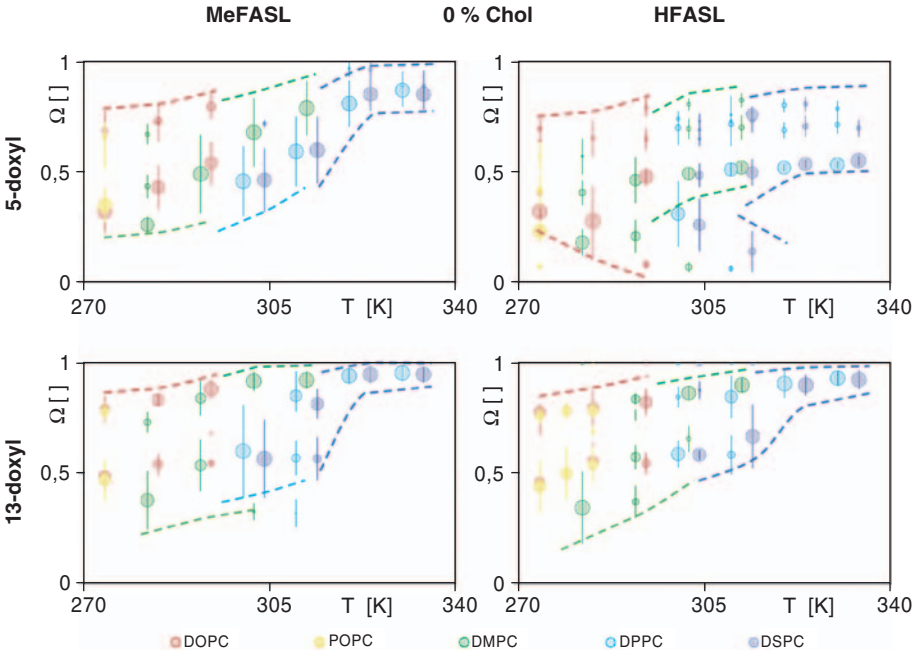

Plate 3 Condensed results of the significant motional patterns of the 5-doxyl and 13-doxyl MeFASL and HFASL spin probes in DSPC, DPPC, DMPC, POPC and DOPC membranes without cholesterol. The temperature range was from 20 K below to 20 K above the main phase transition temperature of the corresponding lipid. The free rotational space Ω is shown on the *y*-axis, as the main characteristics of the rotational restriction and a measure of anisotropy of rotational motion of a spin probe (see page 154 in this volume).

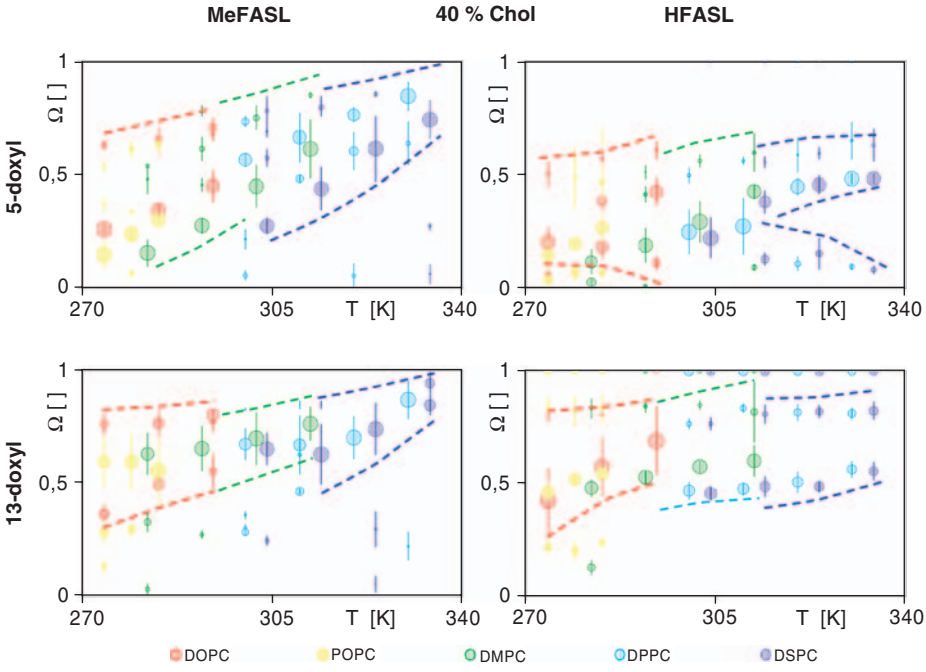

Plate 4 Condensed results of the significant motional patterns of the 5-doxyl and 13-doxyl MeFASL and HFASL spin probes in DSPC, DPPC, DMPC, POPC and DOPC membranes with 40 molar% of cholesterol. The temperature range was from 20 K below to 20 K above the main phase transition temperature of the corresponding lipid (without cholesterol). The free rotational space Ω is shown on the *y*-axis, as the main characteristics of the rotational restriction and a measure of anisotropy of rotational motion of a spin probe (see page 155 in this volume).

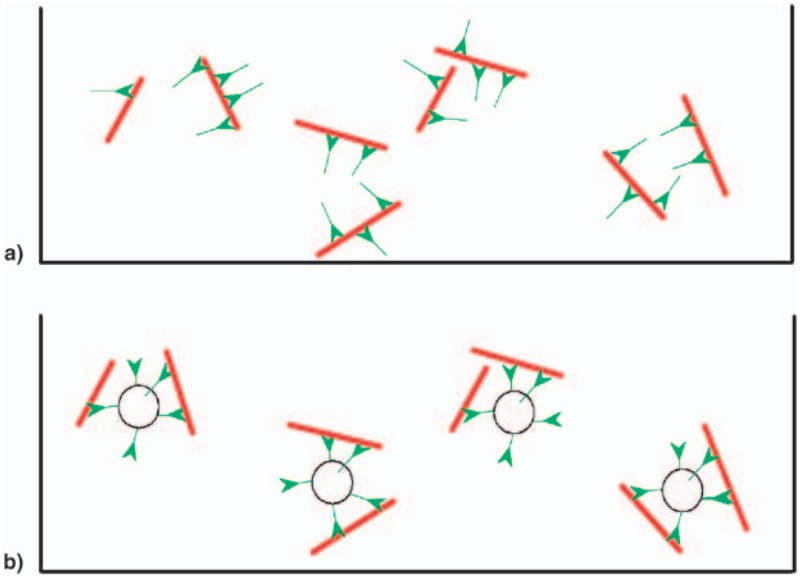

Plate 5 Schematic representation of protein–lipid interaction. Schematic view of (a) myosin II (green) and putative binding to actin (red) and (b) myosin II (bound to lipid vesicles) and actin (see page 234 in this volume).

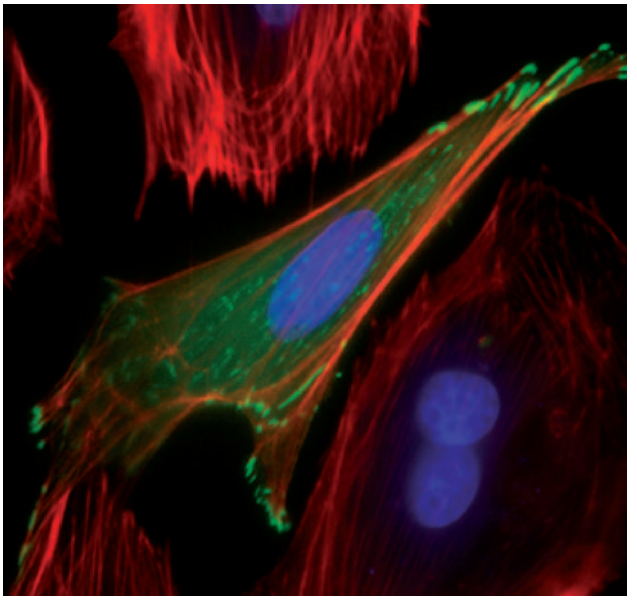

Plate 6 Fluorescence images. Fluorescence image of a single capillary endothelial cell expressing GFP-vinculin (green), stained for F-actin with Alexa phalloidin (red) and nuclei with DAPI (blue). Note: how each actin stress fiber is anchored into focal adhesions at its distal ends (bar = 10 μm). Reproduced with permission from Ref. [103], Copyright (c) 2006, Wiley-Liss, Inc. (see page 245 in this volume).

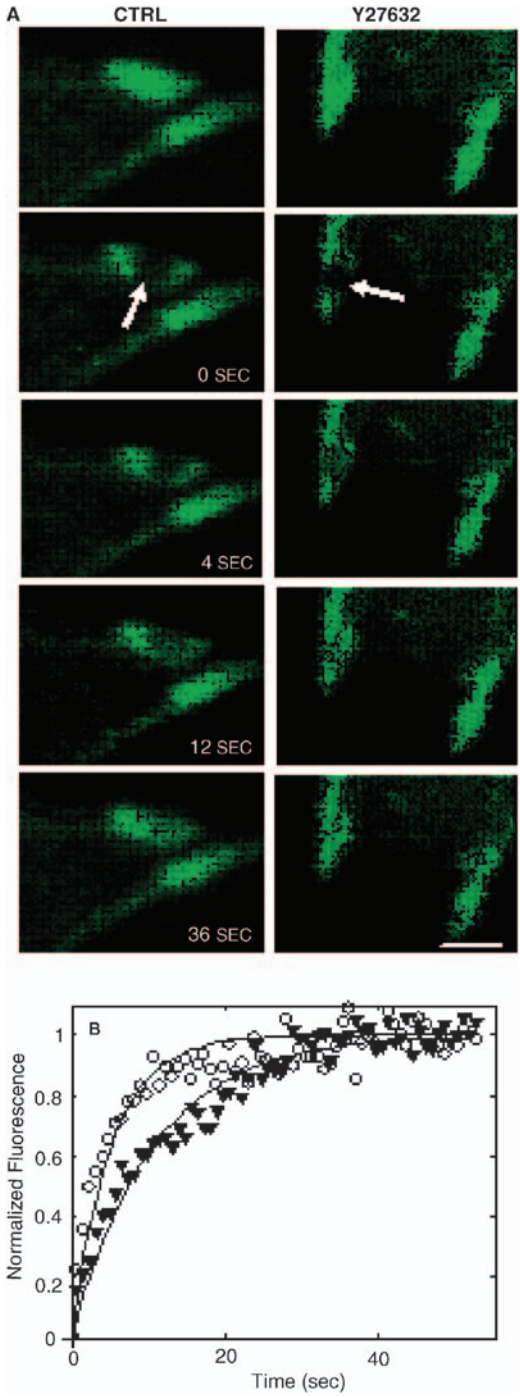

Plate 7 FRAP analysis of GFP zyxin recovery within individual photobleached focal adhesions. (A) Representative images of a FRAP experiment in control *versus* Y27632-treated cells showing that force dissipation accelerates zyxin recovery. Arrows indicate photobleached spots within individual focal adhesions that are analyzed over a period of 36 seconds follow photobleaching (bar = 2 μm). (B) Recovery curve for zyxin in control (open circles) *versus* Y27632-treated cells (closed triangles) from the experiment shown in A; solid lines are curves fit to the data using the method of least squares to estimate the dissociation rate constant k_{OFF} (see page 248 in this volume).

This page intentionally left blank